Theoretical Modelling of Flow in Rotor-Stator Systems

Mear-Stone, Izzi

Award date:
2015

Awarding institution:
University of Bath

Theoretical Modelling of Flow in Rotor-Stator Systems

Leah Isobel Mear - Stone

A thesis submitted for the degree of Doctor of Philosophy

University of Bath

Department of Mechanical Engineering

June 2015

Dedicated to

Susan and Colin Booth
You both encouraged me to start this journey and didn't get to see me finish. Whenever self doubt creeps in I try and remember your kind words.

David John Mear
I wish that I could have shared my venture into the world of engines with you.

Gone but never forgotten.

ACKNOWLEDGEMENTS

I would like to thank Prof. G. D. Lock and Dr M. Wilson for their supervision, advice and general encouragement. I am thankful to Prof. J. M. Owen for both his genuine interest in the work and his guidance throughout this piece of research. I am very grateful to Dr. GeonHwan Cho for his collaboration in the early stages of the buffer ratio model.

This research would not have been possible without the financial assistance of Siemens and the Engineering and Physical Sciences Research Council. I would also like to thank the Institute of Mathematics and Its Applications for awarding me with their travel fund to enable me to attend the 60th American Society of Mechanical Engineers Turbo Expo to present my lead author paper 'Theoretical model to determine effect of ingress on turbine discs', based on the work presented in Chapter 6.

It is also important for me to acknowledge the ongoing support of my family and friends for the last four years. Endless gratitude goes to my mum for the constant supply of pep talks. Chippy, Suze, Jack and all of Bath Roller Derby – thank you for being there and keeping me laughing.

ABSTRACT

The prevention of hot gas ingress between rotating and stationary discs in gas turbines is big business, with experimental and computational research being common in the sector. Experimental rigs, operating at a fraction of the engine size and in simulated fluid dynamic conditions, model the engine environment. Computational Fluid Dynamics (CFD) is used in both academia and industry to model the flow and heat transfer in a turbine. CFD is expensive, time consuming and requires detailed experimental validation. The engine designer has a need for simpler, faster mathematical modelling methods, ultimately to be used in 1D design codes. The research in this thesis stems from this need for the industrial engine designers to be able to predict the flow, pressure and temperatures in the secondary-air-system. Momentum-integral equations are known to model flow over rotating and stationary discs in isolation. This thesis shows that the momentum-integral equations can be solved together, to successfully model the flow inside a rotor and stator cavity.

New momentum-integral equations are derived, free of the incorrect assumption that swirl ratio inside a rotor-stator cavity does not vary with radius. Two cavity models are described based upon the momentum-integral equations: one for a closed cavity and one for a cavity with sealing flow and no ingress. Both are computationally fast and are shown to give good agreement with experimental measurements and CFD results. Detailed flow structures are given for a range of rotor-stator cavity cases and the results of the models allow conclusions about the flow structure to be drawn. It is found that the outer region, where flow leaves the rotor and is entrained by the stator, is not affected by sealing flow.

As well as complete cavity models, two other models for specific rotor-stator phenomenon have been derived. The effect of ingress on the swirl ratio in the cavity has been modelled, using a momentum balance approach. The buffer ratio and buffering effect, which quantify how the rotor is protected from ingress, have been defined, modelled and validated against measurements of adiabatic effectiveness for four different seal geometries. The model has allowed the calculation of $\Phi'_{min,r}$, the sealing flow rate where the effectiveness on the rotor reaches 95%.

CONTENTS

LIST OF FIGURES

NOMENCLATURE

a	Inner radius of disc
b	Outer radius of disc
BR	Buffer ratio
c	Concentration in the annulus
C_β	Modified swirl ratio
$C_{d,e},\ C_{d,i}$	Discharge coefficients for egress, ingress
$C_{M_o},\ C_{M_s}$	Moment coefficient for rotor or stator
C_P	Pressure coefficient
C_w	Non-dimensional flow rate $[= \dot{m}_o/\mu b]$
$C_{w,e}, C_{w,i}$	Values of C_w for egress, ingress
$C_{w,0}$	Non-dimensional flow rate of sealant
$C_{w,min}$	Minimum value of $C_{w,0}$ to prevent ingress
G	Gap ratio $[= s/b]$
G_c	Seal-clearance ratio $[= s_c/b]$
$\dot{m}$	Mass flow rate
M_o, M_s	Moment on rotor or stator
p	Static pressure
r	Radius
Re_w	Axial Reynolds number in annulus
Re_ϕ	Rotational Reynolds number $[= \rho\Omega b^2/\mu]$
Re'_ϕ	Modified Rotational Reynolds number $\left[= \beta Re_\phi\right]$
s	Distance between rotor and stator discs
s_c	Seal clearance
T	Temperature
T_{an}	Temperature of air in the annulus
T_{ad}	Adiabatic disc temperature
T^*_{ad}	Adiabatic disc temperature for $\Phi_o = \Phi_{min}$

v_r, v_ϕ, v_z	Radial, tangential and axial components of velocity
x	Non-dimensional radial location $[= r/b]$
x_a	Non-dimensional radial location $[= a/b]$
α	Ratio of radial to tangential shear stresses
β	Swirl ratio $[= v_\phi/\Omega r]$
γ	Coefficient of boundary layer thickness
Γ_c	Ratio of discharge coefficients $\left[= C_{d,i}/C_{d,e}\right]$
δ	Boundary layer thickness
$\Delta\, C_p$	Non-dimensional pressure difference
$\Delta\varepsilon$	Buffer effect $[= \varepsilon_r - \varepsilon_s]$
ε	Sealing effectiveness $\left[= C_{w,0}/C_{w,e} = \Phi_0/\Phi_e\right]$
ε_{ad}	Adiabatic effectiveness for rotor $[= (T_{ad} - T_{an})/(T^*_{ad} - T_{an})]$
ε_c	Concentration effectiveness $[= (c_s - c_a)/(c_0 - c_a)]$
ε_r	Effectiveness for rotor $[= (c_r - c_{an})/(c_o - c_{an})]$
ε_s	Effectiveness for stator $[= (c_s - c_{an})/(c_o - c_{an})]$
$\varepsilon_{m_o}, \varepsilon_{m_s}$	Coefficient of mass flow rate for rotor or stator
$\varepsilon_{M_0}, \varepsilon_{M_s}$	Coefficient of moment for rotor or stator
Θ	Ratio of sealing flow rates $[= \Phi_o/\Phi_{min}]$
τ_r	Radial component of shear
τ_ϕ	Tangential component of shear stress
Φ	Non-dimensional sealing parameter $\left[= C_w/2\pi G_c Re_\phi\right]$
λ_T	Turbulent flow parameter $[= 2\pi G_c Re_\phi^{0.2}\Phi_o]$
$\lambda_{T,min}$	Value of λ_T when $C_{w,o} = C_{w,min}$
μ	Dynamic viscosity
ρ	Density
Ω	Angular velocity of rotating disc

Subscripts

a	Superposed flow
ad	Adiabatic
an	Annulus
e	Egress
EI	Externally-induced ingress
i	Ingress
in	Inner Region
$\max$	Maximum
$\min$	Minimum
o	For the rotor / sealing flow for experimental papers
out	Outer region
RI	Rotationally-induced ingress
s	For the stator
0	Value at the surface of a disc
1	Value at $x = 1$
∞	Value far from surface of disc.

Superscripts

$*$	Value with no ingress
$'$	Value with ingress

Acronyms

CFD	Computational Fluid Dynamics
EI	Externally-induced ingress
InSF	Ingress, No Superposed Flow
MLE	Maximum Likelihood Estimation
NGV	Nozzle Guide Vane
ODE	Ordinary Differential Equation
PDE	Partial Differential Equation
RI	Rotationally-induced ingress
SFNI	Superposed Flow, No Ingress
TET	Turbine Entry Temperature

CHAPTER 1 : INTRODUCTION

1.1 FUNDAMENTALS OF TURBINES

A turbine is a rotating mechanism that converts enthalpy into work. There are three main types of turbine, each classified by the fluid they are powered by: steam, wind or gas. A gas turbine can generate a vast amount of power compared to its own size and weight. Gas turbines have three main uses: as engines within the aviation industry, as power generators within the industrial power industry and as mechanical drivers within the gas extraction industry. Depending upon the specific use of the turbine, it will be designed with different priorities: for example maximising life span for power generator turbines or minimising weight for aviation use. Regardless of which specific type of turbine is being considered, they all face the same problem of how to cool the turbine in the most effective way. In order to discuss the cooling system first the engine itself, where the turbine resides, needs to be understood.

1.2 THE JET ENGINE

One example of a gas turbine engine is the jet engine. Used to power aircraft, it is an internal combustion engine that works by utilising the theory of propulsion. This is the principle behind aircraft flight and it is based on Newton's third law, which is commonly phrased as 'to every action there is always an equal and opposite reaction'. Forces come in pairs, so if there is a force (for example created by expelling hot gas from the back of an engine) then in the opposite direction will be force equal to this (here called thrust which provides forward motion of an aeroplane). A jet engine has three main components; the compressor, combustor and turbine. A brief overview of how these components work will be given to allow a greater understanding of the important problems for a modern engine designer. Figure 1.1 shows the basic structure of a typical jet engine, where the flow moves through the engine from left to right.

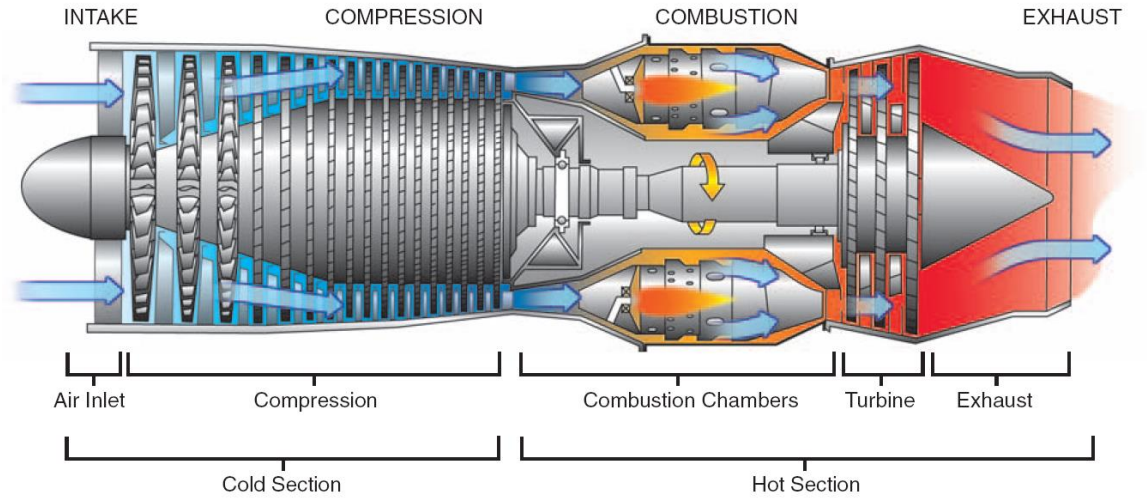

Figure 1.1: Basic structure of a jet engine. FAA (2004).

Stage One: Compressor.

The compressor consists of rows of alternating rotors and stators that reduce in size in the direction of flow. Each pair of one rotor and one stator is called a stage. There can be as many as 20 stages, where each rotor disc can have up to 100 blades.

The goal of the compressor is to make as large a pressure rise as possible; in other words to create a high pressure ratio. A typical compressor can have a pressure ratio of around 30:1, meaning the air leaving the compressor is 30 times more pressurised than that coming in. Inside the compressor, as the blades rotate, air travels over the rotor blades and is accelerated. During this process the kinetic energy of the air is increased. Next as the air travels through the stationary vanes it decelerates, causing its kinetic energy to be converted to pressure. This pressure is then increased incrementally across each stage. The rotors in the compressor are powered by the turbine, via a shaft that runs the length of the engine.

Stage Two: Combustor.

The combustor is where fuel is injected into the air and the mixture is ignited. This creates a sharp temperature increase; the aim is for this increase to be gained with the smallest pressure drop possible. The temperature of the gas as it leaves the combustor, called the turbine entry temperature (TET), is made as high as possible to obtain higher efficiencies. The specific power produced by the engine increases as the TET is increased, so obtaining the highest possible TET is desirable.

The TET inside a jet engine varies depending on the situation: at take off the TET will be the highest, a typical value in modern engines is around 1800 K. Whereas if the aircraft is at cruise, for example while flying over an ocean, the TET will be lower - this helps to preserve the life of the turbine components.

Stage Three: Turbine.

The turbine is where the thermal energy from the combustor can be extracted. It consists of multiple stages of rotor-stator pairs as in the compressor. As the gas exits the combustor it first travels through stator vanes, here called nozzle guide vanes (NGV). As it passes through these vanes the gas is accelerated and reaches close to the speed of sound. Due to the profile of the vanes the gas is then turned and moves over the turbine rotor blades which creates torque, in turn making the rotor disc rotate and the shaft spin (thus powering the compressor).

In the turbine the stator vanes and rotor blades are aligned to give the maximum turning angle possible, this allows the most work to be extracted from the gases. The turbine usually consists of two sections: the first is a high pressure, where the rotor-stator stages are subjected to the highest temperatures; then is the low pressure system, where the temperatures are reduced as the gas expands.

The materials in the turbine can and are subjected to temperatures higher than their melting points. This is made possible by taking some of the colder air from the compressor and using it to cool the materials in the turbine stage. This cooling is described further in the next section.

1.3 STRUCTURE AND COOLING OF THE TURBINE STAGE

The need for more efficient engines has been the driving factor behind a huge amount of research in the aero and power generation industries. The need for higher efficiencies and therefore higher TET has made the turbine stage subject to tremendous technological advances, most of which centres around its cooling system. This system must be perfectly balanced; if too much cooling flow is supplied then the benefits of the higher TET will be lost as the gas is cooled too much, if not enough

cooling flow is supplied then the engine life span will be affected as the materials are subject to high temperatures. With the design of a fine-tuned cooling system the turbine is able to operate at higher temperatures and efficiencies than ever: this saves money and creates an engine with less environmental impact.

1.3.1 STRUCTURE

In the previous section a brief overview of how the turbine works, and fits into the entire engine, was given. In this section some of the more technical terms are explained to pave the way to explaining the process of modelling a single stage rotor-stator system. The inner workings of a complete turbine are complicated and vary slightly for each engine they are designed for. Figure 1.2 shows a typical turbine stage.

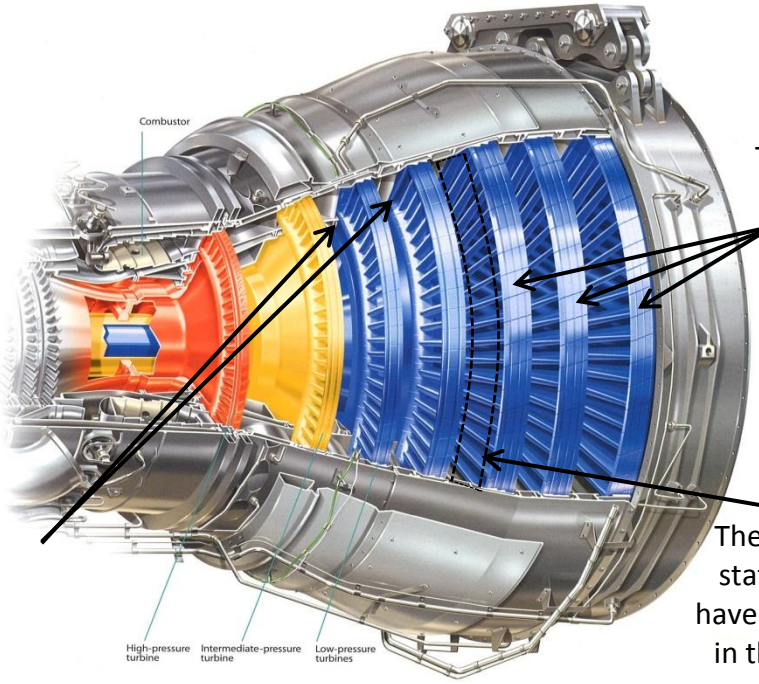

Figure 1.2: Example turbine stage in an engine. Rolls-Royce (2005).

In the turbine there are rows of alternating discs; one stationary (called a *stator*) and one rotating (called a *rotor*), each pair creating one stage. As the turbine consists of many single rotor-stator stages and as the flow physics is similar in each, often only one stage need be considered at a time. The space between the two discs is called a *wheelspace*. The area above the wheelspace, where the hot gas flows through the rotor blades and stationary vanes, is called the *annulus*. The flow travelling through the vanes and blades in the annulus is called the *mainstream* flow. Any flow from further along the stage being considered is called *downstream* and any flow from further back in the turbine is called *upstream*. Stopping hot mainstream flow from entering the wheelspace is crucial in limiting damage to the discs. When hot mainstream gas enters the wheelspace, this is called *ingress*.

A more detailed single stage rotor-stator configuration is shown in Figure 1.3. Beneath the NGVs and the rotor blades is a *rim seal*, it is this that stops some of the flow from the annulus entering into the wheelspace. The rim seal shown in Figure 1.3 is a simple lip, extending from both the rotor and stator, with a gap in the axial direction. The gap between the seal, the *seal clearance*, must be as small as possible while still enabling the rotor to move. The exact design of these rim seals is subject to

much research by engine manufacturers. The benefits of different rim seal designs are explored in the literature review.

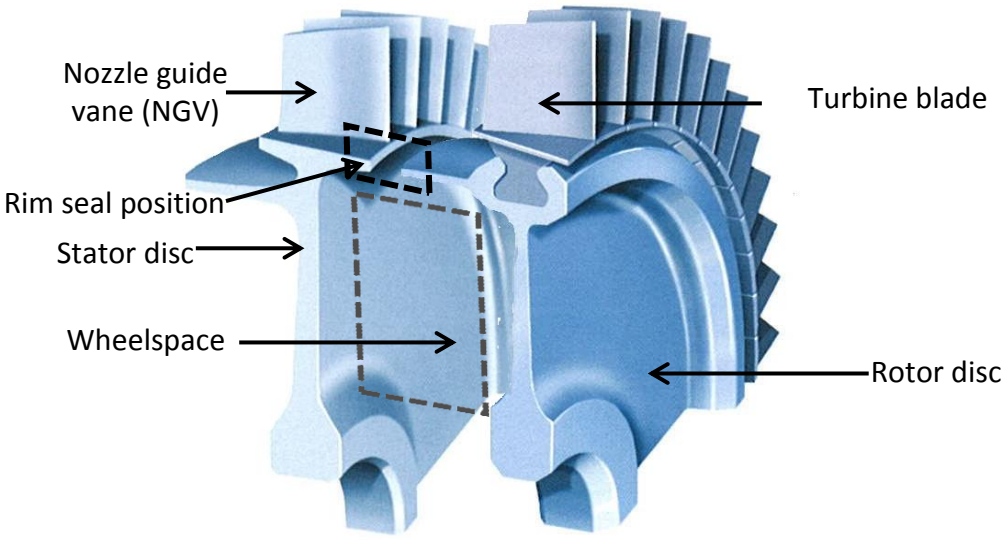

Figure 1.3: Close up of a quarter of a rotor-stator disc system. Adapted from Rolls Royce (2005).

1.3.2 COOLING

A fraction of the air in the compressor is diverted straight to the turbine to use as *cooling air*. Cooling air that is taken from the compressor will be used in two ways in a single turbine stage. It will either be supplied directly to the base of the wheelspace to pressurise the cavity in the aim of preventing ingress, or it will be used to cool blades and vanes. As the mainstream flow is gas straight from the combustor it is often above the melting point of the blades and vanes. Cooling air is directed into passages inside the blades and vanes which exit through small holes creating a film of cool air on the surface of the metals, protecting them. Film cooling is not directly related to this work; only the use of cooling air to pressurise the wheelspace cavity will be considered.

Mainstream flow not only enters the wheelspace but also leaves it again. The flow of gas from the annulus into the wheelspace is called *ingress* and the flow of gas in the opposite direction, from the wheelspace into the annulus, is called *egress*. The flow is always due to pressure differences between the annulus and the wheelspace, but there are multiple causes of these pressure differences. The flow through the vanes and blades in the annulus creates a non-axisymmetric unsteady distribution of pressure. This causes *Externally Induced (EI) Ingress:* where ingress occurs due to the annulus pressure being greater than the pressure in the wheelspace.

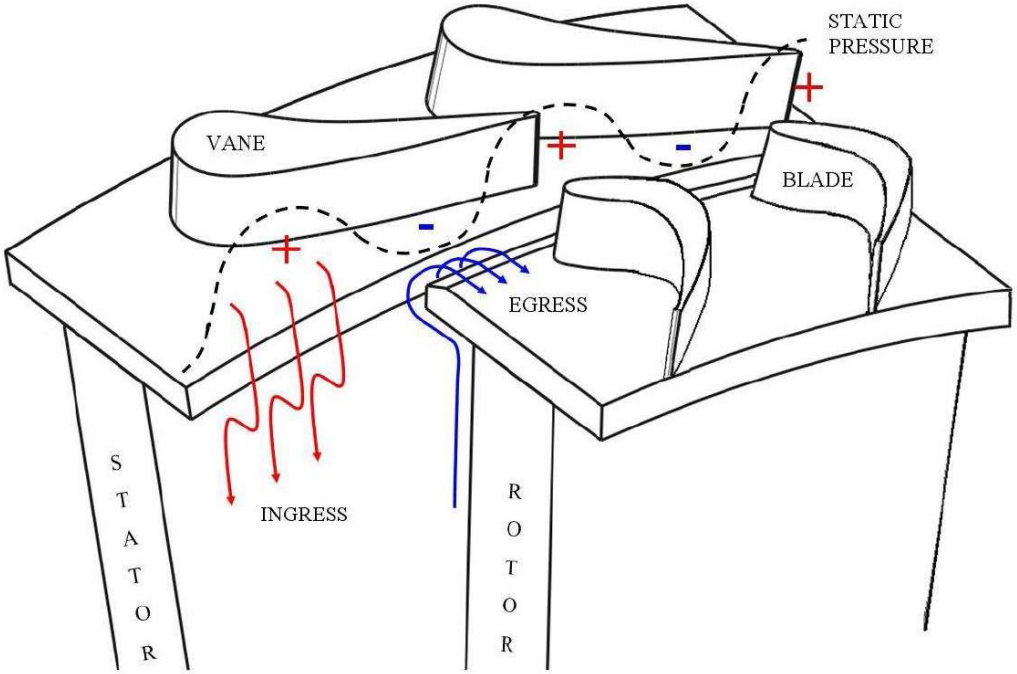

Figure 1.4: Variation of static pressure in a turbine annulus. Red arrows indicate hot-gas ingress and blue cooler egress; corresponding to regions of high and low pressure with respect to the wheelspace, respectively. Sangan (2011).

Another cause of pressure differences is the rotor disc itself. When the disc rotates a radial pressure gradient is created that forces fluid radially outwards, causing egress. This pressure gradient can cause the pressure in the wheelspace to be lower than that in the annulus, causing fluid to move into the wheelspace. This is known as *Rotationally Induced (RI) Ingress.* These two causes are not mutually exclusive, so hot gas can enter the wheelspace because of a combination of both situations described above occurring simultaneously, called *Combined Ingress.*

As explained earlier, to reduce the amount of ingress into the wheelspace, air is taken from the compressor and used to pressurise the cavity. As well as being called *cooling air* the terms *sealing air* or simply *superposed flow* can be used. The less sealing air that is used the better, as any excess sealing air will enter the annulus and reduce the original benefits of raising the TET Different rim seals can be used to minimise the amount of sealing air needed to prevent ingress into the wheelspace.

1.4 RESEARCHING THE INGRESS PROBLEM

Experimental research has often led the way for studying the problem of ingress into rotor-stator cavities. By studying how different seals and different amounts of sealing air affect the amount of ingress into a single rotor-stator stage, a greater understanding of the fundamental flow physics within rotor-stator systems is gained. This can inform better engine design through fine tuning both cavity geometries and the amount of sealing flow being supplied. Companies in the gas turbine industry invest a lot of time and money into the design of gas turbines, and any tools that allow costs to be minimised are highly beneficial. Small scale experimental studies are often cheaper than manufacturing and testing full scale engine components. The results can then be scaled to give information about how the components would perform in a full size engine.

As computing power has advanced, computational fluid dynamics (CFD) has

become more useful. CFD involves using a computer-aided design (CAD) model of part of the engine geometry and standard numerical solvers with turbulence models to model the fluid flow. One of the key benefits of using CFD over experimental studies is that highly complex designs that would be expensive to manufacture can be tested easily. Also, models with full scale engine geometries and conditions can be tested, so no scaling is necessary. The downside to this type of testing is that full 3D CFD can take a very long time to produce results (months in some cases) even with high performance computing facilities and CFD models still need to be validated experimentally. Another less used approach is developing theoretical models of the fluid flow. Theoretical modelling has the advantage of being the fastest choice, but it involve solving difficult nonlinear equations and will likely never be accepted by designers and the wider scientific community without extensive validation against experimental data. Still, given the low cost and fast results, it could be argued that theoretical models are of great use to engine designers. Fast models that yield simple approximate results are the type of research that can offer direct benefit, if implemented within 1D design codes. The more accurate the modelling of the individual engine components with a 1D flow code (such as a single rotor-stator cavity), the better informed designers can be from the outset, and the better their designs can ultimately be.

Following on from the extensive experimental work that has been carried out in the University of Bath, details to follow in Chapter 2, the aim of this work is to attempt to replicate the experimental results through theoretical modelling of rotor-stator cavities. This is with an aim to further the understanding of the influence of ingress on the wheelspace. Boundary layer theory has led to the momentum-integral equations that can be used to model flow over rotating and stationary discs. This work will bring together the separate rotor and stator equations and solve them together, creating a simple flow model for a rotor-stator cavity that may be of use to engine designers. The rest of this introduction will outline the background of the momentum-integral equations.

1.5 HISTORY OF THE MOMENTUM-INTEGRAL EQUATIONS

1.5.1 NAVIER-STOKES EQUATIONS

The Navier-Stokes equations are the basic equations for modelling fluid flow. They were originally derived in the 1840s and are partial different equations (PDEs). The exact terms to appear in the equations will be different if the flow being modelled is assumed to be incompressible or compressible, steady or unsteady, 2-dimensional or 3-dimensional. If the fluid flowing over a disc is being modelled then the velocity of the fluid (given in cylindrical coordinates) at location (r, ϕ, z) is $\mathbf{v} = (v_r, v_\phi, v_z)$ where v_r, v_z and v_ϕ are the *radial, axial* and *tangential velocities* of the fluid, respectively. The *Navier-Stokes equations for laminar, incompressible, steady, axisymmetric flow* are given by:

$$\left.\begin{aligned} v_r\frac{\partial v_r}{\partial r}+v_z\frac{\partial v_r}{\partial z}-\frac{v_\phi^2}{r}&=-\frac{1}{\rho}\frac{\partial p}{\partial r}+\nu\left(\nabla^2 v_r-\frac{v_r}{r^2}\right)\\ v_r\frac{\partial v_\phi}{\partial r}+v_z\frac{\partial v_\phi}{\partial z}+\frac{v_r v_\phi}{r}&=\nu\left(\nabla^2 v_\phi-\frac{v_\phi}{r^2}\right)\\ v_r\frac{\partial v_z}{\partial r}+v_z\frac{\partial v_z}{\partial z}&=-\frac{1}{\rho}\frac{\partial p}{\partial z}+\nabla^2 v_z \end{aligned}\right\} \tag{1.1}$$

where

$$\nabla^2=\frac{\partial^2}{\partial r^2}+\frac{1}{r}\frac{\partial}{\partial r}+\frac{\partial^2}{\partial z^2}$$

and p is the static pressure. When modelling fluid flow the Navier-Stokes equations are not used alone. The *Continuity Equation* is used to take account of the continuity of mass, given by

$$\frac{\partial v_r}{\partial r}+\frac{v_r}{r}+\frac{\partial v_z}{\partial z}=0 \tag{1.2}$$

which gives a constraint that the velocities must satisfy. *The Continuity Equation* and the *Navier-Stokes equations for turbulent, incompressible, steady, axisymmetric flow* are given by:

$$\left.\begin{aligned} \frac{\partial \bar{v}_r}{\partial r}+\frac{\bar{v}_r}{r}+\frac{\partial \bar{v}_z}{\partial z}&=0\\ \bar{v}_r\frac{\partial \bar{v}_r}{\partial r}+\bar{v}_z\frac{\partial \bar{v}_r}{\partial z}-\frac{\bar{v}_\phi^2}{r}&=-\frac{1}{\rho}\frac{\partial \bar{p}}{\partial r}+\nu\left(\nabla^2\bar{v}_r-\frac{\bar{v}_r}{r^2}\right)-\frac{1}{r}\frac{\partial\left(r\overline{v'_r{}^2}\right)}{\partial r}-\frac{1}{r}\frac{\partial(\overline{v'_r v'_z})}{\partial z}+\frac{\left(\overline{v'_\phi{}^2}\right)}{r}\\ \bar{v}_r\frac{\partial \bar{v}_\phi}{\partial r}+\bar{v}_z\frac{\partial \bar{v}_\phi}{\partial z}+\frac{\bar{v}_r\bar{v}_\phi}{r}&=\nu\left(\nabla^2\bar{v}_\phi-\frac{\bar{v}_\phi}{r^2}\right)-\frac{1}{r}\frac{\partial\left(r\overline{v'_\phi v'_r}\right)}{\partial r}-\frac{\partial\left(\overline{v'_\phi v'_z}\right)}{\partial z}+\frac{\left(\overline{v'_r v'_\phi}\right)}{r}\\ \bar{v}_r\frac{\partial \bar{v}_z}{\partial r}+\bar{v}_z\frac{\partial \bar{v}_z}{\partial z}&=-\frac{1}{\rho}\frac{\partial \bar{p}}{\partial z}+\nu\nabla^2\bar{v}_z-\frac{1}{r}\frac{\partial(r\overline{v'_z v'_r})}{\partial r}-\frac{\partial\left(\overline{v'_z{}^2}\right)}{\partial z} \end{aligned}\right\} \tag{1.3}$$

The velocities in the turbulent equations are given by the Reynolds decomposition, this is when a quantity such as velocity, v, is segmented into two parts: average and fluctuating. For example: $\mathrm{v_i}=\overline{\mathrm{v}}_\mathrm{i}+\mathrm{v}'_\mathrm{i}$. The over-bar denotes the average part and the prime denotes the fluctuating part. The average part can be gained by a time-average or a space-average and is actually a numerical operator called the Reynolds operator, which has its own algebraic rules. The extra terms on the right hand side of the turbulent equations ($\overline{(\mathrm{v}'.\nabla)\mathrm{v}'}$ in vector notation) are due to extra stresses caused by the turbulence of the fluid and are called Reynolds stresses.

The flows of interest within gas turbines are highly turbulent, so if these flows are to be modelled it is the turbulent equations that must be solved. This is a difficult task as the solutions to the Navier-Stokes equations for turbulent flow are 3D and time-dependent. Some solutions can be found numerically and as computational power has increased there are more and more numerical turbulence models trying to do just that. These are explored in Chapter 2. It is worth noting that it is not yet known if solutions *always* exist for the Navier-Stokes equations. Some analytical solutions exist, for example for the case of laminar steady flow. The Clay Mathematics Institute has a list of *Millennium Prize Problems* that contains some of the most important unsolved problems in the world of mathematics today. The *Navier-Stokes smoothness and existence* problem features on this list.

1.5.2 BOUNDARY LAYER EQUATIONS

Before the Navier-Stokes equations had been developed, the theory of 'ideal' (now known as *inviscid*) fluids was the only method used to model fluid flow. Inviscid fluids have no resistance to shear stresses. The equations of motion as stated by Euler gave the basis of the model. The results found by this theory did not correspond to what was seen experimentally. It gave rise to d'Alembert's paradox which stated that no drag acts on a body that moves through a fluid. It was the neglect of viscous forces that caused this paradox. A separate branch of science developed, studying the interactions of *viscous* fluids. In this theory the interactions of the particles were considered. This branch gave rise to the Navier-Stokes equations and was developed alongside experimental data for validation. It remained separate from the study of inviscid flow and this separation caused a problem. The conditions at the boundary, where a solid surface and a fluid meet, were constantly in question. Either there was *slip*, meaning tangential velocity was positive, or there was *no slip*, meaning relative velocity at the surface was zero. For slow moving fluids it could be seen experimentally that there was no slip. For faster moving fluids this condition could not be seen. Prandtl (1905) had a theory, which came to be known as the theory of boundary layers, which allowed the two branches of science to merge. The paper directly addressed the problem of the condition at the boundary. Prandtl considered a surface with fluid flowing over it and suggested that far from the surface, the viscous forces were negligible and very close to the surface, they had to be taken into account. So there was no slip on the surface but the velocity increased to some value, given by the theory of inviscid flow. Until this value was reached the flow was contained in a thin layer, coined a *boundary layer*. In this layer the theory of viscous flow, namely the Navier-Stokes equations with new assumptions, could be applied.

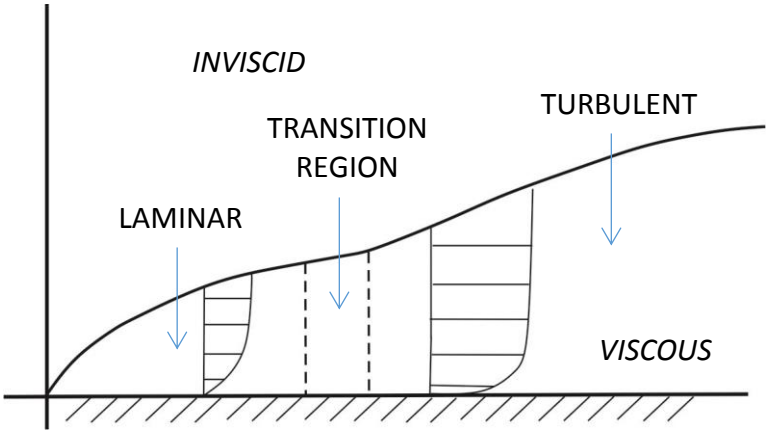

Figure 1.5: Classic boundary layer flow profile over a flat plate

Figure 1.5 shows the development of a boundary layer over a flat plate. The boundary layer thickness grows with distance from the leading edge. To start the flow is laminar but can transition to turbulent flow. Dividing the flow into viscous and inviscid areas made the problem easier to solve. By carrying out an order of magnitude analysis (where the approximate magnitude of each term in an equation is found, and then any terms with small magnitude may be ignored), Prandtl derived what came to be known as *the boundary layer equations:*

$$\left.\begin{aligned} \frac{\partial v_r}{\partial r}+\frac{v_r}{r}+\frac{\partial v_z}{\partial z}&=0 \\ v_r\frac{\partial v_r}{\partial r}+v_z\frac{\partial v_r}{\partial z}-\frac{v_\phi^2}{r}&=-\frac{1}{\rho}\frac{\partial p}{\partial r}+\frac{1}{\rho}\frac{\partial \tau_r}{\partial z} \\ v_r\frac{\partial v_\phi}{\partial r}+v_z\frac{\partial v_\phi}{\partial z}+\frac{v_r v_\phi}{r}&=\frac{1}{\rho}\frac{\partial \tau_\phi}{\partial z} \\ 0&=-\frac{\partial p}{\partial z} \end{aligned}\right\} \quad (1.4)$$

where τ_r is the *radial shear stress* and τ_ϕ is the *tangential shear stress.* These were derived from the continuity equation and the Navier-Stokes equations as stated in (1.3), using the boundary layer assumptions as summarised by Owen and Rogers (1989) for a rotor-stator system (as shown in Figure 1.3):

1. The axial component of velocity is much smaller in magnitude than the tangential or radial components of velocity: $|v_z| \ll |v_\phi|, |v_r| \Rightarrow v_z \approx 0$. (As very little flow is seen to move axially in rotor-stator systems).
2. The rate of change of any variable (except pressure) axially is greater than its rate of change radially or tangentially: $\frac{\partial \mathbf{v}}{\partial z} \gg \frac{\partial \mathbf{v}}{\partial r}$ and $\frac{\partial \mathbf{v}}{\partial z} \gg \frac{\partial \mathbf{v}}{\partial \phi} \Rightarrow \frac{\partial \mathbf{v}}{\partial r}, \frac{\partial \mathbf{v}}{\partial \phi} \approx 0$. (As properties such as the velocity vary greatly from the stator to the rotor).
3. Pressure is only a function of radius: $p = p(r) \Rightarrow \frac{\partial p}{\partial \phi}, \frac{\partial p}{\partial z} = 0$.

These assumptions are valid over most of the system, based on expected behaviour, for modelling flow within the boundary layers in a rotor-stator system. A rotor-stator system is described in detail in Chapter 3. The boundary layer equations are still partial differential equations, but they are parabolic instead of elliptic. This simplification allows approximate solutions to be found. Blasius (1908) provided further details into the concepts set out in Prandtl (1905) and soon the theory that started out as equations for steady two dimensional laminar boundary layer flow were expanded upon. Equations were derived for the cases of three-dimensional laminar and turbulent flow.

Firstly, the pressure far from the disc can be replaced by p_c to denote the pressure in the core. Secondly assuming the flow in the core is inviscid the following expression can be applied: $\partial p/\partial r = -v^2{}_{\phi,\infty}/r$. The three simplified boundary layer equations are the *continuity equation,*

$$\frac{\partial (r v_r)}{\partial r}+\frac{\partial (r v_z)}{\partial z}=0 \quad (1.5)$$

the *radial momentum equation*,

$$\frac{\partial (r {v_r}^2)}{\partial r}+\frac{\partial (r v_z v_r)}{\partial z}-v_\phi^2=-v_{\phi,\infty}^2+\frac{r}{\rho}\frac{\partial \tau_r}{\partial z} \quad (1.6)$$

and the *tangential momentum equation,*

$$\frac{\partial \left(r^2 v_r v_\phi\right)}{\partial r}+\frac{\partial \left(r^2 v_z v_\phi\right)}{\partial z}=\frac{r^2}{\rho}\frac{\partial \tau_\phi}{\partial z}. \quad (1.7)$$

These equations model incompressible, axisymmetric, steady and turbulent flow. They can be approximated by the momentum-integral equations which will be described in the next chapter.

1.6 OBJECTIVES

The main objective of this work is to theoretically model the different flow structures occurring in a single stage rotor-stator cavity, principally through the solving of the momentum-integral equations. This involves predicting the flow structures and behaviour in four key situations:

- Closed Cavity: flow between a rotor and stator where no fluid enters or leaves the system.
- Superposed Flow, No Ingress: where sealing air is supplied to the cavity but there is no ingress into the system.
- Ingress, No Superposed Flow: where there is ingress into the system but no sealing air is supplied.
- Ingress and Superposed Flow: where there is flow entering and leaving the wheelspace.

In the past the momentum-integral equations have been defined to model fluid flow over a rotating disc and a stationary disc. The aim is to couple and then solve the separate momentum-integral equations to model the recirculating flow between a rotor and stator disc. The models should:

- Be able to predict radial variations of swirl ratio and mass flow rates within the cavity, as well as moment and pressure coefficients.
- Study the effect of sealing flow rate on above quantities.
- Have a short computation time (making the model useful for implementation into design codes) and to not be too computationally intensive (i.e. able to run on one desktop computer without the need for parallel processing).
- Be validated against available experimental and computational results.

The momentum-integral equations in their current form have been derived assuming that swirl ratio in the rotor-stator cavity is constant. It has been shown experimentally that this is not the case. Another objective is to derive the momentum-integral equations where swirl ratio is *not* assumed to be constant with radius, then to also model the cavities using these new equations, assessing the differences between the solutions to these new momentum-integral equations and the original equations.

1.7 THESIS OVERVIEW

Chapter 1 has given context to the research, detailing the wider background of the specific problem to be modelled in this work.

Chapter 2 contains a review of the relative literature concerning the study of rotor-stator systems from a sealing air systems perspective. The review covers three types of literature: experimental results from small-scale engine representative rigs, results given by computational fluid dynamics and those presenting mathematical models applicable to rotor-stator systems.

Chapter 3 describes the first of two cavity models. A hypothesised flow structure is given for a rotor-stator system that has no flow entering or leaving its cavity, along

with details of an iterative scheme that solves the original momentum-integral equations to model the flow within the cavity. The results are compared to experimental data and the comparison is qualitatively good. The variable momentum-integral equations are derived and a second version of the iterative cavity model is detailed, once again giving qualitatively good results.

Chapter 4 describes the derivation of a model for a rotor-stator system with sealing flow, otherwise known as superposed flow, being supplied to the system at a low radial location. For this case the cavity is split into two distinct models: one for the lower part of the cavity where the flow behaves differently and one for the rest of the cavity. Two iterative solution methods are given: one for the original momentum-integral equations and one for the variable momentum-integral equations. Results are stated for both and compared. The Superposed Flow No Ingress based upon the variable equations shows very good agreement with the swirl ratio distribution from the no ingress CFD model of Lalwani (2014). Good agreement is also gained between the Superposed Flow No Ingress model and experimental measurements of swirl ratio: for an axial seal subject to RI ingress the model initially over predicts the swirl ratio at low sealing flow rates, but as the flow rate increases and the cavity becomes closer to being sealed the agreement improved, with very good agreement at the sealed case.

Chapter 5 describes a model for the effect of ingress on the exit swirl ratio. The model is based upon momentum-balance within the seal clearance and validated against experimental measurements of swirl ratio. The model agrees well with experimental swirl ratio data from a single and double axial seal.

Chapter 6 considers the flow structure in the case of sealing flow and ingress. A theoretical model for the buffering that occurs on the rotor within the wheelspace in the presence of sealing air is detailed, as well as an empirical model for fitting rotor effectiveness measurements.

Chapter 7 states the conclusions of the work, along with recommendations for future work.

It should be noted that part of the unique work for this thesis are the derivations of the *variable momentum-integral equations*. These derivations have been relegated to the appendix in order to make the thesis more reader-friendly and to maintain the flow of the document. It is hoped that the reader will not let this negate their importance.

1.8 PUBLICATIONS

This thesis has produced one publication, based on the work of Chapter 6, which is to be presented at the 2015 ASME Conference in Montreal, Canada:

Mear, I., Owen, J. M., and Lock, G. D., 2015, "Theoretical Model to Determine Effect of Ingress on Turbine Discs" ASME Paper GT2015-42326.

Another publication is in preparation, based on the work of Chapter 3 and 4, with the new equations derived in the Appendix:

*Mear, I., Owen, J. M., and Lock, G. D., 2016, "*Boundary-layer Models for Turbulent Flow in Rotor-Stator Systems*".*

CHAPTER 2 : LITERATURE REVIEW

This literature review is divided into three sections: the background to the momentum-integral equations, the flow structure between a rotor and stator, and finally, relevant studies on ingress.

Section 2.1 follows directly from Chapter 1 where the boundary layer equations were defined. The momentum-integral equations, introduced by von Karman to approximate the boundary layer equations, will be used extensively in this work, so the background of the equations is presented here. The modelling of fluid flow over rotating and stationary discs by the use of the momentum-integral equations is summarised. Three physical situations are modelled: a rotor in stationary fluid, a rotor in rotating fluid and a stator in rotating fluid.

Section 2.2 looks at research around on the basic flow structure between a rotor and a stator, specifically at engine-representative conditions. Velocity profiles are considered and flow regimes relevant to engine conditions are identified.

Finally, Section 2.3 looks at studies concerning rotor-stator system with ingress. Studies looking at how the amount of ingress can be quantified are summarised and the advantages of the three branches of research (experimental, theoretical and computational) are accessed.

2.1 MOMENTUM INTEGRAL EQUATIONS

A method to find an approximate solution to the boundary layer equations (1.5)-(1.7) was first set out by von Karman (1921). New ordinary differential equations (ODEs) were derived to approximate the boundary layer equations. These approximate equations are easier to solve, as instead of finding a solution that satisfies the partial differential equations (1.5)-(1.7) at every point, a solution to the new equations can be found where the solution satisfies the same boundary conditions of the original problem. These new ODEs were gained by integrating the original PDEs across the boundary layer from $z = 0$ to $z = \delta$ using the following boundary conditions:

$$\begin{gathered} v_r(0) = 0, v_z(0) = 0 \; and \; v_\phi(0) = v_{\phi,0}, \tau_r(0) = \tau_{r,0}, \tau_\phi(0) = \tau_{\phi,0} \; at \; z = 0 \\ v_r \to 0, v_z \to v_{z,\infty}, v_\phi \to v_{\phi,\infty}, \tau_r \to 0, \tau_\phi \to 0 \; at \; z = \delta \end{gathered} \tag{2.1}$$

where the subscript notation '∞' means the value far from the disc and '0' means on the surface of the disc. Once integrated and rearranged (1.5)-(1.7) become what are known as the *momentum-integral equations:*

$$\dot{m}_0 = 2\pi r \rho \int_0^\delta v_r \, dz \tag{2.2}$$

$$\frac{d}{dr}\left(r \int_0^\delta v_r^2 dz \right) - \int_0^\delta \left(v_\phi^2 - v_{\phi,\infty}^2 \right) dz = -\frac{r}{\rho} \tau_{r,0} \tag{2.3}$$

$$\frac{d}{dr}\left(r^2 \int_0^\delta v_r (v_\phi - v_{\phi,\infty}) dz \right) + \frac{\dot{m}_0}{2\pi\rho} \frac{d\left(r v_{\phi,\infty} \right)}{dr} = -\frac{r^2}{\rho} \tau_{\phi,0} \tag{2.4}$$

In the paper von Karman also solved these equations numerically for different physical scenarios by employing 'similarity solutions'. The solution is *assumed* to have a certain form and this is then used to find the true solution. The assumed forms of the velocities are

$$v_r(z) = \alpha(r)\left[v_{\phi,0}(r) - v_{\phi,\infty}(r)\right]f(\eta) \tag{2.5}$$

$$v_\phi(z) = v_{\phi,0}(r) - \left[v_{\phi,0}(r) - v_{\phi,\infty}(r)\right]g(\eta) \tag{2.6}$$

where

- $\eta = z/\delta$ is the non-dimensional boundary layer thickness, so $0 \leq \eta \leq 1$.
- $\alpha(r) = \tau_{r,0}/\tau_{\phi,0}$
- $f(\eta)$ and $g(\eta)$ are chosen to give good approximations to the velocity profiles.

Although $f(\eta)$ and $g(\eta)$ are functions that are chosen, there are constraints on their form because they have to allow v_r and v_ϕ to satisfy the boundary conditions as given above. This means $f(\eta)$ and $g(\eta)$ must satisfy the following:

$$f(0) = 0, f(1) = 0 \text{ and } g(0) = 0, g(1) = 1 \tag{2.7}$$

To find a form for these functions von Karman (1921) suggested the use of the *1/7th power law profiles*:

$$f(\eta) = \eta^{\frac{1}{7}}(1 - \eta) \text{ and } g(\eta) = \eta^{\frac{1}{7}} \tag{2.8}$$

which can be used in (2.5) and (2.6).

2.1.1 HISTORY OF THE 1/NTH POWER LAW

These profiles were originally found to give good approximations for the velocity profiles of turbulent flow in pipes. The general power-law velocity equation for pipe flow, as stated in Owen and Rogers (1989), is given by

$$\frac{u}{v^*} = C\left(\frac{\rho v^* z}{\mu}\right)^{\frac{1}{n}} \tag{2.9}$$

where u is the component of velocity parallel with the pipe, z is normal to the pipe and v^* is the frictional velocity, defined as

$$v^* = \left(\frac{\tau_0}{\rho}\right)^{\frac{1}{2}} \tag{2.10}$$

and τ_0 is the shear stress at the surface. For turbulent pipe flow both C and n are found empirically to give good agreement for the velocity profiles at different Reynolds numbers. Nikuradse (1932) validated equation (2.9) experimentally, showing that provided n increases as Reynolds number increases the equation holds. Figure 2.1 shows experimental validation for four different Reynolds numbers, stated at the top of each plot. Within the plot R denotes the length of the pipe.

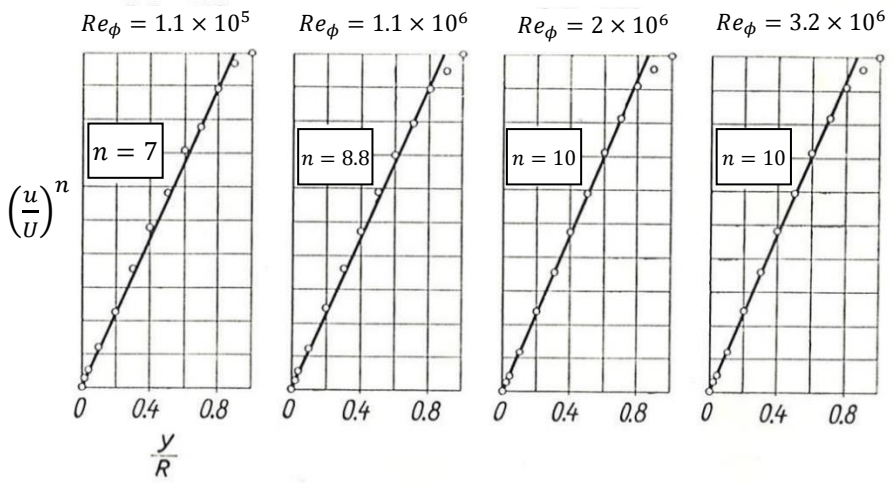

Figure 2.1: Velocity distribution in smooth pipes. Verification of the assumption in equation (2.9). Adapted from Schlichting (1968).

Equations (2.9) and (2.10) can be restated to give

$$\frac{\tau_0}{\rho U^2} = K\left(\frac{\nu}{Ub}\right)^{\frac{2}{n+1}} \tag{2.11}$$

where b is the radius of the pipe, U is velocity at the axis of the pipe and $K := C^{-\frac{2n}{n+1}}$. Values of C and K were found by Wieghardt (1946), as stated in Table 2.1 (taken from Owen and Rogers (1989)).

$\boldsymbol{n}$	7	8	9	10
$\boldsymbol{C(n)}$	8.74	9.71	10.6	11.5
$\boldsymbol{K(n)}$	0.0225	0.0176	0.0143	0.0118

Table 2.1: Empirical constants of Wieghardt (1946)

The power law profile along with the values found by Wieghardt (1946) approximate the velocity profiles well over a range of different Reynolds numbers. Logarithmic power laws were also derived, but these are difficult to work with algebraically, and so the $1/n$ power law was favoured. According to Owen and Rogers (1989) by choosing the appropriate n (and therefore C) in the power law equation for a given Reynolds number, the difference between the logarithmic and the power law velocity profile is less than 1%.

Substitution of the power law

By using (2.8) in the velocity profiles (2.5) and (2.6), and substituting those similarity solutions into (2.2), (2.3) and (2.4) the momentum-integral equations have a form where some of the integrals can be explicitly evaluated:

$$\dot{m}_0 = 2\pi r\rho\alpha\left(v_{\phi,0} - v_{\phi,\infty}\right)\int_0^\delta \eta^{\frac{1}{7}}(1-\eta)\,dz \tag{2.12}$$

$$\frac{d}{dr}\left(r\alpha^2\left(v_{\phi,0} - v_{\phi,\infty}\right)^2\int_0^\delta \eta^{\frac{2}{7}}(1-\eta)^2 dz\right) - \int_0^\delta\left(\left[v_{\phi,0} - \left(v_{\phi,0} - v_{\phi,\infty}\right)\zeta^{\frac{1}{7}}\right]^2 - v_{\phi,\infty}^2\right)dz = -\frac{r}{\rho}\tau_{r,0} \tag{2.13}$$

$$\frac{d}{dr}\left(r^2\alpha\left(v_{\phi,0}-v_{\phi,\infty}\right)\int_0^{\delta}\eta^{\frac{1}{7}}(1-\eta)\left\{v_{\phi,0}-\left[v_{\phi,0}-v_{\phi,\infty}\right]\eta^{\frac{1}{7}}-v_{\phi,\infty}\right\}dz\right) + \frac{\dot{m}_0}{2\pi\rho}\frac{d\left(rv_{\phi,\infty}\right)}{dr} = -\frac{r^2}{\rho}\tau_{\phi,0} \tag{2.14}$$

Notice that $v_{\phi,0}$ and $v_{\phi,\infty}$ do not depend on η, so can be taken outside of the integrals. These integrals can then be evaluated by applying a change of variables ($dz = \delta\, d\eta$), and simplification will yield three equations expressed only in terms of ODEs, with no integrals:

$$\dot{m}_0 = \frac{49\pi}{60}\rho r\alpha\left(v_{\phi,0}-v_{\phi,\infty}\right)\delta \tag{2.15}$$

$$\frac{343}{1656}\frac{d}{dr}\left(r\alpha^2\delta\left(v_{\phi,0}-v_{\phi,\infty}\right)^2\right)-\delta\left[\frac{1}{8}\left(v_{\phi,0}^2-v_{\phi,\infty}^2\right)-\frac{7}{72}\left(v_{\phi,0}-v_{\phi,\infty}\right)^2\right]=\frac{-r}{\rho}\tau_{r,0} \tag{2.16}$$

$$\frac{49}{720}\frac{d}{dr}\left(r^2\alpha\delta\left(v_{\phi,0}-v_{\phi,\infty}\right)^2\right)+\frac{\dot{m}_0}{2\pi\rho}\frac{d}{dr}\left(rv_{\phi,\infty}\right)=\frac{-r^2}{\rho}\tau_{\phi,0} \tag{2.17}$$

These equations describe the fluid flow in a boundary layer over a rotor or stator when using appropriate values for $v_{\phi,0}$, $v_{\phi,\infty}$ and δ. An advantage of using the power law profile is that an explicit expression for the shear stress at the surface can be found, allowing $\tau_{\phi,o}$ and $\tau_{r,o}$ to be simplified in the equations above.

As detailed in Childs (2010) by using the power law profile, the following expression for stress can be derived:

$$\tau_{r,0} = -0.0225\rho\left(\frac{\mu}{\rho\delta}\right)^{\frac{1}{4}}\left(v_{\phi,0}-v_{\phi,\infty}\right)^{\frac{7}{4}}(1+\alpha^2)^{\frac{3}{8}} \tag{2.18}$$

$$\tau_{\phi,0} = 0.0225\rho\left(\frac{\mu}{\rho\delta}\right)^{\frac{1}{4}}\left(v_{\phi,0}-v_{\phi,\infty}\right)^{\frac{7}{4}}\alpha(1+\alpha^2)^{\frac{3}{8}} \tag{2.19}$$

Note that these are specifically for $n = 7$, and that they could be stated for a general n where 0.0225 would be replaced by Weighardt's 'K' as prescribed in Table 2.1. These expressions (2.18) and (2.19) can be substituted into the momentum-integral equations (2.15), (2.16) and (2.17).

$$\dot{m}_0 = \frac{49\pi}{60}\rho r\alpha\left(v_{\phi,0}-v_{\phi,\infty}\right)\delta \tag{2.20}$$

$$\frac{343}{1656}\frac{d}{dr}\left(r\alpha^2\delta\left(v_{\phi,0}-v_{\phi,\infty}\right)^2\right)-\delta\left[\frac{1}{8}\left(v_{\phi,0}^2-v_{\phi,\infty}^2\right)-\frac{7}{72}\left(v_{\phi,0}-v_{\phi,\infty}\right)^2\right] = r0.0225\left(\frac{\mu}{\rho\delta}\right)^{\frac{1}{4}}\left(v_{\phi,0}-v_{\phi,\infty}\right)^{\frac{7}{4}}(1+\alpha^2)^{\frac{3}{8}} \tag{2.21}$$

$$\frac{49}{720}\frac{d}{dr}\left(r^2\alpha\delta\left(v_{\phi,0}-v_{\phi,\infty}\right)^2\right)+\frac{\dot{m}_0}{2\pi\rho}\frac{d}{dr}\left(rv_{\phi,\infty}\right) = -r^2 0.0225\left(\frac{\mu}{\rho\delta}\right)^{\frac{1}{4}}\left(v_{\phi,0}-v_{\phi,\infty}\right)^{\frac{7}{4}}\alpha(1+\alpha^2)^{\frac{3}{8}} \tag{2.22}$$

The equations look complicated in this form, but by substituting in values of velocity at the surface, $v_{\phi,0}$, and far from the surface, $v_{\phi,\infty}$, that represent the expected conditions in different physical situations the equations will appear in a form in which they can be solved.

The following subsection will look at three physical cases that have been derived by different authors. First the equations model fluid flow over a rotating disc in a stationary fluid, then over a rotating disc in rotating fluid and finally over a stationary disc.

2.1.2 ROTATING DISC IN STATIONARY FLUID

von Karman (1921) used the momentum integral equations to model flow in the boundary layer of fluid near a rotating disc, known as a 'free disc'. The following quantities

$$v_{\phi,0} = \Omega r, \qquad v_{\phi,\infty} = 0 \tag{2.23}$$

are used in equations (2.20), (2.21) and (2.22), where Ω denotes the angular speed of the rotor disc. As shown in Owen and Rogers (1989) the equations become

$$\dot{m}_0 = \frac{49\pi}{60}\rho\Omega r^2\alpha\delta \tag{2.24}$$

$$\frac{343}{1656}\left[3 + \frac{2r}{\alpha}\frac{d\alpha}{dr} + \frac{r}{\delta}\frac{d\delta}{dr}\right] - \frac{1}{36\alpha^2} = -0.0225\left(x^2 Re_\phi\right)^{-\frac{1}{4}}\frac{(1+\alpha^2)^{\frac{3}{8}}}{\alpha}\left(\frac{\delta}{r}\right)^{-\frac{5}{4}} \tag{2.25}$$

$$\frac{49}{720}\left[4 + \frac{r}{\delta}\frac{d\delta}{dr} + \frac{r}{\alpha}\frac{d\alpha}{dr}\right] = 0.0225\left(x^2 Re_\phi\right)^{-\frac{1}{4}}\frac{(1+\alpha^2)^{\frac{3}{8}}}{\alpha}\left(\frac{\delta}{r}\right)^{-\frac{5}{4}} \tag{2.26}$$

By assuming that α is not a function of r then the following equations hold,

$$\frac{\dot{m}_0}{\mu r} = 0.2186\left(x^2 Re_\phi\right)^{\frac{4}{5}} \tag{2.27}$$

$$C_M = 0.07288 Re_\phi^{-\frac{1}{5}} \tag{2.28}$$

$$\delta_o = 0.5261\left(x^2 Re_\phi\right)^{-\frac{1}{5}}|1-\beta|^{\frac{3}{5}} r \tag{2.29}$$

for *local non-dimensional flow rate*, *moment coefficient* and *boundary layer thickness* respectively. Recall that these equations have been derived assuming a 1/7th power law. The corresponding equations assuming a generalised 1/nth power law are given by

$$\frac{\dot{m}_0}{\mu r} = \frac{2n^2\pi\alpha\gamma}{(n+1)(2n+1)}\left(x^2 Re_\phi\right)^{\frac{n+1}{n+3}} \tag{2.30}$$

$$C_M = \frac{6n^2\pi\alpha\gamma}{(n+1)(n+2)(2n+1)} Re_\phi^{-\frac{2}{n+3}} \tag{2.31}$$

2.1.3 ROTATING DISC IN ROTATING FLUID

Owen and Rogers (1989) showed that to use the momentum integral equations to model flow in the boundary layer of rotating fluid on a rotating disc the following quantities

$$v_{\phi,0} = \Omega r, \qquad v_{\phi,\infty} = \Omega r\beta \tag{2.32}$$

are used in equations (2.20), (2.21) and (2.22). The fluid rotates with angular speed ω and β is the *swirl ratio*, defined as the ratio of these two angular speeds, so

$$\beta = \frac{\omega}{\Omega} \tag{2.33}$$

When the rotor is being modelled a subscript 'o' is used such that $\alpha := \alpha_o$, $\delta := \delta_o$ and $\dot{m}_0 = \dot{m}_o$. For the previous equations, modelling a rotating disc in a stationary fluid, an equation for the boundary layer thickness could be gained where the numerical

coefficient was a known value, 0.5261. Now that the equations also have the variable swirl ratio involved the value is not known. The expression is now given by

$$\delta_o = \gamma_o \left(x^2 Re_\phi\right)^{-\frac{1}{5}} |1-\beta|^{\frac{3}{5}} r \tag{2.34}$$

where γ_o is a coefficient that must be solved for. After substituting (2.32) and into (2.20), (2.21) and (2.22), noting that only α_o and γ_o are functions of r, the equations will be:

$$\frac{\dot{m}_0}{\mu r} = \frac{49}{60}\pi \alpha_o \gamma_o \left(x^2 Re_\phi\right)^{\frac{4}{5}} (1-\beta)^{\frac{8}{5}} \tag{2.35}$$

$$\frac{343}{1656}\left(\frac{18}{5} + \frac{2x}{\alpha_o}\frac{d\alpha_o}{dx} + \frac{x}{\gamma_o}\frac{d\gamma_o}{dx}\right) - \frac{1+8\beta}{36(1-\beta)\alpha_o^2} = -0.0225\frac{(1+\alpha_o^2)^{\frac{3}{8}}}{(1-\beta)\alpha_o \gamma_o{}^{\frac{5}{4}}} \tag{2.36}$$

$$\frac{49}{720}\left(\frac{23+37\beta}{5(1-\beta)} + \frac{x}{a_o}\frac{d\alpha_o}{dx} + \frac{x}{\gamma_o}\frac{d\gamma_o}{dx}\right) = 0.0225\frac{(1+\alpha_o^2)^{\frac{3}{8}}}{(1-\beta)\alpha_o \gamma_o{}^{\frac{5}{4}}} \tag{2.37}$$

Here the equations have been put in the form of non-dimensional radius $x = r/b$, where b is the radius of the disc. In deducing these equations it has been assumed, in order to make the analysis easier, that β is not a function of r. This is against what is observed experimentally.

In order to solve the rotor differential equations presented above numerically, initial conditions for α_o and γ_o are needed. There are analytical solutions, shown below, that can be used to provide these. The solutions (2.38) and (2.39) are derived assuming that α_o and γ_o are independent of x (i.e. that they are constant with radius) and that the flow starts exactly at the centre of the disc, so at $x = 0$.

$$\alpha_o(\beta) = \left[\frac{2300(1+8\beta)}{49(1789-409\beta)}\right]^{\frac{1}{2}} \tag{2.38}$$

$$\gamma_o(\beta) = \frac{81(1+\alpha_o^2)^{\frac{3}{8}}}{49(23+37\beta)\alpha_o} \tag{2.39}$$

These analytical solutions depend upon the value of β, the swirl ratio.

Solutions to (2.36) and (2.37) are presented in Owen and Rogers (1989) in tabulated form for flow over a full disc. The solutions are constant with radius.

2.1.4 STATIONARY DISC IN ROTATING FLUID

To use the momentum integral equations to model the flow over a stator the same method of evaluating derivatives as for the rotor must be used. For the stator the following expressions

$$v_{\phi,0} = 0, \qquad v_{\phi,\infty} = \Omega r \beta \tag{2.40}$$

can be substituted into equations (2.20), (2.21) and (2.22). When the stator is being modelled a subscript 's' is used such that $\alpha := \alpha_s$, $\delta := \delta_s$ and $\dot{m}_0 = \dot{m}_s$. As shown in Owen and Rogers (1989) the following equation for stator boundary layer thickness holds,

$$\delta_s = \gamma_s \left(x^2 \beta Re_\phi\right)^{-\frac{1}{5}} r \tag{2.41}$$

After evaluating the derivatives, noting that only r, α_s and γ_s are functions of r (or equivalently x), the equations will be:

$$\frac{\dot{m}_s}{\mu r} = -\frac{49\pi}{60}\left(x^2\beta Re_\phi\right)^{\frac{4}{5}}\alpha_s\gamma_s \tag{2.42}$$

$$\frac{343}{1656}\left(\frac{18}{5}+\frac{2x}{\alpha_s}\frac{d\alpha_s}{dx}+\frac{x}{\gamma_s}\frac{d\gamma_s}{dx}\right)+\frac{2}{9{\alpha_s}^2}=\frac{0.0225(1+\alpha_s^2)^{\frac{3}{8}}}{\alpha_s{\gamma_s}^{\frac{5}{4}}} \tag{2.43}$$

$$\frac{49}{720}\left(\frac{-37}{5}+\frac{x}{\alpha_s}\frac{d\alpha_s}{dx}+\frac{x}{\gamma_s}\frac{d\gamma_s}{dx}\right)=\frac{-0.0225(1+\alpha_s^2)^{\frac{3}{8}}}{\alpha_s{\gamma_s}^{\frac{5}{4}}} \tag{2.44}$$

No analytical solutions of these equations exist where α_s is real and constant. To the author's knowledge, although these stator equations are stated in Owen and Rogers (1989), no solutions have been published.

2.1.5 CONTINUITY OF MASS FLOW BETWEEN ROTOR-STATOR

The system of interest for this work is a rotor-stator cavity. In order to use momentum-integral equations to model a cavity, the solutions to the ODEs (2.36) and (2.37) for the rotor and (2.43) and (2.44) for the stator must be coupled together. Owen and Rogers (1989) show how to bring together the solutions from the equations for the rotating disc in rotating fluid and stationary disc in rotating fluid by using the mass flow rates. Assuming that there is no sealing flow, then for a basic rotor-stator cavity there must be equality of the mass flow rates on the rotor and the stator, such that

$$\dot{m}_o + \dot{m}_s = 0 \tag{2.45}$$

By substituting (2.35) and (2.42) into (2.45) gives

$$\frac{49\pi}{60}\left(x^2 Re_\phi\right)^{\frac{4}{5}}\left[\alpha_o\gamma_o(1-\beta)^{\frac{8}{5}}-\alpha_s\gamma_s\beta^{\frac{4}{5}}\right]=0 \tag{2.46}$$

By assuming constant values for α_o, γ_o, α_s and γ_s, the equation above can be solved to find a constant value of β to approximate the rotation between the rotor and stator, denoted β^*. Owen (1988) assumed $\alpha_s = \alpha_o(1) = 0.553$ and $\gamma_s = \gamma_o(1) = 0.0983$, both gained by setting $\beta = 1$ in (2.38) and (2.39), and found that $\beta^* = 0.426$.

2.2 FLOW STRUCTURE BETWEEN ROTOR-STATOR DISCS

In the previous sections equations for modelling the turbulent flow over rotor and stator discs were derived. Currently the equations for the rotor and stator only exist in isolation. To bring the rotor and stator together and solve the equations as a system requires an understanding of the fluid structure between the discs.

Batchelor (1951) proposed that there were two families of solutions for the Navier-Stokes equations; one where the discs were infinite and one where they were finite. Batchelor stated that von Karman's (1921) solution was a specific case in the family of solutions for the infinite disc. From the solutions Batchelor deduced that if the Reynolds number was sufficiently large and the discs were a finite distance apart then there was a rotating core between the discs. This would mean there are separate boundary layers on the rotor and stator. The fluid from the stator would move radially inwards and axially across into the rotating core. Fluid on the rotor would move radially outwards while entraining fluid axially from the rotating core.

Stewartson (1953) claimed that the flow structure between a rotor and stator took a different form. Through theoretical modelling and simple experiments what

Stewartson observed contradicted some of Bachelor's findings: there was no core rotation. Instead the rotor-stator flow structure behaved more like a free-disc with tangential velocity continually falling until it reaches zero on the stator, rather than having the plateau expected if there is a core. It was not known which hypothesis was correct. The velocity profiles hypothesised by Batchelor and Stewartson are shown in Figure 2.2.

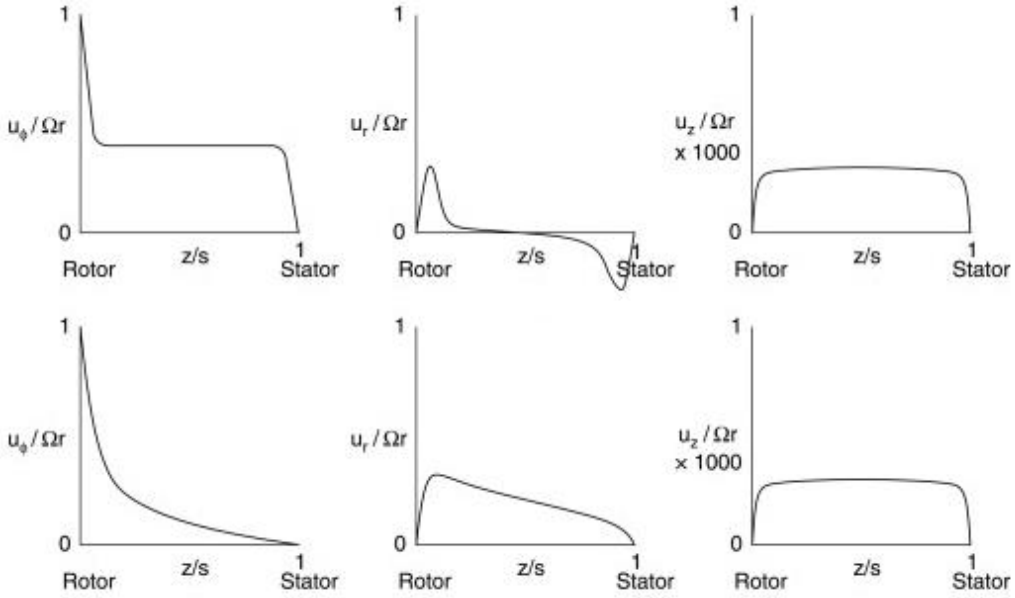

Figure 2.2: Velocity profiles for Batchelor flow (top row) and Stewartson flow (bottom row). Childs (2010).

The first indication that both flow types could occur were shown numerically by Grohne (1955) and experimentally by Picha and Eckert (1958). Grohne found numerical solutions of the von Karman equations for various Reynolds numbers. For low Reynolds numbers Stewartson type flow was present, but higher Reynolds numbers the flow was of the Batchelor type. Picha and Eckert (1958) used aerodynamic probes to take velocity measurements between the two the rotor and stator. If the discs were covered with a shroud then Batchelor type flow was observed and if there was no shroud then it was Stewartson type flow: so both flow structures could be seen experimentally. The reason for both flow structures being valid mathematically was first discovered by Mellor, Chapple et al. (1968) who found that solutions of the von Karman equations are not unique. This was later proved rigorously by Kreiss and Parter (1983).

As outlined in Childs (2010) the amount of superposed flow supplied to rotor-stator cavities will change the flow structure. In general when no or low amounts of sealing flow are supplied there will be a rotating core and therefore Batchelor type flow. As more sealing flow is supplied the core rotation will be suppressed until eventually there will be no core and the Stewartson type flow will be seen.

Daily and Nece (1960) studied the flow inside an enclosed rotor-stator system both experimentally and theoretically. Four different flow regimes inside the cavity were categorised based upon the *gap ratio*, G, and the rotational Reynolds number, Re_ϕ. The gap ratio is

$$G = s/b \tag{2.47}$$

where s is the distance between the discs. The four regimes are shown in Figure 2.3. Regimes [1] and [3] which are for small clearances have merged boundary layers, so there will be no rotating core. Regimes [2] and [4] with large clearances have separate boundary layers and so have the Batchelor type flow structure. The study also found four empirical expressions for the *moment coefficient*, C_M, on one side of the disc. For the two turbulent regimes these are:

$$C_M = 1.85G^{\frac{1}{10}}Re_\phi^{-\frac{1}{2}} \quad - \ Regime\ [2]$$
$$C_M = 0.0510G^{\frac{1}{10}}Re_\phi^{-\frac{1}{5}} \quad - \ Regime\ [4] \tag{2.48}$$

these correlations can be seen in Figure 2.4 where the open circles are the experimental data.

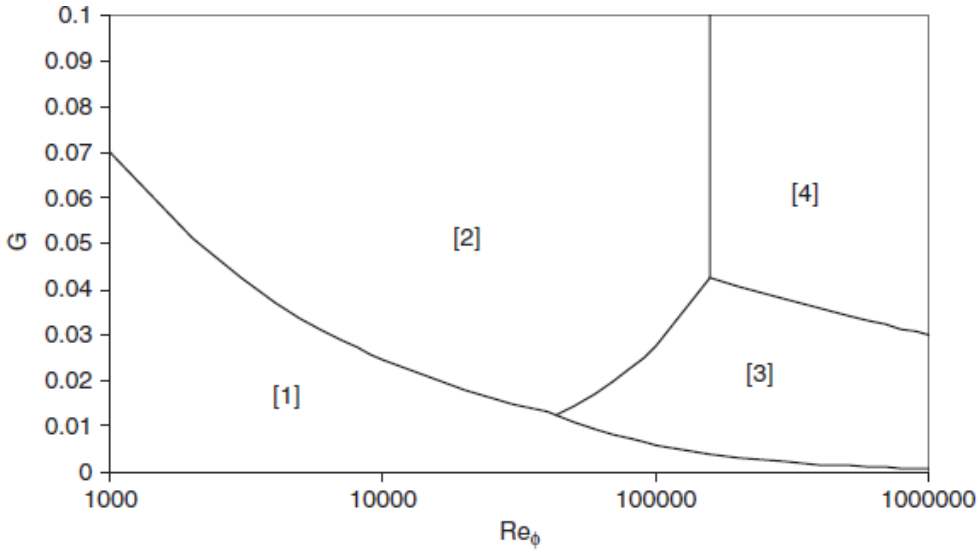

Figure 2.3: Flow regimes for an enclosed rotor-stator wheelspace from Daily and Nece (1960) [1] Laminar flow, small clearance; [2] Laminar flow, large clearance; [3] Turbulent flow, small clearance; [4] Turbulent flow, large clearance. Childs (2010).

The rotor-stator cavities of interest within gas turbines are typically in Regime [4] where $Re_\phi > 10^5$ and $G > 0.05$. Dorfman (1963) found a theoretical expression for the moment coefficient on a free disc, by solving (2.3) and (2.4) assuming a logarithmic velocity profile. The equations were solved over different ranges and combined to give a single equation

$$C_M = 0.491\left(\log\left(Re_\phi\right)\right)^{-2.58} \tag{2.49}$$

which is valid over the range $10^4 < Re_\phi < 10^9$.

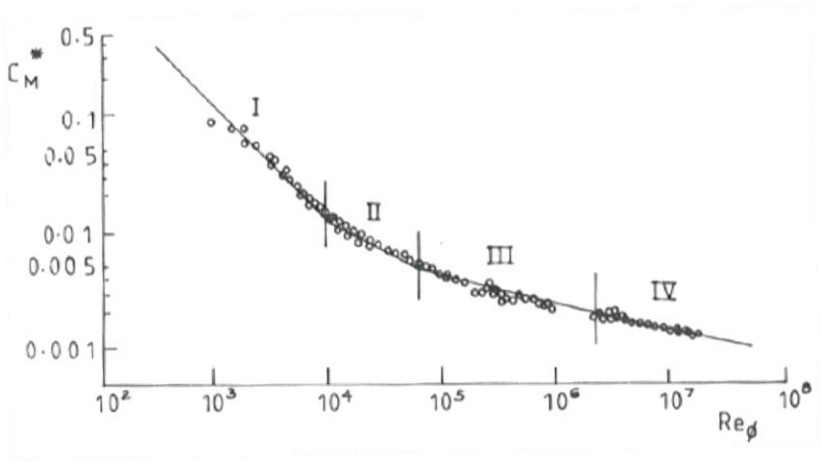

Figure 2.4: Variation of moment coefficient with Reynolds number. Four theoretical correlations [straight lines] and experimental data [open circles]. Owen and Rogers (1989).

The discovery of the flow regimes as a function of gap ratio and Reynolds numbers made many researchers assume that the angular speed of the core, and therefore the swirl ratio, would be constant with radius and would change only with gap ratio and Re_ϕ. Dijkstra and van Heist (1983) solved the Navier-Stokes equations for laminar flow in a rotor-stator system numerically using a finite difference method. The study showed the swirl ratio was not constant with radius, and that the swirl ratio was influenced by a shroud. At a radial location of $x \approx 0.9$ the swirl was measured to be around $\beta \approx 0.3$ without a shroud, and $\beta \approx 0.5$ with a shroud.

Morse (1991) also investigated the radial variation of swirl ratio in an enclosed rotor-stator cavity numerically.

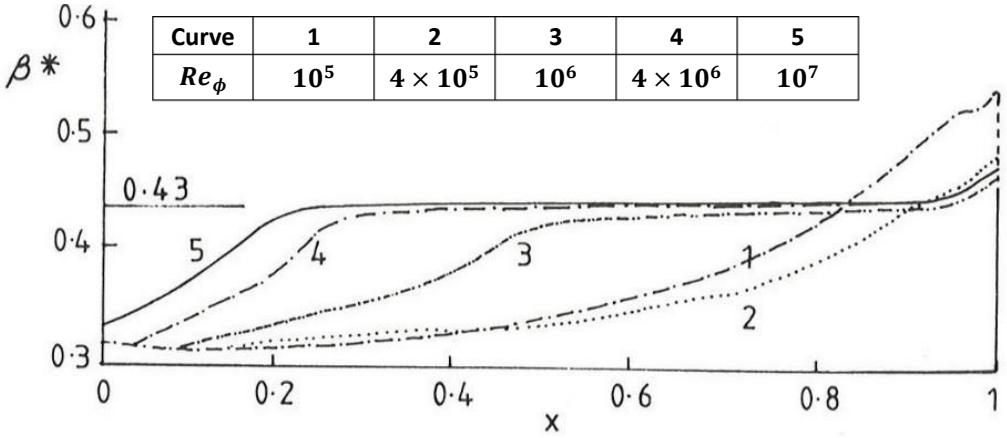

Curve	1	2	3	4	5
Re_ϕ	10^5	4×10^5	10^6	4×10^6	10^7

Figure 2.5: Effect of Re_ϕ on radial variation of β^* for $G = 0.1$. Morse (1991).

Figure 2.5 shows that in general the higher the value of Re_ϕ the larger the 'plateau region' in the wheelspace where $\beta \approx 0.43$, very close to the $\beta = 0.426$ predicted by Owen (1988). This is due to the flow transitioning from laminar to turbulent flow at lower radii. Next rotor-stator systems with the presence of sealing air are considered.

2.3 PREVENTION OF INGRESS

2.3.1 EXPERIMENTAL MEASUREMENTS

As described in the introduction, rotor-stator cavities are subject to ingress – where fluid is drawn into the cavity. The following section covers how ingress can be

prevented by the use of sealing flow which can change the flow structure. This will be discussed more in Chapter 4.

The previous section looked at the flow structure between rotor-stator discs with no regard for any ingress that could occur. Typically between a rotor and stator there will be ingress (the movement of fluid into the wheelspace). In order to prevent ingress, the wheelspace is pressurised by the addition of sealing air (also known as superposed flow), as shown in Figure 2.6.

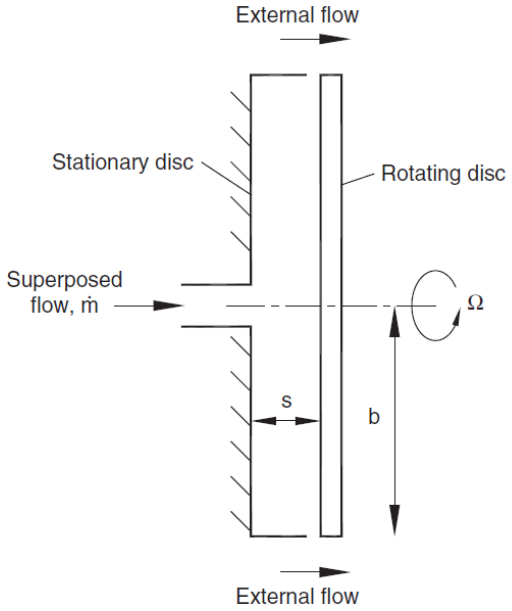

Figure 2.6: A rotor-stator wheelspace with external flow. Childs (2010).

Figure 2.6 depicts a rotor-stator cavity where there is a stationary shroud; typically there is a complex rim seal protecting the wheelspace from the annulus flow, rather than a simple shroud. The rim seal designs often have rim seal features on both the rotor and the stator. Some basic schematics are shown in Figure 2.7 below, where the vanes and blades typically present in the annulus have been visually omitted for simplicity. There are three main types of rim seals, categorised by where the gap is positioned: axial, radial and mitred clearance.

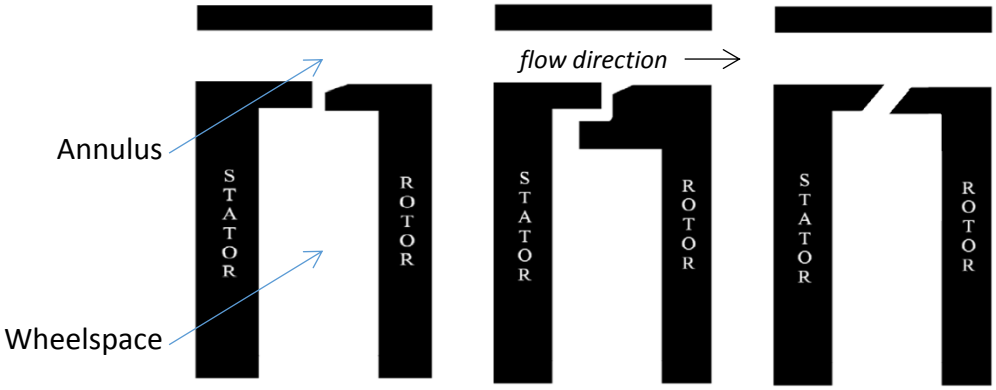

Figure 2.7: Axial, radial and mitred Rim seals respectively. [Adapted from Sangan *et al.* (2013c)]

Bayley and Owen (1970) carried out one of the earliest studies into the causes of what is now called RI ingress. A classical rotor-stator set up with an axial clearance seal and radial superposed flow was used. There was no annulus on the rig, so past the rim seal was open atmosphere. It was found that increasing the superposed sealing flow

rate, $C_{w,0}$, increased the moment coefficient C_M. The *non-dimensional sealing flow rate*, $C_{w,0}$, was defined as

$$C_{w,0} = \frac{m_o}{\mu b} \tag{2.50}$$

where b is the outer radius of the disc. It was also found that C_M was not affected by the gap ratio G. By using a simple orifice model (the next section details the principles behind such a model) a prediction for how the minimum amount of sealing flow needed to prevent ingress, $C_{w,min}$, was found. It was coined the '*Bayley-Owen criterion for RI ingress'* and was given by

$$C_{w,min} = 0.61 G_c Re_\phi \tag{2.51}$$

where the $G_c \coloneqq s_c/b$ with s_c being the width of the seal clearance.

Phadke and Owen (1988 a,b,c) were three papers studying sealing of a rotor-stator system. The studies involved taking pressure and concentration measurements in a cavity as well as using some flow visualisation techniques. Various rim seal geometries were tested in a shrouded rotor-stator system with different conditions in the annulus: stationary, quasi-axisymmetric and non-axisymmetric external flow in Phadke and Owen (1988 a,b,c) respectively. In Phadke and Owen (1988a) the experiments found the values of minimum sealing flow rate, $C_{w,min}$, for each seal with different configurations; for example changing the size of the clearance ratio, G_c, between the rotor and stator and changing the rotational Reynolds number. This meant correlations between $C_{w,min}$, G_c and Re_ϕ could be found. For example for all axial clearance seals, $C_{w,min}$ increases with G_c and Re_ϕ. So as the distance between the discs gets larger, or the rotational Reynolds number increases, more sealing flow is needed to seal the system. It was found that the radial seals performed best, followed by the mitred seal and finally the axial. The research created a foundation for determining the types of ingress.

Phadke and Owen (1988b) contained the findings on two flow regimes; one 'rotation-dominated regime' that became known as RI ingress and one 'external flow dominated regime', now known as EI ingress. When there is external flow in the annulus the axial flow Reynolds number, Re_w is an important parameter. It is defined as:

$$Re_W = \frac{\rho W b}{\mu} \tag{2.52}$$

where W is the axial velocity of the flow in the annulus. In Phadke and Owen (1988b) it was found that:

- For small Re_w/Re_ϕ, RI ingress occurs and $C_{w,min}$ increases as Re_ϕ increases.
- If $Re_w = 0$ then $C_{w,min} \propto Re_\phi$.
- For large Re_w/Re_ϕ, EI ingress occurs and $C_{w,min} \propto Re_w$.

These correlations can be seen in Figure 2.8 for an axial seal.

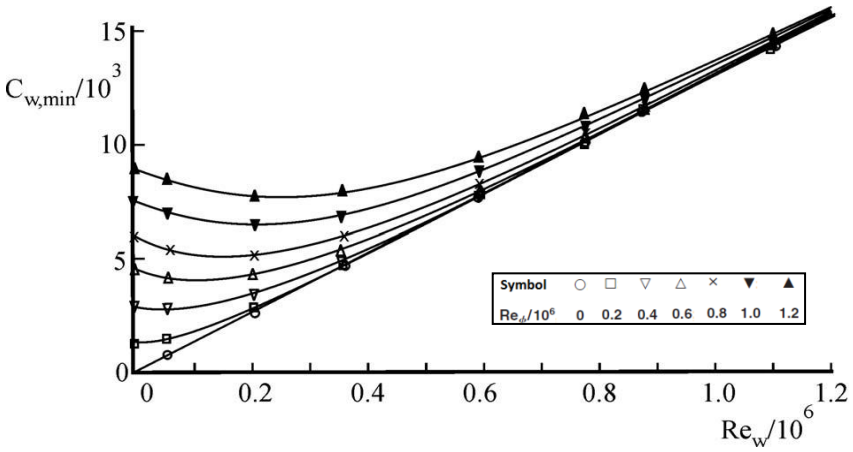

Figure 2.8: Variation of minimum sealing flow with Reynolds number for axial seal. Phadke and Owen (1988b)

Recall that *Externally Induced (EI)* Ingress is caused by the unsteady pressure distribution in the annulus. Phadke and Owen (1988c) found that for EI ingress the value of $C_{w,min}$ increased with P_{max} according to the following empirical formula:

$$C_{w,min} = 2\pi K G_c P_{max}^{\frac{1}{2}} \tag{2.53}$$

Here P_{max} is the *maximum non-dimensional circumferential static pressure difference* measured in the external-flow annulus and K is another empirical constant, unrelated to that of Weighardt (1946). These types of correlations are very useful for engine designers a it gives an approximation of how much sealing flow is needed to protect the cavity from ingress for given flow conditions.

Sangan *et al.* (2011a,b) have improved upon a purely empirical correlation and have found a theoretical model to predict $C_{w,min}$ for specific seals. Sangan *et al.* (2011a) describes the construction of a single stage rotor-stator rig at the University of Bath, presents experimental measurements of sealing effectiveness on the stator disc and applies the theoretical orifice model of Owen (2011b) to the experimental data for EI ingress. Sangan *et al.* (2011b) presents experimental measurements of sealing effectiveness and applies the theoretical orifice model of Owen (2011a) to the experimental data for RI ingress.

In both Sangan *et al.* (2011a) and Sangan *et al.* (2011b) experimental measurements of CO_2 concentration were measured in three key locations to track how much ingress entered the wheelspace, for EI and RI ingress respectively. The index of the concentration measurements c_s, c_o and c_a denotes the location at which is measurement is taken: 's' at some radial location on the stator, 'o' in the sealant flow and 'a' in the annulus. In the experiments the annulus flow had a value of c_a that was the same as the CO_2 content of air and c_o is set as the sealing air is seeded with a certain percentage of CO_2 that is known. The concentration measurements on the stator are recorded at several locations between $0.55 < r/b < 0.993$ but only one radial location at a time is used to find c_s. The rig is shown in Figure 2.9. The measurements are used to find *sealing effectiveness based upon concentration*, ε_c,

$$\varepsilon_c = \frac{c_s - c_a}{c_o - c_a} \tag{2.54}$$

at the different radial locations. If $\varepsilon_c = 0$ then it must be that $c_s = c_a$, meaning the concentration on the stator is the same as that in the annulus, so ingress is at a maximum. If $\varepsilon_c = 1$ then it must be that $c_s = c_o$, meaning that the concentration on

the stator is the same as that sealing flow. In other words the sealing flow has not been diluted by the presence of any annulus flow, so there is no ingress entering the wheelspace. The quantity of particular interest is $C_{w,min}$, the *minimum amount of sealing flow to prevent ingress,* it is the first value of sealing flow at which $\varepsilon_c = 1$.

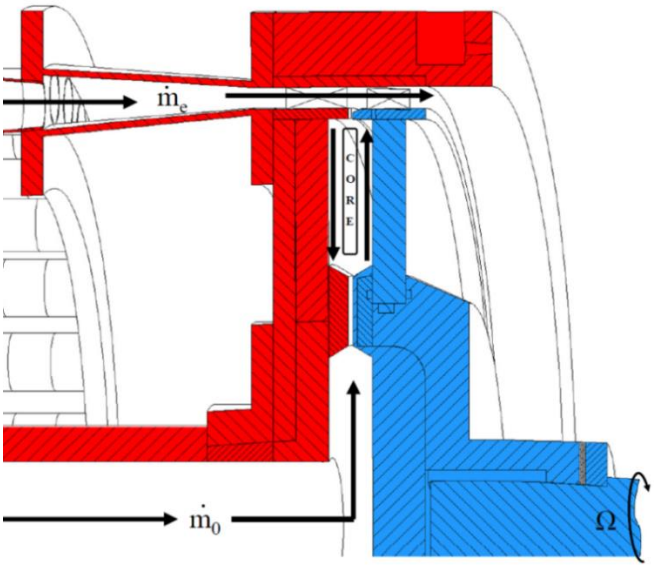

Figure 2.9: Experimental rig at University of Bath, stator in red, rotor in blue. (Sangan 2011)

Effectiveness values can be measured at various sealing flow rates, $C_{w,o}$, at a single radial location (typically at $r/b = 0.958$ unless otherwise stated) in order to see how different seals perform. Only a single radial location is considered because the distribution is found to be constant with radius. Figure 2.10 shows the variation of concentration effectiveness with $C_{w,0}$ for the different values of Re_ϕ at $r/b = 0.958$. Data is shown for an axial-clearance and a radial clearance seal.

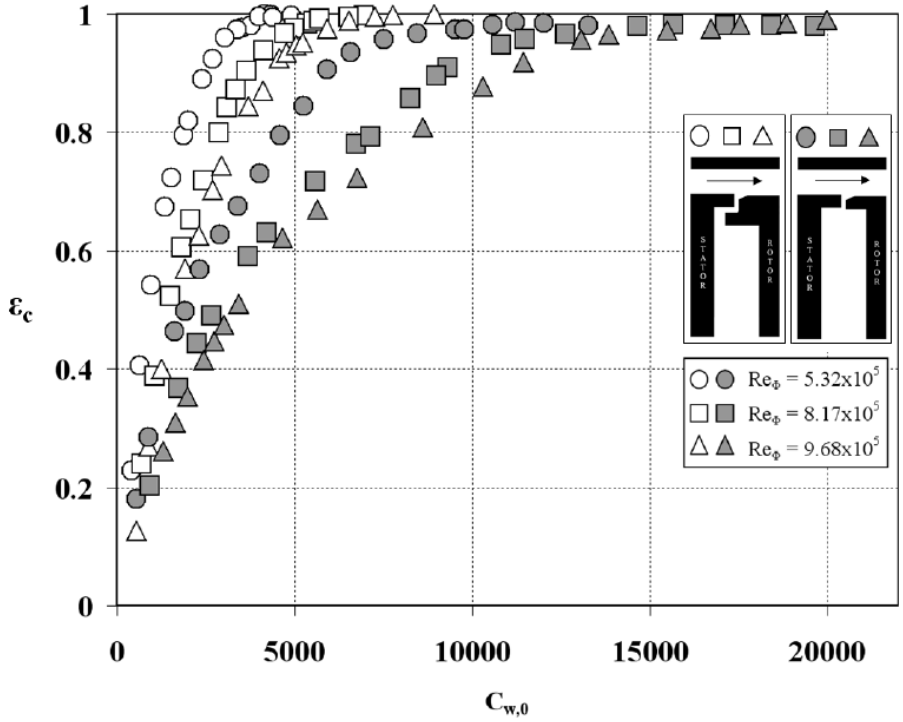

Figure 2.10: Effect of Reynolds number on concentration effectiveness and sealing flow rate for axial [grey symbols] and radial seal [white symbols] Sangan *et al.* (2013a)

It can be seen that as the sealing flow rate increases, the effectiveness tends to 1. When the effectiveness is exactly one, the system is fully sealed so no ingress occurs. The aim is to find the minimum sealing flow rate value at which $\varepsilon = 1$, $C_{w,min}$, this value is useful because it means no sealing flow is being applied unnecessarily and decreasing the efficiency. The results of Sangan *et al.* (2011a) show that the radial clearance seal requires far less sealing flow than the axial clearance seal to become fully sealed. For both seal geometries as Re_ϕ increases, the value of $C_{w,min}$ increases.

A new parameter *the non-dimensional sealing parameter,* Φ_o, is defined in the paper, where

$$\Phi_o = \frac{C_{w,0}}{2\pi G_c Re_\phi} \tag{2.55}$$

Similarly Φ_{min} is defined as

$$\Phi_{min} = \frac{C_{w,min}}{2\pi G_c Re_\phi} \tag{2.56}$$

Usefully when plotting the effectiveness values against Φ_o instead of $C_{w,o}$, the data for each different Re_ϕ value collapses onto a single curve, as shown in Figure 2.11 for the axial seal. This is useful because it means a single value of Φ_{min} can be found for one seal (rather than many values of $C_{w,min}$ that depend upon Re_ϕ).

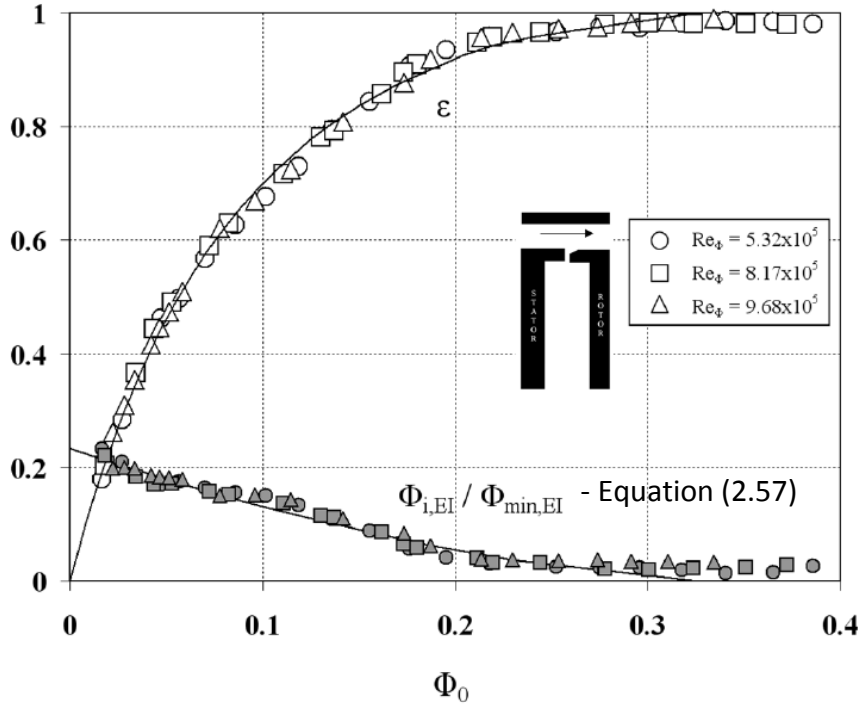

Figure 2.11: Effectiveness measurements and ingress flow rates against sealing flow rate for the axial seal Sangan *et al.* (2011a)

Also shown in Figure 2.11 are measurements of Φ_i, *the non-dimensional ingested flow rate parameter*, scaled as Φ_i/Φ_{min} where

$$\frac{\Phi_i}{\Phi_{min}} = \frac{\Phi_i}{\Phi_o}\frac{\Phi_o}{\Phi_{min}} = \left[\frac{1}{\varepsilon} - 1\right]\frac{\Phi_o}{\Phi_{min}} \tag{2.57}$$

The figure also contains two theoretical curves: one for ε and one for Φ_i/Φ_{min}. These are gained from the orifice model which is described below, specifically the *EI effectiveness equation* for $\Phi_o/\Phi_{min,EI}$. The orifice model theory was set out by Owen

(2011a) and Owen (2011b) and validated against experimental results in Sangan *et al.* (2011a) and Sangan *et al.* (2011b). The orifice model is able to provide a very accurate fit. Similar plots are found in the same way for the RI experiments of and Sangan, Zhou *et al.* (2011b). The only difference between the experimental procedure for RI and EI ingress is in the mainstream flow in the annulus. For the EI experiments a flow is supplied in the annulus, whereas none is supplied in the RI experiments. In order to distinguish between the two different experimental conditions values of $\Phi_{min,EI}$ and $\Phi_{min,RI}$ are found.

Although this type of fitting is far less general than the empirical correlations of Phadke and Owen (1988), in regards to flow conditions, the predictions are far more accurate. The fitting is based upon a model where the constants have physical meaning. The model is outlined in the next section.

2.3.2 ORIFICE MODEL

As outlined in Owen (2011a) the concept behind the *orifice model* is that the gap between the rotor and the stator, the seal clearance, S_c, can be thought of as an 'orifice ring'. Flow can then be considered passing into and out the wheelspace by passing through this orifice ring, where inflow and outflow are divided into small regions, δA_i and δA_e respectively. This simplifies the complex mixing flows that occur in the seal clearance. The orifice ring, complete with ingress and egress, is shown in Figure 2.12.

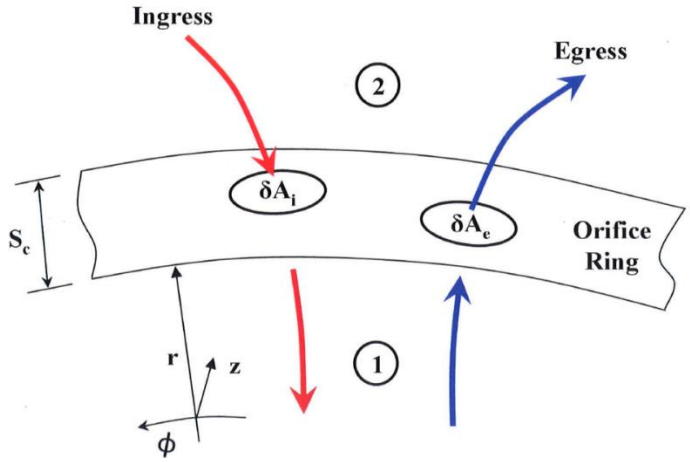

Figure 2.12: Seal clearance modelled as an orifice ring, with ingress and egress. Owen (2011a).

The numbers 1 and 2 are used to denote the wheelspace and the annulus respectively, such that the pressure inside in wheelspace is denoted p_1 and the pressure in the annulus p_2. The pressure in the annulus is not constant so two additional parameters are used: Δp, the time-average peak-to-trough static pressure difference in the annulus, and ΔC_p, the non-dimensional pressure difference in the annulus.

Owen (2011a) and Owen (2011b) took the concept of the orifice model further and derived the *orifice equations* for RI and EI ingress. These extensive equations were solved for various cases over the two papers and are the ground work for the *effectiveness equations* which were developed after the initial papers and stated in Sangan *et al*. (2011a) and Sangan *et al.* (2011b), for EI and RI respectively. The *EI and RI effectiveness equations* provide a way to fit experimental measurements of effectiveness, ultimately allowing a specific value for the minimum amount of sealing flow required to seal a specific rim seal to be found.

Orifice Equations for RI Ingress

Owen (2011a) derived the orifice equations for both compressible incompressible flow. The incompressible RI equations were solved analytically, showing that non-dimensional ingress, non-dimensional egress and the sealing effectiveness ε depend upon three variables: $\Theta_o \coloneqq \Phi_o/\Phi_{min}$, $\Gamma_c \coloneqq C_{d,i}/C_{d,e}$ and swirl of fluid in annulus. In the model the flow is assumed to be inviscid, therefore *discharge coefficients for ingress and egress*, defined as $C_{d,i}$ and $C_{d,e}$ respectively, are introduced to take account of viscous losses. These coefficients depending on the specific rim seal design and must be determined empirically. Discharge coefficients had been presented in earlier models such as that by Chew (1991) who gave an empirical model for the case where there is no ingress and it was validated against the experiments measurements of concentration by Graber *et al.* (1987). Chew (1991) stated that the theoretical results showed that the amount of swirl in the annulus did not affect the amount of sealing flow required to prevent ingress.

Returning to Owen (2011a), the key parameter is the *sealing effectiveness*, ε, and it allows for easy comparisons of rim seal performance. It is given by:

$$\varepsilon = 1 - \frac{C_{w,i}}{C_{w,e}} = \frac{C_{w,o}}{C_{w,e}} \tag{2.58}$$

where $C_{w,i}, C_{w,e}$ and $C_{w,o}$ are the non-dimensional mass flow rates of the ingress, egress and sealing flow respectively. When the system is sealed, there is no ingress, so $\varepsilon = 1$. If there is no sealing flow being supplied then $C_{w,o} = 0 \Rightarrow \varepsilon = 0$.

By changing Γ_c, the value of Φ_{min} is not affected, but the shape of the effectiveness curve is. This can be seen below in Figure 2.13, where Γ_c is being varied between 0.5 and 1.5.

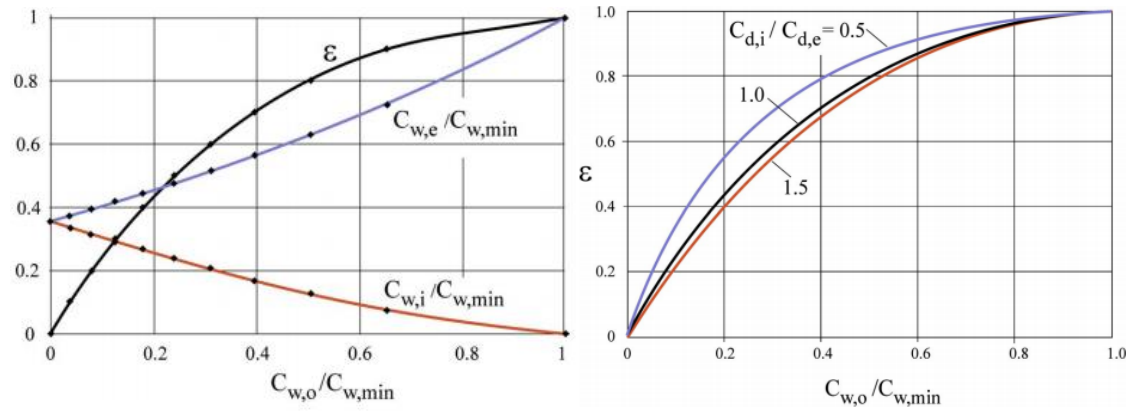

(a) (b)

Figure 2.13: Variation of $C_{w,e}$, $C_{w,i}$ and ε with sealing flow rate $C_{w,o}$ for RI ingress. Adapted from Sangan (2011). (a) external swirl zero and $\Gamma_c = 1$, (b) only external swirl zero

When there is no sealing flow, then ingress is at a maximum then the following holds:

$$\Theta_{i,max} = \Phi_{e,min} = \frac{1}{2\sqrt{2}} \tag{2.59}$$

equivalently,

$$C_{w,i,max} \approx 0.35 C_{w,min} \tag{2.60}$$

This result shows that the maximum ingress (when there is no sealing flow) is approximately 35% of the minimum flow needed to seal the system.

The equation with the greatest practical importance, which can be derived as a consequence of the orifice equations, is the *RI effectiveness equation:*

$$\frac{\Phi_o}{\Phi_{min,RI}} = \frac{\varepsilon}{\left[1+(1-\varepsilon)^{\frac{1}{2}}\right]\left[1+\Gamma_c^{-2}(1-\varepsilon)\right]^{\frac{1}{2}}} \tag{2.61}$$

where $\Gamma_c \coloneqq C_{d,i}/C_{d,e}$. This equation can be used to fit experimental data, as detailed further on in this Section.

Orifice Equations for EI Ingress

Externally Induced (EI) ingress is driven by non-axisymmetric unsteady distribution of pressure in the annulus. An arbitrary circumferential variation of pressure and radial velocity in the annulus is given by Figure 2.14, where θ is the angle between N nozzle guide vanes in a turbine and is defined as

$$\theta = \frac{N}{2\pi}\phi \tag{2.62}$$

In equation (2.62) the variable ϕ is the angular coordinate in the 360° annulus, such that $0 < \phi < 2\pi/N$ and $0 < \theta < 1$. The pressure at some location in the wheelspace, p_1, is assumed to be axisymmetric, hence it appears constant in the Figure. The pressure in the annulus, p_2, is not axisymmetric and as such p_2 is a time-averaged static pressure. When $p_2 > p_1$ ingress occurs and when $p_1 > p_2$ egress occurs.

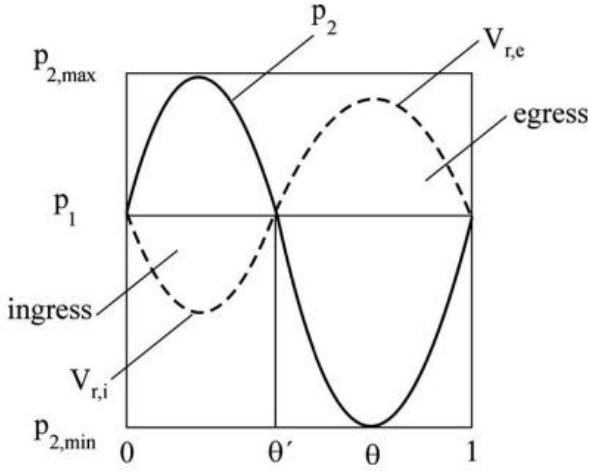

Figure 2.14: Circumferential variation of pressure and radial velocity in the annulus. Sangan (2011).

Owen (2011b) derives the incompressible equations for EI ingress and solves them by assuming that the circumferential pressure distribution in the annulus has a saw-tooth form. The analytical solutions found from the orifice model equations with the saw-tooth model assumption once again showed that non-dimensional ingress, non-dimensional egress and the sealing effectiveness ε depend upon the variables $\Theta_o \coloneqq \Phi_o/\Phi_{min}$, $\Gamma_c \coloneqq C_{d,i}/C_{d,e}$ and swirl of fluid in annulus, just as for the RI case. The variation of ε with Θ_o is very similar to the RI case, as depicted in Figure 2.13.

The equation with the greatest practical importance, which can be derived as a consequence of the orifice equations, is the E*I effectiveness equation:*

$$\frac{\Phi_o}{\Phi_{min,EI}} = \frac{\varepsilon}{\left[1+\Gamma_c^{-2/3}(1-\varepsilon)^{2/3}\right]^{3/2}} \tag{2.63}$$

This equation can be used to fit experimental data, as detailed below.

Use of the Effectiveness Equations

Zhou *et al.* (2011) details the explicit *effectiveness equations* (from the orifice model) along with a statistical method for fitting experimental data with the equation. The statistical method is called *maximum likelihood estimation* and the basics of the method are covered in Myung (2001). In the original orifice equations there were two empirical constants that needed to be determined: $C_{d,i}$ and $C_{d,e}$. By using the effectiveness equations the two constants that need to be determined now become $\Phi_{min,EI}$ (or $\Phi_{min,RI}$) and Γ_c. The statistical method works by finding the values of $\Phi_{min,EI}$ and Γ_c that were most likely to have produced the measurements that are being fitted. The method was rigorously validated and it was found to provide an accurate fit in over 90% of cases when fitting at least 16 data points. One of the fits can be seen in Figure 2.11 for the axial seal data.

Another important parameter to designers that can be readily gained from the orifice model is Φ_i, the *non-dimensional flow rate of the ingress.* Written $\Phi_{i,EI}$ and $\Phi_{i,RI}$ for the cases of EI and RI ingress respectively and defined as

$$\Phi_{i,EI} = \Phi_{min,EI} \frac{1-\varepsilon}{\left[1+\Gamma_c^{-2/3}(1-\varepsilon)^{2/3}\right]^{3/2}} \tag{2.64}$$

$$\Phi_{i,RI} = \Phi_{min,RI} \frac{1-\varepsilon}{[1+(1-\varepsilon)^{1/2}][1+\Gamma_c^{-2}(1-\varepsilon)]^{1/2}} \tag{2.65}$$

These equations use the same values of the empirical constants $\Phi_{min,EI}$ (or $\Phi_{min,RI}$) and Γ_c as found when fitting with the effectiveness equations. Figure 2.11 shows the axial seal effectiveness data fitted with equation (2.64).

2.3.3 COMPUTATIONAL FLUID DYNAMICS

Computational Fluid Dynamics is a newer branch of modelling fluid flow and is constantly improving as computing power increases. CFD works by the user creating a virtual space or object using a mesh grid. The partial differential Navier-Stokes equations are then solved numerically at each location on the mesh, creating a *complete velocity field*. This allows complete flow visualisation at each time step. One key advantage of CFD is that quantities can be calculated at any point on the mesh, rather than just at the locations where instrumentation has been placed (a limitation of experimental measurements). Also flow can be visualised without experimental apparatus disrupting the flow.

CFD models can be broadly categorised into two types: turbulent flow *simulations* and turbulence *models.* In the simulations the partial differential Navier-Stokes equations are solved for a complete velocity field which represents one possible outcome for the flow. Two common simulations are *Large Eddy Simulations* (LES) and *Direct Numerical Simulation* (DNS). In the turbulence-models approach, the Reynolds Averaged Navier-Stokes (RANS) equations are solved for mean values of the velocity. This requires obtaining the Reynolds stresses via some other model.

Applications to Modelling Rotor-Stator Systems

It is possible to model the entire annulus in 3D but this is very computationally intensive. Full 3D unsteady CFD computations require large computers and could still take weeks if not months to run a simulation. Some CFD studies use only a segmented domain, so only a small section of the rotor-stator system is modelled, for example a

90° sector; this allows the computation time to be cut down significantly. Some studies such as Mirzamoghadam *et al.* (2009) found that the computations carried out in the segmented domain matched that of the 360 degree computations, but others such as Jakoby *et al.* (2004) found they did not. Jakoby *et al.* (2004) found that the 360° domain unsteady computations would manifest large scale rotating structures which increased ingestion into the wheelspace. These structures rotated at 80% of the rotor speed and were only present when the sealing flow was low. Julien *et al.* (2010) showed that increasing the sealing flow rate will remove these structures.

Another factor that affects computational time is whether the models are steady or unsteady. Unsteady computations take longer but the results are generally used more extensively as they are likely to be more representative of real situations. Jakoby *et al.* (2004) compared many different CFD models to experimental data. The steady-state model over a small sector gave the worst agreement whereas the unsteady 360° model gave best agreement, but obviously there is a large difference in computational cost.

For steady-state models a 'frozen-rotor' approach is possible; this means that the rotor blade position relative to the stator vanes is fixed within the model. Studies have shown that the relative position of the blades to the vanes affects the amount of ingress that will enter the wheelspace, this is not surprising given that the changing circumferential pressure is driving ingress. *Rabs et al.* (2012) ran steady computations at four different blade locations, comparing these to both experiments and unsteady computations. It was found neither the average steady computations nor the unsteady computations agreed with experimental results of effectiveness. The blade position was affecting the amount of ingress into the system. However, the unsteady results were in very good agreement with the steady computations at a blade position of -0.28 and -0.05. This suggests that if the appropriate blade position is chosen, the lengthy unsteady computations could be replaced with frozen rotor steady computations that take only hours.

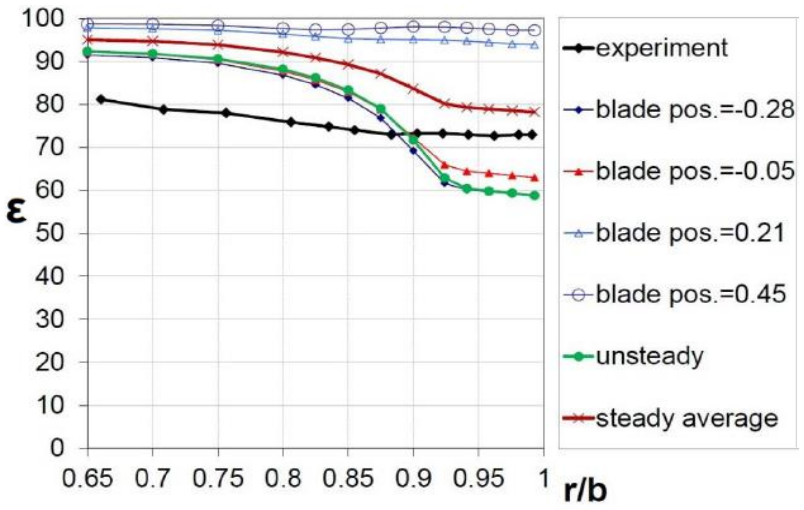

Figure 2.15: Comparison of radial variation of effectiveness by experimental measurements and CFD models (unsteady and steady for four blade positions). Adapted from Rabs *et al.* (2012).

Rather than choosing a positions for the rotor blade Lalwani (2014) removed the blade completely. Steady CFD computations were carried out modelling the University of Bath experimental rig wheelspace geometry (as shown in Figure 2.9) for

an axial and radial rim seal. The model contained three domains: a stator domain (with vane), a wheelspace domain and a rotor domain (with no rotating blades). Radial distributions of stator effectiveness were validated against experimental measurements. The agreement was good across a range of flow rates for $x < 0.87$, but in the outer part of the cavity the CFD predicted a decrease in effectiveness that was not seen experimentally.

Figure 2.16 shows the radial variation of swirl ratio for different sealing flow rates from the unbladed CFD and experimental measurements. There is acceptable agreement between the two, given that the model is designed to be a quick computational tool in comparison to unsteady CFD models.

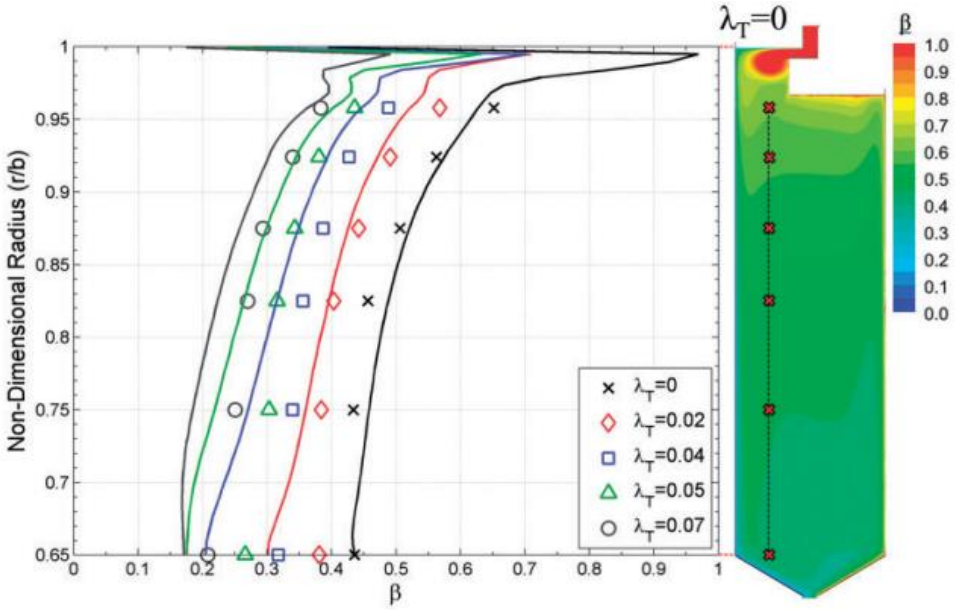

Figure 2.16: Variation of radial distribution of swirl ratio with sealing flow rate from experimental measurement [symbols] and steady unbladed CFD model [lines]. Lalwani *et al.* (2015).

Note that the *turbulent flow parameter* λ_T is used, where

$$\lambda_T = C_{w,o} Re_\phi^{-0.8} = 2\pi G_c Re_\phi^{0.2} \Phi_o \tag{2.66}$$

This is synonymous to varying the sealing flow rate, as it happens that for the conditions in Figure 2.16, $\lambda_T \approx \Phi_o$. As outlined in Pountney *et al.* (2012) the flow structure in a rotor-stator cavity is governed by heat and mass transfer and is a viscous phenomenon, whereas ingress flow into the cavity is an inviscid phenomenon. As such Φ_o, a inviscid term is used when ingress is the important factor being considered (such as for effectiveness measurements). On the other hand λ_T is used when considering quantities such as swirl ratio which give a measure of the flow structure. Note that by equation (2.27) from von Karman (1921) it can be seen that $\lambda_T = 0.22$ is the limit of flow that can be entrained by a free disc.

An advantage of CFD over experimental measurements is the ability to get the same information from the rotor and stator, without dealing with increased measurement difficulties on and near rotating surfaces. Measurements on the stator are typically not problematic to achieve, but trying to measure quantities such as concentration on the rotor surface is difficult. This means calculating effectiveness is hard on the rotor. There are no such problems with CFD where the effectiveness on both the rotor and stator are computed. Figure 2.17 shows the effectiveness results from the steady CFD computations of Lalwani (2014). Due to the flow structure within

the wheelspace, the effectiveness on the rotor and stator is different. The effectiveness on the stator is lower than that of the rotor. This is because the sealing air attaches itself to the rotor, creating a buffering effect that reduces the amount of ingested fluid that can reach the surface of the rotor. Studies of the rotor effectiveness and the buffering effect are considered in the next section.

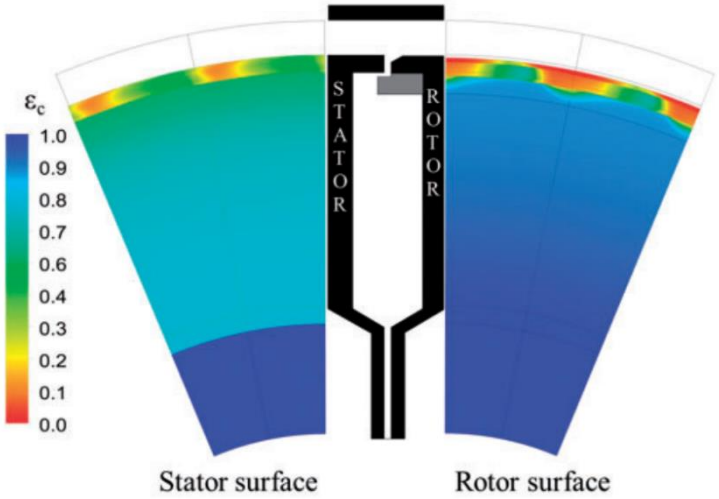

Figure 2.17: Effectiveness measurements on the rotor and stator from steady CFD computations. Lalwani (2014).

2.3.4 EFFECTIVENESS ON THE ROTOR

Chew *et al.* (1994) described a combined experimental and CFD study of the sealing effectiveness on the rotor and stator. Radial distributions of sealing effectiveness for two different sealing flow rates (one sealed, and one with ingress) were computed using a 3D CFD model, and the computations were compared with experimental measurements at four radial locations. The results showed that the rotor effectiveness was higher than that on the stator at most radial locations, and it was concluded that the cool sealing flow shields the rotor disc from the ingested flow.

Pountney *et al.* (2012) studied the effect of ingress on the rotor using the same experimental rig as Sangan *et al.* (2011a). Using thermochromic liquid crystal (TLC), measurements of the temperature were made on the rotor. From the solution of Fourier's equation, the adiabatic effectiveness of the rotor was calculated; defined by

$$\varepsilon_{ad} := \frac{T_{ad} - T_{an}}{T_{ad}^* - T_{an}} \tag{2.67}$$

where T_{ad} is the adiabatic wall temperature when ingress occurs, T_{an} is the temperature in the annulus, and T_{ad}^* is the adiabatic wall temperature when the wheel-space is fully sealed, so that there is no ingress. Concentration measurements on the stator were also taken, so effectiveness on the rotor (ε_{ad}) and stator (ε_c) could be compared. It is assumed effectiveness measured by temperature or concentration are equivalent due to the analogy between heat and mass transfer.

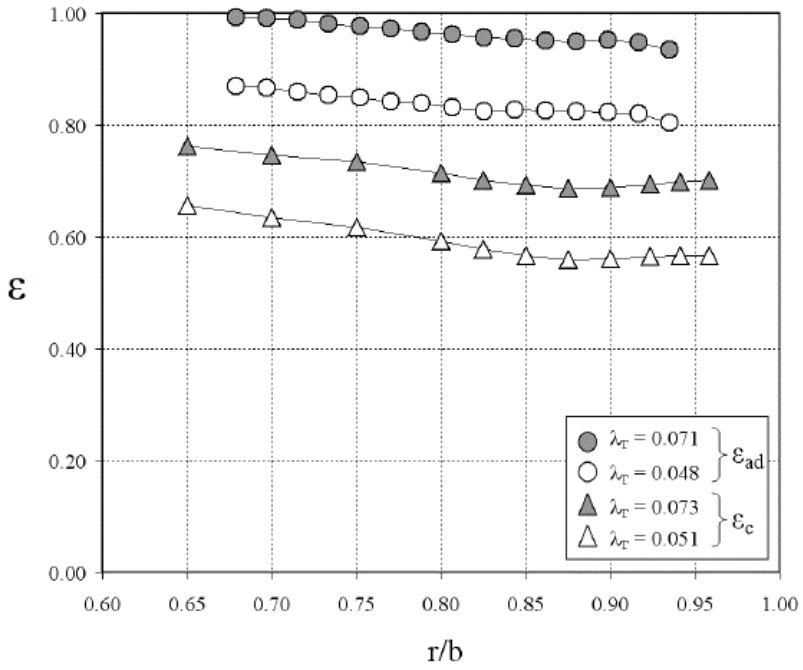

Figure 2.18: Effect of ingress on radial distribution of effectiveness (Pountney *et al.* (2012))

Figure 2.18 shows radial distribution of effectiveness on the rotor and stator for two flow rates. At each radial location $\varepsilon_c > \varepsilon_{ad}$, with ε_{ad} typically being around 20% smaller, this is attributed to the thermal buffering, that is the protection of the rotor from hot gas ingress by the sealing flow attaching to the rotor. It can be seen that ε_{ad} decreases monotonically with radius.

Pountney *et al.* (2012) also predicted the adiabatic effectiveness for the rotor with a simple model. The thermal buffer ratio, η, was defined as the ratio of the flow rate on the stator, to that on the rotor for a given effectiveness value:

$$\eta = \left[\frac{\Phi_{o,c}}{\Phi_{o,ad}}\right]_{\varepsilon_c=\varepsilon_{ad}} \tag{2.68}$$

It is a measure of how much the rotor is buffered, or protected, from the ingress. For each i^{th} value of ε_{ad} measured experimentally, the buffer ratio, η_i, was calculated by taking the corresponding $\Phi_{o,ad}$, and using the EI effectiveness equation, (2.63), to find $\Phi_{o,c}$ based upon ε_{ad}. This is best seen by considering in Figure 2.19. After calculating η_i for each data point it was found that these did not vary much with sealing flow rate, and it was suggested that the definition of the buffer ratio could be rewritten as

$$\eta = \frac{\Phi_{min,c}}{\Phi_{min,ad}} = \left[\frac{\Phi_{o,c}}{\Phi_{o,ad}}\right]_{\varepsilon_c=\varepsilon_{ad}} \tag{2.69}$$

where $\Phi_{min,c}$ is the value of Φ_o as $\varepsilon_c \to 1$ and $\Phi_{min,ad}$ is the value of Φ_o as $\varepsilon_{ad} \to 1$. It was suggested that an average η could be found. It was then hypothesized that the buffer ratio was given by the following:

$$\eta = \exp(K\lambda_{T,min}) \tag{2.70}$$

A value of the empirical constant K could be found for each data point by equating the η_i values with the model:

$$K_i = \frac{\lambda_{T,c,min}}{\ln(\eta_i)} \tag{2.71}$$

where $\lambda_{T,c,min}$ happens to be equivalent to $\Phi_{min,c}$ for these experimental conditions. Once the constant had been found for each i^{th} point, an average K could be found. Finally by using the definition (2.69), with the average η, a value of $\Phi_{min,ad}$ can be calculated by $\Phi_{min,ad} = \Phi_{min,c}/\bar{\eta}$.

The model was then used to fit the rotor effectiveness measurements by using the effectiveness equation values for $\Phi_{o,c}$ together with the average η in equation (2.69). The measurements of rotor effectiveness, ε_{ad}, and stator effectiveness, ε_c, were taken for two rotational speeds: *on-design* ($Re_w/Re_\phi = 0.538$) and *overspeed* ($Re_w/Re_\phi = 0.326$). For the on-design case buffer ratio model provided acceptable agreement with the experimental data given in the paper. For the overspeed case, shown in Figure 2.19, agreement between the model of ε_{ad} and data deviates for $\Phi_o < 0.05$, suggesting perhaps the curve should have a steeper gradient.

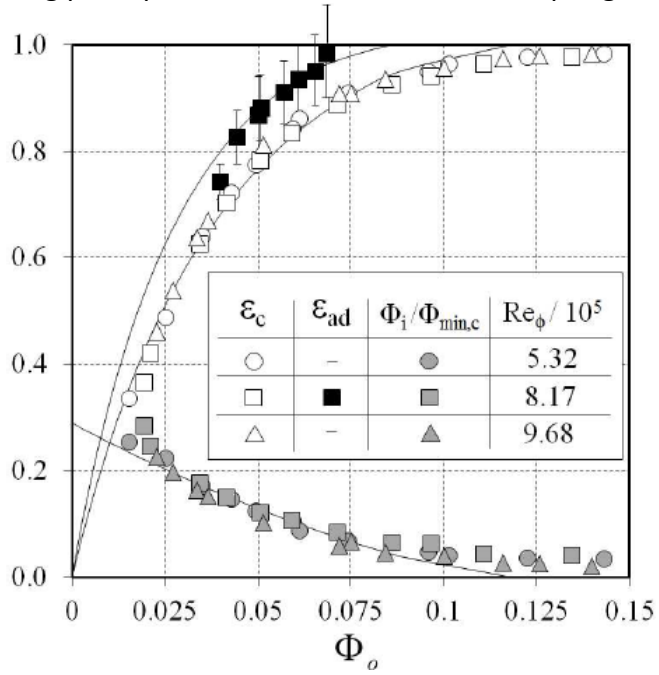

Figure 2.19: Variation of adiabatic and concentration effectiveness with sealing flow. Pountney *et al.* (2012)

Tian *et al*. (2014) also studied the difference between effectiveness on the rotor and the stator based on both concentration and temperature. The study used 3D steady CFD to study the effect of ingress on the distribution of temperature and concentration on both the rotor and stator. They concluded that effectiveness values on the rotor determined from the computed temperatures or concentrations were consistent. This was concluded based on the radial distributions of effectiveness as shown in Figure 2.20. This is important because it shows that the similarity between mass flow and energy holds.

Even though the conclusion is as expected the relative difference shown in Figure 2.20 between the rotor and stator effectiveness values is far smaller than expected. The differences shown by Pountney *et al.* (2012) were around 20%, but in the results of Tian *et al*. (2014) show only around a 2% difference. Another experimental study by Cho *et al.* (2015), to be detailed below, showed the difference to be between 10 to 20%. As this was done for four different seal geometries and was

experimental rather than computational it can be concluded that the values of Tian *et al*. are unexpectedly small.

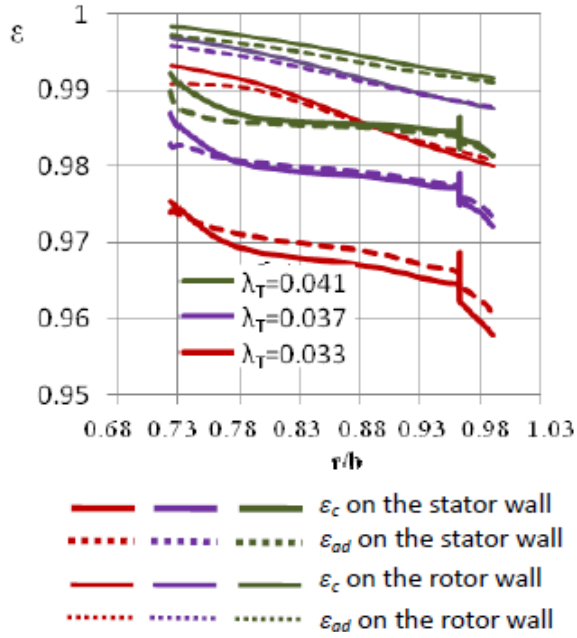

Figure 2.20: Radial distribution of effectiveness based on concentration and temperature. Tian *et al.* (2014)

A different buffer ratio definition was given by Tian *et al.* (2014):

$$\eta = \frac{\varepsilon_c}{\varepsilon_{ad}} \tag{2.72}$$

Radial variations of this new buffer ratio were plotted for different flow rates. It was concluded that that the thermal buffer ratio η increases as the sealing flow rate increases. This is in contrast to the constant buffer ratio of Pountney *et al.* (2012).

Cho *et al.* (2015) calculated effectiveness on both the rotor and the stator for four different seal geometries: axial, radial, double axial and double radial. Temperature measurements on the rotor were made by infra-red sensors at two radial locations, $r/b = 0.937$ and $r/b = 0.81$. The stator effectiveness measurements were made in the same way as for Sangan *et al.* (2011a). As mentioned above, the percentage difference between the rotor and stator was found to be around 15%. Data from this paper is fitted by a new buffering model, detailed in Chapter 6, and the fits were included in Cho *et al.* (2015).

2.4 SUMMARY

In this chapter the ingress problem for engine-representative rotor-stator systems has been introduced. Leading on from the introduction, where the boundary layer equations (PDEs) were defined Section 2.1 covered the history of the momentum-integral equations (ODEs) which approximate the boundary layer equations. Equations were stated for modelling the fluid flow over rotating and stationary discs in preparation for bringing those two sets of equations together to model the rotor-stator cavity. The flow structure of rotor-stator cavities for different flow conditions was discussed in Section 2.2, with the flow regimes and their dependent parameters being defined. Typical values of swirl ratio and empirical correlations of moment coefficients were shown. Finally the study of ingress was

covered in Section 2.3. Research has been presented from the three key research areas studying rotor-stator fluid dynamics: experimental, theoretical and computational. Each area has its own advantages and disadvantages and these have been discussed. The behaviour of important parameters in the rotor-stator cavity have been summarised, such as using effectiveness on the rotor and stator as well as the concept of the minimum amount of sealing flow used to protect a cavity. The experimental work carried out at the University of Bath was reviewed as the data will be used to validate the theoretical models defined as part of this work. The orifice model of Owen (2011) was summarised to show how theoretical modelling can give insights into physical mechanisms. The buffering phenomenon was introduced with comparison of available theoretical models given.

CHAPTER 3 : CLOSED CAVITY MODEL

This chapter describes the derivation of a model for a rotor-stator system that has no flow entering or leaving its cavity. This is a hypothetical situation as in reality the rotor and stator would always have a gap between them. However, it is still of use to have a model for this case as it approximates behaviour when the system is fully sealed. It is the simplest cavity model and as such the equations will be at their most basic. Even though a hypothetical situation is being modelled the model is still compared to experimental measurements. This provides the best validation that can be hoped for, for such a model.

The model consists of two equations to describe the flow on the rotor, and two for the stator. The solutions of the equations are then used in the mass continuity equation which is solved to find continual, non-constant swirl within the wheelspace cavity. Two versions of the Closed Cavity model are presented in this chapter: the *original* and *variable* momentum-integral equation model. The *original momentum-integral equation model* solves the previously published momentum-integral equations where the swirl ratio in the core is assumed to be constant. There are two equations for the rotor and two for the stator and they are uncoupled. The *variable momentum-integral equation model* solves newly derived momentum-integral equations where the swirl ratio is a variable. There are still two differential equations (DEs) for the rotor and two DEs for the stator but for this case there is a fifth DE for the swirl ratio. All the equations depend on each other so they are coupled.

In Section 3.1 the flow structure within an enclosed rotor-stator system is discussed. In Section 3.2 a new method for solving existing (called 'original') momentum-integral equations is outlined, and the results are presented and discussed. Then in sections 3.3 new momentum-integral equations (the 'variable' equations) are derived. A new solution method is also outlined and then results are shown. A summary of the key results is given in Section 3.4. Many symbols are used in this chapter and these are derived in the nomenclature.

3.1 CLOSED CAVITY FLOW STRUCTURE

Assuming a Batchelor type flow structure, as discussed in Section 2.2, within the rotor-stator cavity the flow will travel radially upwards on the rotor, radially inwards on the stator and there will be a rotating core at the centre. A simplified flow structure diagram is shown in Figure 3.1.

As the flow moves radially upwards in the rotor, the boundary layer on the disc entrains fluid from the core. At some non-dimensional radial location, $x = x_{out}$, the flow will stop being entrained and will instead leave the rotor boundary layer. This is characterized by a decrease in the mass flow rate over the disc. The region above $x = x_{out}$ is coined the *outer region*. In the outer region, on the stator side, fluid is entrained into the stator boundary layer. Moving radially inwards (past $x = x_{out}$) the fluid leaves the stator boundary layer as it is entrained into the rotating core.

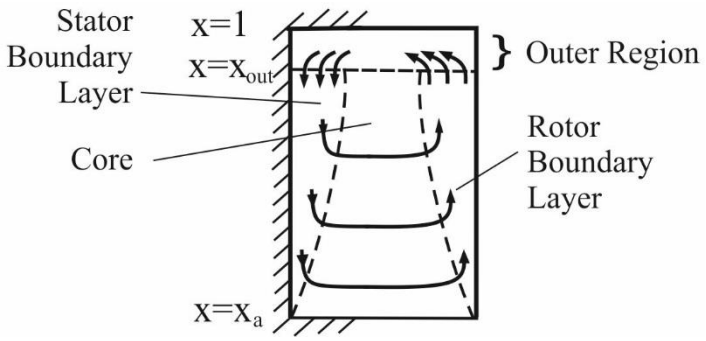

Figure 3.1: Simplified flow structure for a closed rotor-stator cavity

As the rotor and stator discs inside gas turbines are attached to a shaft, the wheelspace is an annular section rather than a cylindrical section. This is captured in the model by the use of $x = x_a$ where x_a is the non-dimensional inner radius of the cavity. In dimensional form the inner radius is denoted by a and the outer radius by b. If an entire disc was being modelled $x_a = 0$ would be set, whereas if a cavity with a shaft was being modelling $x_a = 0.6$ could be set, for example. When different values of x_a are set, this is to simulate different cavity sizes.

Recall that this is not a physically realisable situation (as in reality the rotor and stator would always have a gap between them) but it is useful to have a model for this case as it approximates behaviour when the system is fully sealed.

It is important to note that the boundary layers on the rotor and stator will not be the same thickness (consider equations (2.34) and (2.4) for the boundary layer thickness of the rotor and stator respectively). The simplified flow structure figures in this thesis (such as Figure 3.1) are not suggesting the thicknesses of the boundary layers will be the same, and the entire sketches are not to scale, they are simply to aid discussion of the flow structure.

3.2 ORIGINAL MOMENTUM-INTEGRAL EQUATION MODEL

3.2.1 EQUATIONS

Modelling the Rotor

To model the flow over the rotating surface the momentum-integral equations for a rotating disc in a rotating fluid can be used. Equations (2.36) and (2.37), presented in the literature review, can be uncoupled so that the equations can be solved independently. Shown as (3.1) and (3.2), these equations describe the flow in the rotor boundary layer, where α_o and γ_o are both functions of x and a distribution for $\beta(x)$ must be supplied.

$$\frac{d\alpha_o}{dx} = \frac{\alpha_o}{x(1-\beta)}\left[\frac{-6696}{343}F_o + \frac{46(1+8\beta)}{343\alpha_o^2} + \frac{23+37\beta}{5} - \frac{18}{5}(1-\beta)\right] \tag{3.1}$$

$$\frac{d\gamma_o}{dx} = \frac{\gamma_o}{x(1-\beta)}\left[\frac{11736}{343}F_o - \frac{46(1+8\beta)}{343\alpha_o^2} - 2\left\{\frac{23+37\beta}{5}\right\} + \frac{18}{5}(1-\beta)\right] \tag{3.2}$$

where

$$F_o = \frac{0.0225(1+\alpha_o^2)^{\frac{3}{8}}}{\alpha_o \gamma_o^{\frac{5}{4}}} \tag{3.3}$$

The term F_o has no special significance and does not represent a physical quantity; it does however allow the equations to be expressed on a single line and generally improves readability. It is also a term that appears in the same form in the both rotor and stator equations, so it makes sense for it to be a term that is emphasised.

It is important to note that when these equations were derived it was assumed that β was constant with radius, however a non-constant β could, and will, be used when solving the equations. In the interest of brevity, the value of β at $x = x_a$ is denoted 'β_a' and the value of β at $x = 1$ is denoted 'β_1'.

Equations (3.1) and (3.2) can also be written in an equivalent but simplified form as

$$\frac{d\alpha_o}{dx} = \frac{\alpha_o}{x(1-\beta)}\left[\frac{-6696}{343}F_o + \frac{46(1+8\beta)}{343\alpha_o^2} + 11\beta + 1\right] \tag{3.4}$$

$$\frac{d\gamma_o}{dx} = \frac{\gamma_o}{x(1-\beta)}\left[\frac{11736}{343}F_o - \frac{46(1+8\beta)}{343\alpha_o^2} - \frac{4}{5}(23\beta + 7)\right] \tag{3.5}$$

Even though this form is simpler, it does not preserve the symmetry between the equations in the same way as the 'long-hand' form shown originally.

Initial Conditions for the Rotor Equations

In order to solve the rotor differential equations presented above numerically, initial conditions for α_o and γ_o at x_a are needed. The analytical solutions to these differential equations, shown in the literature review as (2.38) and (2.39), can be used to provide these initial conditions where α_o and γ_o are both functions of β. When using these equations to find values for the initial conditions at $x = x_a$, β will be defined as β_a. For the Closed Cavity model the fluid is best modelled with $\beta_a = 0$ as there is no fluid being supplied to have a positive swirl ratio value.

When modelling the Closed Cavity it is assumed that the rotor boundary layer starts, and therefore has zero thickness, at $x = x_a$. As γ_o is proportional to δ_o, the boundary layer thickness, instead of using the equation above for $\gamma_o(\beta)$ it is simply set as close to zero as possible, typically $\gamma_o = 10^{-6}$.

Modelling the Stator

To model the flow over a stationary disc the momentum-integral equations for a stationary disc in a rotating fluid can be used. Uncoupling equations (2.43) and (2.44) gives (3.6)-(3.7). In these equations, describing flow in the stator boundary layer, α_s and γ_s are both functions of x. Unlike the rotor, the equations have no β term and are therefore independent of the swirl ratio.

$$\frac{d\alpha_s}{dx} = \frac{\alpha_s}{x}\left[\frac{6696}{343}\left(\frac{0.0225(1+{\alpha_s}^2)^{\frac{3}{8}}}{\alpha_s{\gamma_s}^{\frac{5}{4}}}\right) - \frac{1656}{343}\frac{2}{9{\alpha_s}^2} - 11\right] \tag{3.6}$$

$$\frac{d\gamma_s}{dx} = \frac{\gamma_s}{x}\left[\frac{11736}{343}\left(\frac{-0.0225(1+{\alpha_s}^2)^{\frac{3}{8}}}{\alpha_s{\gamma_s}^{\frac{5}{4}}}\right) + \frac{1656}{343}\frac{2}{9{\alpha_s}^2} + \frac{92}{5}\right] \tag{3.7}$$

Initial Conditions for the Stator Equations

No analytical solutions of these equations exist where α_s is real, so the initial conditions must be set without any guidance. As for the rotor, whose boundary layer starts at $x = x_a$ it is assumed that the stator boundary layer starts at $x = 1$. Hence in order to make the expression for the boundary layer thickness on the stator, δ_s, be zero at $x = 1$ it must be that γ_s is as close to zero as numerically possible, typically $\gamma_s = 10^{-6}$. This fixes one initial condition for the stator at $x = 1$, which will be denoted $\gamma_{s,1}$. An initial condition for α_s must also be chosen, denoted $\alpha_{s,1}$, this is typically $\alpha_{s,1} = 10^{-4}$ however as shown in Figure 3.2 the choice does not affect the solution of the equation or model.

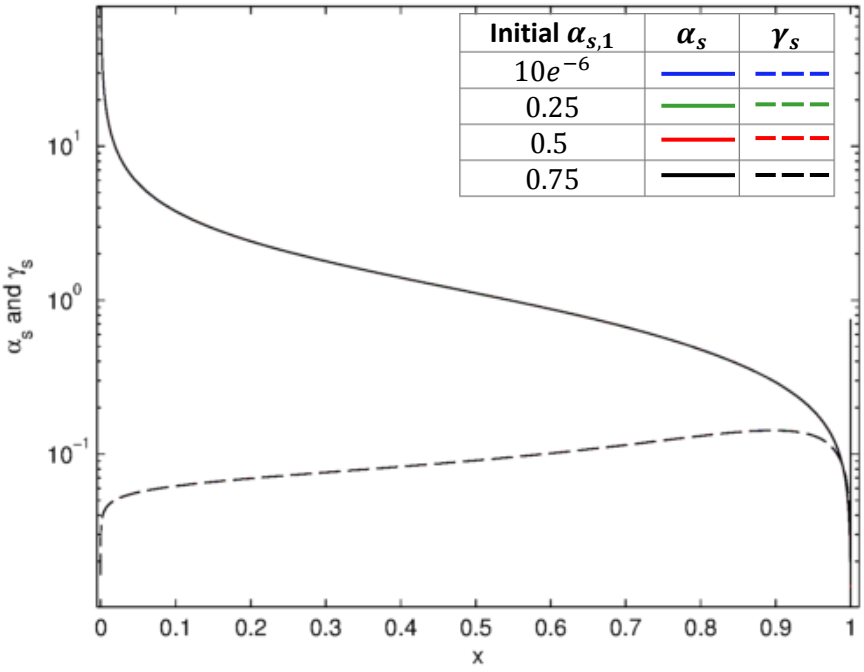

Figure 3.2: Perturbation of stator initial condition $\alpha_{s,1}$, where $\gamma_{s,1} = 10^{-6}$

Figure 3.2 shows how the radial solutions to the stator equations change with different initial conditions. Regardless of the value of $\alpha_{s,1}$ set, there appears to be convergence at all radial locations as no significant variations can be observed. It is worth reiterating that the integration on the stator is performed radially inwards, so the initial condition is at $x = 1$ and the solver is running *right to left* in the Figure.

Conservation of Mass

The equations for the rotor and stator need to be brought together, in order to model a wheelspace cavity. The mass flow rates on the rotor and stator as shown in (2.35) and (2.42) can be written in non-dimensional forms. The non-dimensional mass flow rate on the rotor, $C_{w,o}$, is

$$C_{w,o} := \frac{\dot{m}_o}{\mu b} = \frac{2\pi n^2 \alpha_o \gamma_o}{(n+1)(2n+1)} (1-\beta)^{\frac{2(n+1)}{n+3}} Re_\phi^{\frac{n+1}{n+3}} x^{\frac{3n+5}{n+3}} \tag{3.8}$$

for the general 1/n[th] power law. The non-dimensional mass flow rate on the stator, $C_{w,s}$, is

$$C_{w,s} := \frac{\dot{m}_s}{\mu b} = \frac{-2\pi \alpha_s \gamma_s n^2}{(n+1)(2n+1)} \beta^{\frac{n+1}{n+3}} Re_\phi^{\frac{n+1}{n+3}} x^{\frac{3n+5}{n+3}} \tag{3.9}$$

once again for the general 1/nth power law. Now the *turbulent flow parameter* is defined as $\lambda_{T,o}$ for the *rotor* where

$$\lambda_{T,o} \coloneqq C_{w,o} Re_{\phi}^{-\frac{n+1}{n+3}} \tag{3.10}$$

and as $\lambda_{T,s}$ for the *stator* where

$$\lambda_{T,s} \coloneqq C_{w,s} Re_{\phi}^{-\frac{n+1}{n+3}} \tag{3.11}$$

By using (3.8) and (3.9) in (3.10) and (3.11) respectively, expressions for the rotor and stator turbulent flow parameter are gained:

$$\lambda_{T,o} = \frac{2\pi n^2}{(n+1)(2n+1)} \alpha_o \gamma_o (1-\beta)^{\frac{2(n+1)}{n+3}} x^{\frac{3n+5}{n+3}} \tag{3.12}$$

$$\lambda_{T,s} = \frac{-2\pi n^2}{(n+1)(2n+1)} \alpha_s \gamma_s \beta^{\frac{n+1}{n+3}} x^{\frac{3n+5}{n+3}} \tag{3.13}$$

For $n = 7$ these become

$$\lambda_{T,o} = \frac{49\pi}{60} \alpha_o \gamma_o (1-\beta)^{\frac{8}{5}} x^{\frac{13}{5}} \tag{3.14}$$

$$\lambda_{T,s} = -\frac{49\pi}{60} \alpha_s \gamma_s \beta^{\frac{4}{5}} x^{\frac{13}{5}} \tag{3.15}$$

As the continuity of mass must apply for the case of the Closed Cavity, it is known that

$$\dot{m}_o + \dot{m}_s = 0 \tag{3.16}$$

This can be written equivalently as

$$\lambda_{T,o} + \lambda_{T,s} = 0 \tag{3.17}$$

By substituting equation (3.14) and (3.15) into (3.17) this gives

$$\frac{2\pi n^2}{(n+1)(2n+1)} x^{\frac{13}{5}} \left[\alpha_o \gamma_o (1-\beta)^{\frac{2(n+1)}{n+3}} - \alpha_s \gamma_s \beta^{\frac{n+1}{n+3}} \right] = 0 \tag{3.18}$$

or, for $n = 7$,

$$\frac{49\pi}{60} x^{\frac{13}{5}} \left[\alpha_o \gamma_o (1-\beta)^{\frac{8}{5}} - \alpha_s \gamma_s \beta^{\frac{4}{5}} \right] = 0 \tag{3.19}$$

henceforth called the *continuity equation.* This equation allows the rotor and stator to be coupled together by the swirl ratio within the cavity. As there is no flow entering or leaving the system for a closed cavity this means mass is conserved from the rotor to the stator. The continuity equation contains solutions from the rotor equations (α_o and γ_o), solutions from the stator equations (α_s and γ_s) and the swirl ratio (β). By substituting the solutions for α_o, γ_o, α_s and γ_s into this equation and then solving the continuity equation, a distribution of swirl ratio can be found that couples the rotor and stator.

3.2.2 SOLUTION METHOD

In order to create a rotor-stator cavity model, the equations in the previous subsection have to be solved such that the results are coupled. The rotor and stator equations do not depend upon each other – so the differential equations can be solved separately. However, an iterative method is introduced in order to find a 'global' swirl ratio distribution that satisfies both the rotor and stator differential equations as well as the continuity equation.

The α and γ equations are solved simultaneously within MATLAB for both the rotor and the stator. They are solved using the vector functional form by one of the many built in solvers for ordinary differential equations (ODEs). Once the solution algorithm (detailed below) for the Closed Cavity was established three different solvers were tested: `ode45` – one step solver based up a 4/5th order explicit Runge-Kutta formula, `ode23` – one step solver using explicit 3rd order Runge-Kutta formula and `ode15s` – a variable order solver using backwards differentiation formulae. All three solvers yielded the same results in similar computation times with similar step sizes. The solver ode15s has been used throughout this work due to it typically having a slightly quicker computation time.

To solve the rotor equations, numerical integration is performed from $x = x_a$ to $x = 1$: this is with increasing radius and in the direction of flow. To solve the stator equations they must be integrated in the direction of decreasing radius, such that the integration is still done in the direction of the flow. This means a change of variables is required to solve the stator equations (3.6) and (3.7). By setting $y = 1 - x$ the equations can be solved in the direction of flow. Figure 3.3 shows the two integration directions for the rotor and stator equations. Notice that changing the integration starting radius on the rotor, x_a, is equivalent to changing the integration end point on the stator, where $y_a = 1 - x_a$.

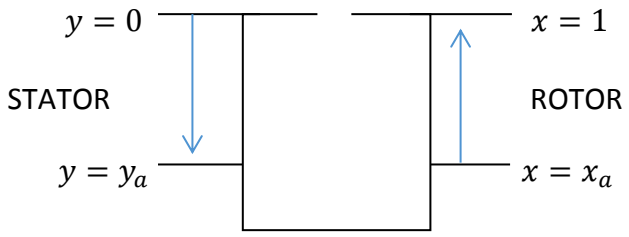

Figure 3.3: Integration ranges of rotor and stator equation

Solution Method Summary

The solution method is outlined in Figure 3.4 below and summarised here. The rotor and stator equations are solved independently after using appropriate initial conditions, and then the results are used in the continuity equation which is solved to determine a new β distribution. This new β distribution is put into the rotor equations and the equations for α_o and γ_o are solved again. This process of finding a new β distribution and re-solving the rotor equation then iterates until β is unchanged. As the stator contains no β terms it does not need to be re-solved. The β distribution being unchanged is the basis of the *convergence criterion*: for the model an *absolute error tolerance* is set and after each iteration the swirl ratio distributions from the current (β_i) and previous iteration (β_{i-1}) are compared at every radial location. If the *maximum absolute error* between the two is less than the *error tolerance* that is set then the model is considered converged. If the maximum absolute error between the two distributions is greater than the error tolerance then the model completes another iteration. Typically 0.05% is used as an error tolerance. Smaller tolerances can be applied, but this will make the computation time considerably larger for very small changes in the results.

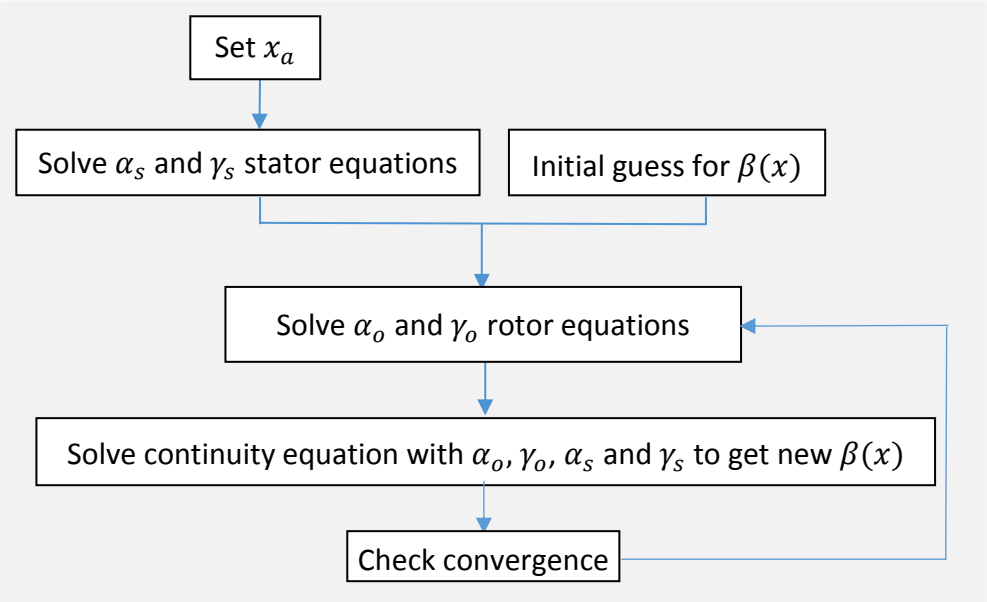

Figure 3.4: Solution Procedure for Closed Cavity Model with Original Momentum-Integral Equations

Solving the Continuity Equation

In the beginning of this section, the acquisition of solutions to the rotor and stator equations was discussed. The second discusses the solutions to the continuity equation. The continuity equation, (3.19), is equivalent to a quadratic equation,

$$a\beta^2 + b\beta + c = 0 \tag{3.20}$$

where the coefficients are defined as

$$a = 1, b = -2 - \left(\frac{\alpha_s\gamma_s}{\alpha_o\gamma_o}\right)^{\frac{5}{4}}, c = 1 \quad \text{such that} \quad (\alpha_o\gamma_o)^{\frac{5}{4}} \neq 0 \tag{3.21}$$

and as such can be solved directly for β. These coefficients can be used in the standard solution for a quadratic equation, to give a value of β. Any negative values are deemed physically unrealistic and are therefore ignored leaving a unique positive solution.

Note that because $\alpha_o, \gamma_o, \alpha_s$ and γ_s are all functions of x there will be a different value of β at each different non-dimensional radial location. Therefore the continuity equation must be solved many times, although this is not a problem computationally as β is known analytically from the solution of the quadratic equation, as discussed above.

Technically the rotor variables α_o and γ_o also depend upon β (see equation (3.1) and (3.2)), but this will be a β distribution from the previous iteration. For each i^{th} time the rotor is solved the continuity equation can be thought of as shown below:

$$(1-\beta_i)^{\frac{8}{5}}\alpha_o(x,\beta_{i-1})\gamma_o(x,\beta_{i-1}) - \beta_i^{\frac{4}{5}}\alpha_s(x,\beta_{i-1})\gamma_s(x,\beta_{i-1}) = 0 \tag{3.22}$$

where β_i is being found from values of α_o and γ_o that are based on previous step β_{i-1}. This means in order for the method to be considered converged the final solution (i.e. the final distribution of swirl ratio) should be based upon a β_i value that has not changed too greatly from the previous iteration, β_{i-1}.

Full Procedure Details

The following steps give the details for the Closed Cavity model based on the solution of the original momentum-integral equations.

Step 0: Initial Conditions for the Model
Inputs: x_a, initial condition $\alpha_{s,1}$ and error tolerance.

Step 1: Solve stator equations
Inputs: Initial condition for stator $\alpha_{s,1}$.
Outputs: $\alpha_s(x), \gamma_s(x)$
By assuming that the boundary layer on the stator always starts from zero thickness at $x = 1$ then one of the initial conditions is always fixed: $\gamma_{s,1} \cong 0$. Now the stator equations (3.6) and (3.7) can be solved numerically, using a built in MATLAB solver such as ode15s.

Step 2: Initial guess for $\beta(x)$ distribution
Inputs: chosen form for distribution (e.g. Linear)
Outputs: $\beta(x)$
Set a guess for the distribution of β radially. The default is simply a linear increase from $\beta_a = 0$ to $\beta_1 = 1$.

Step 3: Solve rotor equations
Inputs: $\beta(x)$, initial condition for rotor: value for α_o at $x = x_a$
Outputs: $\alpha_o(x), \gamma_o(x)$
As β_a has been fixed at zero and the analytic equation (2.38) gives the initial condition for the rotor α_o (namely $\alpha_o = 0.162$ for $\beta_a = 0$). As mentioned above γ_o is approximately zero. Now the rotor equations (3.1) and (3.2) can be solved numerically, using a built in MATLAB solver such as ode15s.

Step 4: Solve the continuity equation
Inputs: $\alpha_o(x), \gamma_o(x), \alpha_s(x), \gamma_s(x)$
Outputs: $\beta(x)$
The continuity equation (3.19) is solved at a set number of radial locations between x_a and 1 (typically 100). This is done by using the standard solution for a quadratic equation using the coefficients in (3.21).

Step 5: Convergence Check
Inputs: β_i and β_{i+1}
The convergence criterion (as described above) is checked. If the procedure is considered to have converged then the results produced by step 4. are output as the final results. If the model is *not* considered converged then the $\beta(x)$ output of step 4. is considered the new $\beta(x)$ guess and the method continues from step 3.

The final solution for the Closed Cavity model takes the form of five continuous functions from $x = x_a$ to $x = 1$: Two to describe the rotor flow (α_o, γ_o), two to describe the stator flow (α_s, γ_s) and the swirl ratio (β). The next section outlines how these variables can be used to calculate other quantities inside the wheelspace.

There are two 'guesses' that can affect the procedure: the first is the initial estimate of $\beta(x)$ and the second is the initial value for α_s on the stator. The procedure has been shown to be insensitive to both of these estimates.

3.2.3 RESULTS FOR ORIGINAL MOMENTUM-INTEGRAL EQUATIONS

After successful completion of the solution procedure, five continuous distributions will be known: $\alpha_o(x), \gamma_o(x), \alpha_s(x), \gamma_s(x)$ and $\beta(x)$. From these results many physical quantities can be calculated, which can then be compared to experimental and computational results to validate the model. Shown in the following section will be swirl ratios, mass flow rates, pressure and moment coefficients.

Swirl Ratio

The swirl ratio distribution, $\beta(x)$, found by solving the continuity equation at each radial location, changes with each iteration. Figure 3.5 shows how the swirl ratio changes with iteration number for a typical run of the Closed Cavity Model. The specific conditions were $\alpha_{s,1} = 0.001,\ \gamma_{s,1} = 10^{-4}, \beta_a = 10^{-6}$ and an error tolerance between the two steps of 0.1%. For case (a) $x_a = 10^{-6}$ and for case (b) $x_a = 0.6$. It can be seen that for both cases the swirl ratio distribution quickly moves away from the initial guess and converges within around eight iterations. Interestingly for case (b) the third iteration gives a more typical 'constant' swirl ratio distribution within the wheelspace. This is probably not significant.

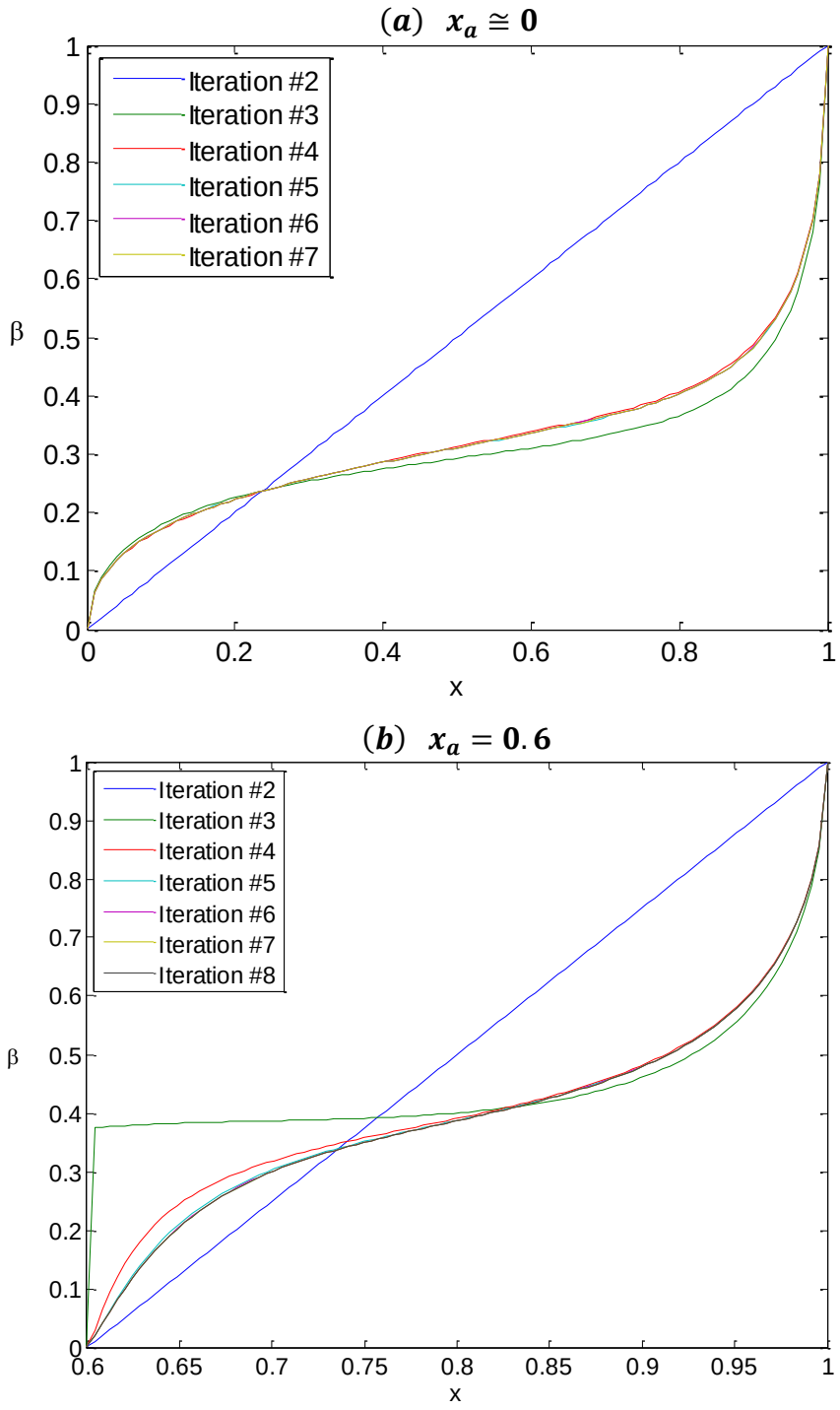

Figure 3.5: Distribution of swirl ratio for increasing iterations for (a) $x_a \cong 0$ and (b) $x_a = 0.6$

Figure 3.5 shows the final converged swirl ratio distribution for the Closed Cavity model with four different starting radius values. Interestingly, no matter where the flow has started in the cavity the swirl ratio seems to converge onto a single solution. This has interesting implications for the engine designer: it suggests that the flow structure is likely to be unaffected by changes in the radius of the wheelspace for the case of no ingress. As far as the author knows there is no experimental evidence for or against this.

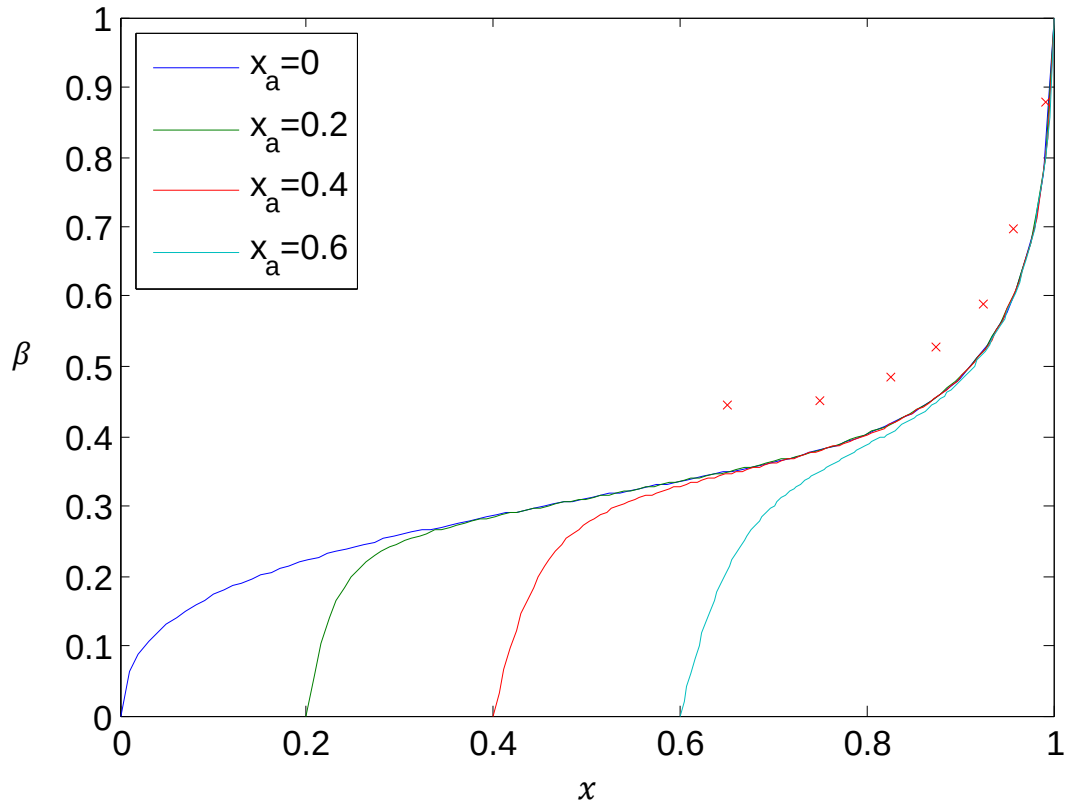

Figure 3.6: Variation of swirl ratio with radius for Closed Cavity Original Model for four cavity sizes. (Solid lines denote theoretical model, crosses denote experimental data)

The red crosses in shown in Figure 3.6 are experimental measurements of swirl ratio taken on the University of Bath 1-stage rig detailed in Sangan *et al.* (2014). They are for an axial clearance seal with no superposed flow where $x_a \cong 0.65$. Note that this experimental configuration is *not* what is being modelled by the closed cavity model: the theoretical model does not include any ingress whereas the experiment would have been subject to ingress. In fact, as no sealing air was supplied the experiment would have subject to a maximum amount of ingress. It is shown in Chapter 5 that EI ingress increases the swirl ratio, so it is unsurprising that the data, which is affected by ingress, has a higher swirl ratio at all radial locations than predicted by the model. It is encouraging that the agreement with experimental data is qualitatively good.

Turbulent Flow Parameter

Recall the expressions for the non-dimensional turbulent flow parameter for the rotor, $\lambda_{T,o}$, and the stator, $\lambda_{T,s}$, given by (3.14) and (3.15). These can be calculated by using the final results for $\alpha_o(x), \gamma_o(x), \alpha_s(x), \gamma_s(x)$ and $\beta(x)$.

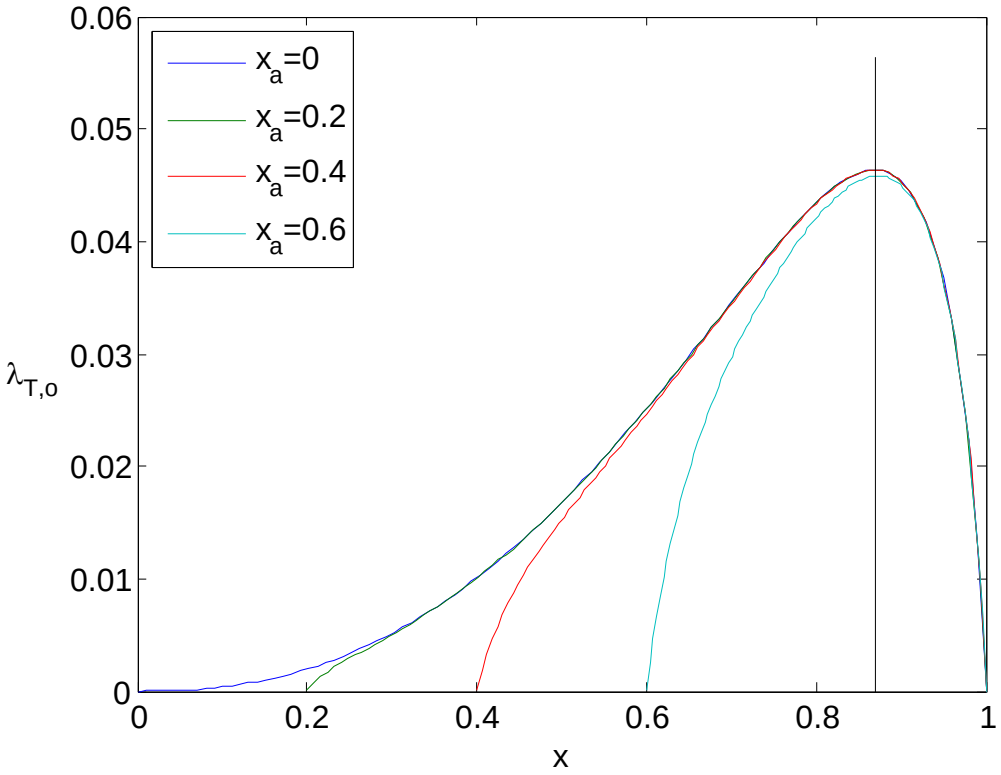

Figure 3.7: Variation of mass flow rate within the rotor boundary layer with radius for Closed Cavity Model (for four starting radius values).

Figure 3.7 shows the effect of increasing the starting radius on the mass flow rate within the boundary layer on the rotor, and therefore the stator too. (As the mass flow rate on the stator is equal and opposite in sign to the rotor mass flow rate – see (3.17)). x_{out} is defined as the non-dimensional radial location at which the flow rate on the rotor reaches its maximum; the turning point of the mass flow captures the location at which flow begins leaving the rotor and flow is instead entrained by the stator. The maximum is found numerically and interestingly no matter at which radial location the flow starts, the location of x_{out} remains fixed (to 2dp) *at* $x_{out} = 0.87$.

The black vertical line in Figure 3.7 shows this value of x_{out}. (For $x_a \cong 0, 0.2, 0.4$ the exact result is $x_{out} = 0.8684$ and for $x_a = 0.6$ is it $x_{out} = 0.8714$). Also notice that the mass flow rate in the *outer region* is independent of the origin of the flow – all cases converge. The mass flow rate being zero at $x = x_a$ is as expected (due to the initial conditions $\gamma_o = 0$ and $\beta_a = 0$). The mass flow rate being zero at $x = 1$ is as expected as no flow is leaving the cavity.

Pressure

The final converged swirl ratio distribution can be used to calculate the *pressure coefficient,* C_p, within the wheelspace, which can also be compared to experimental measurements. The same limitations as described above apply when comparing the experimental measurements to the theoretical model (namely that the experiments are *not* carried out in a closed cavity). The *pressure coefficient,* C_p, is related to the *static pressure in the wheelspace,* p, such that

$$C_p = \frac{p - p_{ref}}{\frac{1}{2}\rho\Omega^2 b^2} \tag{3.23}$$

where p_{ref} is some reference pressure at radial location x_{ref}. Sangan *et al.* (2014) showed that C_p can be calculated by simply integrating the swirl:

$$C_p = 2\int_{x_{ref}}^{1} x\beta^2\, dx \tag{3.24}$$

Figure 3.8 shows the effect of increasing the starting radius on the pressure coefficient, calculated using (3.24) based on the results of the model, where x_{ref} has been set to x_a. Also shown are experimental measurements of C_p from Sangan *et al.* (2014). Unsurprisingly for the case of $x_a = 0.6$, C_p is under-predicted (this can be attributed to the presence of ingress in the experimental results). Interestingly there is good agreement between the results of the model and the experiments when $x > 0.8$ where $x_a \leq 0.2$.

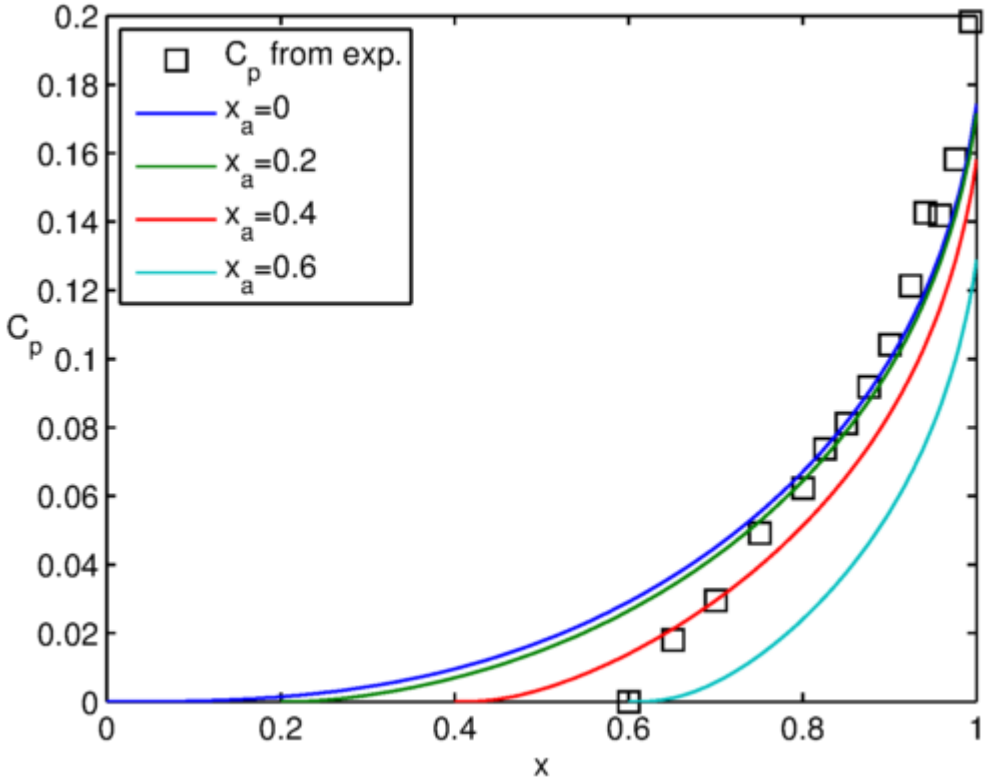

Figure 3.8: Variation of pressure coefficient with radius for Closed Cavity Model, for four cavity sizes.

Moments

Another quantity that can be calculated from the results of the model are moments on the rotor and stator discs. By definition, the *moment on a disc* is given by

$$M_0 = -\int_a^b A\tau_{\phi,0} r\, dr = -\int_a^b 2\pi r\tau_{\phi,0} r\, dr.$$

where $A = 2\pi(b^2 - a^2)$ is area of the disc, a is the inner radius and b is the outer radius. Firstly considering a rotor disc, and substituting in an identity for the shear stress, $\tau_{\phi,0}$,

$$\tau_{\phi,0} = -\rho K[\Omega r(1-\beta)]^{\frac{7}{4}}\left(\frac{\mu}{\rho\delta_o}\right)^{\frac{1}{4}}(1+\alpha_o^2)^{\frac{3}{8}} \tag{3.25}$$

$$\tau_{\phi,0} = -\rho K[\Omega r(1-\beta)]^{\frac{2n}{n+1}}\left(\frac{\mu}{\rho\delta_o}\right)^{\frac{2}{n+1}}(1+\alpha_o^2)^{\frac{n-1}{2(n+1)}}$$

where δ_o is given by (2.34). Applying a change of variables $x = r/b$ to use non-dimensional radius, the *moment on the rotor* becomes

$$M_o = 2\pi\rho\Omega^2 b^5 Re_\phi^{-\frac{1}{5}}\int_{x_a}^{1} x^{\frac{18}{5}}(1-\beta)^{\frac{8}{5}}\left[K\frac{(1+\alpha_o^2)^{\frac{3}{8}}}{\gamma_o^{\frac{1}{4}}}\right]dx \tag{3.26}$$

Consider the *moment coefficient for the rotor*, C_{M_o},

$$C_{M_0} := \frac{M_0}{\frac{1}{2}\rho\Omega^2 b^5} \Rightarrow C_{M_o} = 4\pi Re_\phi^{-\frac{1}{5}}\int_{x_a}^{1} x^{\frac{18}{5}}(1-\beta)^{\frac{8}{5}}\left[K\frac{(1+\alpha_o^2)^{\frac{3}{8}}}{\gamma_o^{\frac{1}{4}}}\right]dx$$

By using this new expression to define a new identity, the Reynolds number can be separated within the above equation

$$C_{M_o} = \varepsilon_{M_o} Re_\phi^{-\frac{1}{5}} \tag{3.27}$$

where ε_{M_o} is given by

$$\varepsilon_{M_0} = 4\pi K\int_{x_a}^{1}\frac{(1+\alpha_o^2)^{\frac{3}{8}}}{\gamma_o^{\frac{1}{4}}}x^{\frac{18}{5}}(1-\beta)^{\frac{8}{5}}\,dx \tag{3.28}$$

Notice that if it is assumed that all the variables are constant with radius, then the following simple algebraic expression can be derived

$$\varepsilon_{M_0} = 4\pi K(1-\beta)^{\frac{8}{5}}\frac{(1+\alpha_o^2)^{\frac{3}{8}}}{\gamma_o^{\frac{1}{4}}}\frac{5}{23}\left[1-x_a^{\frac{23}{5}}\right] \tag{3.29}$$

Using the solutions of the rotor equations α_o and γ_o along with the swirl distribution, a value for ε_{M_0} can be calculated. In Owen and Rogers (1989) ε_{M_0} is given as a direct formula, as β, α, γ are considered independent of x and integration is done from $x_a = 0$:

$$\varepsilon_{M_0} = \frac{49\pi}{4140}(1-\beta)^{\frac{8}{5}}(23+37\beta)\alpha_o\gamma_o \tag{3.30}$$

Note on nomenclature: Throughout this work the term of most importance will be ε_{M_0}, rather than C_{M_0}, due to it being separate from the effects of Re_ϕ. As ε_{M_0} could be considered the 'moment coefficient coefficient' which is a rather long winded name, ε_{M_0} will simply be called the moment coefficient. The more 'classical' moment coefficient C_{M_o} being easily recoverable from the values of ε_{M_0}. Note that within Coren *et al.* (2009) ε_{M_0} is called the 'core rotation rate factor'. The same applies to ε_{M_s}, defined below.

Similarly the *moment on the stator, M_s,* is given by

$$M_s = -2\pi b^3\int_{x_a}^{1} x^2\tau_{\phi,0}\,dx \tag{3.31}$$

The identity for the shear stress, $\tau_{\phi,0}$, over a stator disc is

$$\tau_{\phi,0} = \rho K \left(\frac{\mu}{\rho \delta_s}\right)^{\frac{1}{4}} (\Omega r \beta)^{\frac{7}{4}} (1+\alpha_s^2)^{\frac{3}{8}} \tag{3.32}$$

where δ_s is given by (2.41). Applying a change of variables $x = r/b$ to use non-dimensional radius, the *moment on the stator* becomes

$$M_s = -2\pi\rho\Omega^2 b^5 Re_\phi^{-\frac{1}{5}} \int_{x_a}^{1} x^{\frac{18}{5}} (1-\beta)^{\frac{8}{5}} \left[K \frac{(1+\alpha_o^2)^{\frac{3}{8}}}{\gamma_o^{\frac{1}{4}}} \right] dx \tag{3.33}$$

the *moment coefficient for the stator, C_{M_s},* is

$$C_{M_s} := \frac{M_s}{\frac{1}{2}\rho\Omega^2 b^5} \Rightarrow C_{M_s} = -\frac{4\pi}{\rho\Omega^2 b^2} Re_\phi^{-\frac{1}{5}} \int_{x_a}^{1} x^{\frac{18}{5}} \beta^{\frac{4}{5}} K \frac{(1+\alpha_s^2)^{\frac{3}{8}}}{\gamma_s^{\frac{1}{4}}}\, dx \tag{3.34}$$

and finally another coefficient, ε_{M_s}, is

$$\varepsilon_{M_S} = -4\pi K \int_{x_a}^{1} \frac{(1+\alpha_s^2)^{\frac{3}{8}}}{\gamma_s^{\frac{1}{4}}} x^{\frac{18}{5}} \beta^{\frac{4}{5}}\, dx \tag{3.35}$$

Using the solutions of the stator equations α_s and γ_s along with the swirl distribution, a value for ε_{M_s} can be calculated. As the solutions α_s and γ_s are initially found as with respect to y, it is of use to define ε_{M_S} where the integral is in terms of that variable, $y = 1 - x$. Therefore an equivalent coefficient after a change of variables is given by

$$\varepsilon_{M_S} = 0.2827 \int_0^{y_a} (1-y)^{\frac{18}{5}} \beta(y)^{\frac{4}{5}} \frac{(1+{\alpha_s}^2(y))^{\frac{3}{8}}}{\gamma_s(y)^{\frac{1}{4}}}\, dy \tag{3.36}$$

The values for both $\varepsilon_{M_o}$and ε_{M_s} are found by using the continuous distributions of α_o, γ_o and β in (3.28) and of α_s, γ_s and β in (3.35) respectively. The integrals can then be evaluated numerically to give the results in Table 3.1 for different x_a values. The moments on the rotor and stator are not the same; typically there is around a ten percent difference.

x_a	ε_{M_o}	ε_{M_s}	Error (%)
0.000	0.035	0.032	9.429
0.200	0.035	0.032	9.654
0.400	0.035	0.031	10.399
0.600	0.032	0.028	12.983

Table 3.1: Moment coefficients for Original Closed Cavity Model

Lalwani (2014) used CFD to model the fluid flow within the Bath rig but with *no ingress.* The model was created by setting the flow conditions in the annulus to purely outflow, this prevented any ingress regardless of the flow supplied. Lalwani found the moment on the rotor when there was no ingress and no superposed flow to be 0.0314, which was calculated with cavity size $x_a = 0.642$. This gives very good agreement with the Closed System model value of $\varepsilon_{M,o} = 0.032$ at $x_a = 0.6$.

3.2.4 SUMMARY

This subsection has shown that the two sets of differential equations describing flow over a rotating and stationary disc within a rotating fluid can be coupled together and successfully solved using a newly developed iteration method. The method is not computationally intensive, with a single run typically taking around 15 seconds on a mid-range desktop computer, and is able to give key information about the wheelspace.

It was found that the model was insensitive to guesses of initial distribution of swirl ratios and of the initial condition for α_s. Good qualitative agreement was found between the model and the experimental measurements of swirl ratio of Sangan *et al.* (2014) for an axial seal. Good quantative agreement was found between the model and the experimental measurements of pressure coeffcicent of Sangan *et al.* (2014) for an axial seal. The only like-with-like comparison was between the model and the moment coeffcicents found by the no ingress steady state CFD model of Lalwani (2014); the agreement was exact.

3.3 VARIABLE MOMENTUM-INTEGRAL EQUATION MODEL

Although the original momentum-integral equations have been solved in a new way, coupled through the continuity equation, both the equations were derived assuming that the swirl ratio was constant with radius. It can be seen from both the theoretical and experimental results that this is in fact *not true* – the swirl ratio does vary with radius. In this section the momentum-integral equations have been re-derived and solved, where the swirl ratio has been taken as a function of radius.

The new equations create a system of five coupled equations, which requires a new solution algorithm. The equations will be stated, a new solution algorithm outlined and results shown.

3.3.1 EQUATIONS

The full derivations for these equations can be seen in Appendix A. *The variable momentum integral equations for the rotor* are:

$$\frac{d\alpha_o}{dx} = \frac{\alpha_o}{x(1-\beta)}\left[\frac{-6696}{343}F_o + \frac{46(1+8\beta)}{343\alpha_o^2} + 6x\frac{d\beta}{dx} + \frac{23+37\beta}{5} - \frac{18}{5}(1-\beta)\right] \tag{3.37}$$

$$\frac{d\gamma_o}{dx} = \frac{\gamma_o}{x(1-\beta)}\left[\frac{11736}{343}F_o - \frac{46(1+8\beta)}{343\alpha_o^2} - \frac{47x}{5}\frac{d\beta}{dx} - 2\left\{\frac{23+37\beta}{5}\right\} + \frac{18}{5}(1-\beta)\right] \tag{3.38}$$

where

$$F_o = \frac{0.0225(1+\alpha_o^2)^{\frac{3}{8}}}{\alpha_o \gamma_o^{\frac{5}{4}}} \tag{3.39}$$

Once again F_o, and F_s below, have no special significance but it makes the equations more compact. If β was constant then the $d\beta/dx$ term would be zero and equation (3.37) and (3.38), would be exactly (3.1) and (3.2) respectively.

The *variable momentum integral equations for the stator* are:

$$\frac{d\alpha_s}{dx} = \frac{\alpha_s}{x}\left[\frac{6696}{343}F_s - \frac{1656}{343}\frac{2}{9{\alpha_s}^2} - 11 - \frac{6x}{\beta}\frac{d\beta}{dx}\right] \tag{3.40}$$

$$\frac{d\gamma_s}{dx} = \frac{\gamma_s}{x}\left[\frac{-11736}{343}F_s + \frac{1656}{343}\frac{2}{9{\alpha_s}^2} + \frac{92}{5} + \frac{51x}{5\beta}\frac{d\beta}{dx}\right] \tag{3.41}$$

where

$$F_s = \frac{0.0225(1+\alpha_s^2)^{\frac{3}{8}}}{\alpha_s \gamma_s^{\frac{5}{4}}} \tag{3.42}$$

If β was constant then the $d\beta/dx$ term would be zero and equation (3.40) and (3.41), would be exactly (3.6) and (3.7) respectively.

In their current form these equations cannot be solved using the same method presented in the previous section. The presence of the new $d\beta/dx$ term in each equation means there are now five rather than four differential equations. To solve the two rotor and stator equations an explicit equation for $d\beta/dx$ is required. This can be gained by differentiating the continuity equation for the closed cavity, as stated in equation (3.19) but restated here in simplified form:

$$\alpha_o \gamma_o (1-\beta)^{\frac{8}{5}} = \alpha_s \gamma_s \beta^{\frac{4}{5}} \tag{3.43}$$

Differentiating the continuity equation with respect to x (assuming $\alpha_o, \gamma_o, \alpha_s, \gamma_s$ and β are functions of x) and rearranging gives

$$\frac{d\beta}{dx} = \frac{\left[\frac{d(\alpha_o\gamma_o)}{dx}(1-\beta)^{\frac{8}{5}} - \frac{d(\alpha_s\gamma_s)}{dx}\beta^{\frac{4}{5}}\right]}{\left[\alpha_o\gamma_o\frac{8}{5}(1-\beta)^{\frac{3}{5}} + \alpha_s\gamma_s\frac{4}{5}\beta^{\frac{-1}{5}}\right]} \tag{3.44}$$

In order to simplify this expression, the equations for $d(\alpha_o\gamma_o)/dx$ and $d(\alpha_s\gamma_s)/dx$ (which are known from the derivation of the rotor and stator equations) can be substituted into (3.44). After much algebraic manipulation, which can be seen in Appendix A3.1, (3.44) simplifies to

$$\frac{d\beta}{dx} = \frac{\beta}{x}\frac{144}{49}\left[F_o + (1-\beta)F_s - \frac{49}{60}\right] \tag{3.45}$$

where F_o and F_s are as defined above in (3.39) and (3.42) respectively. Notice that this equation for $d\beta/dx$ depends upon α_s, γ_s and α_o, γ_o. This equation must be substituted into the *varaible momentum-integral equations* for the rotor and stator for them to be solved; this means that the rotor and stator equations have become *fully coupled*. Each differential equation for one of the terms (e.g. α_o) depends upon all the other variables (so $\alpha_s, \gamma_s, \alpha_o, \gamma_o$ and β continuing the example). In other words, the rotor equations depend upon the stator variables and vice versa. This means a new solution method is required for solving the variable momentum-integral equations.

3.3.2 SOLUTION METHOD

As the rotor and stator equations are now coupled (i.e. the rotor equations contain stator variables α_s and γ_s and the stator equations contains rotor variables α_o and γ_o), whichever set of equations are solved first (rotor or stator) they require an initial distribution of α and γ for the other disc.

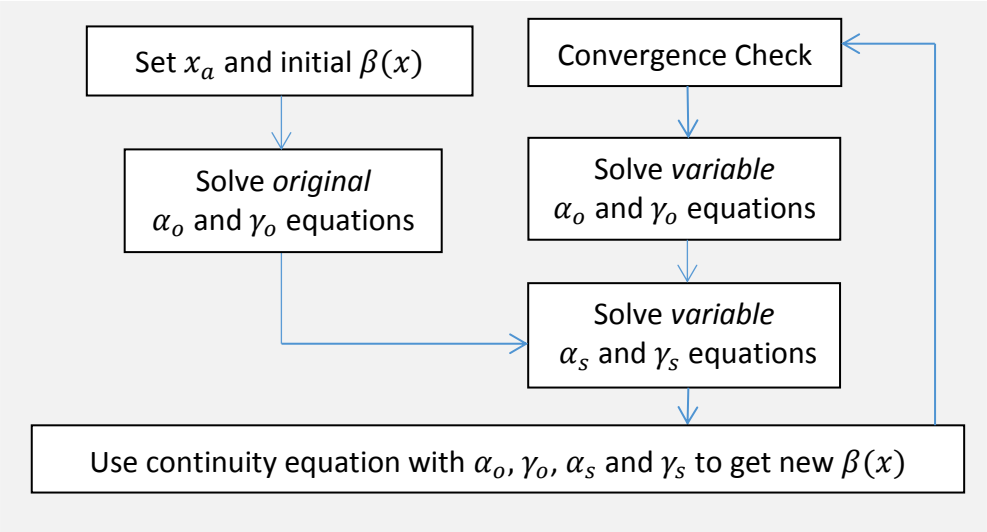

Figure 3.9: Solution Procedure for Closed Cavity Model with Variable Momentum-Integral Equations

Figure 3.9 shows the solution procedure for the Closed Cavity model based upon the variable momentum-integral equations. To start the *original* momentum-integral rotor equations (3.1) – (3.3) are solved, these have no dependence on stator terms α_s and γ_s due to having no $d\beta/dx$ term. To solve those equation a 'guess' for the initial swirl ratio distribution is used, in exactly the same way as the previous procedure. This gives three continuous distributions: α_o, γ_o and β. These distributions are then substituted directly into the *variable* stator equations for α_s and γ_s. Once the two variable stator equations are solved, all the results are substituted into the continuity equation which is solved for a new β distribution. Now the procedure enters the key iteration loop: the α_s and γ_s distributions from the variable stator equations, along with the new $\beta(x)$ distribution are substituted into the variable rotor equations – allowing them to be solved. The solutions from the variable rotor equations, α_o and γ_o, are then used in the variable stator equations, allowing them to be solved. All the results from that step in are used in the continuity equation which is then solved to find an updated β distribution. The convergence is checked and the iteration continues until the β distribution is unchanged. The structure is given in detail below.

Step 0: Initial Conditions for the Model
Inputs: x_a, initial condition $\alpha_{s,1}$ and error tolerance.

Step 1: Initial guess for $\beta(x)$ distribution
Inputs: chosen form for distribution (e.g. Linear)
Outputs: $\beta(x)$
Set a guess for the distribution of β radially. The default is simply a linear increase from $\beta_a = 0$ to $\beta_1 = 1$.

Step 2: Solve *original* momentum-integral rotor equations
Inputs: $\beta(x)$, initial condition for α_o
Outputs: $\alpha_o(x), \gamma_o(x)$
As β_a has been fixed at zero and the analytic equation (2.38) gives the initial conditions for the rotor α_o (namely $\alpha_o = 0.162$ for $\beta_a = 0$). As mentioned earlier γ_o is

approximately zero. Now the rotor equations (3.1) and (3.2) can be solved numerically, using a built in MATLAB function such as ode15s.

Step 3: Solve *variable* momentum-integral stator equations
Inputs: $\alpha_o(x), \gamma_o(x), \beta(x)$ and an initial condition for stator: value for $\alpha_{s,1}$
Outputs: $\alpha_s(x), \gamma_s(x)$
The values of $\alpha_o(x)$, $\gamma_o(x), \beta(x)$ are substituted into (3.45), (3.40) and (3.41). The latter two equations are solved numerically using initial conditions $\gamma_{s,1} \cong 0$ and with the supplied value of $\alpha_{s,1}$.

Step 4: Solve the continuity equation
Inputs: $\alpha_o(x), \gamma_o(x), \alpha_s(x), \gamma_s(x)$
Outputs: $\beta_i(x)$
The continuity equation (3.19) is solved numerically at a set number of radial locations between x_a and 1 (typically 100). This is done by using the standard solution for a quadratic equation using the coefficients in (3.21). (Note that this $\beta(x)$ distribution can be considered 'semi-variable' as it is based upon $\alpha_o(x), \gamma_o(x)$ from the *original* equations and $\alpha_s(x), \gamma_s(x)$ from the *variable* equations).

Step 5: Solve *variable* momentum-integral rotor equations
Inputs: $\alpha_s(x), \gamma_s(x), \beta(x)$
Outputs: $\alpha_o(x), \gamma_o(x)$
The values of $\alpha_s(x)$ and $\gamma_s(x)$ from the variable stator equations of Step 3. are substituted into (3.45), (3.37) and (3.38). The latter two equations are solved numerically using initial conditions $\gamma_o \cong 0$ and analytic equation (2.38) gives the value of the initial condition α_o (namely $\alpha_o = 0.162$ for $\beta_a = 0$).

Step 6: Solve *variable* momentum-integral stator equations
Inputs: $\alpha_o(x), \gamma_o(x), \beta(x)$ and an initial condition $\alpha_{s,1}$.
Outputs: $\alpha_s(x), \gamma_s(x)$
The values of $\alpha_o(x)$, $\gamma_o(x), \beta(x)$ are substituted into (3.45), (3.40) and (3.41). The latter two equations are solved numerically using initial conditions $\gamma_{s,1} \cong 0$ and with the supplied value of $\alpha_{s,1}$.

Step 7: Solve the continuity equation
Inputs: $\alpha_o(x), \gamma_o(x), \alpha_s(x), \gamma_s(x)$
Outputs: $\beta_{i+1}(x)$
The continuity equation (3.19) is solved numerically at a set number of radial locations between x_a and 1 (typically 100). This is done by using the standard solution for a quadratic equation using the coefficients in (3.21). (Note that this $\beta(x)$ distribution can be considered 'fully-variable' as it is based upon $\alpha_o(x), \gamma_o(x)$ from the variable equations and $\alpha_s(x), \gamma_s(x)$ from the variable equations).

Step 8: Convergence Check
Inputs: β_i and β_{i+1}
In this step the convergence criterion is checked. If the difference between the swirl ratio distribution from the previous step (β_i) and the current step (β_{i+1}) is within the

error tolerance specified (typically 0.5%) then the results produced by step 7. are output as the final results. If the difference is *not* within the error tolerance then the model is not converged. The $\beta(x)$ distribution output of step 7. is considered the new $\beta(x)$ guess and the method continues from step 5.

This method has more steps than the previous original momentum-integral procedure, simply because it requires the original equations to be solved before the variable equations. Even with these extra steps, the computation time does not increase drastically, typically around 30 seconds.

3.3.3 RESULTS FOR VARIABLE MOMENTUM-INTEGRAL EQUATION MODEL

The following section presents results from the variable momentum-integral closed cavity model. The two inputs for the model are a value for x_a, an initial condition for α_s and the absolute error tolerance. The results are present for four different values of x_a, $\alpha_{s,1} = 0.001$ and an absolute error tolerance of 0.1%. It is known from a sensitivity analysis that the value of $\alpha_{s,1}$ does not change the results from the model. The error tolerance specified will affect how many iterations the model runs through and as such the computation time.

Swirl

The swirl ratio distribution, $\beta(x)$, found by solving the continuity equation (3.19) at each radial location, changes with each iteration.

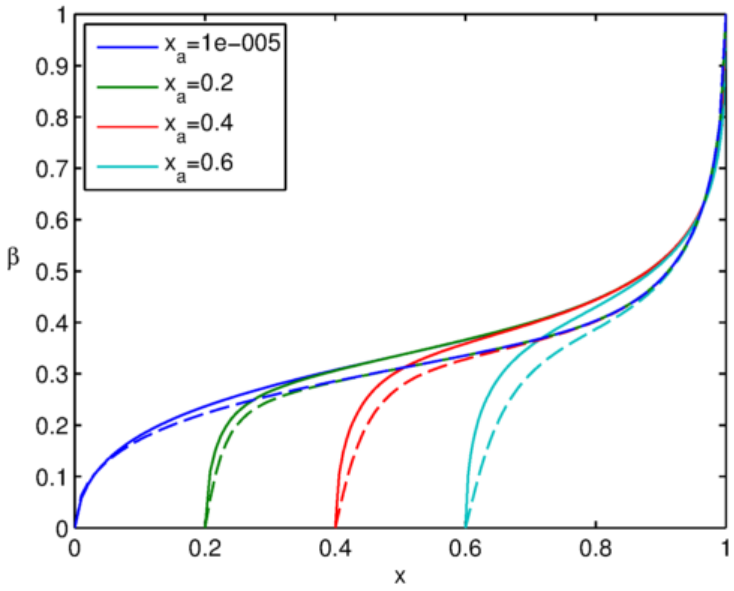

Figure 3.10: Variation of swirl ratio with radius for Closed Cavity Variable Model for four cavity sizes. (Solid lines denote variable model, dashed lines denote original model)

Figure 3.10 shows the swirl ratio distributions for the four different starting radius locations for the variable momentum-integral closed cavity model [solid lines] and the original momentum-integral closed cavity model [dashed lines]. The variable equations have given higher swirl ratio distributions which are closer to the expected solution of $\beta = 0.43$. Both the variable and the original model were solved for exactly the same initial conditions: $\alpha_s = 0.001, \gamma_s = 10^{-4}, \beta_a = 10^{-6}$ and an error tolerance of 0.1%.

Turbulent Flow Parameter

Recall that the expressions for the non-dimensional turbulent flow parameter for the rotor, $\lambda_{T,o}$, and the stator, $\lambda_{T,s}$, given by (3.14) and (3.15) can be calculated by using the final results for $\alpha_o(x), \gamma_o(x), \alpha_s(x), \gamma_s(x)$ and $\beta(x)$. Figure 3.11 shows how the turbulent flow parameter results from the Original Closed Cavity Model (dashed lines) compare to the results for the Variable Closed Cavity Model. The trends are very similar, apart from the Variable Model producing lower values of the turbulent flow parameter. This is to be expected because the swirl ratio distribution has increased at most radial locations – this corresponds to a decrease in $\lambda_{T,o}$ (which can be seen by considering the $(1-\beta)$ term in (3.14)).

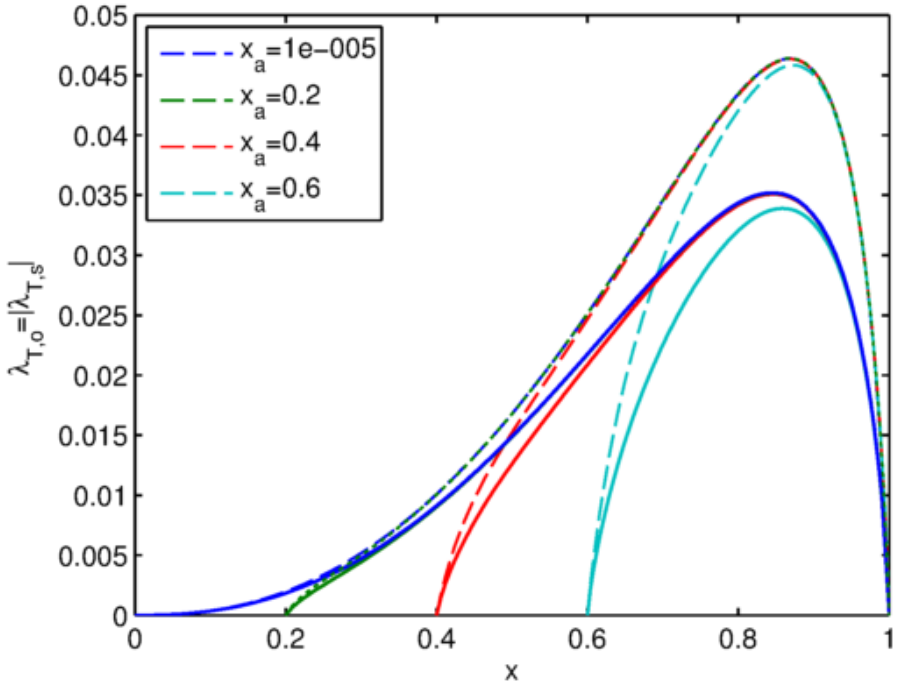

Figure 3.11: Variation of turbulent flow parameter with radius for Closed Cavity Model for four cavity sizes. (Solid lines denote variable model, dashed lines denote original model)

As for the original momentum-integral model it can be seen that the starting radius does not significantly affect the turning point of the flow. The two models predict very similar x_{out} locations. The edge of the outer region for cases $x_a = 0, 0.2$ and 0.4 is given by $x_{out} = 0.85$ and for $x_a = 0.6$ it is $x_{out} = 0.86$. It is therefore shown that the position of the outer region is invariant with starting radius.

Pressure

Recall that pressure coefficient C_p can be calculated using the values swirl ratio found from the model by using (3.24). Figure 3.12 shows a comparison between the pressure coefficient based upon three cavity sizes ($x_a = 0, 0.4, 0.6$) from the original model [dashed lines], variable model [solid lines] and the experiments of Sangan *et al.* (2014) [symbols]. Recall that for the experimental data $x_{ref} = 0.6$ but the size of the disc is $x_a = 0$.

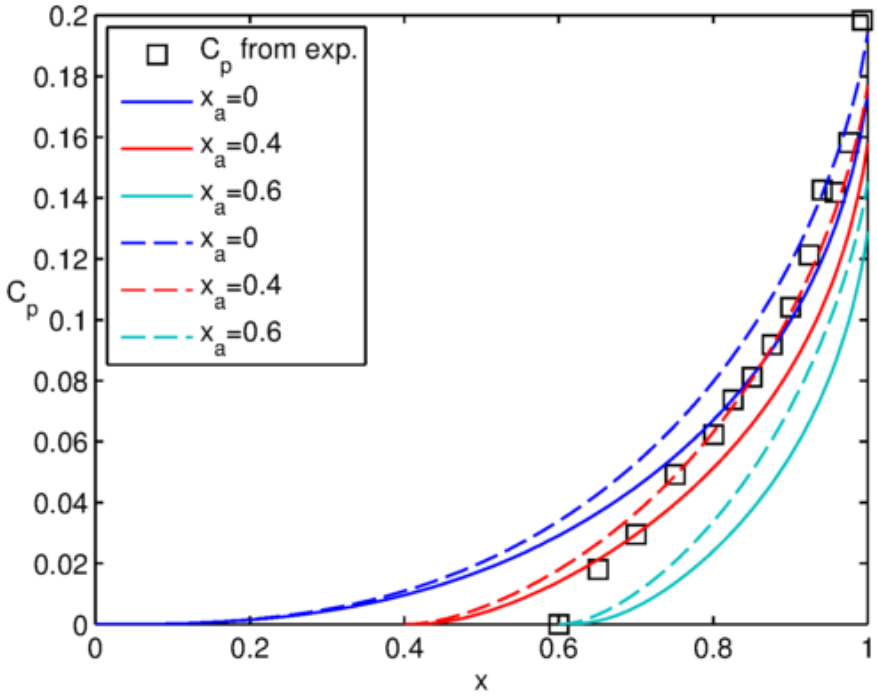

Figure 3.12: Variation of pressure coefficient with radius for Closed Cavity Model for four cavity sizes. (Solid lines denote variable model, dashed lines denote original model)

Unsurprisingly the values of pressure coefficient from variable model are higher than from the original model. There is good agreement between C_p at $x_a = 0.4$ found from the variable model and the experimental measurements.

Moments

As for the Original Closed Cavity Model the values for both the moment coefficients ε_{M_o} and ε_{M_s} are found by using the continuous distributions of α_o, γ_o and β in equation (3.28) and of α_s, γ_s and β in (3.35) equation respectively. The integrals can then be evaluated numerically to give the results shown in Table 3.2 for different x_a values. The Variable Closed Cavity Model gives moments on the rotor and stator that are effectively identical – giving a model that has moments that balance.

x_a	ε_{M_o}	ε_{M_s}	Error (%)
0	0.037	0.037	1.379
0.2	0.037	0.037	0.947
0.4	0.036	0.037	0.700
0.6	0.034	0.034	0.400

Table 3.2: Moment coefficients for Variable Closed Cavity Model

The results are for the model with the same standard initial conditions as above: $\alpha_{s,1} = 0.001, \gamma_{s,1} = 10^{-4}$, $\beta_a = 10^{-6}$ and an error tolerance of 0.1%.

3.4 SUMMARY

An iterative scheme has been developed to bring together the momentum-integral equations that describe flow over the rotor and stator by using the continuity equation. This has created a model to describe flow in an enclosed rotor-stator system

where there is no sealing air and no ingress. It has been shown that the iterative cavity scheme works such that the equations solve and can produce results that seem physically reasonable.

The method is not computationally intensive, with a single run typically taking 15 seconds on a mid-range desktop computer, and is able to give key information about the wheelspace. It was found that the model was insensitive to guesses of initial distribution of swirl ratios and of the initial condition for α_s.

The expected flow structure in an enclosed rotor-stator cavity has been outlined, with the presence of an outer region (where flow is entrained on the stator) being confirmed by the mass flow rate calculations. The results from both the original and variable momentum-integral equations have shown that the location of the outer region is independent of cavity size.

As well as solving the original momentum-integral equations, new *variable* momentum-integral equations were derived without the assumption that the swirl ratio was constant with radius. This meant a new differential β term was present in the equations. An explicit expression for the differential β equation was derived using the continuity equation, and the solution procedure was altered to be able to solve the system of five coupled ODEs. The swirl ratio results from the variable momentum-integral equations were higher at each radial location compared with the original results, with a difference of less than 10% across all radial locations. This corresponded to lower pressure coefficients and mass flow rates. The moments on the rotor increased by around 5% and the moments on the stator by around 17%. These changes led to the moments on the rotor and stator being equal from the results of the variable momentum-integral equations compared to the results from the original momentum-integral equations where there was around 12% difference.

As this model is for a theoretical physical situation, there is no experimental data to offer direct comparison. Nonetheless good qualitative agreement was found between the model and the experimental measurements of swirl ratio and pressure coeffcicents of Sangan *et al.* (2014) for an axial seal. A like-with-like comparison was available between the model and the moment coeffcicents found by the no ingress steady state CFD model of Lalwani (2014); the agreement was exact for the variable momentum-integral eqution.

CHAPTER 4 : SUPERPOSED FLOW, NO INGRESS MODEL

This chapter describes the derivation of a model for a rotor-stator system with sealing flow, otherwise known as superposed flow, being supplied to the cavity at a low radial location. This model is one step closer to the engine scenario, as there is now sealing flow, however there is no ingress taken account of within the model. In reality, unless enough sealing air has been supplied to seal the wheelspace, there will be ingress into the system. It is still of use to have a model for this case as it is a stepping stone towards a cavity model where the equations can take account of ingress. Also it can be used to isolate the effects of sealing flow and ingress – studying them separately could lead to greater understanding of the flow dynamics in the wheelspace.

The model is built upon the Closed Cavity Model and once again consists of two equations to describe the flow on the rotor, and two for the stator. The solutions of the equations are then used in the mass continuity equation which is solved to find a non-constant swirl ratio distribution within the wheelspace cavity. The comparisons with experimental measurements for sealed cavities provide good validation to the theory.

Section 4.1 describes the flow structure within a cavity with superposed flow and no ingress; it differs from that of the Closed Cavity as it includes an 'inner region' as well as a core and outer region. An introduction to the solution procedure for this model is also given. In Section 4.2 and 4.3 models for the inner region and core/outer region are proposed respectively. Section 4.4 and 4.5 contain the results of the model based upon the original and variable momentum-integral equations respectively. Finally Section 4.6 contains the conclusions.

4.1 FLOW STRUCTURE FOR SUPERPOSED FLOW, NO INGRESS CAVITY

The 'Superposed Flow, No Ingress' (SFNI) Model is used to approximate what would happen in a rotor-stator cavity that has superposed (aka 'sealing') flow entering the system at non-dimensional radial location $x = x_a$. The superposed flow enters the cavity with a flow rate denoted $\lambda_{T,a}$ and there is flow leaving the system, at $x = 1$, with the same flow rate. Below is the theoretical flow structure in the cavity for the SFNI situation, which will be modelled in this chapter.

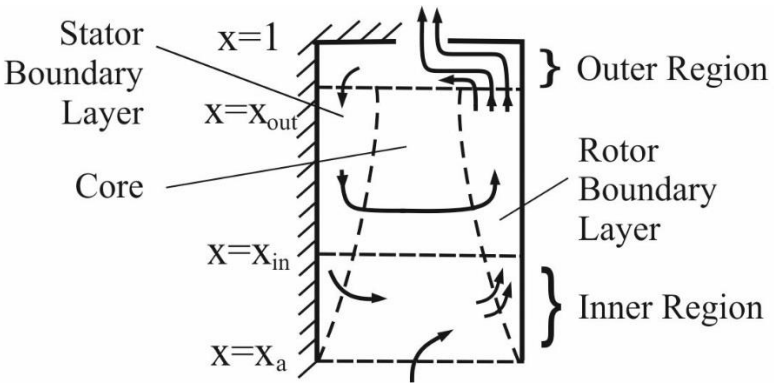

Figure 4.1: Simplified flow structure for a rotor-stator cavity with superposed flow and no ingress (positive inlet swirl)

Figure 4.1 shows the flow structure for the SFNI cavity where there is a superposed radial flow with positive swirl ($\beta_a > 0$), at $x = x_a$, the non-dimensional inner radius of the cavity. As with Closed Cavity, there are two distinct boundary layers on the rotor and stator; with fluid travelling radially outwards on the rotor and radially inwards on the stator.

At the bottom of the cavity is the *inner region,* which extends from x_a to x_{in}. This is where the superposed flow and the flow from the stator is entrained into the boundary layer on the rotor. The radial location x_{in} marks the first position where the continuity equation is satisfied. The more superposed flow that is supplied to the cavity, the longer radially it takes for the rotor boundary layer to entrain the flow and subsequently the location of x_{in} will move radially outwards (meaning the inner region gets larger). Past x_{in} all the superposed fluid has been entrained by the boundary layer on the rotor and the core will start to rotate to ensure that continuity is satisfied; the fluid rotates at a speed that ensures that the net radial flow rate in the boundary layers is equal to the superposed flow rate. Fluid will flow radially inwards on the stator boundary layer, radially outward on the rotor boundary layer and axially from the stator to the rotor outside the boundary layers. As for the Closed Cavity, the core extends to x_{out} beyond which is the *outer region.* Fluid in the outer region leaves the boundary layer on the rotor, flows axially across the outer region and is entrained onto the boundary layer on the stator. Additionally some fluid (with a flow rate equal the superposed flow rate) leaves the system through the rim seal. Recall that it was found from the solutions to the Closed Cavity model that x_{out} was not influenced by x_a.

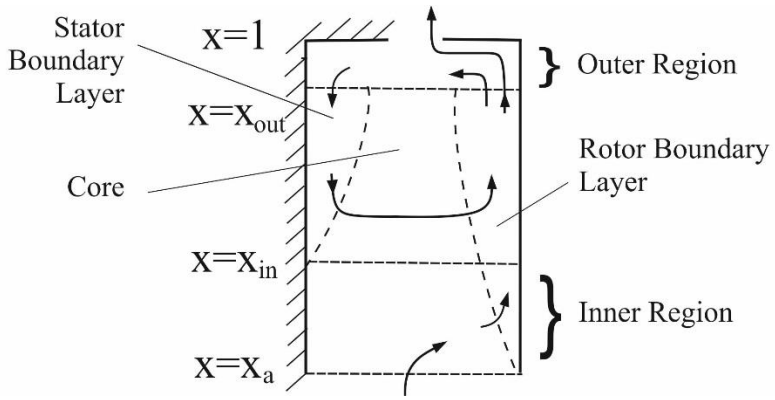

Figure 4.2: Simplified flow structure for a rotor-stator cavity with superposed flow, no ingress (zero inlet swirl)

If the superposed flow supplied to the cavity has zero swirl ratio then there is no radial inflow on the stator in the inner region, as depicted in Figure 4.2. This can be seen by considering equation (3.11) for $\lambda_{T,s}$ which contains a β term such that the variable will become zero whenever $\beta = 0$. The rest of the model will be the same as described above, with the exception that the stator boundary layer will end at x_{in} rather than x_a. The flow structure for both cases described above can be modelled in a similar way to the Closed Cavity: an iterative scheme is used to solve the original or variable momentum integral equations. The key change is that the model will be split into two distinct parts: One being the inner region, and the other being the combination of the core and outer region. A brief overview is given below.

General Overview of the Solution Procedure

The first step is to model the inner region. This can be done given the following initial conditions:

- x_a - a non-dimensional starting radius
- β_a - swirl of sealing flow rate
- α_s - an initial guess for the ratio of the shear stresses at the outer radius
- $\lambda_{T,a}$ - a value for the sealing flow rate

There are different models to account for whether the sealing flow has *zero* or *positive* inlet swirl ratio. If the sealing flow entering the system has *positive swirl* ($\beta_a > 0$), then the flow will be as shown in Figure 4.1; the stator flow carries on into the inner region. If the sealing flow entering the system has *zero swirl* ($\beta_a = 0$) then the flow will be as in Figure 4.2; there will be no flow over the stator in the inner region.

After the inner region has been modelled a value of x_{in} will have been found and radial distributions of $\alpha_s, \gamma_s, \alpha_o, \gamma_o$ and β will be available for $x_a < x < x_{in}$. Beyond this point continuity is satisfied at all radial locations and the values of $\alpha_s, \gamma_s, \alpha_o, \gamma_o$ and β at x_{in}, denoted $\alpha_{s,in}, \gamma_{s,in}, \alpha_{o,in}, \gamma_{o,in}$ and β_{in} respectively, can be used as initial conditions for the second part of the model – the combined core and outer region. The combined core and outer region is solved iteratively in the same way as the Closed Cavity, finding distributions of $\alpha_s, \gamma_s, \alpha_o, \gamma_o$ and β for $x_{in} < x < 1$. Finally the two distributions can be put together to form a continuous solution over the range $x_a < x < 1$.

4.2 MODELLING THE INNER REGION

The *inner region* is the lower portion in the wheelspace where continuity of the mass flow rates is not satisfied. This means the continuity equation cannot be used to find the swirl ratio so the complete swirl ratio distribution in the inner region must be *supplied* rather than solved for. Three different assumed swirl ratio distributions are explored in the next three subsections*: zero swirl, constant swirl* and *free vortex flow*.

4.2.1 ZERO INLET SWIRL

The simplest case is to assume that the sealing flow has zero inlet swirl, such that $\beta(x) = 0$. With zero swirl there will be no boundary layer on the stator and this means the continuity equation at x_{in} will be given by

$$\frac{49\pi}{60}\left[\alpha_{o,in}\gamma_{o,in}(1-\beta_{in})^{\frac{8}{5}} - \alpha_{s,in}\gamma_{s,in}\beta_{in}^{\frac{4}{5}}\right] = \lambda_{T,a}x_{in}^{-\frac{13}{5}} \tag{4.1}$$

where $\beta = 0$. By rearrangement an explicit expression for x_{in} is gained:

$$x_{in} = \frac{60}{49\pi}\left[\frac{\lambda_{T,a}}{\alpha_{o,in}\gamma_{o,in}}\right]^{\frac{5}{13}} \tag{4.2}$$

In order to find make use of (4.2) values of $\alpha_{o,in}$ and $\gamma_{o,in}$ need to be supplied.

One approximation can be gained by using the analytic solutions for the rotor, (2.38) and (2.39) for α_o and γ_o respectively. When $\beta = 0$ then $\alpha_o = 0.1620$ and $\gamma_o = 0.526$ which leads to an *analytical expression for the size of the inner region:*

$$x_{in} = 1.79\lambda_{T,a}^{\frac{5}{13}} \tag{4.3}$$

From this expression it can be seen that increasing the value of the sealing flow rate will increase the value of x_{in}. The inner region will fill the entire wheelspace (such that $x_{in} = 1$) when $\lambda_{T,a} = 0.219$.

As there is no x_a term within the analytic solutions for the rotor the simple approximation (4.3) cannot predict changes to the flow structure should the cavity be smaller. If $x_a > 0$ then it would be expected that x_{in} would increase, but the analytic expression for the size of the inner region cannot capture that behaviour. Therefore equation (4.3) is limited to only being used for a whole disc and if other cavity sizes want to be explored, such as modelling a wheelspace with a shaft, then a different approach is needed. The equation (4.3) can be thought of as an upper bound for the value of x_{in}.

By assuming that the rotor entrains fluid like a free disc, values of α_o and γ_o can be found for use in equation (4.2). For a free-disc the swirl ratio throughout the whole cavity is assumed to be zero. The equations to describe the flow on the rotor, the *free-disc equations*, are given by (3.1) and (3.2) with $\beta = 0$, which leads to

$$\frac{d\alpha_o}{dx} = \frac{\alpha_o}{x}\left[\frac{-6696}{343}F_o + \frac{46}{343\alpha_o^2} + 1\right] \tag{4.4}$$

$$\frac{d\gamma_o}{dx} = \frac{\gamma_o}{x}\left[\frac{11736}{343}F_o - \frac{46}{343\alpha_o^2} - \frac{28}{5}\right] \tag{4.5}$$

where

$$F_o = \frac{0.0225(1+\alpha_o^2)^{\frac{3}{8}}}{\alpha_o \gamma_o^{\frac{5}{4}}} \tag{4.6}$$

By using a numerical ODE solver, the above can be solved for any x_a. The solutions α_o and γ_o of (4.4) and (4.5), can be used in equation (4.2) to find how x_{in} varies with sealing flow rate. The values for x_{in}, the edge of the inner region, found from these *free disc rotor equations* solutions are compared to the analytical equation below in Figure 4.3.

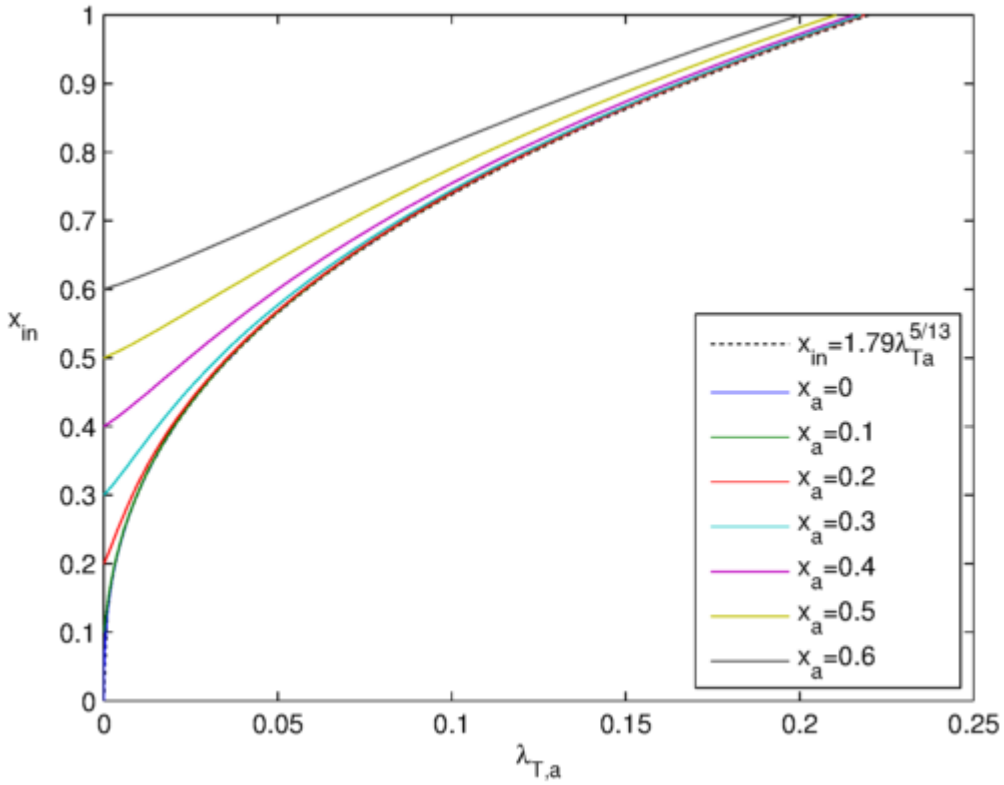

Figure 4.3: Variation of edge of inner region with superposed flow rate from rotor free disc equations (for a range of cavity sizes)

Figure 4.3 shows the variation of the location of x_{in} with x_a based upon equation (4.2) where α_o and γ_o have been found from the free disc equations. Also shown, as a dotted line, is the analytical equation (4.3). For $x_a = 0$ the free-disc solutions agrees exactly with the analytical expression in the prediction for the size of the inner region. As the cavity size decreases it takes slightly less flow overall to seal the wheelspace. The results suggest that if the wheelspace is large then the inner region can be quite large. The smaller the cavity the more linear the relation between x_{in} and $\lambda_{T,a}$.

Another factor that would affect the value of x_{in} is if the sealing flow had positive value of swirl ($\beta_a > 0$) as it entered the cavity. As seen in Figure 2.5, which shows the radial distribution of β for an enclosed rotor-stator computed by Morse (1991), at $x = 0$ the initial swirl value was $\beta_a \approx 0.3$ for $10^5 < Re_\phi < 10^7$. To account for this possibility a swirl ratio within the inner region with positive inlet swirl needs to be modelled. As discussed in Section 4.1, if $\beta_a > 0$ then the flow structure will change such that there will be flow on the stator within the inner region. If the fluid has a higher value of swirl ratio then it is expected that the sealing flow will take longer to be entrained by rotor boundary layer, subsequently increasing x_{in}. When the value of the inlet swirl is positive then the distribution of swirl ratio throughout the inner region needs to be decided upon. Two models are explored in the next sections: constant positive swirl and a free vortex distribution.

4.2.2 CONSTANT SWIRL

The simplest approach is to assume the swirl ratio within the inner region is constant. This will mean there will be both rotor and stator flow within the inner

region. The flow will be modelled by the momentum-integral equations, originally presented in Chapter 3. Recall the original momentum-integral equations for the rotor are

$$\frac{d\alpha_o}{dx} = \frac{\alpha_o}{x(1-\beta)}\left[\frac{-6696}{343}F_o + \frac{46(1+8\beta)}{343\alpha_o^2} + \frac{23+37\beta}{5} - \frac{18}{5}(1-\beta)\right] \tag{4.7}$$

$$\frac{d\gamma_o}{dx} = \frac{\gamma_o}{x(1-\beta)}\left[\frac{11736}{343}F_o - \frac{46(1+8\beta)}{343\alpha_o^2} - 2\left\{\frac{23+37\beta}{5}\right\} + \frac{18}{5}(1-\beta)\right] \tag{4.8}$$

where

$$F_o = \frac{0.0225(1+\alpha_o^2)^{\frac{3}{8}}}{\alpha_o\gamma_o^{\frac{5}{4}}} \tag{4.9}$$

with the term F_o having no special significance and not representing a specific quantity; it does however improve readability. The original momentum-integral equations for the stator

$$\frac{d\alpha_s}{dx} = \frac{\alpha_s}{x}\left[\frac{6696}{343}\left(\frac{0.0225(1+{\alpha_s}^2)^{\frac{3}{8}}}{\alpha_s{\gamma_s}^{\frac{5}{4}}}\right) - \frac{1656}{343}\frac{2}{9{\alpha_s}^2} - 11\right] \tag{4.10}$$

$$\frac{d\gamma_s}{dx} = \frac{\gamma_s}{x}\left[\frac{11736}{343}\left(\frac{-0.0225(1+{\alpha_s}^2)^{\frac{3}{8}}}{\alpha_s{\gamma_s}^{\frac{5}{4}}}\right) + \frac{1656}{343}\frac{2}{9{\alpha_s}^2} + \frac{92}{5}\right] \tag{4.11}$$

(originally presented in Chapter 3 as equations (3.40) and (3.4)) can be used to model this situation. The original, rather than the variable, equations are used because $d\beta/dx = 0$ when the swirl is constant. Instead of solving for β, a fixed value β_a is set and the equations are solved explicitly with a constant distribution of $\beta(x) \coloneqq \beta_a$. As a fixed constant radial distribution of swirl ratio is being assumed and continuity does not have to be satisfied at every point there is no iterative scheme, the equations are simply solved once.

To find x_{in} for different superposed flow rates, $\lambda_{T,a}$, the solutions to the above equations (α_o, γ_o, α_s and γ_s) are used together with a constant β to calculate the turbulent flow parameter for the rotor,

$$\lambda_{T,o} = \frac{49\pi}{60}\alpha_o\gamma_o(1-\beta)^{\frac{8}{5}}x^{\frac{13}{5}} \tag{4.12}$$

and stator

$$\lambda_{T,s} = -\frac{49\pi}{60}\alpha_s\gamma_s\beta^{\frac{4}{5}}x^{\frac{13}{5}} \tag{4.13}$$

Then the radial location where the continuity equation,

$$\lambda_{T,o} = \lambda_{T,a} + \left|\lambda_{T,s}\right| \tag{4.14}$$

is first satisfied, defined as x_{in}, is found. It can be written explicitly as:

$$x_{in} = \left[\frac{\lambda_{T,a}}{\frac{49\pi}{60}\left(\alpha_o\gamma_o(1-\beta)^{\frac{8}{5}} - \alpha_s\gamma_s\beta^{\frac{4}{5}}\right)}\right]^{\frac{5}{13}} \tag{4.15}$$

It is worth noting that equations (4.10) and (4.11) only need to be solved once as there are no β terms present, so β_a will not affect α_s and γ_s.

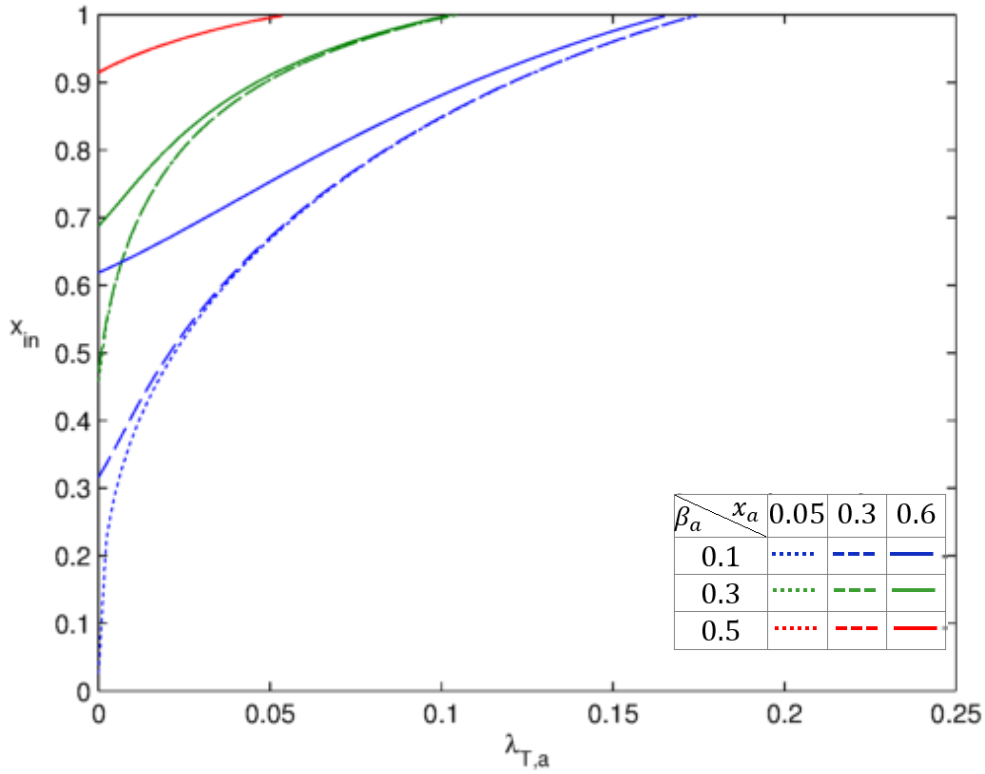

Figure 4.4: Variation of edge of inner region with superposed flow rate from original momentum-integral eqns for three constant swirl values and three cavity sizes.

Figure 4.4 shows the results from the constant swirl inner region model, giving predictions of how x_{in} varies for different x_a and β_a values. This model has the swirl ratio having a large effect on the size of the inner region. It is suspected that this effect is too large, as the flow structure breaks down at relatively low superposed flow rates. For example when $\beta_a = 0.2$ then if $\lambda_{T,a} > 0.1$ the value of $x_{in} > 1$. This means that the cavity would be entirely inner region, and so would not be able to be modelled by core and outer region above that flow rate. As the behaviour of this constant swirl model does not seem to be as desired, another distribution of swirl ratio is assumed – this time the swirl is variable with radius.

4.2.3 FREE VORTEX

The size of inner region is expected to depend upon the swirl ratio of the superposed flow entering the cavity, similar to how the source region in rotating cavity flow is dependent on swirl ratio. The flow entering the cavity at x_a may have high swirl ratio. Recall the definition of swirl ratio

$$\beta = \frac{V_\phi}{\Omega r} \tag{4.16}$$

where V_ϕ is the tangential component of velocity, Ω is the rotational speed and r is the radius. For rotating cavities Childs (2010) suggests that inside the source region (the lower radial region of the cavity), the tangential component of velocity can be modelled as a free vortex. Furthermore that if angular momentum is to be conserved then it must be that

$$V_\phi r = constant = C \tag{4.17}$$

where C is the *vortex strength*, which does not vary with radius. The inner region in a rotor-stator cavity with superposed flow can be thought of as a source region for the rotor, meaning the same model could be applied in this situation. An explicit expression for the swirl ratio for a free vortex can be obtained using the assumption of conserved angular momentum.

As the radial location of particular interest is $x = x_a$ (i.e. at $r = a$) let

$$C \coloneqq V_{\phi,a} a \tag{4.18}$$

By using assumption (4.17) in definition of swirl ratio equation (4.16), the general from of the swirl ratio distribution within a free vortex can be gained:

$$\beta = \frac{V_{\phi,a} a}{\Omega r^2} \tag{4.19}$$

From the swirl definition equation (4.16), at $x = x_a$, i.e. at $r = a$ it must be that

$$\beta_a = \frac{V_{\phi,a}}{\Omega a} \tag{4.20}$$

Now by rearranging (4.20) and substituting it into (4.19) it can be seen it can be seen explicitly how β depends on the value β_a,

$$\beta = \frac{V_{\phi,a}}{\Omega}\left(\frac{a}{r^2}\right) = \beta_a a \left(\frac{a}{r^2}\right) = \beta_a \left(\frac{a^2}{x^2 b^2}\right) \tag{4.21}$$

and the *swirl ratio for the free vortex* is

$$\beta = \beta_a \left(\frac{x_a}{x}\right)^2 \tag{4.22}$$

Figure 4.5 shows the distribution of the swirl ratio, from equation (4.22), where $\beta_a = 0.1, 0.3, 0.5$ and $x_a = 0.05, 0.3, 0.6$ (where the vertical black lines denote different x_a values).

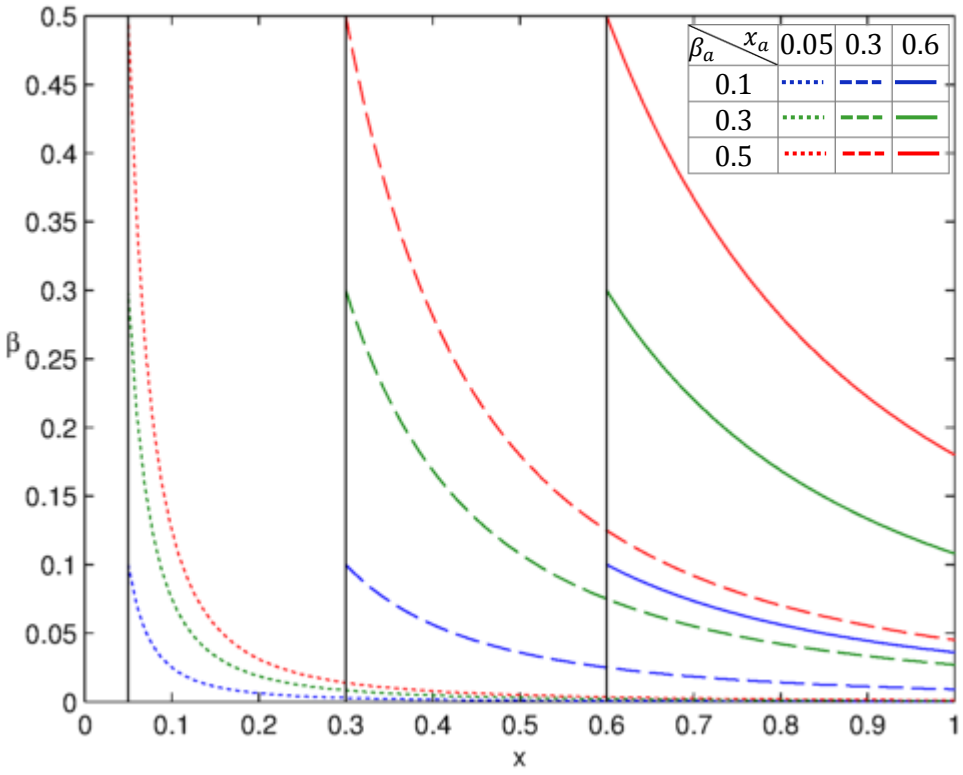

Figure 4.5: Swirl ratio distributions for free vortex flow within the inner region (various x_a and β_a)

This swirl ratio distribution that has been derived for the free-vortex can be used directly in the *original momentum-integral equations* to give the *free-vortex equations.* Wherever a β term appears in the rotor equations (4.23) and (4.24), the known swirl ratio for the free vortex (4.22) can be substituted in. The *free-vortex equations for the rotor* are

$$\frac{d\alpha_o}{dx} = \frac{\alpha_o x}{x^2 - x_a^2\beta_a}\left[\frac{-6696}{343}F_o + \frac{46}{343\alpha_o^2} + \frac{368\beta_a}{343\alpha_o^2}\left(\frac{x_a}{x}\right)^2 + 11\beta_a\left(\frac{x_a}{x}\right)^2 + 1\right] \quad (4.23)$$

$$\frac{d\gamma_o}{dx} = \frac{\gamma_o x}{x^2 - x_a^2\beta_a}\left[\frac{11736}{343}F_o - \frac{46}{343\alpha_o^2} - \frac{368\beta_a}{343\alpha_o^2}\left(\frac{x_a}{x}\right)^2 - \frac{92\beta_a}{5}\left(\frac{x_a}{x}\right)^2 - \frac{28}{5}\right] \quad (4.24)$$

where F_o is as defined in (4.9). As the original momentum-integral stator equations have no dependence on β, the *stator free-vortex equations* will be no different to the original *stator momentum-integral equations* (see (4.10) and (4.11)).

As for the previous sections, the solutions of the equations (4.10), (4.11), (4.23) and (4.24) are used to find the flow rates on both the rotor and the stator, which are in turn used to see where the continuity equation is first satisfied, by equation (4.15).

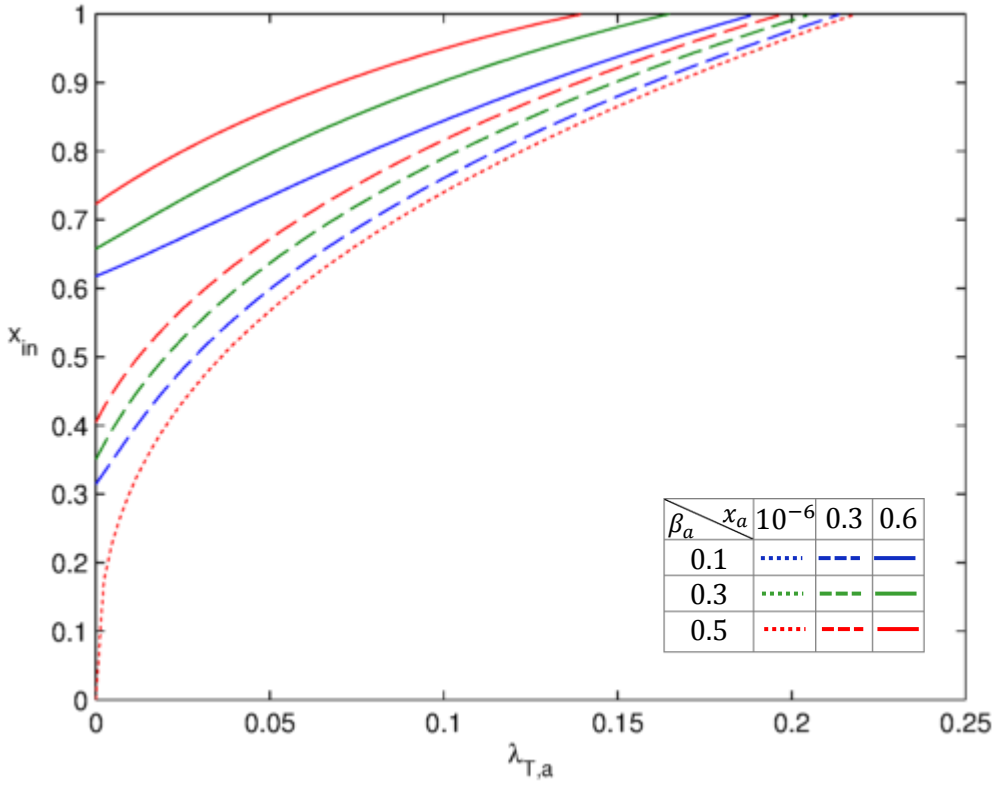

Figure 4.6: Variation of location of x_{in} with superposed flow rate for Original Free Vortex Equations (various x_a and β_a)

Figure 4.6 shows how the inner region location varies with superposed flow rate, from the original free vortex equations. The results are shown for three starting radial locations ($x_a = 10^{-6}, 0.3, 0.6$) and three inlet swirl values ($\beta_a = 0.1, 0.3, 0.5$). For a full disc ($x_a \approx 0$) the gradient of the beta distribution is very steep, making the distribution effectively zero for all radial locations. This means that regardless of the value of the inlet swirl β_a, the relation between x_{in} and $\lambda_{T,a}$ is unchanged and is exactly the analytical solution (4.3) and hence all solutions overlap (making the green

and blue dotted lines disappear). The overall trends are the same as for the zero and constant swirl models: as x_a and β_a increase so does the location of x_{in}. However, unlike the results from the constant swirl inner region model, at high sealing flow rates the effect of changing inlet swirl is not negligible. In fact the effect of the inlet swirl on x_{in} is seen at all flow rates. If β_a increases the value of x_{in} increases for any amount of sealing flow: the change in inlet swirl causes a small shift of the entire distribution. The effect is smaller than was seen for the constant swirl model.

Recall that one reason for investigating an alternative β distribution in the inner region was that the constant swirl model was showing a flow structure that was all inner region (i.e. no core or outer region) for small cavities ($x_a \approx 0.6$) and high inlet swirls ($0.3 < \beta_a < 0.5$). For the free vortex model this effect is less pronounced. These cases, denoted by solid lines, show there is still the affect that $x_{in} > 1$ for some flow rates, but this is only for $\lambda_{T,a} > 0.14$ compared to $\lambda_{T,a} > 0.06$ for the constant swirl model. The flow structure is retained for around double the flow rates.

Variable equations Approach

For the earlier assumed distributions of swirl ratio in the inner region (zero and constant inlet swirl) the differential of the swirl ratio would have been zero. This means the *variable* momentum integral equations and the *original* integral equations, presented in the previous chapter, would be identical. For the case of the free vortex the equations would not be identical as the differential term is non-zero. Given expression (4.22) for the swirl ratio, the differential of the swirl ratio is

$$\frac{d\beta}{dx} = -2\beta_a \frac{x_a^2}{x^3} \tag{4.25}$$

This means that the variable equations can be used in the inner region. Substituting equation (4.25) into the variable momentum-integral equations (3.37) and (3.38) gives the *variable free-vortex equations:* two for the rotor

$$\frac{d\alpha_o}{dx} = \frac{\alpha_o x}{x^2 - x_a^2\beta_a}\left[\frac{-6696}{343}\left(\frac{0.0225(1+\alpha_o^2)^{\frac{3}{8}}}{\alpha_o \gamma_o^{\frac{5}{4}}}\right) + \frac{46}{343\alpha_o^2} + \frac{368\beta_a}{343\alpha_o^2}\left(\frac{x_a}{x}\right)^2 + \beta_a\frac{x_a^2}{x^2} + 1\right] \tag{4.26}$$

$$\frac{d\gamma_o}{dx} = \frac{\gamma_o x}{x^2 - x_a^2\beta_a}\left[\frac{11736}{343}\left(\frac{0.0225(1+\alpha_o^2)^{\frac{3}{8}}}{\alpha_o \gamma_o^{\frac{5}{4}}}\right) - \frac{46}{343\alpha_o^2} - \frac{368\beta_a}{343\alpha_o^2}\left(\frac{x_a}{x}\right)^2 + \frac{2}{5}\beta_a\frac{x_a^2}{x^2} - \frac{28}{5}\right] \tag{4.27}$$

And substituting eq. (4.25) into the variable momentum-integral equations (3.40) and (3.41) for the stator gives,

$$\frac{d\alpha_s}{dx} = \frac{\alpha_s}{x}\left[\frac{6696}{343}\left(\frac{0.0225(1+\alpha_s^2)^{\frac{3}{8}}}{\alpha_s \gamma_s^{\frac{5}{4}}}\right) - \frac{1656}{343}\frac{2}{9{\alpha_s}^2} + 1\right] \tag{4.28}$$

$$\frac{d\gamma_s}{dx} = \frac{\gamma_s}{x}\left[\frac{-11736}{343}\left(\frac{0.0225(1+\alpha_s^2)^{\frac{3}{8}}}{\alpha_s \gamma_s^{\frac{5}{4}}}\right) + \frac{1656}{343}\frac{2}{9{\alpha_s}^2} - 2\right] \tag{4.29}$$

Notice that for the stator equations the β terms completely disappear. This is because all the differential terms are of the form:

$$\frac{x}{\beta}\frac{d\beta}{dx} \tag{4.30}$$

which for the free vortex, using (4.22) and (4.25) happens to give exactly -2.

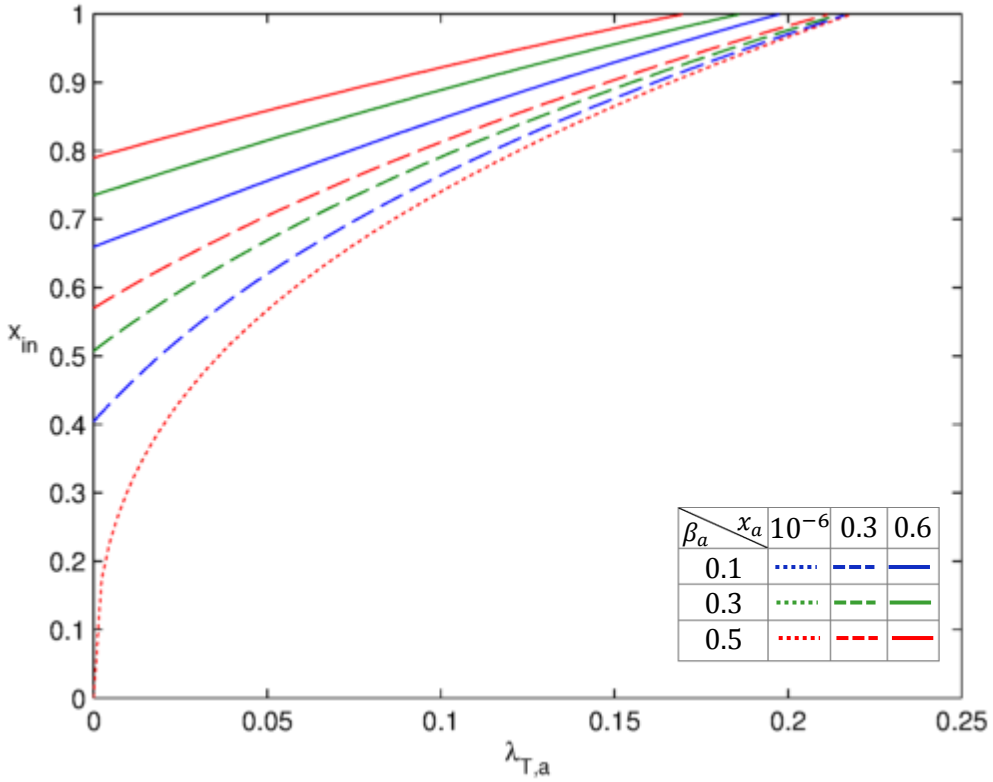

Figure 4.7: Variation of location of x_{in} with superposed flow rate for Variable Free Vortex eqns (various x_a and β_a)

Figure 4.7 shows how the inner region location varies with superposed flow rate, this time based upon the variable free vortex equations, for a range of inlet swirl values (β_a) and cavity starting values (x_a). When compared to Figure 4.6, which shows the results from the original free vortex equations, it can be seen that the variable equations predict a larger x_{in} value for the same sealing flow rate and inlet swirl. This means the variable free vortex equations show a larger effect of cavity size on the values of x_{in}. This is caused by the extra $d\beta/dx$ term. Note as in Figure 4.6 the results for all β_a values when $x_a = 10^{-6}$ are exactly the analytical solution (4.3) and hence all solutions overlap, making the green and blue dotted lines disappear.

As for the results from the model with constant swirl ratio in the inner region, the higher the turbulent flow parameter the smaller the effect of β_a. However this time the effect is never negligible as it was for the constant swirl model. It is thought that the results produced with the free vortex assumption are far more representative of the real situation with a cavity than the constant swirl assumption. Furthermore it is thought that the variable free vortex equations are a better model due to the larger values of $\lambda_{T,a}$ yielding slightly smaller x_{in} values. This means the wheelspace doesn't fill with the inner region until higher sealing flow rates. The distributions of x_{in} with $\lambda_{T,a}$ are more linear at high x_a and β_a. Even though x_{in} is still greater than 1 for some flow rates, this is only for $\lambda_{T,a} > 0.16$ which is an improvement compared to $\lambda_{T,a} > 0.14$ for the original free vortex model.

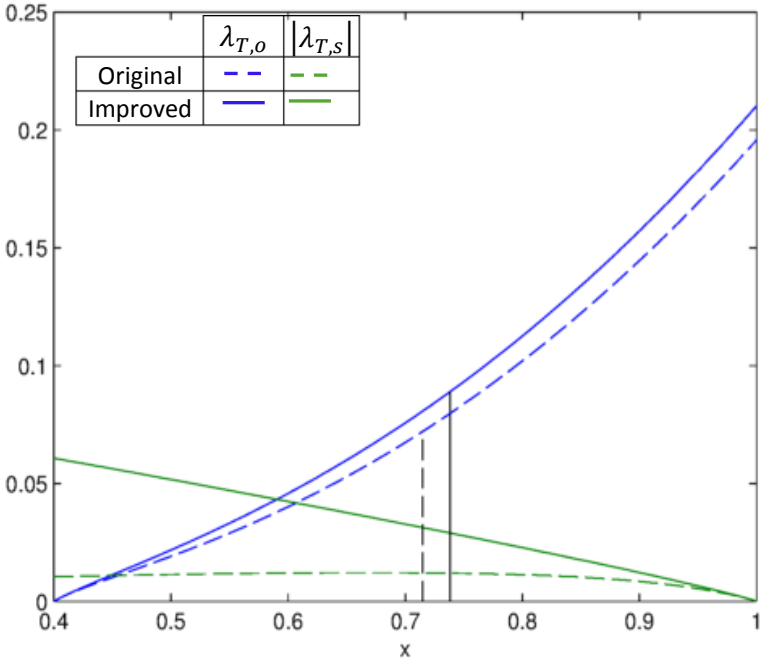

Figure 4.8: Radial variation of rotor and stator turbulent flow rates for the original and variable free-vortex equations (for $x_a = 0.4, \beta_a = 0.3$ and $\lambda_{T,a} = 0.06$).

For the free vortex model the variable and original equation approaches show quite different results for $x_a > 0$. The variable equations give a model that is more effected by inlet swirl than for the original equations. For a direct comparison, see Figure 4.8 above, where the flow rates $\lambda_{T,o}$ and $\lambda_{T,s}$ are shown for $\lambda_{T,a} = 0.06$ for both the *original* [dashed lines] and *variable* [solid lines] free-vortex equations. The dashed and solid black vertical lines show the x_{in} location for the original and variable equations respectively. For the variable equations, the stator flow rate $\lambda_{T,s}$ has increased compared to the original equations. This results in a larger x_{in} value as there is more flow for the rotor to entrain.

4.2.4 NO INNER REGION

Even though many inner region models have been given above, they are currently not validated against any experimental data. It assumed that the variable free vortex equations give the most realistic results, but in the case that none are deemed suitable the inner region does not need to be modelled. Another option is to instead assume that continuity is satisfied throughout the entire wheelspace and start the computations at some x_{in} value.

One good reason for neglecting the inner region is due to the shape of the cavity within the Bath rig, from which the majority of the data available to validate this work is taken. The experimental rig at the University of Bath where a range of different ingress related experiments are carried out does not consist of a single cavity. There are two cavities, separated by a fixed seal, as can be seen in Figure 4.9. CFD computations of Lalwani (2014), which will also be used for validating the cavity models, have the same geometry of the Bath rig.

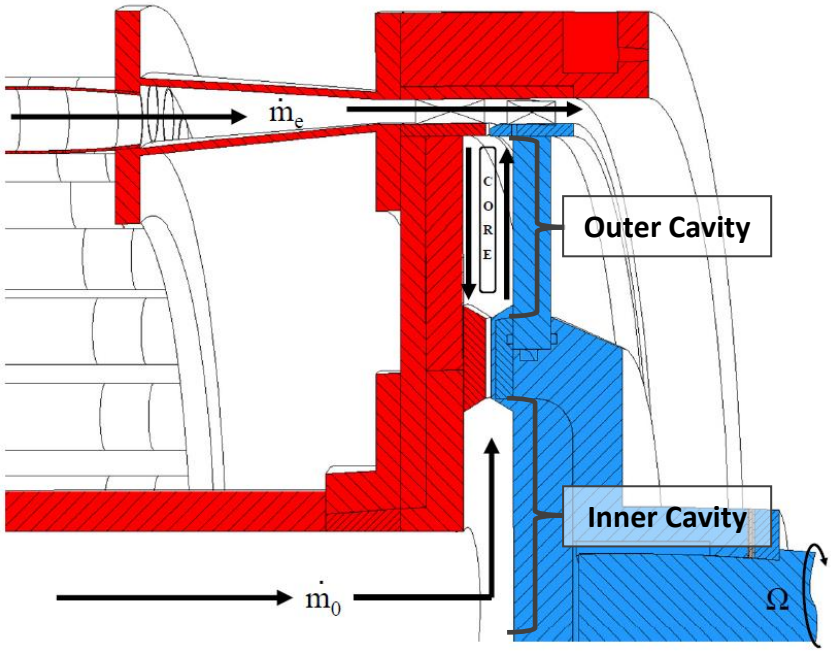

Figure 4.9: Cross-sectional diagram of the Bath rig. [Adapted from Sangan (2011)].

It is suspected that for the specific flow structure in this two-cavity set-up the inner region is in the inner cavity and that the flow has already developed into a core in the outer cavity. Swirl ratio measurements are taken in the outer cavity at seven radial locations with the lowest location being $x = 0.65$. To make direct comparisons between experimental measurements and the theory, a version of the model where x_{in} is set as an initial condition instead of being computed based on the flow rate is needed. Simply called the 'No Inner Region' Model it works by using the analytical equations (2.38) and (2.39) to find initial conditions for α_o and γ_o based on the value of β_a. For this model subscript a is equivalent to subscript in such that $\beta_a \equiv \beta_{in}$ and $x_a \equiv x_{in}$.

4.3 MODELLING THE CORE AND OUTER REGION

Once the inner region has been modelled using one of the models described in Section 4.2, the core and the outer region are solved using a similar iterative method as for the Closed System. Previously the Closed Cavity model started at $x = x_a$, however now the method starts at $x = x_{in}$ to take account of the inner region. Even though the iterative method is the same the continuity equation has changed – now the non-dimensional turbulent sealing flow rate parameter $\lambda_{T,a}$ is involved. Solving the new continuity equation is detailed in 4.3.3. Firstly consider how the initial guess for the swirl ratio needed to solve the rotor and stator equations changes due to the presence of the inner region.

4.3.1 INITIAL SWIRL RATIO DISTRIBUTION

For the Closed Cavity Model the initial guess for the radial distribution of β was simply a linear increase between $\beta = 0$ and $\beta_1 = 1$. For the Superposed Flow, No Ingress model it is assumed that the distribution is linear between β_{in} and β_1. As the inner region can be modelled in a variety of different ways, the value of β_{in} will depend upon the specific model being used. If an inner region model is being supplied

then β_{in} is calculated from the assumed swirl distribution in the inner region however if no inner region model is being supplied then β_{in} is simply another input to be set

Now that there is superposed flow within the cavity the swirl in the core will be lower, meaning that the swirl ratio at the exit of the wheelspace (denoted β_1) will be less than 1. This value of β_1 will depend upon the flow parameter $\lambda_{T,a}$ and can be found analytically, this is detailed below.

Analytic solution for swirl ratio at exit of wheelspace

In the outer region the flow from the rotor is progressively entrained by the boundary layer on the stator, and the continuity equation (4.35) is satisfied. At $x = 1$ it is assumed there is no flow on the stator is zero, so $\gamma_s = 0$. It is assumed all of the flow leaving the cavity leaves via the rotor boundary, so $\lambda_{T,o} = \lambda_{T,a}$. It therefore follows from (4.14) that at the exit of the cavity ($x = 1$) the following holds

$$\frac{49\pi}{60}\alpha_o\gamma_o(1-\beta_1)^{\frac{8}{5}} = \lambda_{T\,a} \tag{4.31}$$

which gives

$$\beta_1 = 1 - \left[\frac{60\lambda_{T,a}}{49\alpha_{o,1}\gamma_{o,1}\pi}\right]^{\frac{5}{8}} \tag{4.32}$$

where the subscript $o, 1$ denotes a variable on the rotor at location $x = 1$. This analytic solution for swirl ratio at exit of wheelspace can be used when generating an initial guess for the distribution of swirl ratio in the core and outer region. For an initial condition before the rotor equations have been solved β_1 is calculated from equation (4.32), but instead of using $\alpha_{o,1}$ and $\gamma_{o,1}$ (which are not known yet) the values $\alpha_{o,in}$ and $\gamma_{o,in}$ from the inner region model are used. As for the Closed Cavity model the SFNI model is found to be independent of the form of this initial guess.

4.3.2 ROTOR INITIAL CONDITIONS

As well as initial conditions for β, initial conditions for the rotor must be known. As β_{in} is some fixed value at x_{in} and continuity must be satisfied at that radial location, then the initial conditions on the rotor can be calculated directly from the continuity equation. At x_{in} the stator equations will give values of $\alpha_{s,in}$ and $\gamma_{s,in}$ this means $\lambda_{T,s}$ is fixed. In order to find $\alpha_{o,in}$ and $\gamma_{o,in}$, the initial conditions on the rotor which satisfy continuity, then the following equation is used

$$X_{o,in} \coloneqq \alpha_{o,in}\gamma_{o,in} = (1-\beta)^{-\frac{8}{5}}\left[\alpha_{s,in}\gamma_{s,in}\beta_{in}^{\frac{4}{5}} + \frac{60}{49\pi}\lambda_{T\,a}x^{-\frac{13}{5}}\right] \tag{4.33}$$

As the product of the two rotor variables is fixed, but the individual values are not then a value needs to be assumed for $\alpha_{o,in}$ (or equally $\gamma_{o,in}$). Two ways to choose a value for $\alpha_{o,in}$ are:

- Use the value of α_o from the analytic expression (2.38) based on β_{in}
- Use the value of $\alpha_{o,in}$ from the inner region model

Then $\gamma_{o,in}$ can be calculated by

$$\gamma_{o,in} = \frac{X_{o,in}}{\alpha_{o,in}} \tag{4.34}$$

Both methods of finding $\alpha_{o,in}$ do not affect the final results of the model.

4.3.3 ITERATIVE SWIRL RATIO DISTRIBUTION

The *continuity equation for the Superposed Flow, No Ingress model* is

$$\frac{49\pi}{60}\left[\alpha_o\gamma_o(1-\beta)^{\frac{8}{5}} - \alpha_s\gamma_s\beta^{\frac{4}{5}}\right] = \lambda_{T_a}x^{-\frac{13}{5}} \tag{4.35}$$

Solving this equation for the swirl ratio is more complicated than for the continuity equation for the Closed Cavity due to the extra term involving $\lambda_{T,a}$. The non-zero right hand side means that the equation no longer has an equivalent quadratic form. In order to find a value of β a root-finding algorithm needs to be used – such as the Newton Raphson method. When using the Newton Raphson method, (4.35) is written

$$f(\beta) = \lambda_{T,o} + \lambda_{T,s} - \lambda_{T,a} = 0 \tag{4.36}$$

which, in its full form (for a general n power law) is

$$(1-\beta)^{\frac{2(n+1)}{n+3}}\alpha_o\gamma_o - \beta^{\frac{n+1}{n+3}}\alpha_s\gamma_s - \frac{(n+1)(2n+1)}{2\pi n^2}\lambda_{T,a}x^{-\frac{3n+5}{n+3}} = 0 \tag{4.37}$$

Also needed to use the Newton Raphson method is $f'(\beta)$, which is

$$f'(\beta) = -\frac{2(n+1)}{n+3}(1-\beta)^{\frac{n-1}{n+3}}\alpha_o\gamma_o - \frac{n+1}{n+3}\beta^{\frac{-2}{n+3}}\alpha_s\gamma_s \tag{4.38}$$

There are also plenty of functions built into MATLAB such as `fsolve` which can solve the equation.

4.4 ORIGINAL MOMENTUM-INTEGRAL EQUATIONS

The core and the outer region for the Superposed Flow, No Ingress Cavity model can be modelled using the *original* momentum-integral equations or the *variable* momentum-integral equations. The exact procedure will differ slightly depending on which type of momentum-integral equations are being solved. In the following section the full procedure for the *original* equations (where there is no equation for $d\beta/dx$ term) is considered.

4.4.1 SOLUTION PROCEDURE

The following is the full procedure for the Superposed Flow, No Ingress Cavity Model by solving the original momentum-integral equations. The procedure is outlined in Figure 4.10 and then detailed step by step below.

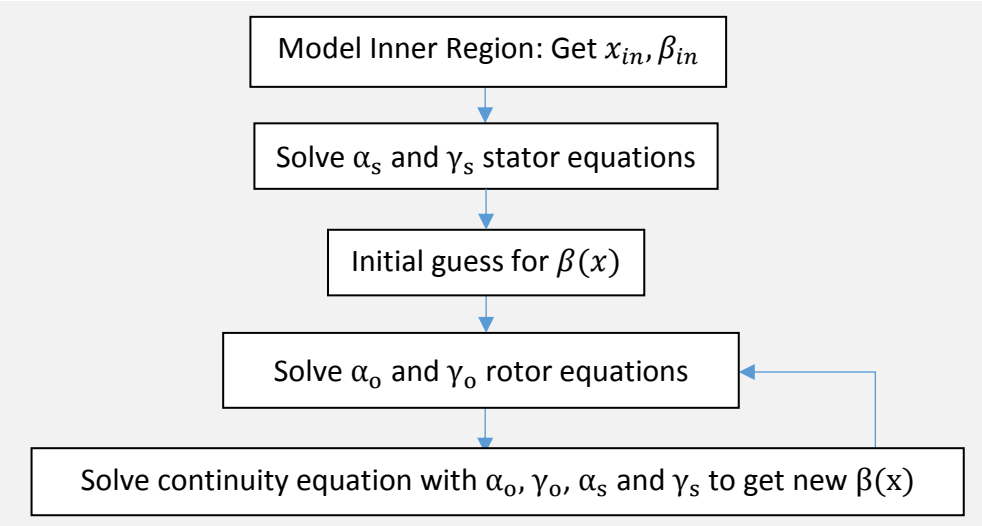

Figure 4.10: Outline of procedure for solving SFNI model with original momentum-integral equations

Step 0: Inner Region Model
Inputs: $x_a, \lambda_{T,a}$ and some assumed β distribution for inner region (e.g. free vortex)
Outputs: x_{in}, β_{in}, $\alpha_{o,in}$ and $\gamma_{o,in}$.

Step 1: Solve stator equations
Inputs: Initial condition for stator: value for α_s at $x = 1$
Outputs: $\alpha_s(x), \gamma_s(x)$
Solve the stator equations (3.1)(3.6) and (3.7) between $x_{in} < x < 1$. The equations do not depend on the swirl ratio, so can be solved once for the entire model.

Step 2: Set initial guess for $\beta(x)$ distribution in core/outer region
Inputs: β_{in}, $\alpha_{o,in}$ and $\gamma_{o,in}$.
Outputs: $\beta(x)$
A guess for the radial distribution of β is simply a linear increase from β_{in} to β_1 where:

$$\beta_1 = 1 - \left[\frac{60\lambda_{T,a}}{49\alpha_{o,in}\gamma_{o,in}\pi}\right]^{\frac{5}{8}} \tag{4.39}$$

Step 3: Solve rotor equations
Inputs: $\alpha_{s,in}, \gamma_{s,in}, \beta(x), \lambda_{T,a}$ and $\alpha_{o,in}$ from inner region model
Outputs: $\alpha_o(x), \gamma_o(x)$
Solve rotor equations (3.1) and (3.2) between $x_{in} < x < 1$. As described above the initial condition for the rotor $\gamma_{o,in}$ is found from (4.34) and (4.33) which become:

$$\gamma_{o,in} = \frac{(1-\beta)^{-\frac{8}{5}}}{\alpha_{o,in}}\left[\alpha_{s,in}\gamma_{s,in}\beta_{in}^{\frac{4}{5}} + \frac{60}{49\pi}\lambda_{T_a}x^{-\frac{13}{5}}\right] \tag{4.40}$$

Step 4: Solve the continuity equation
Inputs: $\alpha_o(x), \gamma_o(x), \alpha_s(x), \gamma_s(x), \lambda_{T,a}$
Outputs: $\beta(x)$
The continuity equation (4.35) is solved numerically. This can be by the Newton-Raphson method or any of the built in MATLAB functions such as `fsolve`. All solvers tested yield the same results.

Step 5: Convergence Check
Inputs: β_i and β_{i+1}
In this step the convergence criterion (as for the Closed Cavity) is checked. If β_i and β_{i+1} are the same within a specified tolerance then the results produced by step 4. are output as the final results as the model is considered converged. If swirl ratios from the two different time steps are too different then the $\beta(x)$ output of step 4 is considered the new $\beta(x)$ guess and the method continues from step 3.

4.4.2 RESULTS FOR ORIGINAL MOMENTUM-INTEGRAL EQUATIONS

Unless otherwise stated, these results have been computed with initial conditions $\gamma_s = 0.0001$ and $\alpha_s = 0.001$. For this model the initial conditions do not affect the solutions of the equations, and therefore do not affect the swirl ratio or other quantities.

The results are divided into four sections:

- Effect of inner region model on swirl ratio and mass flow
- Effect of superposed flow on swirl ratio
- Variation of moment coefficient with sealing flow
- Comparisons with experimental and CFD results

Even though from preliminary work the variable free vortex inner region model was decided to be the most appropriate, as there is no data to validate the models, all the inner region models are considered in the following section. The results are given for the full wheelspace so it can be seen how different inner region models affect the swirl ratio and moment coefficients.

Effect of Inner Region Model on Swirl Ratio and Mass Flow

The following figures explorey how the inner region, or lack of, affects the swirl ratio and mass flow rates of the model. The four cases shown are: zero inlet swirl, constant swirl, free vortex and no inner region as were outlined in Sections 4.2.1, 4.2.2, 4.2.3 and 4.2.4 respectively.

Zero Inlet Swirl

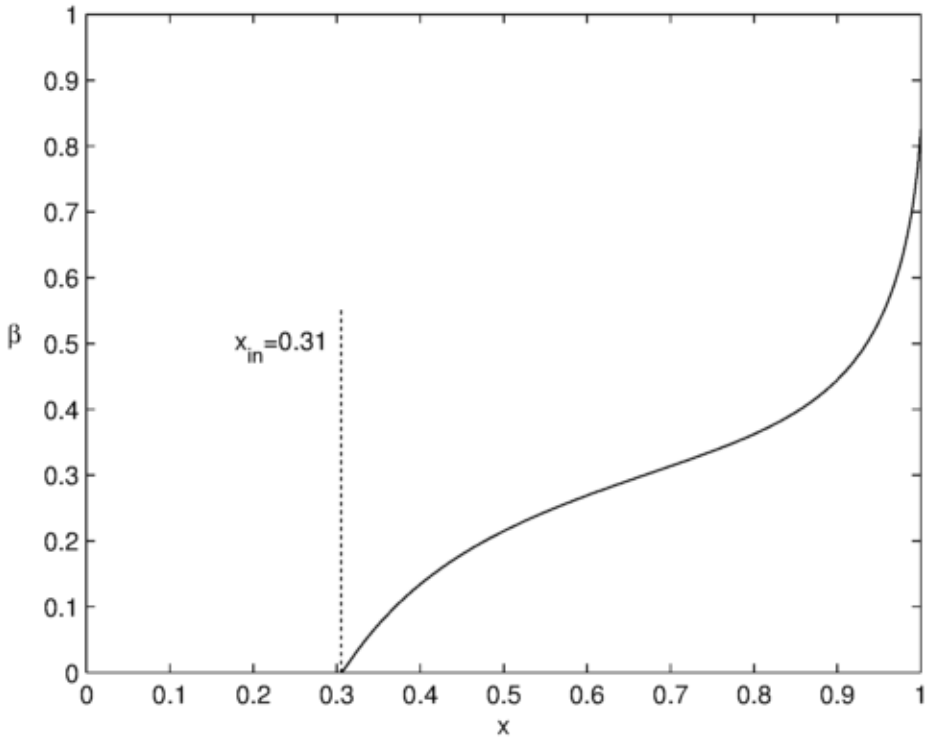

(a)

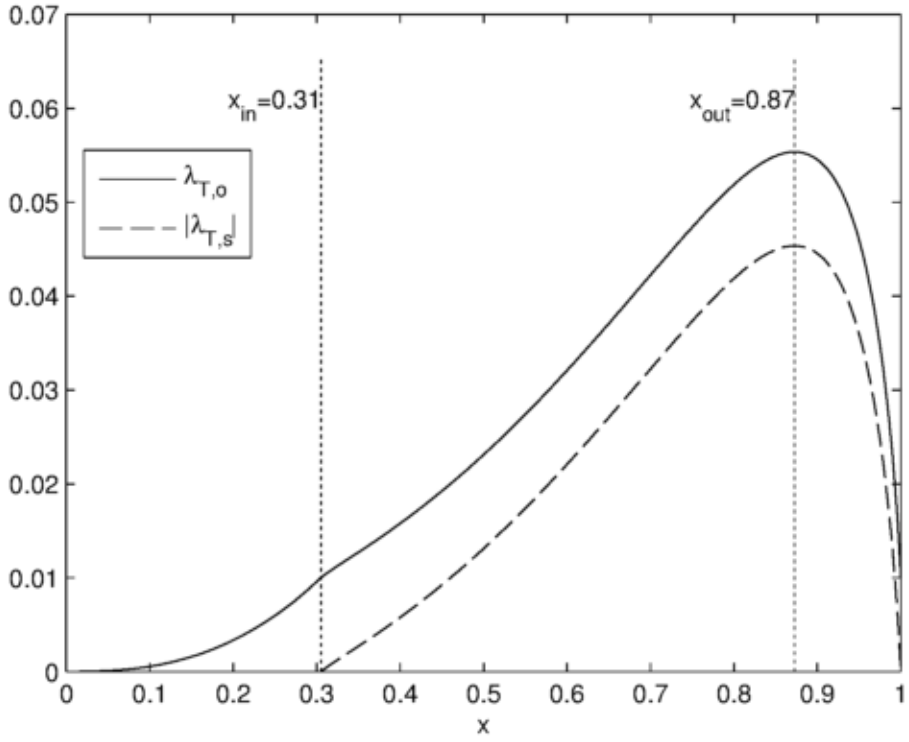

(b)

Figure 4.11: Radial distribution of (a) swirl ratio and (b) mass flow rates from the solutions of the SFNI model with zero inlet swirl inner region model

Figure 4.11 (a) shows the swirl ratio distribution gained from solving the Superposed Flow, No Ingress Model with original momentum-integral equations. By using the Zero Inlet Swirl inner region model with $x_a = 0$ and $\lambda_{T,a} = 0.01$ the value $x_{in} = 0.31$ is gained (see Figure 4.3), as denoted by the dashed line within Figure 4.11 (a). As outlined in the solution procedure, once x_{in} is found, the core and outer region are then modelled for the rest of the wheelspace. This gives the non-zero swirl ratio distribution shown within the Figure. The distribution has a similar shape to the Closed System, but as the superposed flow is positive the exit swirl has been lowered.

Figure 4.11 (b) shows the radial variation of the flow parameters $\lambda_{T,o}$ and $|\lambda_{T,s}|$ for the rotor and stator respectively. Within the inner region, which spans from $0 < x < x_{in} = 0.31$, continuity is not satisfied. At x_{in} and beyond, continuity is satisfied so now $\lambda_{T,o} = |\lambda_{T,s}| + \lambda_{T,a}$. As was found for the Closed Cavity, $x_{out} = 0.87$. For further investigation of x_{out} and its definition see Appendix B.

Constant Swirl

The following two figures study how the inner region with constant swirl affects the swirl ratio and mass flow rates within the wheelspace. For a fixed value of sealing flow, $\lambda_{T,a} = 0.01$, three initial values of β_a are considered. Only one sealing flow rate is shown as even for different flow rates the trends would be the same. Within the inner region Figure 4.12 assumes a constant swirl ratio, Figure 4.14 assumes a free vortex distribution and Figure 4.15 assumes there is no inner region.

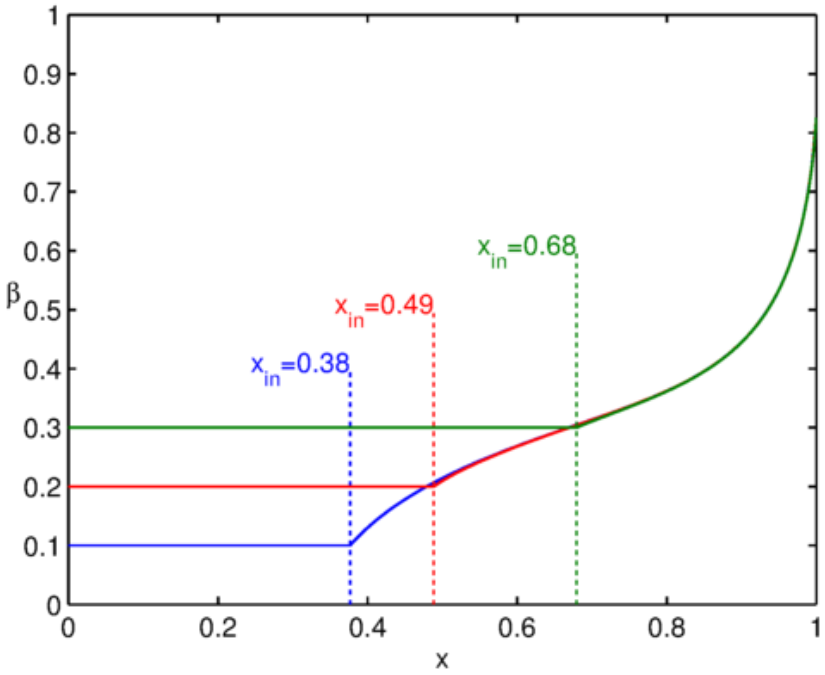

Figure 4.12: Radial variation of swirl ratio from the Superposed Flow, No Ingress cavity model with constant swirl inner region model, where $\boldsymbol{\beta_a = 0.1, 0.2, 0.3}$, $\boldsymbol{x_a = 0}$ and $\boldsymbol{\lambda_{T,a} = 0.01}$.

Figure 4.12 shows the radial distribution of swirl ratio from the SFNI model solved with a constant swirl in the inner region. The dotted lines mark out the edge of the inner region, x_{in}, as computed by the inner region model detailed in Section 4.2.2. As originally shown in Figure 4.4, the value of β_a has quite a large effect on the value of x_{in}. The transition between the two models ('inner region' and 'core plus outer region') is not smooth, but this is not unexpected. The swirl ratio, flow rates, α's and γ's will be continuous, due to how the procedure is designed, but the transition will not necessarily be smooth.

Consider the lowest case shown above, where constant swirl $\beta = 0.1$ is assumed in the inner region. Figure 4.13 shows the radial variation of the flow parameters $\lambda_{T,o}$ and $|\lambda_{T,s}|$ for the rotor and stator respectively. The range $0 < x < 0.38$ is the inner region, where continuity is not satisfied, so $\lambda_{T,o} \neq |\lambda_{T,s}| + \lambda_{T,a}$. In this region sealing flow and flow from the stator is entrained into the rotor boundary layer. This region is modelled using the constant swirl assumption, as detailed in Section 4.2.2. The range $0.38 < x < 0.87$ is the core, and $0.87 < x < 1$ is the outer region. Both these regions are modelled continuously by the original momentum equations, as outlined in Section 4.2. Throughout both these regions continuity is satisfied such that $\lambda_{T,o} = |\lambda_{T,s}| + \lambda_{T,a}$.

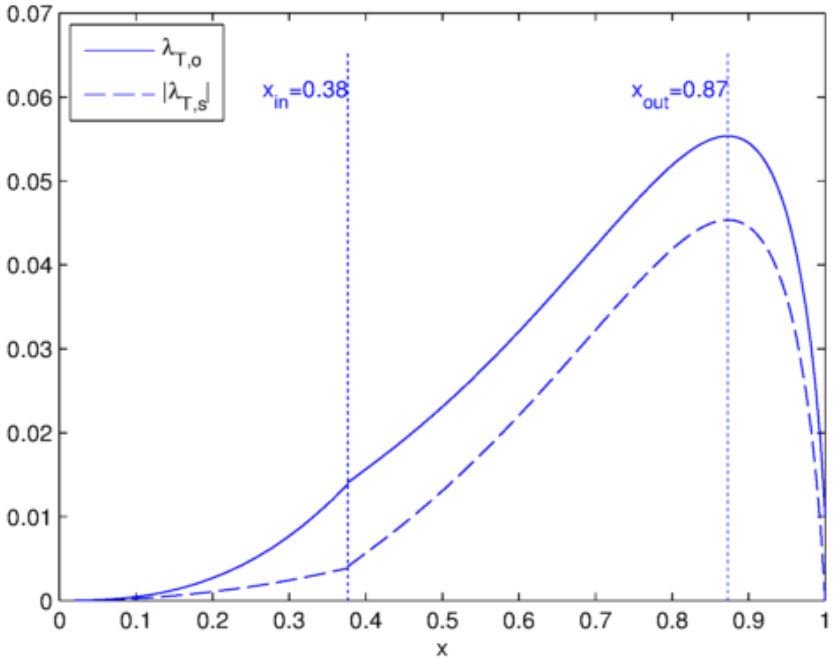

Figure 4.13: Radial variation of turbulent flow parameters $\lambda_{T,o}$ and $|\lambda_{T,s}|$ from the original SFNI model with constant swirl ratio $\beta_a = 0.1$ in the inner region and $\lambda_{T,a} = 0.01$.

Free Vortex

Next the Superposed Flow, No Ingress Model is solved with the assumed free vortex swirl ratio within the inner region. When considering the free vortex recall that there are two versions: one based on the original momentum-integral equations, and one on the variable momentum-integral equation. It was shown in Section 4.2.3 that the variable momentum-integral equations predicted a higher x_{in} for the same $\lambda_{T,a}$ when compared to the original equations.

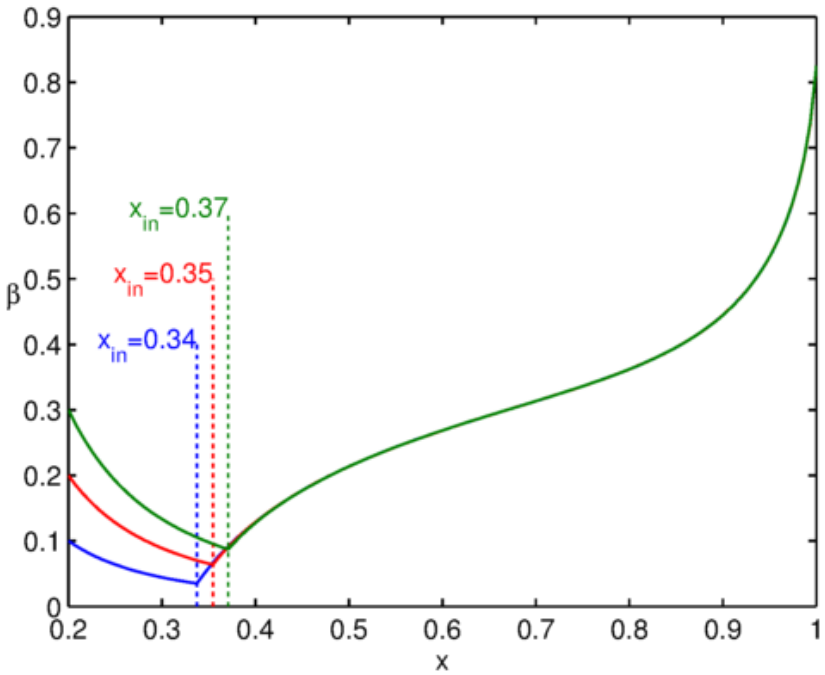

(a) Original Free Vortex Equations (4.23)-(4.24)

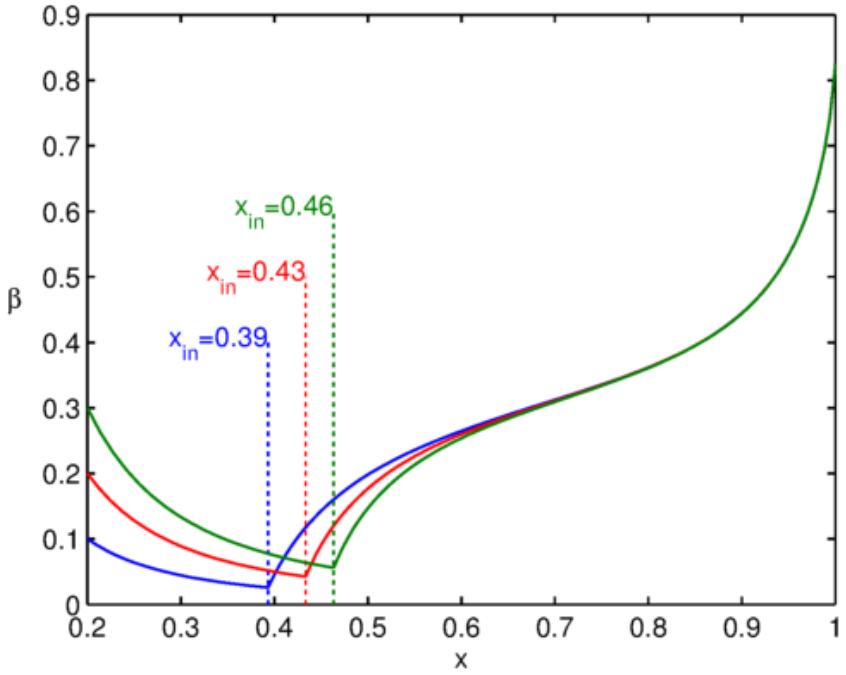

(b) 'Variable' Free Vortex Equations (4.26)-(4.29)

Figure 4.14: Radial variation of swirl ratio from the Superposed Flow, No Ingress cavity model with free vortex inner region model, where $\boldsymbol{\beta_a = 0.1, 0.2, 0.3, x_a = 0.2}$ and $\boldsymbol{\lambda_{T,a} = 0.01}$.

Figure 4.14 (a) and (b) demonstrate the difference between the two free vortex models that were proposed for the inner region in Section 4.2.3, where (a) and (b) show results from the original and variable free vortex equations respectively. Recall that within the original equations, (4.23)-(4.24), there are no differential β terms, whereas for the variable equations, (4.26)-(4.29), there are differential β terms. The three solid lines in the figure correspond to different initial conditions of swirl, namely $\beta_a = 0.1$,0.2 and 0.3 corresponding to blue, red and green respectively.

In Figure 4.14 (a) it can be seen that using the original free vortex model the effect of β_a on the location of x_{in} is nearly negligible. This was originally shown in Figure 4.6, but it can be seen far more clearly here. It is thought that the influence of the initial swirl ratio would be greater than this, hence the variable free-vortex model was derived.

In Figure 4.14 (b), where the variable free vortex model was used, the effect of β_a on the location of x_{in} is greater. This model is probably the most accurate for the inner region as it shows an effect that is greater than that of the original free vortex model, but less than the constant swirl model. To the author's knowledge there are no experimental results to compare these models against.

No Inner Region

Finally the SFNI Model with no inner region is considered. This means that the inlet swirl must be set to some $\beta_a \equiv \beta_{in}$ at some $x_a \equiv x_{in}$. As can be seen in Figure 4.15, even when different initial conditions are applied, there is a 'natural' solution that all the solutions seem to try to converge onto. This solution is the lower bound gained by the model with zero inlet swirl (as shown by Figure 4.16). When the iterative loop is carried out the different distributions of β with each iteration may be above or below this bound. If the solution veers too near to the case of $\beta = 0$ at any radial

location, then there is a risk of the β becoming negative. The stator equation cannot currently solve with negative β values so no solution can be found. This means that for the case of modelling with no inner region, the smallest x_a value where the solution stays far enough away from $\beta = 0$ that solutions can be found is $x_a = 0.2$.
If an initial condition of $x_a < 0.2$ is chosen, the equations will not solve.

If a model for the inner region is used, the distribution of swirl at the point x_{in} will not be smooth (as shown in the above figures). It will be continuous, as β_{in} will be used as an initial condition for the rotor equations used to model the core, but it may not be a smooth transition. This is expected as there are different equations being used in the two distinct regions.

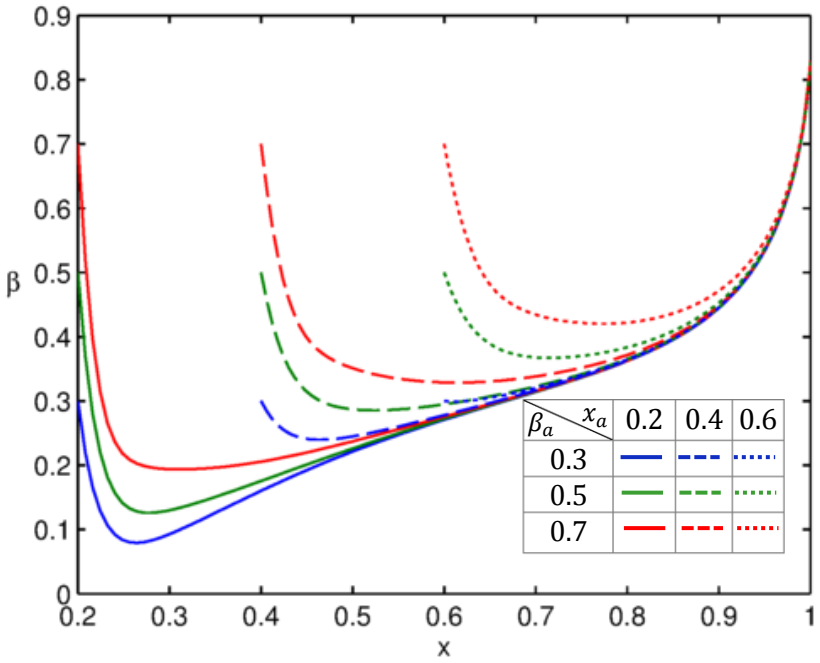

Figure 4.15: Radial variation of swirl ratio from the Superposed Flow, No Ingress cavity model with no inner region model, where $\beta_a = 0.3, 0.4, 0.7, x_a = 0.2, 0.4, 0.6$ and $\lambda_{T,a} = 0.01$.

Figure 4.15 shows results from the model with no inner region for a wide range of starting conditions: $\beta_a = 0.3,0.5,0.7$ and $x_a = 0.2,0.4,0.6$. All the results appear to converge near to the solution from the zero inlet swirl model. The larger the assumed value for the inlet swirl, the flatter the distribution of β inside the core. It can be seen that the inlet swirl does not affect the exit swirl by a significant amount.

Effect of Superposed Flow on Swirl Ratio

The following figures investigate how the radial distribution of swirl ratio is affected by the variation of the sealing flow.

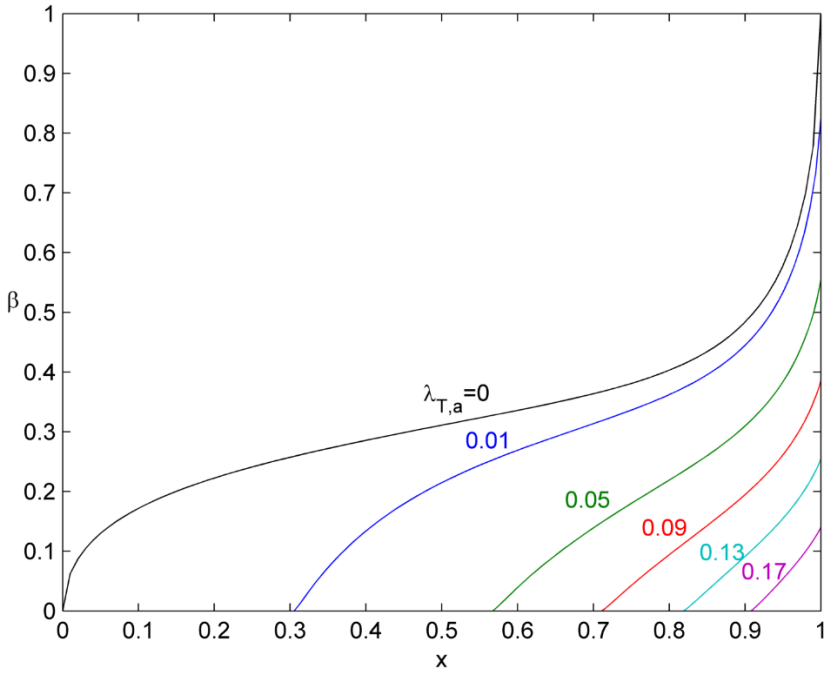

Figure 4.16: Radial variation of swirl ratio from the Superposed Flow, No Ingress cavity model with zero inlet swirl inner region model for $x_a = 0$ and a variety of flow rates.

Figure 4.16 shows the radial distribution of swirl ratio inside the cavity for a variety of values of sealing flow rate where the zero inlet swirl inner region model has been used. As expected increasing the sealing flow rate decreases the swirl ratio within the cavity. From this figure it can be seen that one downside of using the zero inlet swirl inner region model is that the higher the flow rate, the smaller portions of non-zero swirl ratio results within the wheelspace. This means that there is less to compare with the data that could be used to validate the model. (In this figure the $\lambda_{T,a} = 0$ curve is from the Closed System model, and is simply shown for comparison).

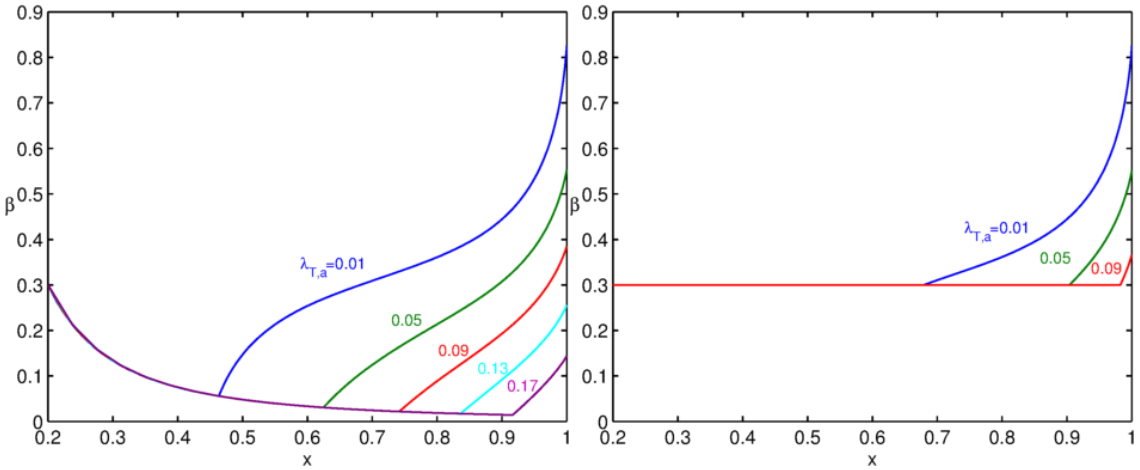

(a) Free Vortex Model ($\beta_a = 0.3$) **(b) Constant Swirl Model ($\beta_a = 0.3$)**

Figure 4.17: Swirl ratio distribution for entire wheelspace when $x_a = 0.2$ from (a) Free Vortex Model and (b) Constant Swirl Ratio Model both with $\beta_a = 0.3$.

Figure 4.17 (a) and (b) the radial distribution of swirl ratio inside the cavity for a range of sealing flow rates for the free vortex and constant swirl inner region models

respectively. Both models start with an initial condition of $\beta_a = 0.3$ and give distributions that are not smooth.

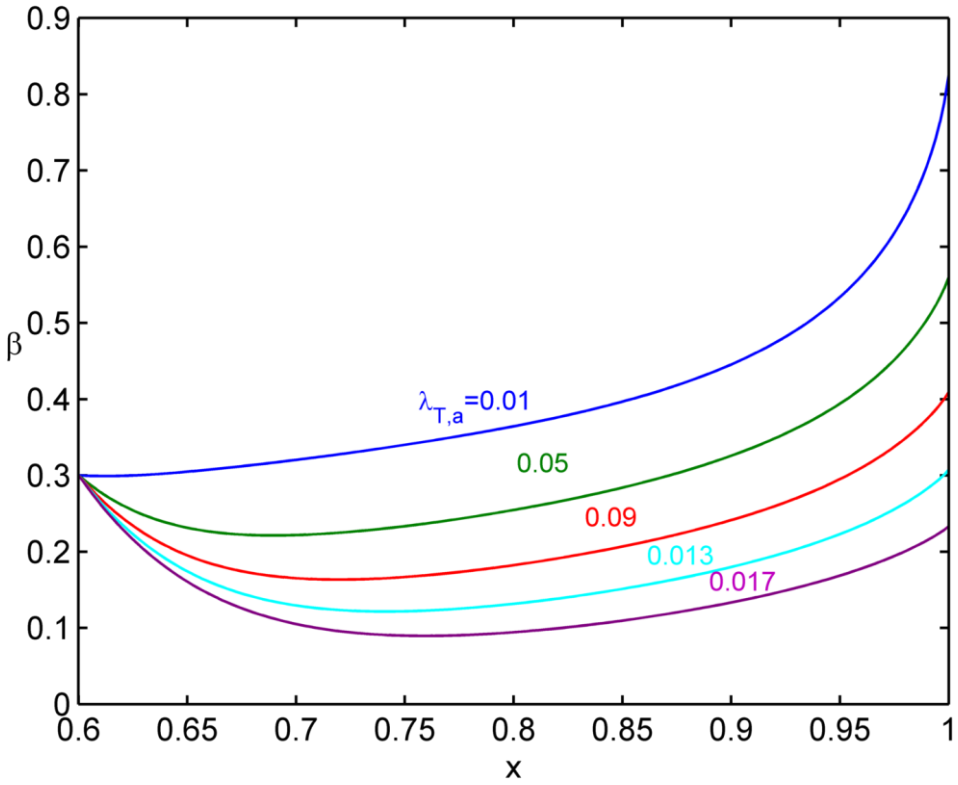

Figure 4.18: Radial swirl ratio distribution for no inner region model where $x_a = 0.6$ and $\beta_a = 0.3$.

Figure 4.18 shows the radial distribution of swirl ratio from the Superposed Flow, No Ingress model with no inner region where the inlet swirl is fixed at $\beta_a = 0.3$ for a range of sealing flow rates. As was originally shown by Figure 4.15 the equations seem resilient to different starting conditions, in that they can still hone in on the same solutions

From the three figures in this subsection it can be seen that either the zero inlet swirl inner region or the no inner region models are the most appropriate way to model the Superposed Flow, No Ingress cavity. They offer the smoothest distributions.

Effect of Superposed Flow on Moment Coefficients

As mentioned in the literature review, as the sealing flow parameter $\lambda_{T,a}$ nears 0.22 the moment coefficient of the rotor should tends towards the moment coefficient of the rotor for the free disc. This is because the core rotation is being suppressed as more sealing flow is being supplied, effectively making the rotor behave like a free disc because $\beta \to 0$. Recall that the momentum coefficient for the rotor, $\varepsilon_{M,o}$, can be calculated from the results of the cavity model using the following equation:

$$\varepsilon_{M_o} = 4\pi K \int_{x_a}^{1} \frac{(1+\alpha_o^2)^{\frac{n-1}{2(n+1)}}}{\gamma_o^{\frac{2}{n+1}}} x^{\frac{4(n+2)}{n+3}} (1-\beta)^{\frac{2(n+1)}{(n+3)}}\, dx \qquad (4.41)$$

The value will vary depending on the cavity size i.e. the value of x_a, and given that there are now two distinct regions to the cavity model the moment is found by integrating over the two parts separately. So $\varepsilon_{M_{o,inner}}$ is found by evaluating the integral (4.41) from x_a to x_{in}, with the values of α_o, γ_o and β from the inner region model and $\varepsilon_{M_{o,core}}$ is found by evaluating the integral (4.41) from x_{in} to 1, with the values of α_o, γ_o and β from the core and outer region model. The total moment coefficient is defined as $\varepsilon_{M_o} := \varepsilon_{M_{o,inner}} + \varepsilon_{M_{o,core}}$.

The moment coefficient on the rotor for the free disc, $\varepsilon_{M,fd}$ is calculated using the solutions of the free disc equations (4.4) and (4.5) within (4.41). For $x_a = 0, 0.4$ and 0.6 the values of $\varepsilon_{M,fd} = 0.0765, 0.0754$ and 0.0692 respectively.

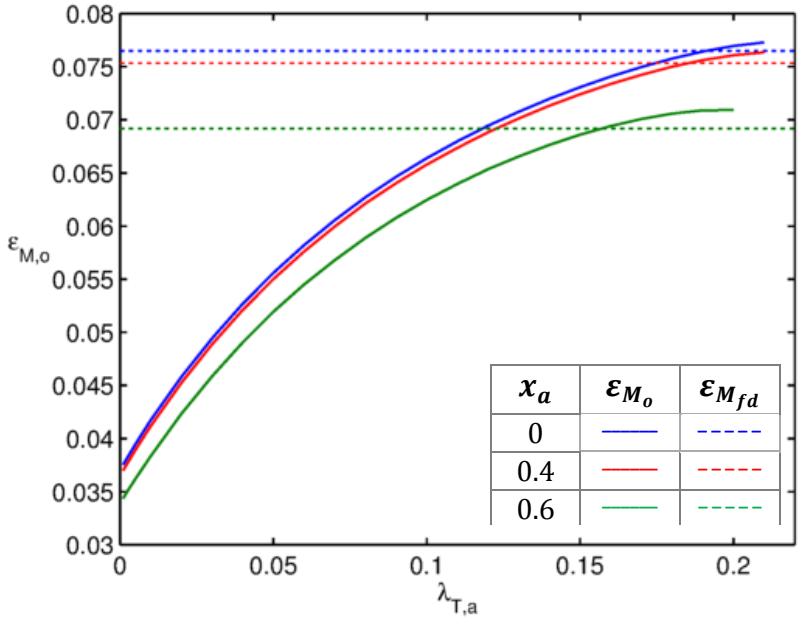

Figure 4.19: Variation of moment coefficient on the rotor with superposed flow rate (from the original Superposed Flow, No Ingress model with zero inlet swirl inner region) for three cavity sizes.

Figure 4.19 shows the moment coefficient on the rotor, as found from the Superposed Flow, No Ingress cavity model with zero inlet swirl model for the inner region. For all cavity sizes the moment coefficient increases with $\lambda_{T,a}$ as expected, with ε_{M_o} nearing $\varepsilon_{M_{fd}}$ at higher sealing flow rates. For the full disc ($x_a = 0$) ε_{M_o} reaches the moment coefficient of the free disc, $\varepsilon_{M_{fd}}$, at around $\lambda_T = 0.19$, which is near the expected result of 0.22. For the smaller values of x_a the moment coefficient reaches $\varepsilon_{M_{fd}}$ at lower values of sealing flow rate. This is unsurprising as it would take less flow to suppress the core rotation within a smaller cavity and as the moment on the free disc will decrease with decreasing cavity size. The larger difference between the moments for $x_a = 0.4$ and $x_a = 0.6$ compared to $x_a = 0.4$ and $x_a = 0$ implies that the relation between the moment and cavity size is not linear.

In order to better understand how the moment coefficient varies in each of the regions the moment can be broken down into the two parts: $\varepsilon_{M_{o,inner}}$ and $\varepsilon_{M_{o,core}}$. Figure 4.20 breaks down the results of Figure 4.19 into the two moments. The moment coefficients of the inner and core regions have opposite trends over the majority of the range of $\lambda_{T,a}$. The moment coefficient of the inner region increases as the size of the

inner region increases with $\lambda_{T,a}$. After an initial increase the moment coefficient of the core decreases as the core is suppressed with increasing $\lambda_{T,a}$.

As the superposed flow increases, the core is suppressed so $\varepsilon_{M_o,core}$ decreases and $\varepsilon_{M_o,inner}$ increases. This highlights the fact that at high flow rates it is the inner region model that is responsible for most of the moment coefficient when the flow is high. The zero inlet swirl model is the inner region model with the highest possible moment coefficient (as it has the lowest swirl ratio). Any other inner region models will result in smaller moment coefficients over values of λ_T.

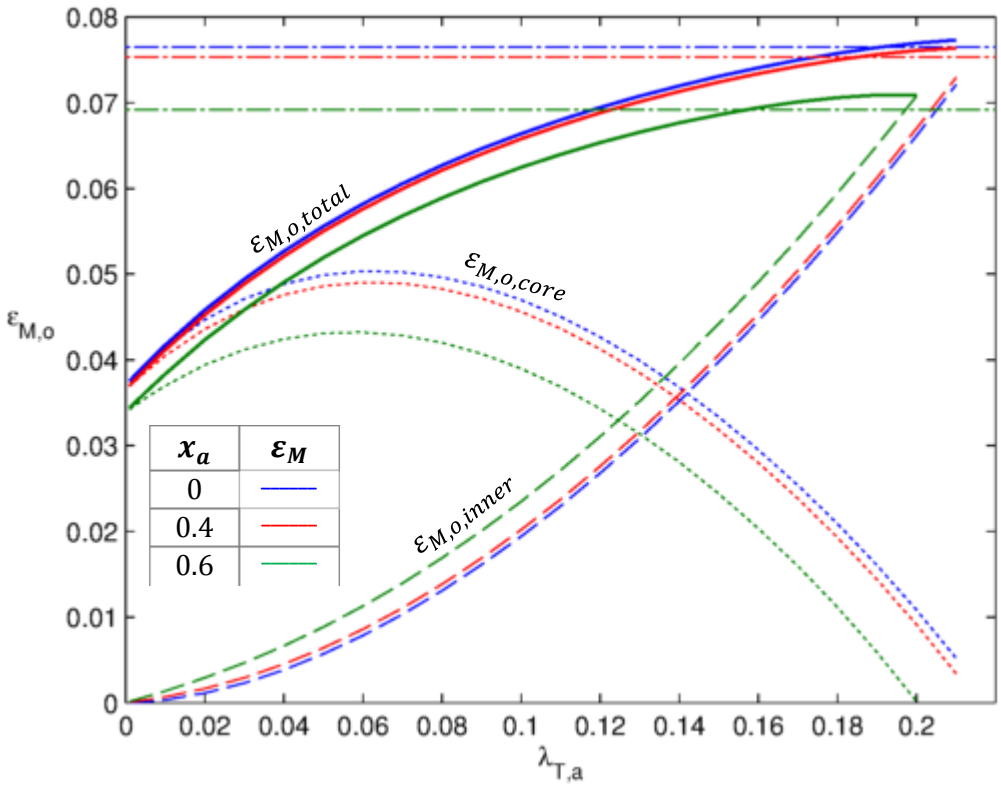

Figure 4.20: Variation of moment coefficient on the rotor with superposed flow rate (from the original SFNI model with zero inlet swirl inner region) for three cavity sizes, separated by flow region.

The moment coefficients shown in Figure 4.20 are shown again in Figure 4.21, but this time plotted along with results from other inner region models. Figure 4.21 shows the moment coefficient on the rotor where the Superposed Flow, No Ingress model has been solved with three different inner region models and three cavity sizes, namely $x_a = 0, 0.4$ and 0.6. The general trend is as expected for all the results (ε_{M_o} increases as $\lambda_{T,a}$ increases, with ε_{M_o} tending towards free disc values) however the actual values of ε_{M_o} vary quite considerably between the three models.

For the inner region models with positive swirl ratio ($\beta > 0$), that is the free vortex model [dashed lines] and the constant swirl model [dotted lines], the moment coefficients are lower than those found by the zero inlet swirl model. This is as increasing the swirl ratio will decrease the moment coefficient.

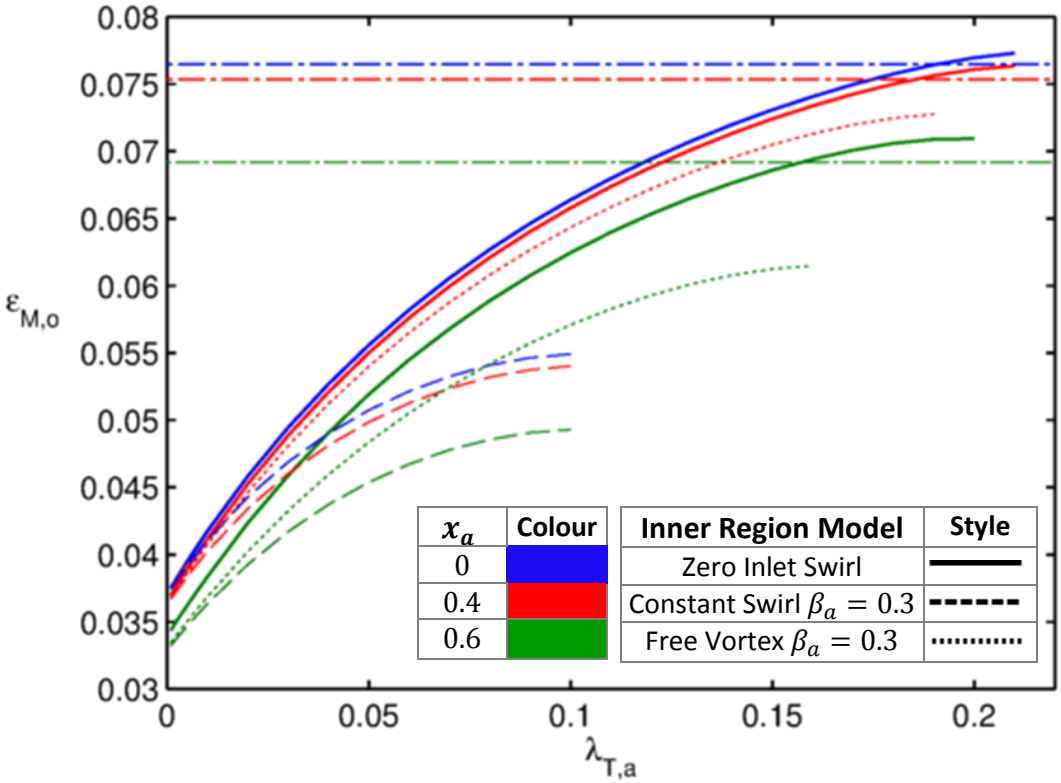

Figure 4.21: Variation of moment coefficient ratio on the rotor with flow parameter for three cavity sizes ($x_a = 0, 0.4$ and 0.6) and three inner region models (zero inlet swirl, constant $\beta_a = 0.3$ and free vortex with $\beta_a = 0.3$).

For the constant swirl model with $\beta_a = 0.3$ the low moment coefficients, that are nowhere near $\varepsilon_{M,fd}$, show that this model is not very appropriate for a rotor-stator system with superposed flow unless β_a is very small. If $\beta_a = 0.05$ then the moments coefficient are very close to those of the zero inlet swirl model, understandably.

The variation of moment coefficient with inlet swirl can be considered when there is no inner region. In Figure 4.22 the SFNI model is solved for fixed $x_a = 0.6$ with three different values of β_a: $0.05, 0.2$ and 0.4. The figure shows how the moment coefficient varies for the SFNI model based upon the original momentum-integral equations where inlet swirl is changed when there is no inner region model. The gradient of the relation between rotor moment coefficient and flow parameter $\lambda_{T,a}$ increases with increasing inlet swirl. The gradient seems to pivot around value $\lambda_{T,a} = 0.1$ such that the moment coefficients *decrease* with increasing inlet swirl between $0 < \lambda_{T,a} < 0.1$ and the moment coefficients *increase* with increasing inlet swirl between $0.1 < \lambda_{T,a} < 0.18$. This seems unlikely to be a physical phenomenon, so can likely be attributed to the equations being unable to capture the correct behaviour in the cavity.

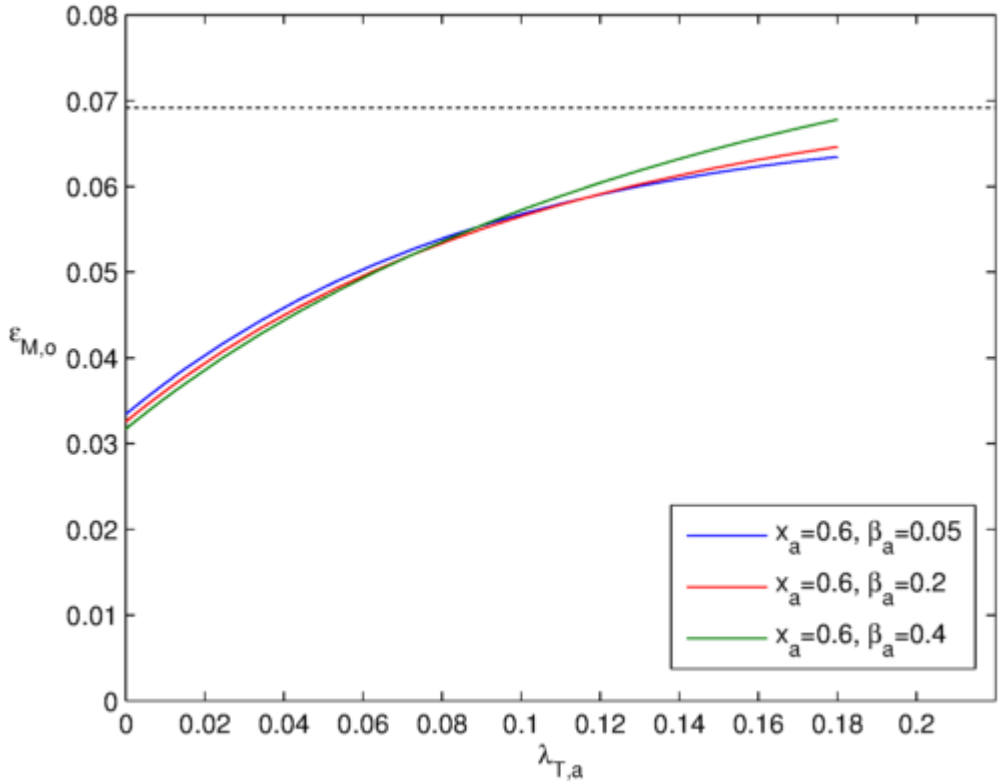

Figure 4.22: Variation of moment coefficient on the rotor with superposed flow rate (from the original SFNI model with no inner region model) for three inlet swirl cases.

Comparisons with experimental and CFD results

In the following section the complete SFNI model with no inner region is compared to experimental and CFD results from the Bath rig. Recall from the literature review that research is typically focused on studying the stator effectiveness for different rim seals in order to determine the minimum amount of flow to prevent ingress, usually quantified in terms of Φ_{min}. The cavity model presented here is not capable of predicting the effectiveness distribution within the cavity, but the orifice model is already able to fit the experimental data. Usefully some of the experimental and CFD studies have also presented swirl ratio measurements and moment coefficients on the rotor for a range of sealing flow rates. Comparisons will be drawn with this data. It is important to note that experimental and CFD results show that swirl ratio is effected by local geometric features, so even though experimental and computational measurements of complicated double seals do exist, the comparisons between the theoretical model and the data are limited to simple axial and radial seals. It is hoped that if the cavity model can predict the correct behaviour for these simple seals it could be adapted to take account of more complex geometric features.

In the literature the minimum amount of flow to prevent ingress is typically quantified in terms of Φ_{min}. The cavity model in this work is described in terms of $\lambda_{T,a}$ instead, equivalent to simply λ_T in other literature. The ingress should be therefore be quantified in terms of $\lambda_{T,min}$. The two parameters are related, as shown in Pountney *et al.* (2013),

$$\lambda_{T,min} = 2\pi G_c Re_\phi^{0.2} \Phi_{min} \tag{4.42}$$

In those experiments carried out at Bath (as in Pountney *et al.* (2013) and Sangan *et al.* (2014)) it just so happened that $\lambda_{T,min} = 1.0042\Phi_{min}$ as $G_c := s_c/b = 2/190 = 0.0105$ and $Re_\phi = 8.12 \times 10^6$. In these papers, and therefore in this work, it is assumed that $\lambda_{T,a} = \Phi_o$ when comparing the model to the data.

Comparisons with experimental results

The following figures show comparisons between the results from the Superposed Flow, No Ingress Cavity model based upon original momentum-integral equations for various inner region models and experimental measurements for a range of flow rates and seals. First measurements of swirl ratio for an axial seal under EI ingress conditions are considered.

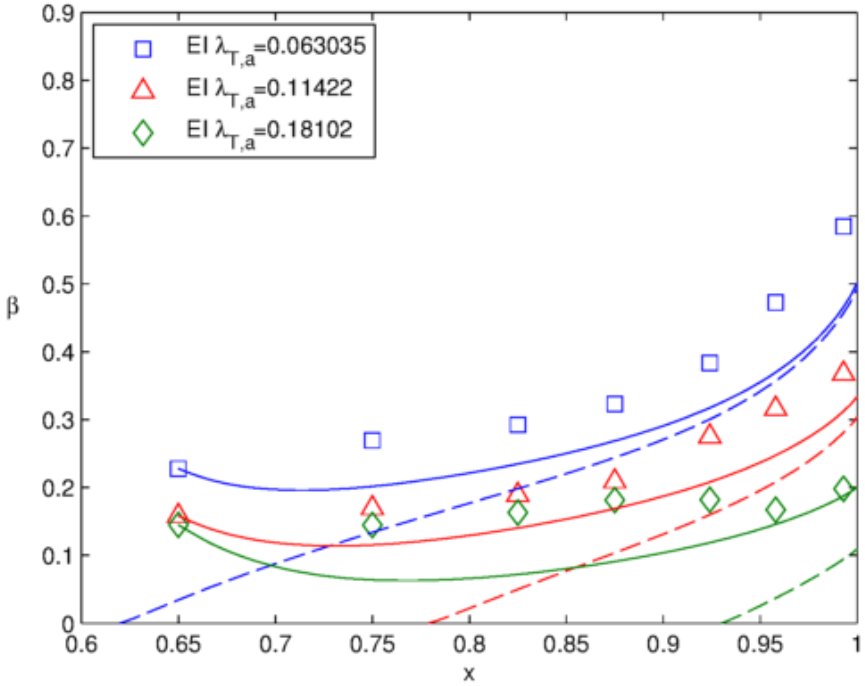

Figure 4.23: Radial variation of swirl ratio for axial seal under EI conditions from experimental measurements of Sangan *et al.* (2014) [Symbols], SFNI Model with No Inner Region [solid lines] and SFNI Model with Zero Inlet Swirl Inner Region Model [dashed lines].

Figure 4.23 gives a comparison of the radial variation of swirl ratio from two versions of the model and experimental measurements, shown are:

- The SFNI Cavity model with no inner region where $x_{in} = 0.65$ and β_{in} has been set to exactly the swirl ratio value from the experiments *[solid lines]*
- The SFNI Cavity model with the 'Zero Inlet Swirl' inner region model where $x_a = 0$ and $\beta_a = 0$ have been set *[dashed lines].*
- Experimental measurements from Sangan *et al.* (2014) *[symbols].*

For all flow rates the model under predicts the swirl ratio. The value of Φ_{min} (and equivalently $\lambda_{T,min}$) for the axial seal is 0.326 for EI ingress, far greater than the flows being considered here. This means there would be significant amount of ingress not taken account of in the model. The experimental results show a small gradient in what is likely the core (from $0.65 < x_a < 0.87$). The results of swirl ratio from the zero inlet swirl inner region model do not give very good agreement with this plateau. As the Bath rig contains an inner seal, it is possible that the presence of the seal increases the

local swirl ratio around $x \approx 0.6$. Due to this all comparisons from this point will also only be between the 'matched' SFNI Model (where the initial value of β has been set to exactly the swirl ratio value from the experiments or computations that the theory is being compared against). This is to account for the presence of the inner seal in the Bath rig.

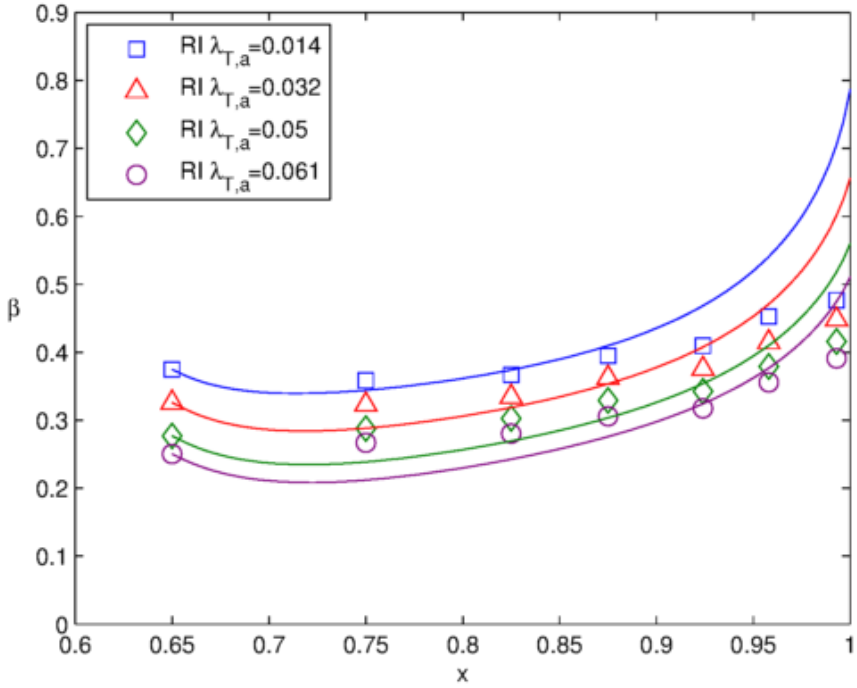

Figure 4.24: Radial variation of swirl ratio for axial seal under RI conditions. [Open Symbols] = Experimental measurements with ingress and [solid lines] = SFNI Model with no inner region model.

Figure 4.24 shows a comparison of the radial distribution of swirl ratio from the SFNI Model with no inner region model and RI experiments for an axial seal. The experimental measurements for this RI case were taken by Sangan *et al.* (2014) but are unpublished. This time only results from the no inner region model have been considered, where once again the initial condition for β_{in} has been gained directly from the experiments. Even though the trends are the same (decreasing swirl for increasing sealing flow) and the agreement is good at lower radial locations, the experiments and the theory deviate towards the exit. The model over predicts the value of swirl above $x_a \approx 0.9$, which corresponds to being within the outer region.

When comparing the model to experimental results, which by definition have been taken with ingress, it would be expected that the higher the flow rate the more accurate the model should be. This is because the model does not take account of ingress and the higher the sealing flow rate the less ingress there is into the system. The maximum difference between the model and the data does decrease with sealing flow rate.

Comparisons with CFD results

Lalwani (2014) used CFD to model the Bath rig but with *no ingress.* The model was created by setting the flow conditions in the annulus to purely outflow, this prevented any ingress regardless of the flow supplied. Using CFD to validate the theoretical model is important for this 'no ingress' case, as experiments typically include ingress.

Figure 4.25 shows a comparison of the swirl ratio results found from the CFD no ingress model and the Superposed Flow, No Ingress modelled with matched inlet swirl. The agreement is very good for the case of $\lambda_{T,a} = 0.018$ and good for $\lambda_{T,a} = 0.037$. The agreement is worse with the higher flow rates, and generally better at lower radial locations. It is important to note that the CFD in this figure was completed for a radial seal, this is the cause of the localised peak in swirl ratio around $x = 0.97$. The dotted vertical lines denote where the radial part of the seal is located in the cavity. This geometric feature would create a local disturbance of the swirl ratio, which would not be captured by the theory. It is surprising that the agreement between the data the theory is better the lower the superposed flow rate, as the lower the flow rate the more ingress, which the theory does not take account of.

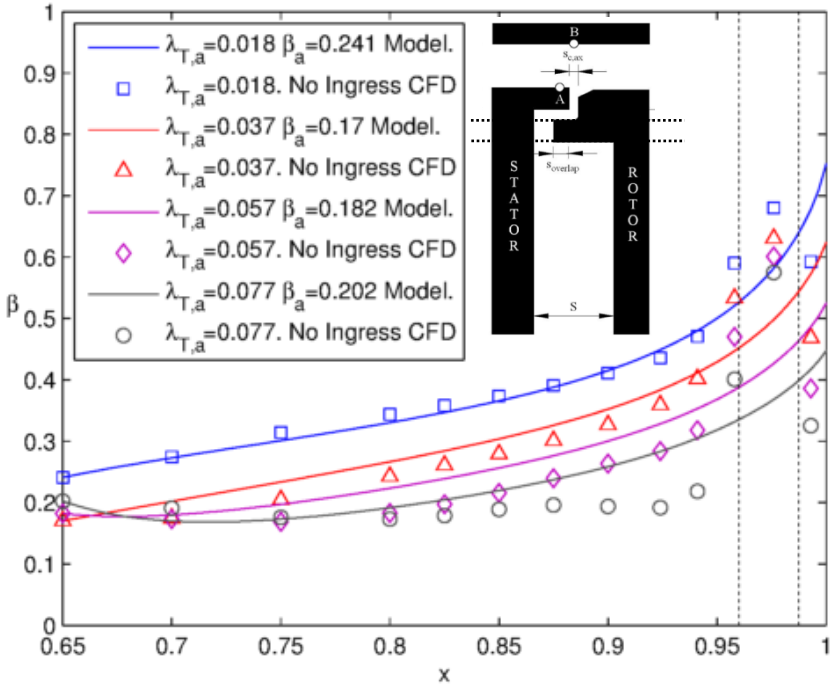

Figure 4.25: Comparison of radial distribution of swirl ratio from matched inlet swirl SFNI model [solid lines] and No Ingress CFD model for radial seal [symbols]

As well as swirl ratios, Lalwani (2014) presented the variation of the moment coefficient for the rotor from two CFD models: one with ingress [circles] and one without [squares]. As can be seen by the symbols in Figure 4.26 it was found that there was agreement between the ingress and no ingress model above $\lambda_{T,a} \approx 0.08$, which agrees with the predicted value of $\lambda_{T,min,RI} = 0.0838$ from Sangan *et al.* (2013c). Even at low flow rates the difference between the ingress and no ingress cases is relatively small. This small effect of ingress on the momentum coefficient on the rotor is beneficial as it means the results from the Superposed Flow, No Ingress model should be applicable to the ingress case too. The moment coefficients from the CFD results were calculated with $x_a = 0.642$, and with a free disc moment coefficient $\varepsilon_{M,fd} = 0.728$. It is not known where this free disc value came from, but by using the solutions of α_o and γ_o from the free disc rotor equations (2.38) and (2.39), with $x_a = 0.642$ it is found that $\varepsilon_{M,fd} = 0.0665$, this value is shown as a dashed line in Figure 4.26.

Figure 4.26 also contains the swirl ratio results from the SFNI model where no inner region model is used with various inlet swirl values, as originally shown in Figure

4.22. The SFNI model starts at $x_a = 0.6$ and are compared with moment coefficients calculated by Lalwani (2014). The agreement is very good, with the high inlet swirl results agreeing at lower flow rates and lower inlet swirl results to agreeing at high flow rates which matches the tendencies of the experimental results (swirl at x_a decreasing with increasing sealing flow rate).

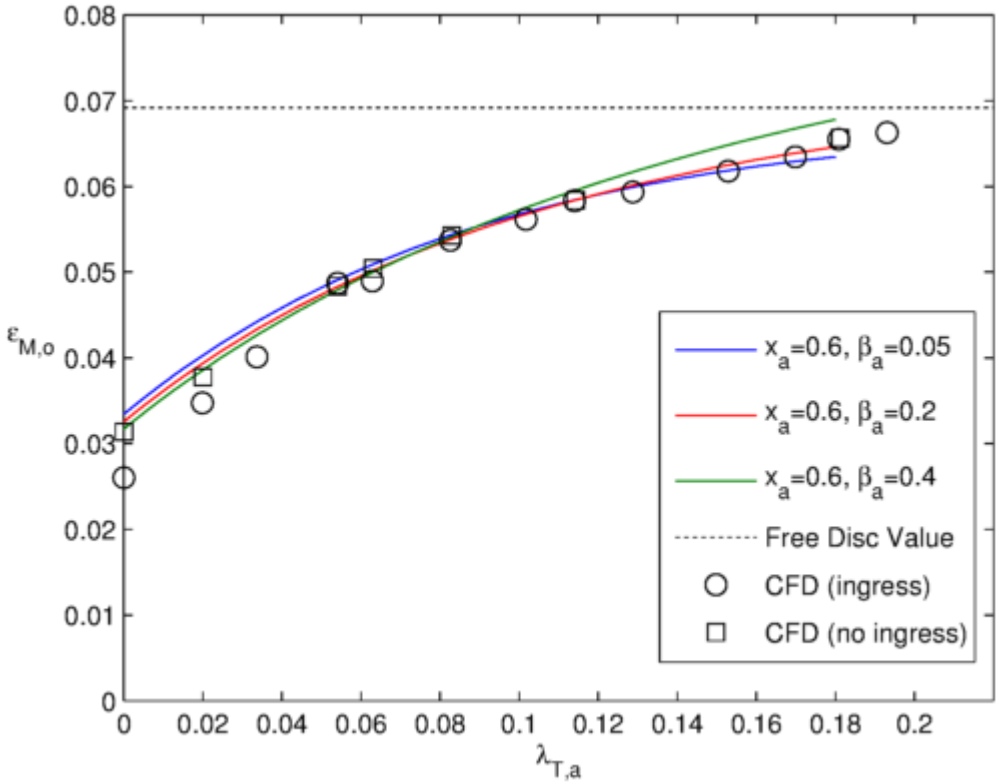

Figure 4.26: Comparison of rotor moment coefficient from matched inlet swirl SFNI model [solid lines] with No Ingress CFD Model for radial seal [symbols]

In this Section the model for a cavity which is subject to superposed flow and no ingress has been derived based upon the original momentum-integral equations. The procedure was based upon the successful Closed Cavity model, but with the continuity equation now including a positive value of superposed flow $\lambda_{T,a}$. Although inner region models have been given, the swirl ratios are not continuously smooth when the inner region models are used, and it is found that positive swirl in the inner region causes the moment coefficients to be much lower than expected. The results from the no inner region model, where typically the flow starts at $x_a = 0.6$, were in reasonable and poor agreement with EI and RI ingress experimental measurements of swirl ratio respectively. There was good agreement with the no ingress CFD model of Lalwani (2014) for the swirl ratios and the moment coefficients.

4.5 VARIABLE MOMENTUM-INTEGRAL EQUATIONS

As with the Closed Cavity Model there are two versions of the SFNI model: *original* and *variable* momentum-integral equation models. The solutions to the *original momentum-integral equation model* were given in the previous section. They involved solving the previously published momentum-integral equations where the swirl ratio in the core is assumed to be constant. There were two equations for the rotor and two for the stator, which were coupled only through the continuity equation.

The *variable momentum-integral equation model* solves newly derived momentum-integral equations, where the swirl ratio is variable, and as such $d\beta/dx$ appears in the equations. There are still two differential equations for the rotor and two for the stator but for this case there is a fifth differential for the swirl ratio, an expression for which can be gained from the continuity equation. In the previous chapter, an expression for $d\beta/dx$ was derived, but now that there is superposed flow in the cavity a new expression must be derived, to account for the continuity equation with the $\lambda_{T,a}$ term being present.

4.5.1 EQUATIONS

The *variable momentum integral equations* derived for the Closed Cavity Model, restated here for convenience, can be used for the Superposed Flow, No Ingress Model. The *variable momentum integral equations for the rotor* are,

$$\frac{d\alpha_o}{dx} = \frac{\alpha_o}{x(1-\beta)}\left[\frac{-6696}{343}F_o + \frac{46(1+8\beta)}{343\alpha_o^2} + 6x\frac{d\beta}{dx} + 11\beta + 1\right] \tag{4.43}$$

$$\frac{d\gamma_o}{dx} = \frac{\gamma_o}{x(1-\beta)}\left[\frac{11736}{343}F_o - \frac{46(1+8\beta)}{343\alpha_o^2} - \frac{47x}{5}\frac{d\beta}{dx} - \frac{4}{5}(23\beta+7)\right] \tag{4.44}$$

and for the stator are,

$$\frac{d\alpha_s}{dx} = \frac{\alpha_s}{x}\left[\frac{6696}{343}\left(\frac{0.0225(1+\alpha_s^2)^{\frac{3}{8}}}{\alpha_s\gamma_s^{\frac{5}{4}}}\right) - \frac{1656}{343}\frac{2}{9{\alpha_s}^2} - 11 - \frac{6x}{\beta}\frac{d\beta}{dx}\right] \tag{4.45}$$

$$\frac{d\gamma_s}{dx} = \frac{\gamma_s}{x}\left[\frac{-11736}{343}\left(\frac{0.0225(1+\alpha_s^2)^{\frac{3}{8}}}{\alpha_s\gamma_s^{\frac{5}{4}}}\right) + \frac{1656}{343}\frac{2}{9{\alpha_s}^2} + \frac{92}{5} + \frac{51x}{5\beta}\frac{d\beta}{dx}\right] \tag{4.46}$$

as derived in Appendix A1 and A2 respectively, and as originally stated in Chapter 3. When applying the variable momentum integral equations to the Superposed Flow, No Ingress model, the equations themselves will not differ however the equation for $d\beta/dx$ will change. Recall that the equation for the differential of the swirl ratio is calculated by differentiating the continuity equation itself. The continuity equation for the SFNI model is not the same as the continuity equation for the Closed Cavity (due to the extra term for the superposed flow rate). The continuity equation for the SFNI Model is given by (4.35). Differentiating the continuity equation with respect to x (assuming $\alpha_o, \gamma_o, \alpha_s, \gamma_s$ and β are functions of x) gives

$$\begin{aligned}&(1-\beta)^{\frac{8}{5}}\left[\frac{d\gamma_o}{dx}\alpha_o + \gamma_o\frac{d\alpha_o}{dx}\right] - \beta^{\frac{4}{5}}\left[\alpha_s\frac{d\gamma_s}{dx} + \gamma_s\frac{d\alpha_s}{dx}\right]\\ &= \frac{d\beta}{dx}\left[\alpha_o\gamma_o\frac{8}{5}(1-\beta)^{\frac{3}{5}} + \alpha_s\gamma_s\frac{4}{5}\beta^{\frac{-1}{5}}\right] - \frac{13}{5}x^{\frac{-18}{5}}\left(\frac{60}{49\pi}\lambda_{Ta}\right)\end{aligned} \tag{4.47}$$

By substituting the equations (4.43)-(4.46) into (3.44) the equation becomes

$$\frac{\alpha_o\gamma_o(1-\beta)^{\frac{8}{5}}}{x}\left[\frac{720}{49}\frac{F_o}{(1-\beta)}-\frac{23+37\beta}{5(1-\beta)}\right]-\frac{\alpha_s\gamma_s\beta^{\frac{4}{5}}}{x}\left[\frac{720}{49}F_s+\frac{37}{5}\right] = \frac{d\beta}{dx}5\left[\alpha_o\gamma_o(1-\beta)^{\frac{3}{5}}+\alpha_s\gamma_s\beta^{\frac{-1}{5}}\right]-\frac{13}{5}x^{\frac{-18}{5}}\left(\frac{60}{49\pi}\lambda_{T_a}\right) \tag{4.48}$$

where all the $d\beta/dx$ terms have been grouped together. Rearranging to make $d\beta/dx$ the subject gives,

$$\frac{d\beta}{dx}=\frac{1}{5x\left[\alpha_o\gamma_o(1-\beta)^{\frac{3}{5}}+\alpha_s\gamma_s\beta^{\frac{-1}{5}}\right]}\left\{\alpha_o\gamma_o(1-\beta)^{\frac{3}{5}}\left[\frac{720}{49}F_o-\frac{23+37\beta}{5}\right]-\alpha_s\gamma_s\beta^{\frac{4}{5}}\left[\frac{720}{49}F_s+\frac{37}{5}\right]+\frac{13}{5}x^{\frac{-13}{5}}\frac{60}{49\pi}\lambda_{T_a}\right\} \tag{4.49}$$

Finally, by using the continuity equation to further simplify the equations (see Appendix A3 for more details) the equation becomes

$$\frac{d\beta}{dx}=\frac{144}{49}\frac{\beta}{x}\frac{\alpha_o\gamma_{_o}(1-\beta)^{\frac{3}{5}}}{\left[-\frac{60}{49\pi}\lambda_{T,a}x^{-\frac{13}{5}}+\alpha_o\gamma_{_o}(1-\beta)^{\frac{3}{5}}\right]}\left\{F_o-\frac{49}{60}+F_s(1-\beta)+\frac{60}{49\pi}\frac{\lambda_{T_a}x^{-\frac{13}{5}}}{\alpha_o\gamma_{_o}(1-\beta)^{\frac{3}{5}}}\left[\frac{49}{72}-F_s\right]\right\} \tag{4.50}$$

where F_o and F_s are defined by (3.3) and (3.42), and which gives exactly (3.45) if $\lambda_{T,a}=0$ is set the equation. This equation for the differential of the swirl ratio can be used in equations (4.43)-(4.46) to give the *variable momentum-integral equations for cavities with superposed flow*. Notice that once again the differential equation couples the rotor and stator equations by depending on $\alpha_o, \gamma_o, \alpha_s$ and γ_s.

4.5.2 PROCEDURE

As was the case when using the variable momentum-integral equations to model the Closed Cavity, the solution procedure needs to be adjusted in order to be able to solve the now coupled rotor and stator equations.

Note on the Inner Region

The way the inner region was modelled for the original momentum-integral equations, as explored in Section 4.2, did not require an iterative scheme, the equations on the rotor and stator were simply solved once. It is not possible for the variable momentum-integral equations to model the inner region in the same way due to the coupled nature of the equations. Modelling the inner region with the variable momentum-integral equations is therefore a difficult task. As well as this difficulty comparison with experimental or CFD data requires setting $x_{in}=0.65$ (and therefore omitting the inner region model), as such it is decided to not pursue modelling the inner region for the variable equations. Instead if an inner region model is desired one of the already presented models can be used (such as the 'variable' free vortex equations).

Step 0: Initial Conditions

Inputs: x_a, β_a, α_s, γ_s and $\lambda_{T,a}$

Step 1: Inner Region Model

Inputs: $x_a, \lambda_{T,a}$ and some assumed β distribution for inner region (e.g. free vortex)

Outputs: x_{in}, β_{in}, $\alpha_{o,in}$ and $\gamma_{o,in}$.

If desired, an inner region model can be used, else simply set $x_{in} = x_a$ and $\beta_{in} = \beta_a$ with $\alpha_{o,in}$ and $\gamma_{o,in}$ found from (2.38) and (2.39).

Step 2: Solve *original* stator equations for Core/Outer Region

Inputs: α_s at $x = 1$ (initial condition from Step 0.)

Outputs: $\alpha_s(x), \gamma_s(x)$

Solve the stator equations (3.1)(3.6) and (3.7) between $x_{in} < x < 1$. These are used as a stepping stone to solve the *variable equations*.

Step 3: Set initial guess for $\beta(x)$ distribution in core/outer region

Inputs: β_{in}, $\alpha_{o,in}$ and $\gamma_{o,in}$.

Outputs: $\beta(x)$

A guess for the radial distribution of β is simply a linear increase from β_{in} to β_1 where:

$$\beta_1 = 1 - \left[\frac{60\lambda_{T,a}}{49\alpha_{o,in}\gamma_{o,in}\pi}\right]^{\frac{5}{8}} \tag{4.51}$$

Step 4: Solve *original* rotor equations

Inputs: $\alpha_{s,in}, \gamma_{s,in}, \beta(x), \lambda_{T,a}$ and $\alpha_{o,in}$ from inner region model

Outputs: $\alpha_o(x), \gamma_o(x)$

Solve rotor equations (3.1) and (3.2) between $x_{in} < x < 1$. As described back in Section 4.3.2 the initial condition for the rotor $\gamma_{o,in}$ is found from (4.34) and (4.33) which become:

$$\gamma_{o,in} = \frac{(1-\beta)^{-\frac{8}{5}}}{\alpha_{o,in}}\left[\alpha_{s,in}\gamma_{s,in}\beta_{in}^{\frac{4}{5}} + \frac{60}{49\pi}\lambda_{T\,a}x^{-\frac{13}{5}}\right] \tag{4.52}$$

Step 5: Solve the continuity equation

Inputs: $\alpha_o(x), \gamma_o(x), \alpha_s(x), \gamma_s(x), \lambda_{T,a}$

Outputs: β_i

The continuity equation (4.35) is solved numerically for many radial locations between $x_{in} < x < 1$. This can be by the Newton-Raphson method or any of the built in MATLAB functions such as `fsolve`. All solvers tested yield the same results.

Note: Now that the original equations have been solved once, a complete solution is available. This means there are values of α_o and γ_o to use in the stator equations are values of α_s and γ_s to use in the rotor equations. It is from here that the 'variable' iterations take over.

Step 6: Solve *variable* momentum-integral stator equations

Inputs: $\alpha_o(x)$, $\gamma_o(x), \beta_i(x)$ and initial conditions at $x = 1$ for α_s and γ_s.

Outputs: $\alpha_s(x), \gamma_s(x)$

The values of $\alpha_o(x)$, $\gamma_o(x), \beta(x)$ from Step 5 are substituted into *variable* stator equations (4.45) and (4.46). The two equations are solved numerically using initial

conditions $0.3 < \gamma_s < 0.5$ (see following section for reasoning) and with the supplied value of α_s at $x = 1$, typically $\alpha_s = 0.001$ unless otherwise stated.

Step 7: Solve *variable* momentum-integral rotor equations
Inputs: $\alpha_s(x), \gamma_s(x), \beta_i(x)$
Outputs: $\alpha_o(x), \gamma_o(x)$
The values of $\alpha_s(x)$ and $\gamma_s(x)$ from the variable stator equations of Step 6 are substituted into (4.43) and (4.44) and are solved numerically using initial conditions $\gamma_{o,in}$ and $\gamma_{o,in}$.

Step 8: Solve the continuity equation
Inputs: $\alpha_o(x), \gamma_o(x), \alpha_s(x), \gamma_s(x), \lambda_{T,a}$
Outputs: β_{i+1}
The continuity equation (4.35) is solved numerically for many radial locations between $x_{in} < x < 1$. This can be by the Newton-Raphson method or any of the built in MATLAB functions such as `fsolve`. All solvers tested yield the same results. (Note that this $\beta(x)$ distribution can be considered 'fully-variable' as it is based upon $\alpha_o(x), \gamma_o(x)$ from the variable equations and $\alpha_s(x), \gamma_s(x)$ from the variable equations).

Step 9: Convergence Check
Inputs: β_i and β_{i+1}
In this step the convergence criterion is checked. If the difference between the swirl ratio distribution from the previous step (β_i) and the current step (β_{i+1}) is within the error tolerance specified (typically 0.1%) then the results produced by step 8 are output as the final results. If the difference is *not* within the error tolerance then the model is not converged. The $\beta(x)$ distribution output of step 8 is considered the new $\beta_i(x)$ guess and the method continues from step 6.

4.5.3 RESULTS

The following section summarises key results that can be gained by using the procedure outline about to model the Superposed Flow, No Ingress cavity based on the variable momentum-integral equations.

Impact of Initial Conditions

For the constant equations, the initial condition chosen for γ_s did not affect the outputs of the model. Considering Figure 4.27, it can be seen that for the variable momentum-integral equations (applied to the cavity with superposed flow) the initial condition γ_s *does* influence the swirl ratio. The top row of figures shows the swirl ratio and the bottom row shows the values of γ_s, both from the final solution of the SFNI model with $x_a = 0.6, \beta_a = 0.1$, $\lambda_{T,a} = 0.05$ and $\alpha_s = 0.001$. The columns each show a different starting initial condition of γ_s. The effect of the initial condition can only be seen very near $x = 1$, so the value of the initial condition for γ_s does affect β_1 but not $\beta(x)$ in general. Recall that the stator equations solve radially inwards, so from right to left in these figures, meaning the initial condition is in fact the value at $x = 1$. For small starting values of γ_s, as the case $\gamma_s = 0.0001$ demonstrates, the steep ascent of the γ_s curve causes a sharp change in gradient in the β curve. For higher initial values of γ_s the solution for γ_s is not smooth. Initial values of $0.03 < \gamma_s < 0.05$ seem to give the smoothest curves for both γ_s and β.

Figure 4.27 is only for one value of the turbulent flow parameter; $\lambda_{T,a} = 0.05$. However the trends are very similar for other flow rates. For smaller values of $\lambda_{T,a}$ the effect of γ_s on β_1 is slightly greater.

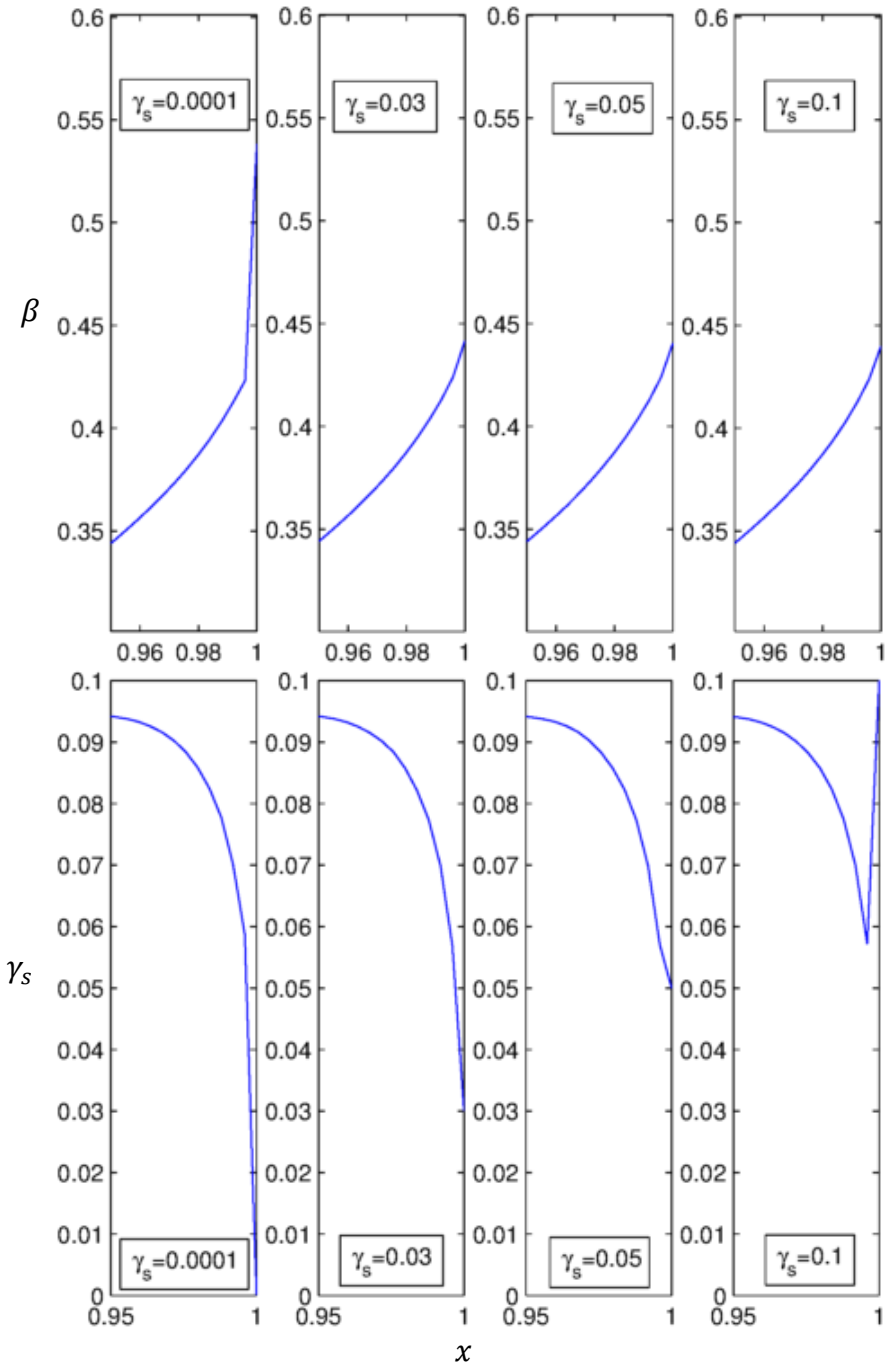

Figure 4.27: Variation of swirl ratio [top row] and γ_s [bottom row] near cavity exit from SFNI model with no inner region model for four initial conditions of γ_s [left to right] where $x_a = 0.6, \beta_a = 0.1$, $\lambda_{T,a} = 0.05$ and $\alpha_s = 0.001$

As γ_s is now greater than zero, the mass flow rate parameter $\lambda_{T,s}$ may be greater than zero at $x = 1$. For there to be no ingress, then $\lambda_{T,s}$ needs to be approximately zero, this means α_s will need to be small. Similar plots, shown in Figure 4.28, were generated to study the effect of α_s. For $\lambda_{T,s}$ to be sufficiently small and the function of α_s to be free of large changes in gradient an initial condition $\alpha_s \approx 0.001$ should be chosen.

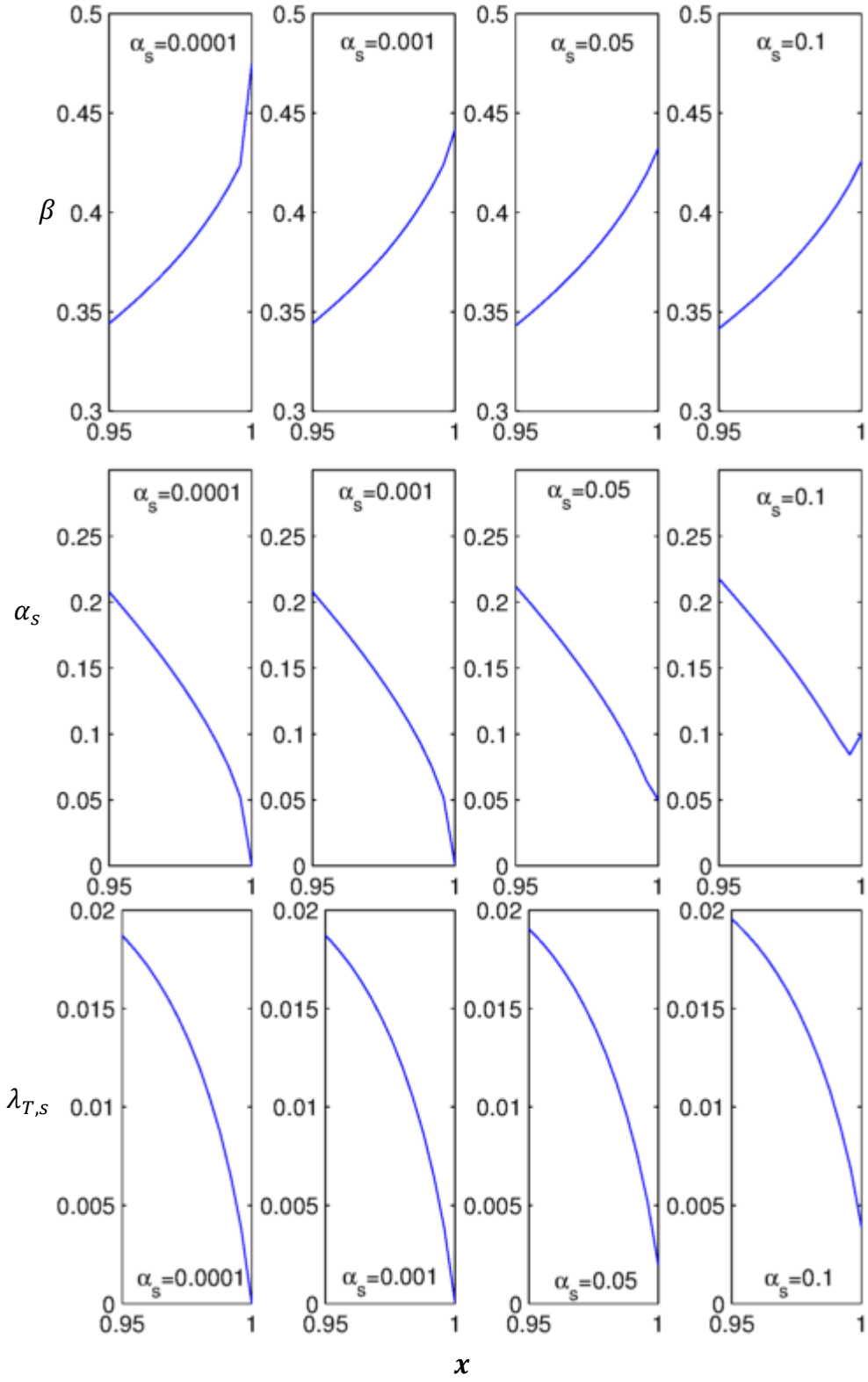

Figure 4.28: Variation of swirl ratio [top row], α_s [middle row] and $\lambda_{T,s}$ [bottom row] near cavity exit from SFNI model with no inner region model for four initial conditions of α_s [left to right] where $x_a = 0.6, \beta_a = 0.1, \lambda_{T,a} = 0.05$ and $\gamma_s = 0.03$

Differences from original equations

All the trends that were shown in the results section for the original SFNI cavity model still hold for the results from the SFNI model based on the variable equations. As for the Closed Cavity model the differences in the solutions from the original and

variable equations are fairly small, with the differences being largest near the exit, especially β_1. As the behaviour is so similar, rather than repeating all the analysis that was carried out for the original equations, a few figures are shown to give a feel for the differences and then the comparisons with experimental and CFD data are given.

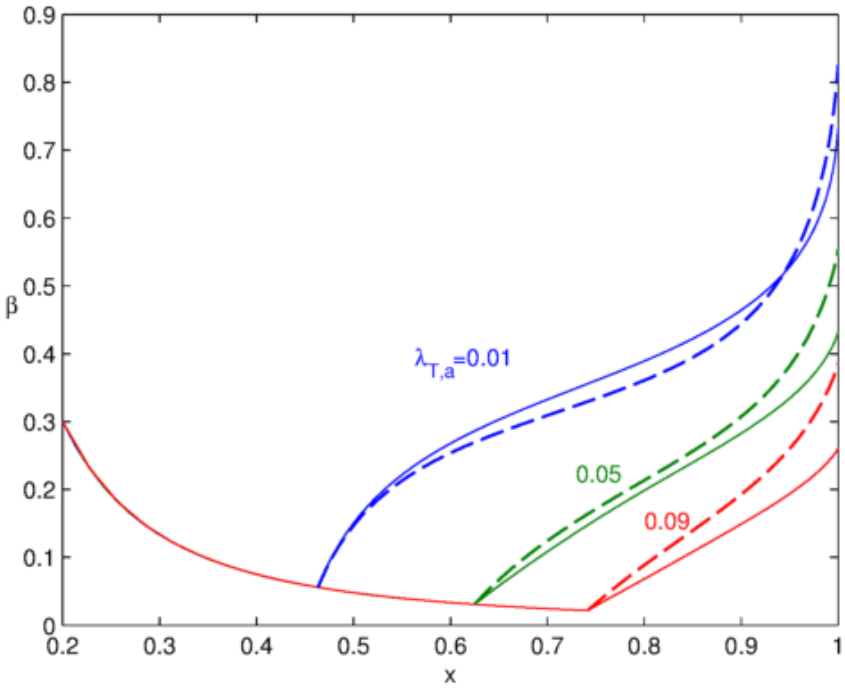

(a) Free Vortex Inner Region Model ($\beta_a = 0.3$)

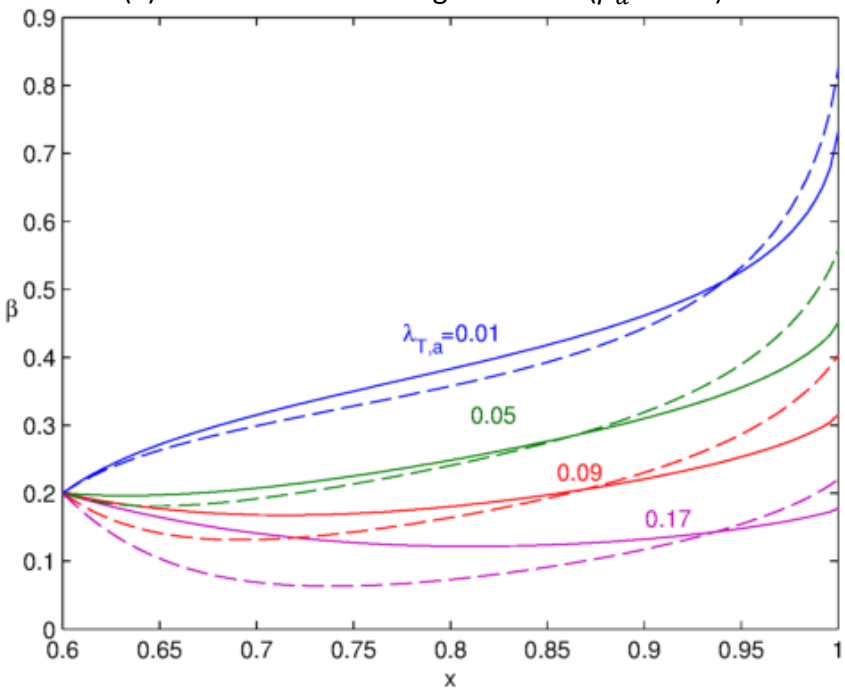

(b) No Inner Region Model ($\beta_a = 0.2$)

Figure 4.29: Comparison between original [dashed lines] and variable [solid lines] SFNI model with no inner region results: radial variation of swirl ratio for $x_a = 0.6, \beta_a = 0.2$ and various sealing flow rates.

Figure 4.29 shows the radial variation of swirl ratio from both the original and the variable models, where they are solved with the same initial conditions:

$\alpha_s = 0.001$ and $\gamma_s = 0.03$. The dashed lines are the results from the original model, and the solid lines form the variable model. Figure 4.29 (a) shows the comparisons for the results from the free vortex inner region model. The swirl ratio results from the variable equations are lower at all radial locations, with the difference between the original and the variable increasing with radius. Figure 4.29 (b) shows the comparisons for the results from the no inner region model. In comparison to the original results, the variable model predicts slightly higher swirl ratio for most radial locations, and then significantly lower swirl ratio at the cavity exit. Overall the swirl ratio distributions are flatter from the variable model.

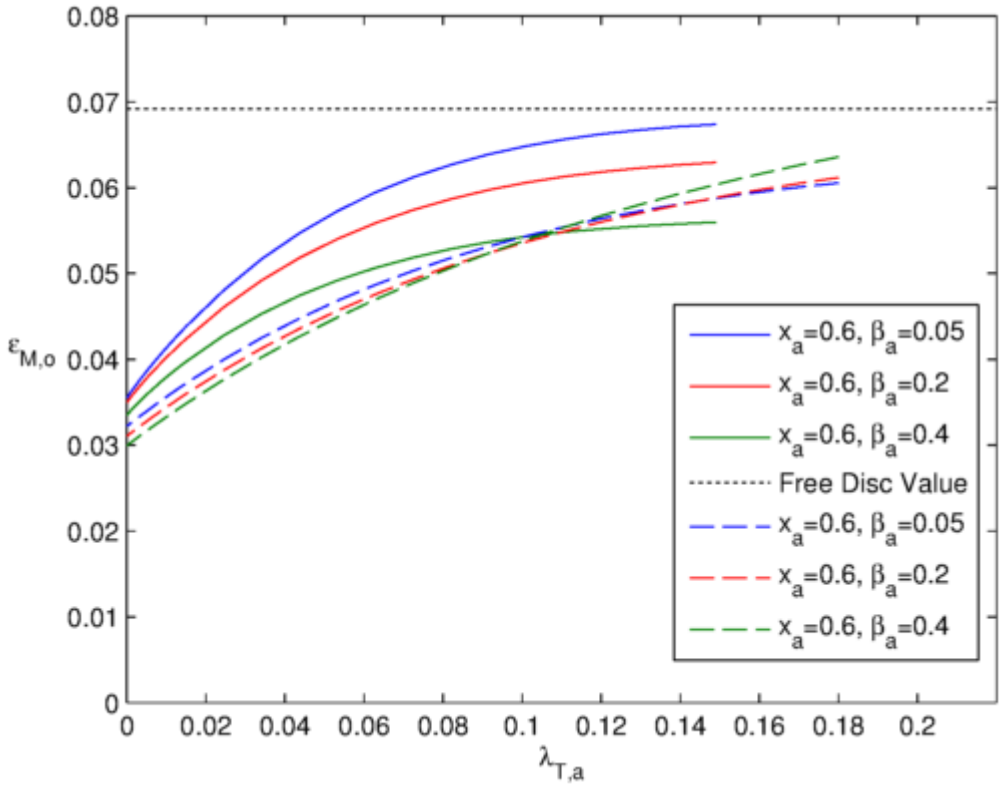

Figure 4.30: Variation of moment coefficient with inlet swirl as predicted by Superposed Flow, No Ingress model with No Inner Region Model based on variable eqns [solid] and original eqns [dashed]

Next the moment coefficients are considered, just for the no inner region model so x_a is fixed at 0.6. The variation of the moment coefficient with inlet swirl is considered in Figure 4.30. Recall that for the SFNI model with no inner region based on the original momentum-integral equations it was found that the inlet swirl affected the gradient of the relationship between $\varepsilon_{M,o}$ and $\lambda_{T,a}$, this can be seen as the dashed lines in Figure 4.30. Also shown are the results for the SFNI model, for exactly the same conditions, based upon the variable momentum-integral, see the solid lines. Interestingly the effect of the inlet swirl on the moments is far greater than for the original equations. The results from the variable equations seem far more realistic as it is to be expected that increasing the inlet swirl would decrease the moment coefficient, regardless of the amount of sealing flow being supplied to the system. This provides further evidence that the variable equations are far better at modelling cavity flow.

Comparisons with experimental results

Recall from the results from the original momentum-integral equations that the best agreement came with no inner region where the swirl ratio was matched with the experiments to provide an initial condition.

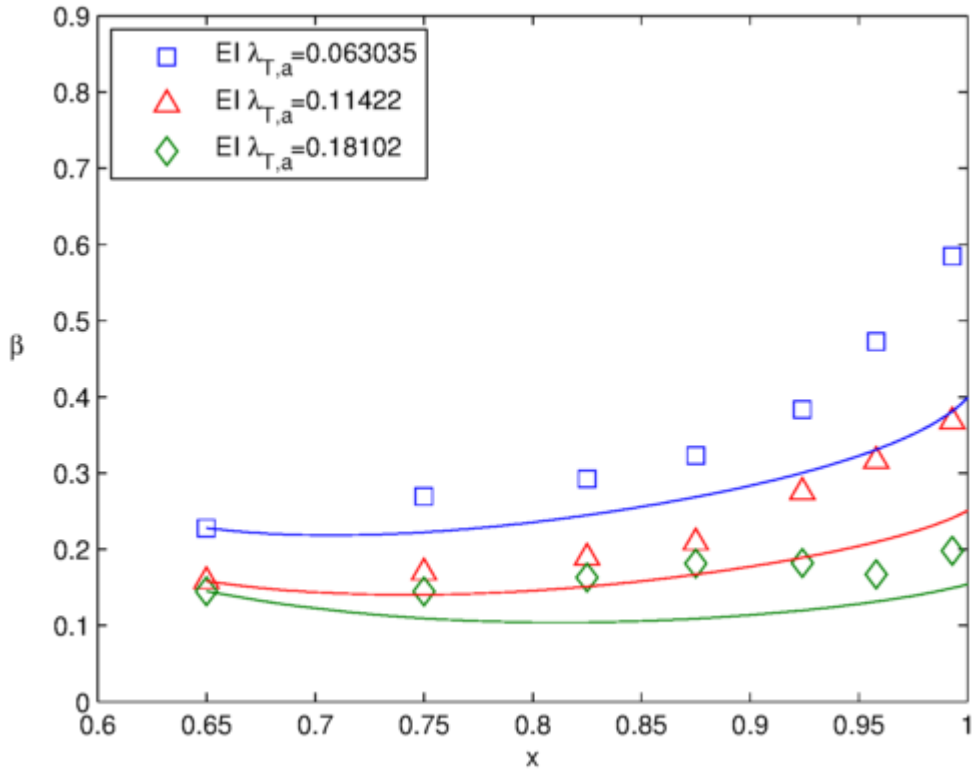

Figure 4.31: Radial variation of swirl ratio for axial seal under EI conditions. [Symbols] = Experimental measurements of Sangan *et al.* (2014), [solid lines] = SFNI Model with variable eqns.

Figure 4.31 gives a comparison between experimental swirl ratio measurements for an axial seal and the predictions of the Superposed Flow, No Ingress model based upon the variable momentum-integral equations. The under prediction is attributed to the fact that the axial seal lets a significant amount of ingress effect the cavity (captured by $\Phi_{min,EI} = 0.326$). Figure 4.29 showed in general the SFNI model based upon the variable momentum-integral equations shows lower predictions of swirl ratio in the outer region. As shown by Figure 4.23 the predictions by the model based upon the original momentum-integral equations already under predicted the swirl ratio, so it unsurprising that the agreement is worse here.

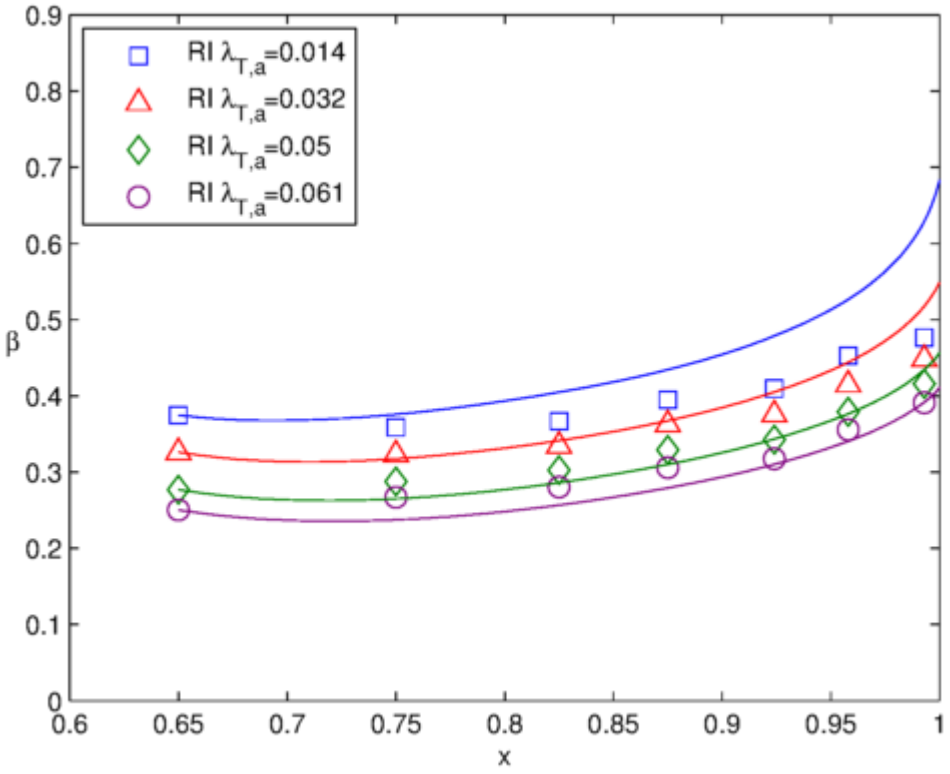

Figure 4.32: Radial variation of swirl ratio for axial seal under RI conditions. [Open Symbols] = Experimental measurements with ingress and [solid lines] = SFNI Model with no inner region model.

Figure 4.32 shows a comparison between experimental measurements of swirl ratio taken by Sangan *et al.* (2014) but unpublished and the variable SFNI model for a range of flow rates. At first it may seem that these results give a worse agreement between the model and the data than for the model based upon the original momentum-integral equation. The results for lowest flow rate $\lambda_{T,a} = 0.014$ for example have a worse agreement with the data than from the original model shown in Figure 4.24. However, the overall trend for these variable equations is correct in that the agreement between the model and the data gets better as $\lambda_{T,a}$ increases and therefore ingress decreases. For the axial seal $\lambda_{T,min,RI} = 0.0838$ as predicted by Sangan *et al.* (2013c), so the case of $\lambda_{T,a} = 0.061$ which shows very good agreement with the data is close to being sealed, and so can be considered representative of a no ingress case.

Comparisons with No Ingress CFD results

This subsection shows comparisons between the SFNI model based upon the variable equations and the CFD model with no ingress of Lalwani (2014), originally discussed in Section 4.4.2.

Figure 4.33 shows a comparison between the CFD and the solutions from the SFNI model based upon the variable momentum-integral equations. It can be seen that the variable momentum-integral equations give good agreement with the experimental results – especially at high radius. This agreement is better than that of the original momentum-integral equations with the same computational data, as shown in Figure 4.25. It shows that given appropriate initial conditions the model can predict the swirl ratio inside the wheelspace well.

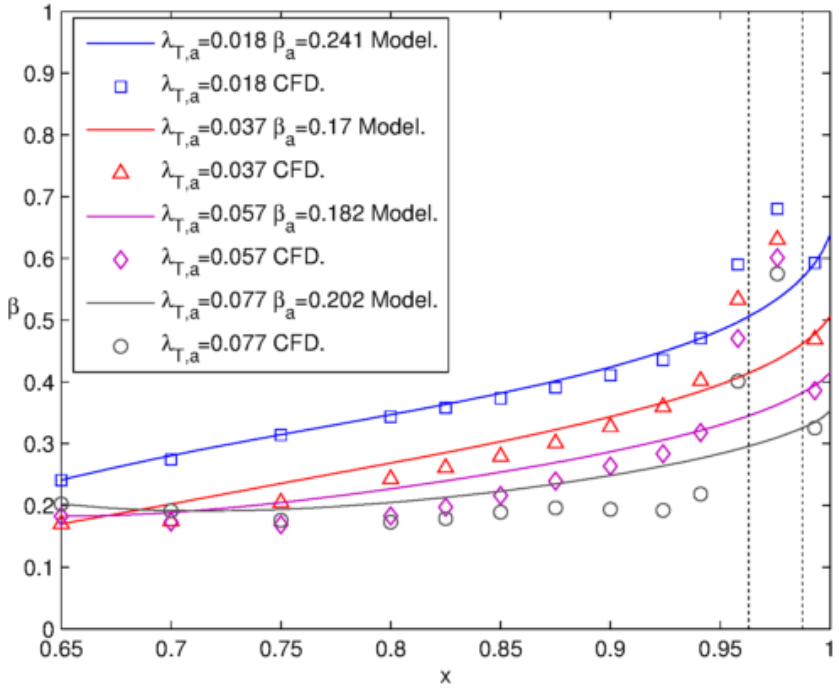

Figure 4.33: Comparison of radial distribution of swirl ratio from SFNI Model with no inner region [solid lines] and No Ingress CFD [symbols] for the radial seal over range of sealing flow rates.

Note that the same CFD model of Lalwani (2014) but *with ingress* had good agreement with the EI ingress experimental measurements. The values of swirl ratio for the ingress case were significantly higher, giving evidence that the swirl ratio is affected by ingress. This is explored further in the next Chapter.

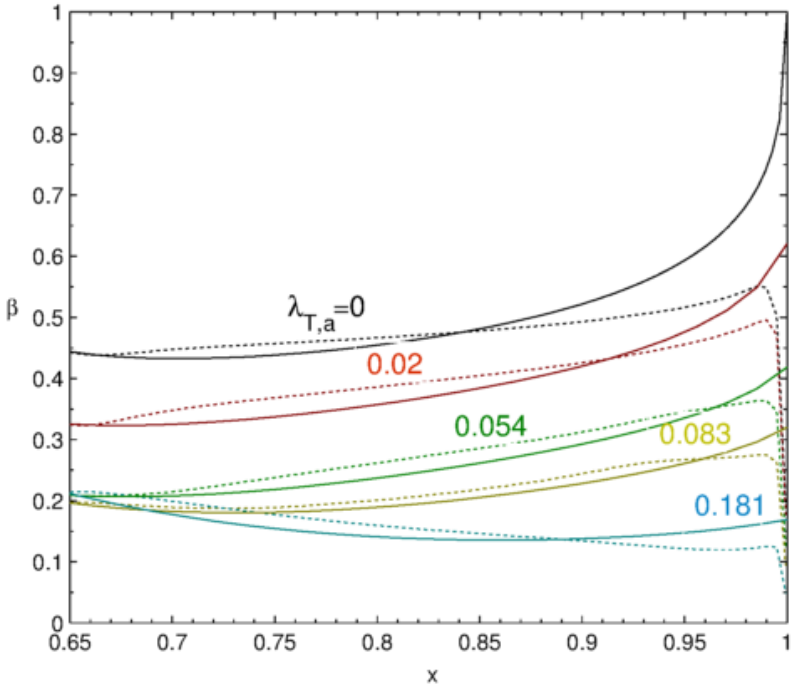

Figure 4.34: Comparison of radial distribution of swirl ratio from SFNI Model with no inner region [solid lines] and No Ingress CFD [dotted lines] for the axial seal over range of sealing flow rates.

Figure 4.34 shows another comparison between the no ingress CFD and the variable SFNI model, this time for an axial seal. The Superposed Flow, No Ingress model uses no inner region model and has matched the initial value of β from the CFD. The

swirl ratio results from the CFD are taken from axial location $z/s = 0.25$ and at $Re_\phi = 8.2 \times 10^5$. There is only a small variation with β axially, so the specific axial location does not impact the comparison. The agreement is fairly good between $0.65 < x < 0.9$, however the results diverge near the exit. This is unsurprising as the CFD has a different condition at $x = 1$ to the theoretical model. The CFD has imposed $\beta_1 = 0$ as an initial condition for the no ingress case.

Returning to the moment coefficients, Figure 4.35 shows the rotor moment coefficient from the no ingress CFD model of Lalwani (2014) and the results from the variable SFNI model based on three different values of inlet swirl. The black dashed line denoted the moment coefficient of a free disc as presented by Lalwani (2014) and the dotted black line presents the free-disc moment coefficient calculated from the momentum-integral equations, as originally shown in Figure 4.26.

At first it may be surprising that the agreement between the two models does not seem very good, especially given the previous two figures have shown the good agreement between the swirl ratios. It is important to note that the true distribution of moment coefficient would be a combination of all three of the fixed β_a curves shown because swirl ratio at x_a is varying with sealing flow rate. This can be seen clearly in Figure 4.34, where β at $x_a = 0.65$ as found from the CFD no ingress model is decreasing with sealing flow (for example $\beta \approx 0.44$ when $\lambda_{T,a} = 0$ and $\beta \approx 0.32$ when $\lambda_{T,a} = 0.02$). This means that to get a true comparison between the CFD model and the SFNI model, then the SFNI model would need to vary β_a with $\lambda_{T,a}$.

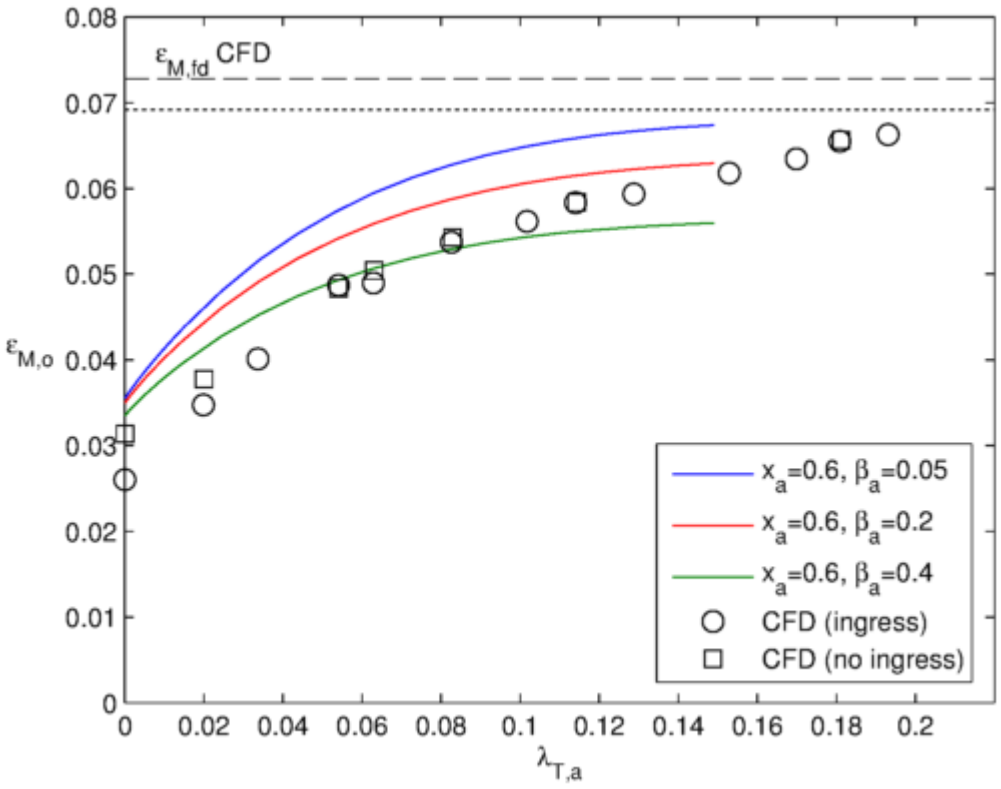

Figure 4.35: Variation of moment coefficient with sealing flow rate from SFNI model with variable momentum-integral equations and CFD no ingress model of Lalwani (2014) for axial seal.

This section has looked at using the variable momentum-integral equations to model a rotor-stator cavity with superposed flow but without ingress. The equations have been derived, including a new differential equation for the swirl ratio, derived

from the continuity equation. A new solution procedure has been outlined, to solve the five coupled ODEs. The results have been compared to those of the model based on the original equations. It was found that the swirl ratio in the outer region decreased, and for fixed inlet swirl models the distribution of swirl ratio was flatter radially which led to better agreement with experimental measurements.

4.6 CONCLUSIONS

This chapter studied the modelling of a rotor-stator cavity subject to superposed flow, but no ingress. A detailed flow structure was hypothesised where the model was separated into two distinct sections: the so called *inner region* (where continuity was not satisfied), and the *core and outer region* (where continuity was satisfied). Modelling the inner region required assuming a distribution for the swirl ratio within that section of the cavity, from which a value of x_{in} could be found (marking the end of the inner region). Three models were proposed: assuming there was no swirl, constant swirl or a free vortex, along with a no inner region approach. The outer and core region could be modelled in a similar way to the Closed Cavity.

Each of the inner region models was able to capture the key behaviour that increasing x_a, β_a or $\lambda_{T,a}$ increases the value of x_{in} (due to a smaller cavity or it taking longer to entrain the flow). It is thought that the free vortex distribution substituted into the variable equations gave the best model, with the value of x_{in} increasing almost linearly for high values of x_a. Even though the inner region models could not be validated as part of this work, it is hoped that this could be done in the future.

An iterative solution procedure was given for both the original and variable momentum-integral equations, where the continuity equation, now including superposed flow, was used to couple the rotor and stator. The swirl ratios and mass flow rates from the models were then presented for range of flow rates. The mass flow rates confirmed the desired flow structure and the swirl ratios showed the expected trend: increasing $\lambda_{T,a}$ decreases β. It was found that the location of the outer region did not vary with sealing flow rate.

The swirl ratios from both the original and variable models were compared to experimental data. As the data were collected in a rig where an inner seal was present, which is thought to locally increase the swirl ratio, the no inner region model was used such that the inlet swirls could be matched directly between the model and the data at $x = 0.65$. Exact agreement would not be expected unless the cases were for $\lambda_{T,a} > \lambda_{T,min}$ as for any flow rate below this the experimental measurements would have been subject to ingress which is not modelled. The results from the model based upon the original momentum-integral equations showed poor agreement with swirl ratio measurements over a range of flow rates for an axial seal subject to RI ingress. For the case over $\lambda_{T,a} = \lambda_{T,min}$ the maximum absolute difference between the model and the 7 data points occurred at the radial location closed to the periphery and was 21%. On average the error between the model and the data was 10%. The agreement with measurements for an axial seal subject to EI ingress was qualitatively good, but gave an under prediction. The results from the model based upon the variable momentum-integral equations show better agreement with the experimental and computational measurements of swirl ratio and moment coefficients. For an axial seal subject to RI ingress the model initially over predicted the swirl ratio at low sealing flow rates, but as $\lambda_{T,a} \rightarrow \lambda_{T,min}$ agreement improved, with very good agreement at

$\lambda_{T,a} = \lambda_{T,min}$. The maximum absolute difference between the model and the data was 11% and the average error across all 7 data points was only 5%. There was also very good agreement between the model based upon the variable equations and the CFD model of Lalwani (2014) that had no ingress present. Given this good agreement it shows this form of modelling has the potential to be just as accurate as CFD only much faster.

Given the improved agreement between the model based upon the variable momentum-integral equations and the experimental and computational measurements compared to the model based upon the original equations, it can be concluded that the differential swirl ratio term is necessary for accurate modelling in the presence of sealing flow.

In conclusion, it is recommended that researchers reconsider the usefulness of the momentum-integral equations and see that they can be a beneficial edition to the modelling of the flows in a rotor-stator system of modern gas turbines. It is also imperative that researchers acknowledge it is essential to include the extra differential term for the swirl ratio within the equations. Regardless of the added complication to the equations, and the extra steps in the iterative solution procedure, the computation time is barely affected by including the extra term and the model is more physically realistic.

CHAPTER 5 : EFFECT OF INGRESS ON EXIT SWIRL

In this chapter the effect of ingress on the swirl ratio at $x = 1$, denoted β_1, is modelled. The experimental measurements of Sangan *et al.* (2014) showed that despite large differences in the amount of ingress to the wheelspace between the axial and radial seal the swirl ratio distributions with radius were very similar. Initially this led the authors to conclude that ingress did *not* affect swirl ratio in the wheelspace. The CFD results of Lalwani (2014) found that there was a difference between the swirl ratios found by the CFD model with and without ingress. Furthermore the results of the SFNI model based upon the variable momentum-integral equations gained better agreement with the experimental measurements of swirl ratio as $\lambda_{T,a} \rightarrow \lambda_{T,min}$ which is equivalent to decreasing the amount of ingress. This leads to the conclusion that ingress does affect the swirl ratio in the wheelspace. This is also evidenced by Gentilhomme *et al.* (2003) who took pressure and concentration measurements in a single stage rotor-stator system and found that highly swirling ingress increased the swirl ratio in the wheelspace. Hills *et al.* (2002) investigated the flow interactions within the rim seal. The flow in a typical rotor-stator wheelspace with ingress and egress was modelled using CFD and compared to experimental data. It was found once again that the swirl ratio was important in affecting the amount of ingress. This Chapter looks at using the cavity model without ingress to predict what would happen with ingress, specifically near the exit of the wheelspace.

A rotor-stator cavity with ingress can be considered into two separate cases: with and without superposed flow. The full details of the case 'Ingress with Superposed Flow' are considered in Chapter 6, so there will be no description of the flow structure in this chapter. In Section 5.1 of this Chapter the flow structure for a cavity with 'Ingress, No Superposed Flow' (InSF) is developed. In Section 5.2 a momentum balance model is derived to model how flows interact across the seal clearance, this leads to a way to use the cavity model without ingress to predict what would happen with ingress. In Section 5.3 the new model is validated against experimental measurements and finally conclusions are given in Section 5.4.

5.1 ROTOR-STATOR FLOW STRUCTURE WITH INGRESS

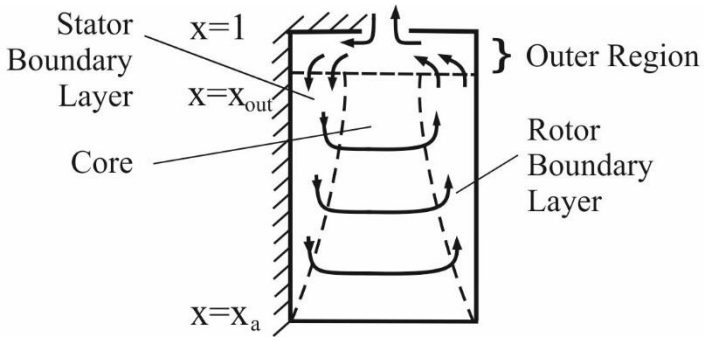

Figure 5.1: Simplified flow structure of Ingress, No Superposed Flow Cavity Model

Figure 5.1 shows the simplified flow structure of a cavity with ingress to the system, but no sealing flow. The flow structure bares similarities to that of the Closed Cavity, in that for both cases there is no net flow into the system. The main difference is in the outer layer, where now there is ingress and egress to and from the system respectively. Conservation of angular momentum will determine the resultant swirl in

the outer region. As the outer region is the source of the boundary layer on the stator, the flow in the boundary layers on the rotor and stator will, in general, be different from that for the Closed Cavity or a cavity that is fully sealed. The differences are likely to be greater in the outer region than in the rest of the wheel-space.

There is ingress into the system with some flow rate, which will be defined as

$$\lambda_{T,i} = \Phi_i 2\pi G_c Re_\phi^{1/5} \tag{5.1}$$

where Φ_i is the *non-dimensional flow rate of the ingress* and G_c is the gap ratio. The already successful orifice model, discussed in the literature review, can be used to find Φ_i based upon the amount of superposed flow rate supplied for a specific seal. Written $\Phi_{i,EI}$ and $\Phi_{i,RI}$ for the cases of EI and RI ingress respectively the equations are given by Sangan *et al.* (2013a) and Sangan *et al.* (2013b):

$$\Phi_{i,EI} = \Phi_{min,EI} \frac{1-\varepsilon}{\left[1+\Gamma_c^{-2/3}(1-\varepsilon)^{2/3}\right]^{3/2}} \tag{5.2}$$

$$\Phi_{i,RI} = \Phi_{min,RI} \frac{1-\varepsilon}{[1+(1-\varepsilon)^{1/2}][1+\Gamma_c^{-2}(1-\varepsilon)]^{1/2}} \tag{5.3}$$

These equations use the same values of the empirical constants $\Phi_{min,EI}$ (or $\Phi_{min,RI}$) and Γ_c as found when fitting with the effectiveness equations.

If a cavity model is to be developed for the case with ingress then there needs to be a way of modelling how the amount of ingress affects the swirl ratio. It is known that there is a sharp drop in swirl ratio across the rim seal, and it is thought that the actual decrease will depend upon the amount of ingress entering the cavity. Given that the only input into the cavity is now the ingress at $x = 1$ it makes sense that the amount of ingress would influence the value of β_1 and that this could act as an initial condition instead of β_a.

5.2 MOMENTUM BALANCE CORRECTION THEORY

It is known that the swirl ratio in the annulus is typically greater than or equal to 2, but within the wheelspace the swirl ratio is never above 1. This means that there is a large decrease in swirl ratio across the seal clearance. Taking a simple view of the interactions within the seal clearance there are two inputs (the ingress from the annulus and the egress outflow flow from the rotor) and two outputs (the ingress flowing onto the stator and the egress leaving the seal clearance), as shown in Figure 5.2. The concentration measurements on the stator are constant even at high radial locations within the wheelspace. This suggests that, regardless of geometry, a large amount of the mixing happens *within* the clearance itself, not in the outer region as was originally hypothesised by Sangan *et al.* (2013a). This is why the flow is divided into two streams exiting and entering the seal clearance from the wheelspace (rather than simply having one stream from a mixing region).

It can be assumed that there would be a momentum balance within the seal clearance. The individual flows in and out of the seal clearance are shown in Figure 5.2. The flow entering the seal clearance (ingress) has β_i and $\lambda_{T,i}$ as the swirl ratio and mass flow rate parameters respectively and the flow leaving the wheelspace (egress) has β_e and $\lambda_{T,e}$ as the swirl ratio and mass flow rate parameters respectively. Therefore, if $\beta_i > \beta_e$, the decrease of momentum from the ingress must equal the increase of momentum to the egress; and vice versa if $\beta_i < \beta_e$. After the mixing in the seal clearance it is assumed that the 'mixed-out' swirl ratio is β_1'.

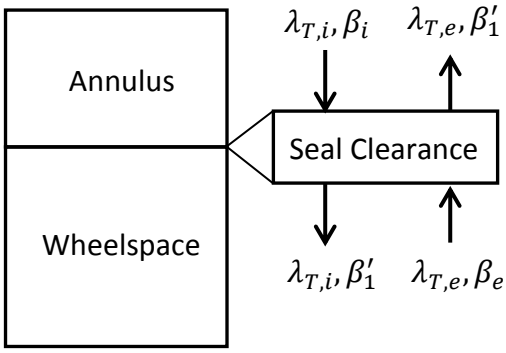

Figure 5.2: Simplified model of the seal clearance between the annulus and wheelspace. (Ingress with flow rate $\lambda_{T,i}$ and swirl ratio β_i, egress with flow rate $\lambda_{T,e}$ and swirl ratio β_e and β_1' a swirl ratio modified by momentum exchange in the seal clearance).

Derivation of momentum-balance correction

Neglecting shear stresses from the surfaces of the seal, angular momentum of the two fluid streams must be conserved. The simplified conservation of angular momentum can be written as the momentum of the inflows is equal to that of the outflows:

$$\lambda_{T,i}\beta_i + \lambda_{T,e}\beta_e = \lambda_{T,e}\beta_1' + \lambda_{T,i}\beta_1' \tag{5.4}$$

Rearranging to make β_1' the subject gives

$$\beta_1' = \frac{\lambda_{T,e}\beta_1 + \lambda_{T,i}\beta_i}{\lambda_{T,e} + \lambda_{T,i}} \tag{5.5}$$

Now given that mass is conserved in the wheelspace, the following holds:

$$\lambda_{T,e} = \lambda_{T,a} + \lambda_{T,i} \tag{5.6}$$

This can be used to remove the need for a direct value of $\lambda_{T,e}$. Substituting the continuity equation (5.6) into (5.5) gives

$$\beta_1' = \frac{\lambda_{T,a}\beta_e + \lambda_{T,i}(\beta_e + \beta_i)}{\lambda_{T,a} + 2\lambda_{T,i}} \tag{5.7}$$

To be able to use this equation to 'correct' the solutions from the cavity models it is assumed that $\beta_e = \beta_1$. Recall that β_1 is the value of swirl when there is *no ingress*, so it is found by the Superposed Flow, No Ingress model. Substituting $\beta_e = \beta_1$ into (5.7) gives

$$\beta_1' = \frac{\lambda_{T,a}\beta_1 + \lambda_{T,i}(\beta_1 + \beta_i)}{\lambda_{T,a} + 2\lambda_{T,i}} \tag{5.8}$$

This is a useful model that allows the swirl ratio at the exit of the wheelspace when there *is ingress*, β_1', to be found when the swirl ratio *without ingress* is known (from previous cavity models).

Momentum Balance Correction for Different Cavities

Even though the equation (5.8) has been derived for a cavity with ingress and superposed flow, and is needed for cavities with ingress, it should still be valid for the cavities with no ingress. For a cavity with no ingress ($\lambda_{T,i} = 0$) then (5.8) gives

$$\beta_1' = \beta_1 \tag{5.9}$$

so as expected there is *no correction* to the swirl.

For a cavity with ingress and no superposed flow ($\lambda_{T,a} = 0$) equation (5.8) reduces to

$$\beta_1' = \frac{\beta_1 + \beta_i}{2} \tag{5.10}$$

In order to make use of this, values of β_i need to be set. For RI, as there is no swirl in the annulus it is thought that $\beta_i = 0$, which can be written $\beta_{i,RI} = 0$; this leads to

$$\beta_1' = \frac{\beta_1}{2} \tag{5.11}$$

For EI it is thought that $\beta_i = 1$, which can be written $\beta_{i,EI} = 1$; this leads to

$$\beta_1' = \frac{\beta_1 + 1}{2} \tag{5.12}$$

Both of these values for β_i will be tested later in this chapter. In order to use equation (5.8) values of $\lambda_{T,i}$ must be known. The following section outlines how $\lambda_{T,i}$ can be found for different rim seal geometries using the theory from the orifice model.

5.2.1 USING MOMENTUM BALANCE CORRECTION

In order to use equation (5.8) values for $\lambda_{T,i}$ and β_i must be supplied. First finding values for $\lambda_{T,i}$ is considered, then the values of β_i will be assessed. A value for the ingress flow rate, $\lambda_{T,i}$, could be approximated; however for a given seal geometry, the already successful orifice model (discussed in the literature review) can be used to find this ingress flow rate.

Relation between $\lambda_{T,a}$ and $\lambda_{T,i}$

The specific flow rate of ingress into the wheelspace will change depending on the rim seal design used to protect the wheelspace and how much sealing air is supplied. As discussed in the literature review, the effectiveness equations (5.2) and (5.3) use the variables Γ_c and Φ_{min} to quantify how specific rim seals will perform over a range of sealing flow rates. For any seal geometry where Γ_c and Φ_{min} are known from fitting experimental measurements of stator effectiveness, the flow rate for the ingress can then be calculated by (5.1). This allows a relation $\lambda_{T,a} = f(\lambda_{T,i})$ to be found for a specific seal. Values of $\lambda_{T,i}$ and $\lambda_{T,a}$ could then be used to calculate β_1'. The specific procedure, with all equations, is given below:

$$\lambda_{T,a} \underbrace{\longrightarrow}_{(1)} \Phi_a \underbrace{\longrightarrow}_{(2)} \varepsilon \underbrace{\longrightarrow}_{(3)} \Phi_i \underbrace{\longrightarrow}_{(4)} \lambda_{T,i}$$

(1) Firstly from a fixed value of superposed flow rate, $\lambda_{T,a}$, along with specific conditions for the experiments (gap ratio, G_c, and rotational Reynolds number, Re_ϕ) calculate Φ_a, the *sealing flow rate parameter:*

$$\Phi_a = \frac{\lambda_{T,a}}{2\pi G_c Re_\phi^{0.2}} \tag{5.13}$$

(2) Secondly, after substituting the values of Φ_{min} and Γ_c gained from the fitting of experimental measurements of effectiveness over a range of sealing flow rates, solve the *EI effectiveness equation*

$$\Phi_a = \frac{\varepsilon}{\left[1 + \Gamma_c^{-\frac{2}{3}}(1-\varepsilon)^{\frac{2}{3}}\right]^{\frac{3}{2}}} \Phi_{min,EI} \tag{5.14}$$

or *RI effectiveness equation*

$$\Phi_a = \frac{\varepsilon}{\left[1+(1-\varepsilon)^{\frac{1}{2}}\right]\left[1+\Gamma_c^{-2}(1-\varepsilon)\right]^{\frac{1}{2}}}\Phi_{min,RI} \tag{5.15}$$

to find the corresponding ε value.

(3) Next, substitute the effectiveness, ε, calculated above and Γ_c into equation (5.2) to calculate a value for $\Phi_{\mathrm{i,EI}}$, or (5.3) to calculate a value for $\Phi_{\mathrm{i,RI}}$.

(4) Finally convert the ingress flow rate parameter back to $\lambda_{T,i}$ form using equation (5.1).

Note that in the equations above the sealing parameter Φ_a is typically called Φ_o in other published literature but this has been changed to remain in line with the subscript a being used for $\lambda_{T,a}$ throughout this work. Following this procedure leads to two separate curves for $\lambda_{T,a} = f(\lambda_{T,i})$, one each for EI ingress and RI ingress. As Φ_{min}, G_c and Γ_c all depend upon the seal design the curves will be different depending on these.

Taking the values of Φ_{min} and Γ_c as found by Sangan *et al.* (2013a), the variation of $\lambda_{T,i}$ with $\lambda_{T,a}$ is shown in Figure 5.3 for a single axial seal for three Re_ϕ conditions and with $G_c = 0.0105$. The flow rates for the RI ingress conditions are far lower than those for the EI conditions.

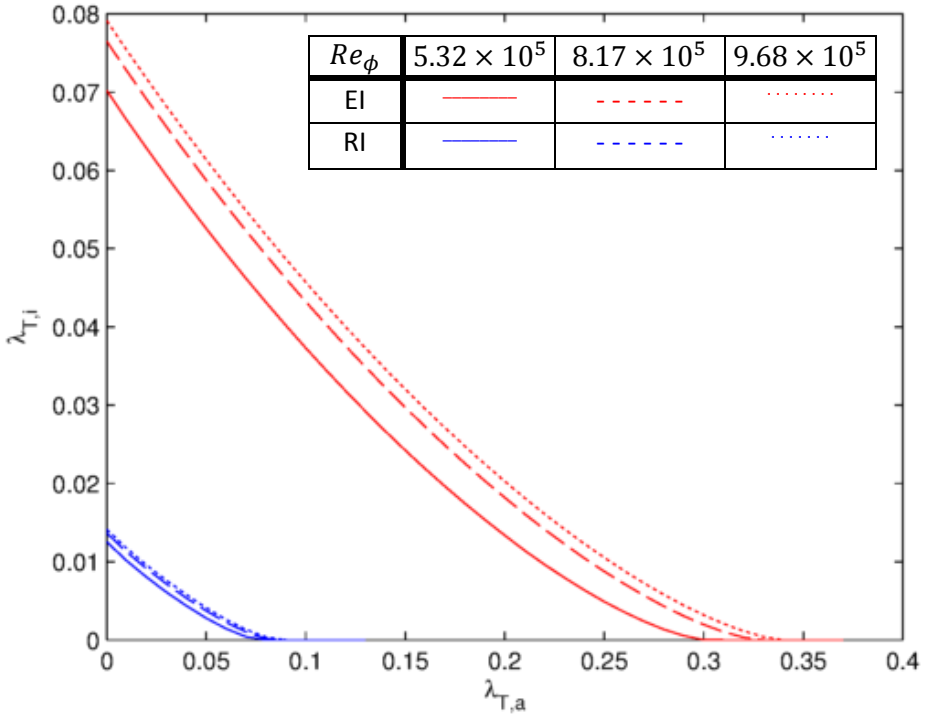

Figure 5.3: Theoretical variation of ingress mass flow rate with superposed mass flow rate for an axial seal (for EI: $\Gamma_c = 0.476, \Phi_{min,EI} = 0.326$ and for RI: $\Gamma_c = 0.342, \Phi_{min,RI} = 0.0838$)

If the variables Φ_i and Φ_a are used instead of $\lambda_{T,i}$ and $\lambda_{T,a}$ then the figure will contain a single curve, as the Φ parameters are non-dimensional with Reynolds number. Figure 5.4 below shows the theoretical variation of ingress flow parameter with superposed flow rate parameter for the radial seal. All three curves for the Re_ϕ values have collapsed onto a single line.

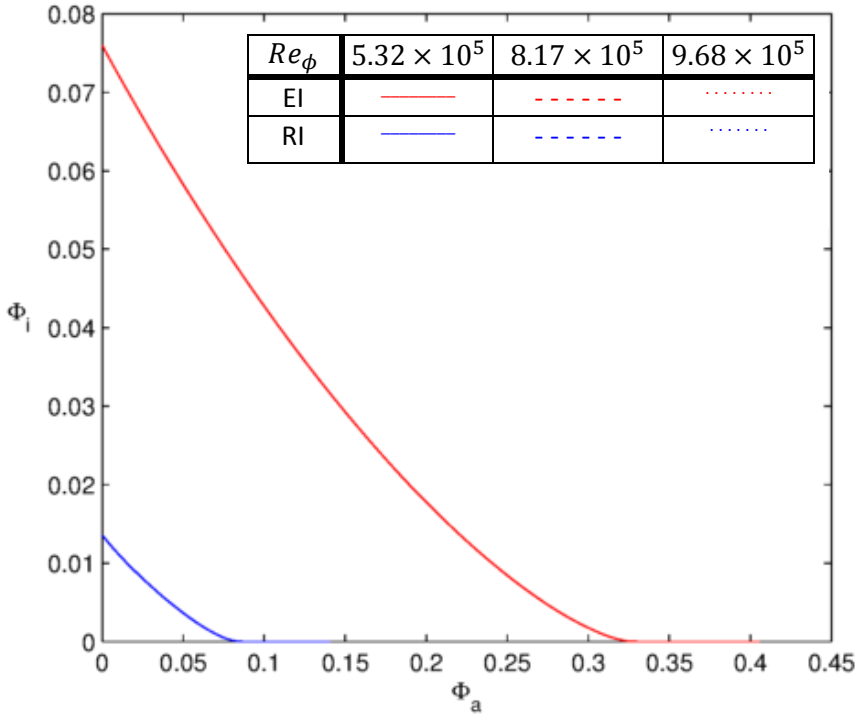

Figure 5.4: Theoretical variation of ingress mass flow rate with superposed mass flow rate for an axial seal (for EI: $\Gamma_c = 0.476, \Phi_{min,EI} = 0.326$ and for RI: $\Gamma_c = 0.342, \Phi_{min,RI} = 0.0838$)

Note that for the case of $Re_\phi = 8.17 \times 10^5$ it so happens that the coefficient relating λ_T and Φ is $2\pi G_c Re_\phi^{1/5} = 1.0042$. So for $Re_\phi = 8.17 \times 10^5$ (which corresponds to 3000rpm) it can be assumed that $\lambda_{T,a} \equiv \Phi_a$ and $\lambda_{T,i} \equiv \Phi_i$. For the rest of this section all figures are for this Reynolds number and assumption.

Application of the Momentum Correction Model

Now that for any superposed flow rate, the corresponding ingress flow rate can be calculated from the theory of the effectiveness equations, as outline above, the swirl correction can be used. Recall the momentum correction equation:

$$\beta_1' = \frac{\lambda_{T,a}\beta_1 + \lambda_{T,i}(\beta_1 + \beta_i)}{\lambda_{T,a} + 2\lambda_{T,i}} \tag{5.16}$$

Once $\lambda_{T,a}$ has been set and a corresponding $\lambda_{T,i}$ found, that leaves only β_1 (the swirl ratio when no ingress is present) and β_i (the swirl ratio of the ingress flow) before a value of the swirl ratio at the exit of the wheelspace when ingress is present, β_1', can be found. A value for β_i can be set as it should be invariant with sealing flow. That leaves only β_1 to be found, which does vary with $\lambda_{T,a}$.

Relation between $\lambda_{T,a}$ and β_1

The value of the swirl ratio when no ingress is present, β_1, can be found from the cavity model presented in Chapter 4, by using the Superposed Flow, No Ingress cavity mode. Radial distributions of swirl ratio in the wheelspace were found for any $\lambda_{T,a}$ and values for β_1 as a function of $\lambda_{T,a}$ are gained simply by taking the value of swirl ratio at $x = 1$. By using the values of the swirl ratio found over a wide range of different superposed flow rates a continuous function of β_1 against $\lambda_{T,a}$ can be found.

Figure 5.5 shows the variation of exit swirl ratio with no ingress (β_1) with

superposed flow ($\lambda_{T,a}$) from the results for the SFNI Model based upon the variable and original momentum-integral equations with no inner region, denoted by the dotted and solid lines respectively. Both are solved for the conditions $x_a = 0.6$ and $\beta_a = 0.3$. As expected both show β_1 decreases with decreasing sealing flow rate, with the original momentum-integral equations model predicting higher values of exit swirl than the variable equations.

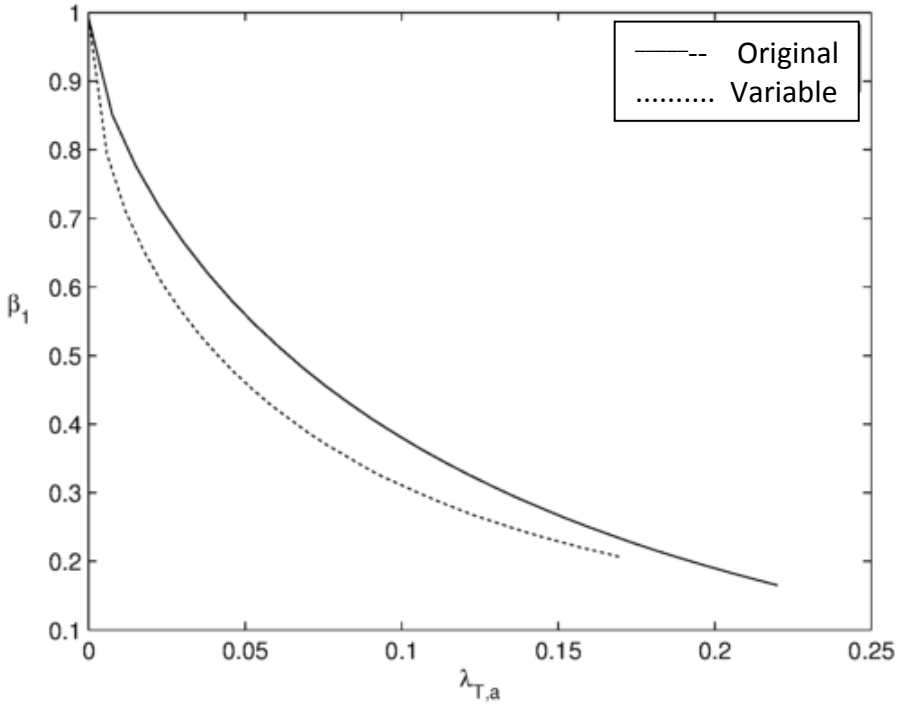

Figure 5.5: Variation of swirl ratio at $x = 1$ with sealing flow rate. From SFNI model with no inner region based upon original [solid line] and variable [dotted line] momentum-integral eqns, $x_a = 0.6$ and $\beta_a = 0.3$.

Notice that the original momentum-integral equation model can be solved up to around $\lambda_{T,a} = 0.22$ but the variable momentum-integral equations can only be solved up to around $\lambda_{T,a} = 0.16$. This is because as the sealing flow rates increase the likelihood of encountering a negative value of swirl ratio at some radial location increases. The cavity models currently cannot cope with negative swirl ratio values, meaning the equations will not solve with negative swirl ratios present. The relations in Figure 5.5 can be used with the $\lambda_{T,a}$ and $\lambda_{T,i}$ relation above within the momentum correction.

5.3 RESULTS

Now it is known how to relate $\lambda_{T,a}$ to both β_1 and $\lambda_{T,i}$, which allows the momentum correction (5.8) to be used in its entirety. The correction will now be used with the theoretical variations of $\lambda_{T,i}$ for a single axial seal found from constants $\Gamma_c = 0.476, \Phi_{min,EI} = 0.326$ for EI ingress and $\Gamma_c = 0.342, \Phi_{min,RI} = 0.0838$ for RI ingress, as presented by Sangan *et al.* (2013a) and Sangan *et al.* (2013b) respectively. Substituting in $\lambda_{T,i}$ for the axial seal for EI and RI ingress and the values of β_1 from the Superposed Flow, No Ingress cavity model based upon the original and variable momentum-integral equations into momentum correction (5.8) gives two new predictions for how the exit swirl will vary if there was EI or RI ingress into the cavity, say $\beta'_{1,EI}$ and $\beta'_{1,RI}$ respectively.

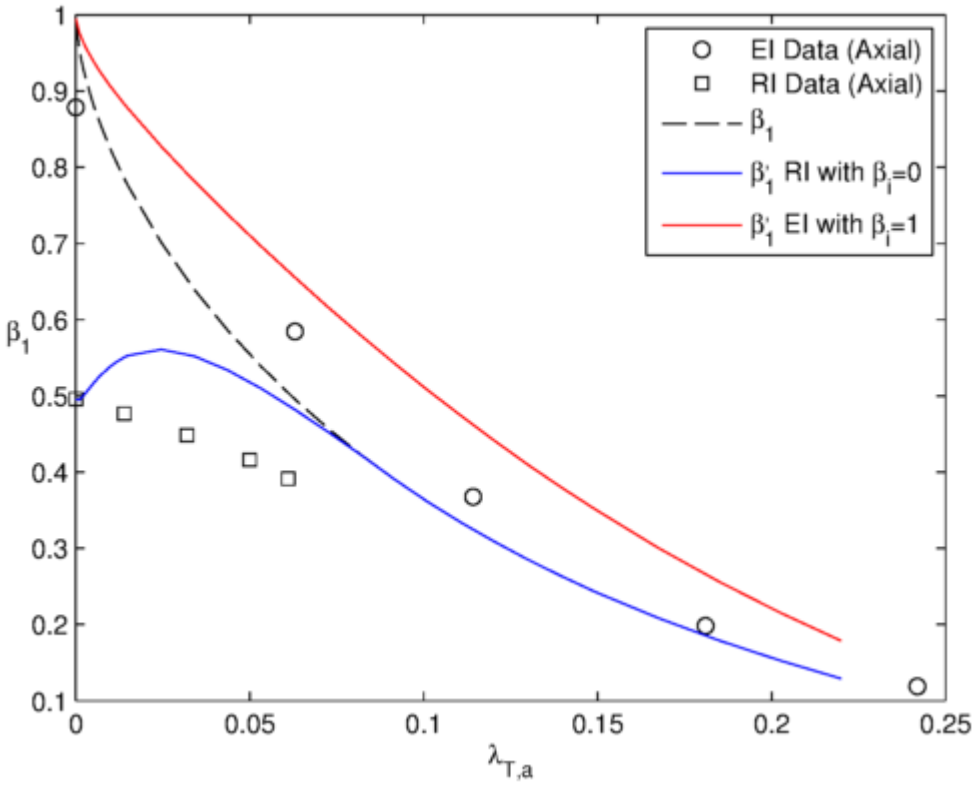

(a) Original Momentum-Integral Equations

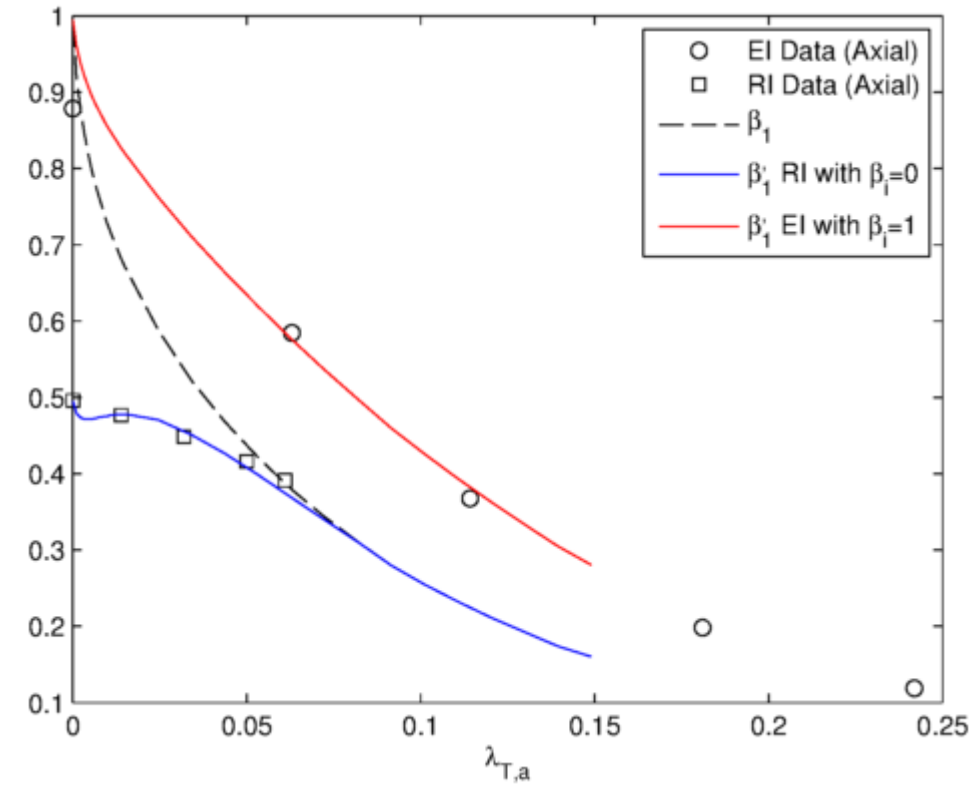

(b) Variable Momentum-Integral Equations

Figure 5.6: Use and validation of the momentum correction applied to a single axial seal

These predictions for the axial seal are shown above in Figure 5.6 (a) and (b) where for the cavity model there was no inner region model, $\alpha_s = 0.001$, $\gamma_s = 0.03$, $x_a = 0.6$ and $\beta_a = 0.05$. The black dashed line denotes the values of exit swirl ratio

with *no ingress* and the red and blue lines denote the corrected exit swirl *with EI ingress* (with $\beta_i = 1$) and *with RI ingress* (with $\beta_i = 0$) respectively. The basic behaviour is as expected, with the EI ingress increasing the swirl ratio and the RI ingress decreasing the swirl ratio, reflecting the trends seen experimentally.

Usefully for the same conditions where effectiveness measurements were taken (which gave rise to constants Φ_{min} and Γ_c) swirl ratio measurements in the wheelspace are available for a smaller range of flow rates at $x = 0.993$. Even though the measurements are not taken at exactly $x = 1$, it is thought that the swirl at $x = 0.993$ is representative enough for these comparisons. If anything they will likely be a slight under-prediction as swirl ratio is seen experimentally to typically increase near the seal clearance (as Fig. (4.23)). These experimental measurements are not used in the model so can act as validation for the momentum balance correction. It can be seen that there is very good agreement between the predictions and the experimental results for both the EI and the RI cases with the β_i values chosen. All the swirl ratio measurements were taken on the Bath rig with the data shown in Figure 5.6 (a) and (b) for the single axial EI ingress case originally presented in Sangan *et al.* (2014) and the RI ingress case being taken by the same authors but unpublished.

Notice that for the RI correction there is a small change in gradient as $\lambda_{T,a} \to 0$. The spread of the experimental data makes it impossible to know if the trend is representative of the real situation or is a quirk of the model. It will be seen in the next section that this shape is caused by the value of β_i. For this first look at the momentum correction, it was assumed that $\beta_{i,EI} = 1$ and $\beta_{i,RI} = 0$. Even though these produced very good agreement with the variable equations it will be useful to see how much β_i changing can affect the model. The next section will look at such an effect.

5.3.1 EFFECT OF β_i

In the momentum balance equation a value for β_i had to be supplied. The values $\beta_{i,RI} = 0$ for RI Ingress and $\beta_{i,EI} = 1$ for EI ingress were suggested above and used in Figure 5.6. The correction with those β_i values showed very good agreement for the axial seal. Figure 5.7 (a) and (b) for $\beta'_{1,EI}$ and $\beta'_{1,RI}$ respectively show how the correction would behave with different β_i values, namely $0, 0.25, 0.5, 0.75$ and 1. These confirm that the best agreement is in fact with values $\beta_{i,RI} = 0$ and $\beta_{i,EI} = 1$.

Both Figure 5.7(a) and (b) show the variation of no ingress values of exit swirl β_1 with sealing flow rate [dashed line] which is the same as for Figure 5.6: from the SFNI cavity model there was no inner region model, $\alpha_s = 0.001$, $\gamma_s = 0.03$, $x_a = 0.6$ and $\beta_a = 0.05$. Figure 5.7(a) shows the momentum correction for EI ingress for a range of different β_i values, along with swirl ratio data from an axial seal subject to EI ingress taken by Sangan *et al.* (2014). Figure 5.7(b) shows the momentum correction for RI ingress for a range of different β_i values, once again also with swirl ratio data from an axial seal for RI ingress.

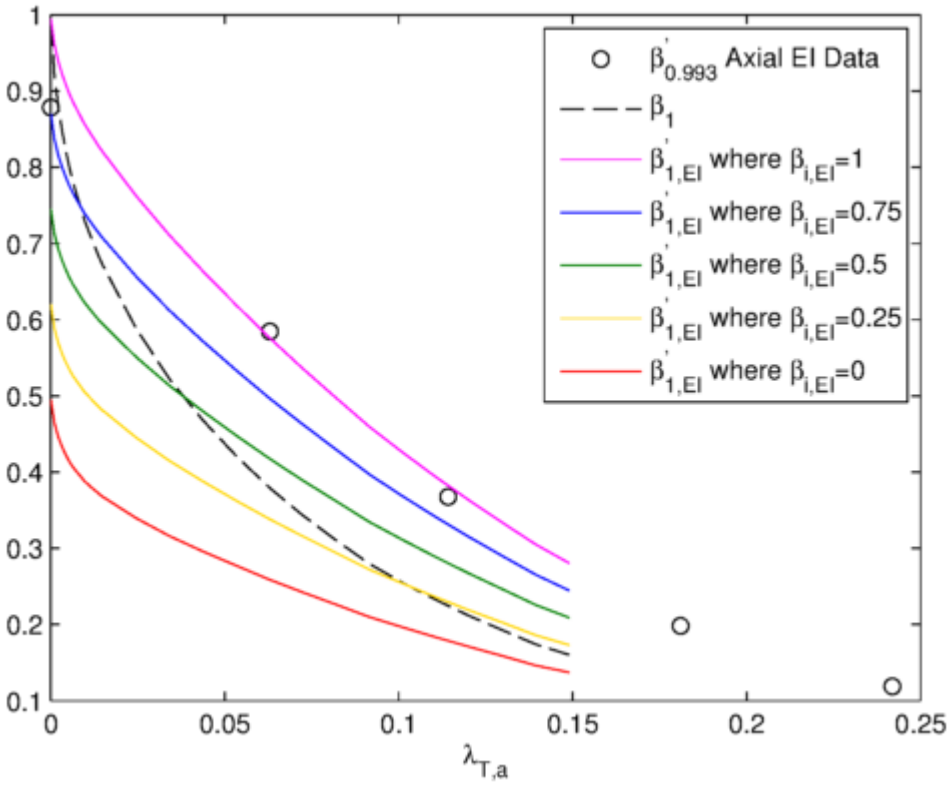

(a) EI Ingress Swirl Ratio Corrections

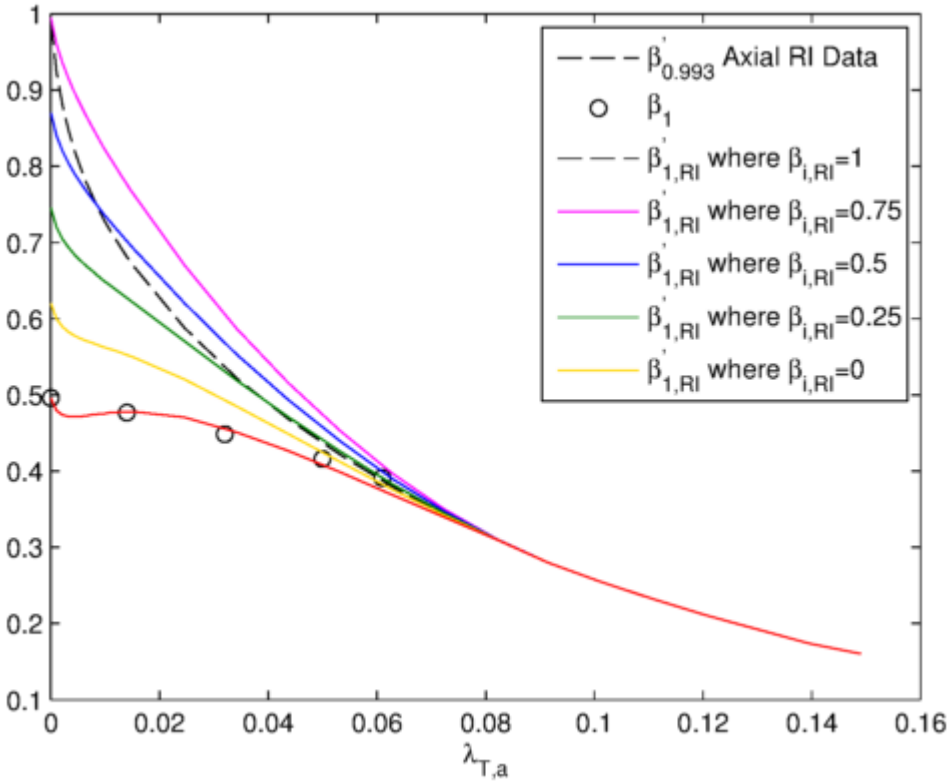

(b) RI Ingress Swirl Ratio Corrections

Figure 5.7: Momentum correction applied to a single axial seal

As β_1 is used in the momentum balance equation to find β_1', the value for β_1' will actually depend upon x_a and β_a because β_1 depends upon x_a and β_a as shown in the results from the Superposed Flow, No Ingress model. The next sections will assess

the effect of changing inlet swirl (β_a) and cavity size (x_a) on the momentum correction.

5.3.2 EFFECT OF INLET SWIRL

Figure 5.8 shows the effect of inlet swirl on the momentum correction for three different inlet swirl values: $\beta_a = 0.05, 0.2, 0.4$. This is where the Superposed Flow, No Ingress cavity model has been solved with the variable momentum-integral equations to provide values of β_1 with $x_a = 0.6$.

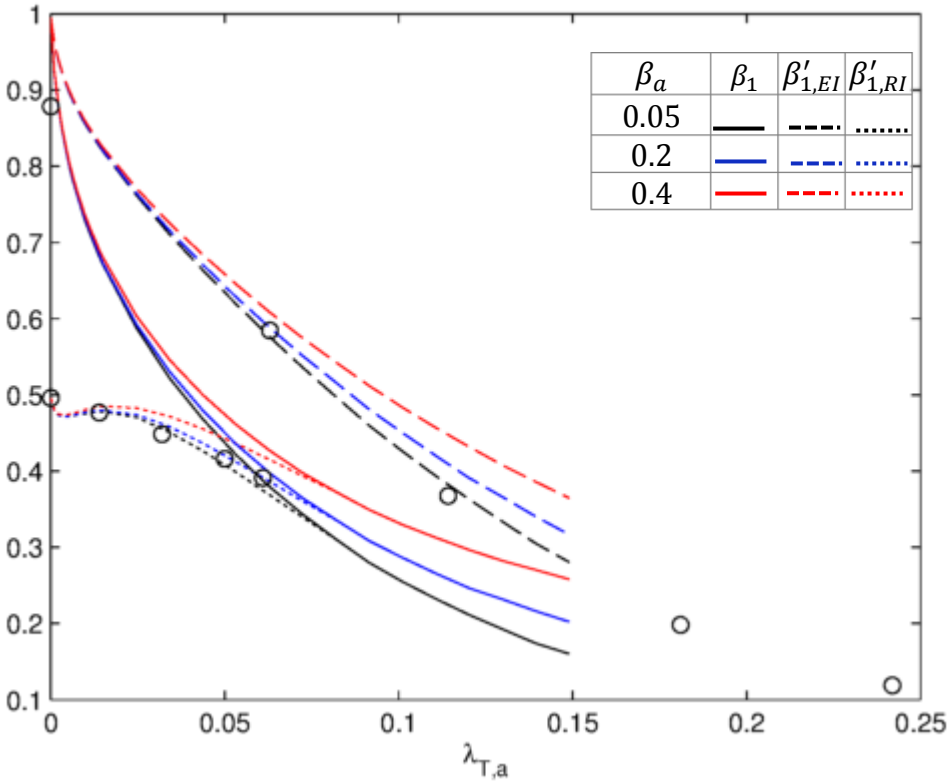

Figure 5.8: Effect of inlet swirl ratio on variation of exit swirl ratio with sealing flow rate (axial seal). (β_1 denotes swirl ratio at $x = 1$ without ingress. $\beta'_{1,EI}$ and $\beta'_{1,RI}$ denote swirl ratio at $x = 1$ with system affected by EI and RI ingress respectively).

The higher the inlet swirl ratio β_a for the no ingress model [dashed lines] the higher the values of β_1. This effect increases with increasing sealing flow rate: the more sealing flow supplied the greater the impact of the inlet swirl on exit swirl. The increase in β_1 with β_a causes the ingress corrections to increase, and this in turn causes worse agreement between predicted and measured values of exit swirl ratio for the axial seal [symbols].

5.3.3 EFFECT OF CAVITY SIZE

For the Closed System cavity size, i.e. the x_a value, did not influence the swirl ratio at high radial locations. This is not true for the cavities with superposed flow model as changing x_a will affect the inner region location x_{in}, which will in turn affect where the core can manifest. As sealing flow rate increases it is therefore expected that the value of β_1 will decrease if the cavity size decreases (i.e x_a increases). This is demonstrated by the results in Figure 5.9, where swirl ratio from the original Superposed Flow, No Ingress model (assuming zero inlet swirl in the inner region) are

shown for four x_a values and three sealing flow rates. These are from the model based on the constant equations for simplicity.

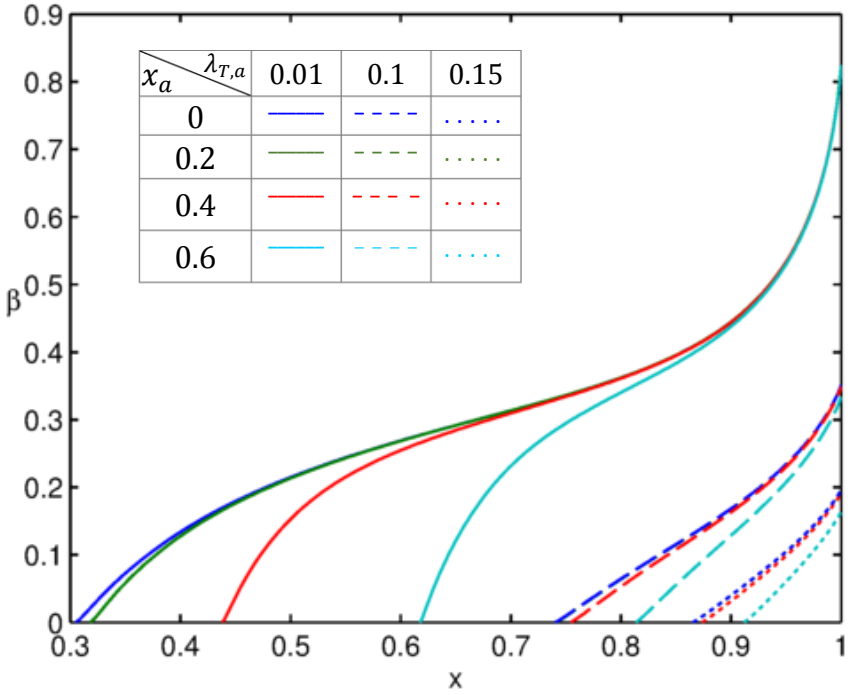

Figure 5.9: Radial variation of swirl ratio from original SFNI model with no inner region for four cavity sizes (unique colours) and three superposed flow rates (unique line styles).

Notice that as $\lambda_{T,a}$ increases, the difference between the swirl ratio values at $x = 1$, β_1, gets larger. For the lowest flow rate, $\lambda_{T,a} = 0.01$ [solid lines], the value of β_1 does not change with cavity size. This explains why there is little variation in the corresponding β_1 curves shown in Figure 5.10 for very low flow rates. Interestingly for all flow rates the results where $x_a = 0$ [blue] and $x_a = 0.2$ [green] are very similar and in fact collapse for the cases of $\lambda_{T,a} = 0.1$ and 0.15 (hence no green can be seen).

Figure 5.10 shows the corresponding effect of cavity size on the β_1 theory. Similar to the trend for varying inlet swirl, the effect is only noticeable at high flow rates and high x_a values. Given that a high sealing flow rate may be supplied to prevent ingress it is important to acknowledge this effect. The momentum correction predictions are influenced at high flow rates by both x_a and β_a: increasing x_a decreases β_1' and increasing β_a increases β_1'. This means that the two effects are likely to counter each other.

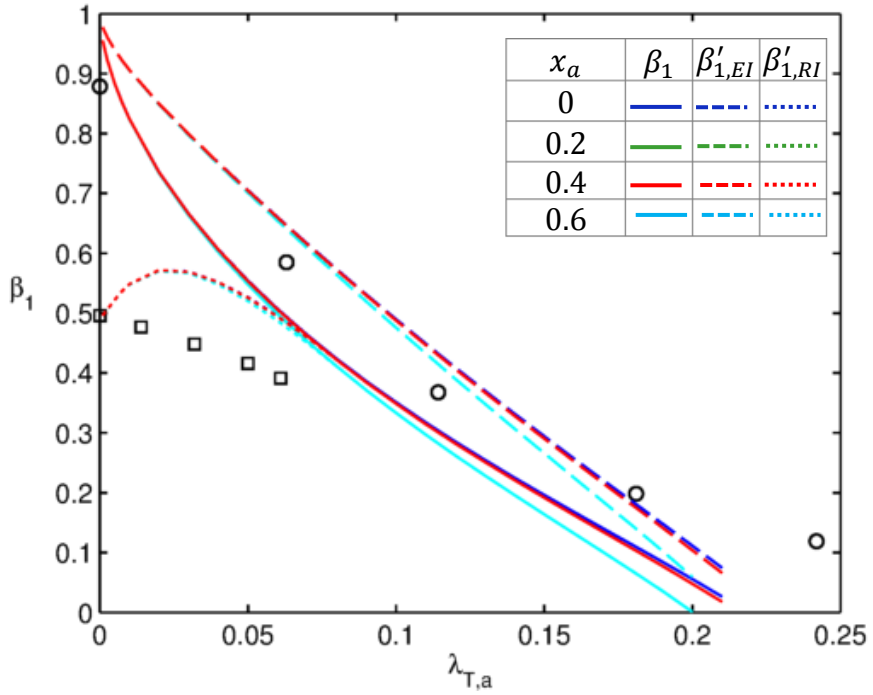

Figure 5.10: Momentum correction based upon original SFNI model solved for four cavity sizes applied to a single axial seal ($x_a = 0, 0.2, 0.4$, and 0.6).

5.3.4 OTHER SEALS

The momentum correction can be used on any seal where Φ_{min} and Γ_c are known, so the variation of $\lambda_{T,i}$ with $\lambda_{T,a}$ can be found. In the results so far the momentum balance correction has only been calculated for a single axial seal. Other seals have been fitted using the effectiveness equations, where the swirl ratios near $x = 1$ is also known, which can be used to validate the correction. The following figures explore the behaviour for the correction applied to the double-axial, radial and double-radial seals, as shown in Figure 5.11.

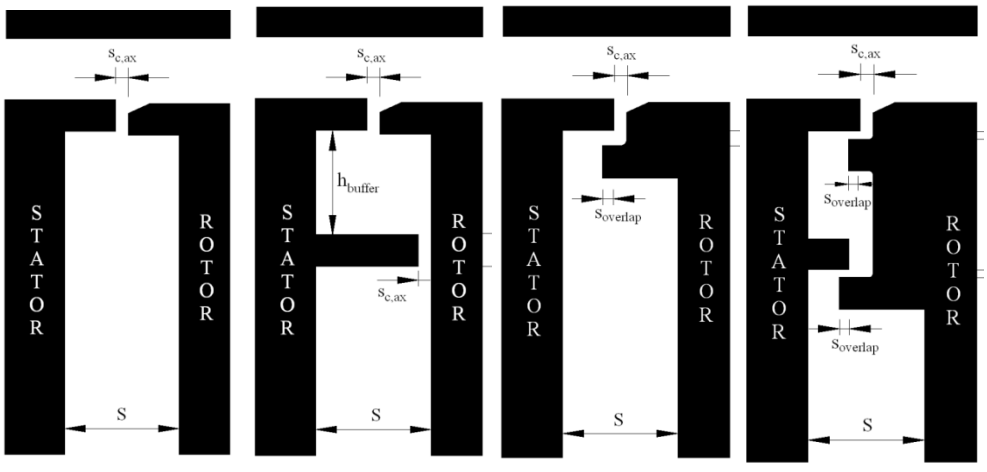

Figure 5.11: Seal geometries axial, double axial, radial and double radial (l-to-r). Sangan *et al.* (2013c).

The swirl ratio measurements for all the new seals, shown in Figure 5.12, were also taken by on the Bath rig, some of which can be seen in Sangan *et al.* (2014), the

rest of which are unpublished. The corresponding Φ_{min} and Γ_c values for each seal are shown in Table 5.1.

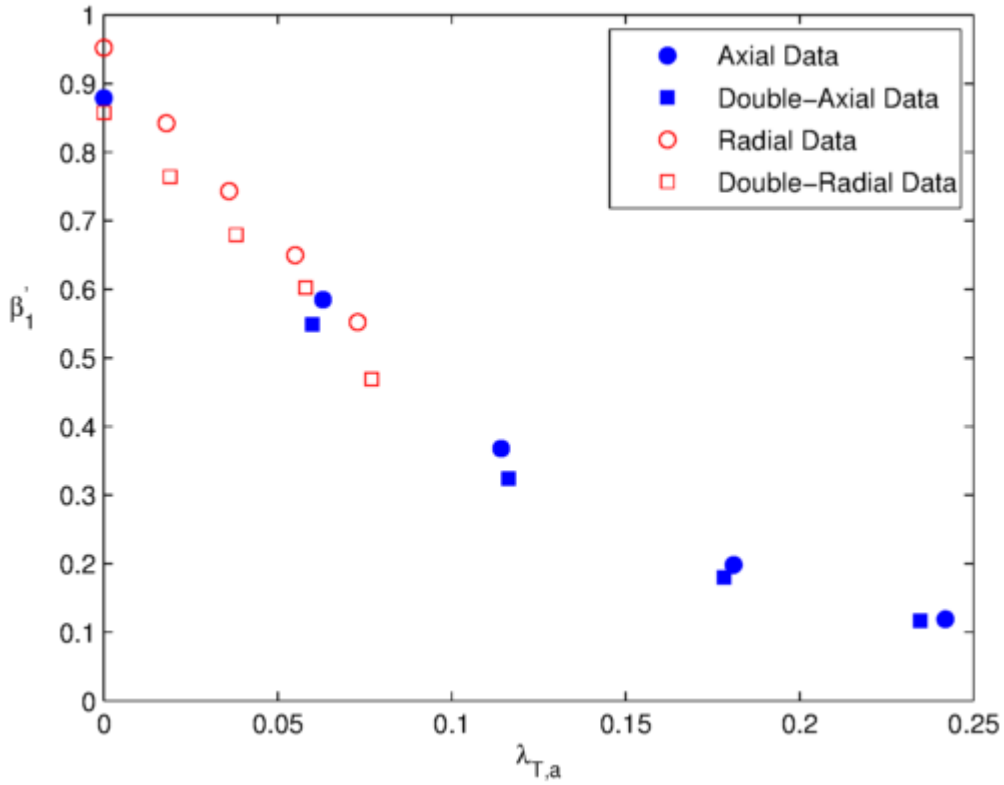

Figure 5.12: Experimental measurements of swirl ratio at $x = 0.993$ taken from Sangan *et al.* (2014)

The range of $\lambda_{T,a}$ values over which $\beta'_{1,EI}$ is known varies for each seal. The axial seal data, already compared to the correlation above, is known over the widest range of $\lambda_{T,a}$ but that still does not reach $\lambda_{T,min}$. Seal performance can be determined from Φ_{min} as shown in Table 5.1, where the axial seal performs worst (requiring the most sealing flow to prevent ingress) and the double radial seal performs best (requiring the least sealing flow). The original notation of Sangan *et al.* (2013c) is also given in the Table 5.1

Seal	Short Name	Φ_{min}	Γ_c
Axial	S1	0.326	0.48
Double Axial	D1	0.156	0.22
Radial	S2b	0.121	1.32
Double Radial	D2	0.0931	1.54

Table 5.1: Effectiveness equation constants for various seal geometries from Sangan *et al.* (2013).

When looking at multiple seals the correction is plotted against $\lambda_{T,a}/\lambda_{T,min}$ (where $\lambda_{T,min} = \Phi_{min}$for this case) in Figure 5.13. The figure shows the EI correction of (5.8) where the no ingress β_1 values are based upon the SFNI cavity model with no inner region and the variable momentum-integral equations where $x_a = 0.6, \gamma_s = 0.03, \beta_a = 0.2$.

Agreement between the correction and swirl measurements is best for the axial seal and worst for the radial seal. The steeper gradient for the radial seals are caught well by the correction, however the $\beta'_{1,EI}$ values for both radial seals are under

predicted. The worse agreement with the radial seals is attributed to the under prediction of Φ_{min} by the effectiveness equations that were presented by Sangan *et al.* (2013), which would in turn lead to an under prediction of the $\lambda_{T,i}$ and ultimately $\beta'_{1,EI}$ values.

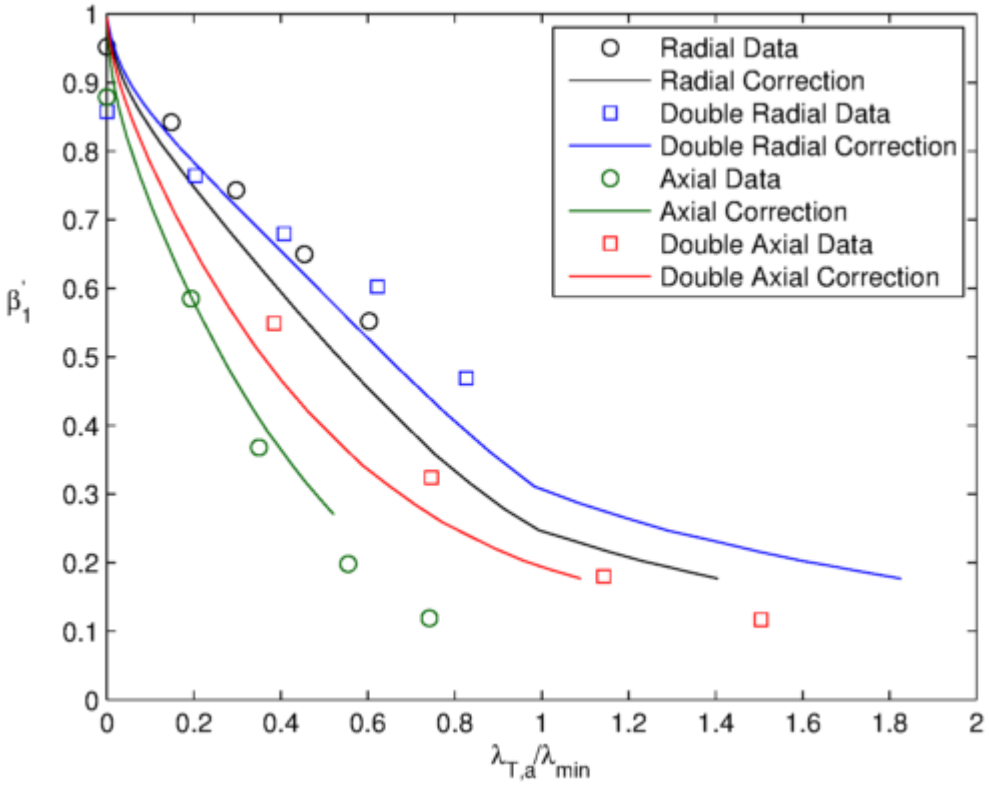

Figure 5.13: Variation of exit swirl ratio with sealing flow for radial, double radial, axial and double axial seal based upon Superposed Flow, No Ingress cavity model solved with variable momentum-integral eqns.

As the seal performance increases the correction shows that the transition between the no ingress swirl β_1 and the ingress swirl $\beta'_{1,EI}$ becomes more distinct (see the blue and black lines for radial and double radial seal respectively). This transition cannot be verified experimentally due to a mismatch in the measurements and predictions. For radial seals the model can predict behaviour for $\lambda_T > \lambda_{T,min}$ but there are no experimental measurements and for the double axial seal where there are two experimental values of $\beta'_{1,EI}$ for $\lambda_T > \lambda_{T,min}$, the model cannot predict swirl at such high flow rates.

Although concrete conclusions cannot be drawn at this stage it is hoped that the simple momentum balance correction can, after further validation from a denser range of experimental data, bring a better understanding of how the ingress and sealing flow interact, especially near the exit of the wheelspace, where it is thought that all of the mixing takes place in the seal clearance itself.

5.4 SUMMARY

This Chapter has considered the effect that ingress has on the swirl ratio in the cavity, and attempted to quantify this effect through a simple model to describe the flow interactions across a seal clearance.

In Section 5.1 of this Chapter the flow structure for a cavity with ingress and no superposed flow was discussed. The two forms of the ingress flow rate were defined: Φ_i, an inviscid parameter (appropriate for flow through the rim seal) and $\lambda_{T,i}$, a viscous parameter (appropriate for flow through the boundary layer).

In Section 5.2 a simple momentum balance model was derived to describe how flows interact across the seal clearance. By assuming that β_e, the swirl ratio on the rotor at high radial location, is in fact a swirl ratio not affected by ingress then the results of the Superposed Flow No Ingress model could be implemented in the model. This lead to an equation that relates the swirl ratio with ingress present to the swirl ratio with no ingress present. This allowed the swirl ratio results from the Superposed Flow No Ingress model at the exit to the wheelspace could be 'corrected' to find the swirl ratio for the case with ingress. The equation depends upon a value β_i, denoted $\beta_{i,EI}$ and $\beta_{i,RI}$ for EI and RI ingress respectively.

In Section 5.3 it was found that only the values $\beta_{i,EI} = 1$ and $\beta_{i,RI} = 0$ gave good agreement with experimental measurements. In general, EI ingress increased the swirl ratio and RI ingress decreased the swirl ratio. The results from the variable momentum-integral equations gave much better agreement with the experimental results. It was shown that increasing the inlet swirl would in turn increase the value of exit swirl with EI and RI ingress present. Decreasing the cavity size radially will decrease the value of exit swirl with EI and RI ingress present. There was good agreement between the model and β_1 experimental measurements for the axial and double axial seals. The model under predicted experimental measurements of swirl ratio for the radial and double radial seals. This is either caused by the under-prediction of Φ_{min} and therefore ingress flow rate by the orifice model for radial seals, or suggests the model needs further refinement. It is suggested that a refinement be the reconsideration of how ingress affects the wheelspace.

Rethinking How Ingress Affects the Wheelspace

In early descriptions of ingress it was hypothesised that the ingress affected the cavity due to of a large injection of mass flow – where this hot gas was entrained by the stator and then recirculated with the rest of the flow. If this is the case then why is there little difference in the radial distribution of swirl ratio and flow structure between the axial and radial seal? Would such a large influx of mass flow not affect the structure much like the effect of increasing the sealing flow rate? It is hypothesised that the amount of flow physically entering the wheelspace is a small fraction of $\lambda_{T,i}$. Instead of $\lambda_{T,i}$ representing the amount of flow entering the *wheelspace* it can be thought of as the amount of flow entering the *seal*, but where the majority of the flow actually subsequently leaves the seal and flows back into the annulus and only a fraction of which penetrate beyond the periferphy of the cavity. This kind of behaviour can be seen by considering the flow visualisation from complex 3D CFD; it can be seen that a large amount of fluid enters the rim seal only to recirculate and leave the seal clearance without actually entering the wheelspace (see Scobie *et al.* (2015) and Zhou *et al.* (2013)).

For this new view of the interactions within the seal clearance the model presented in this Chapter would need adjusting. The seal clearance would have two inputs: the ingress from the annulus and the egress outflow flow from the rotor. Along with two outputs: the ingress flowing onto the stator (which may actually be less than

the ingress entering the seal clearance) and the egress leaving the seal clearance. All these flows are shown in Figure 5.14.

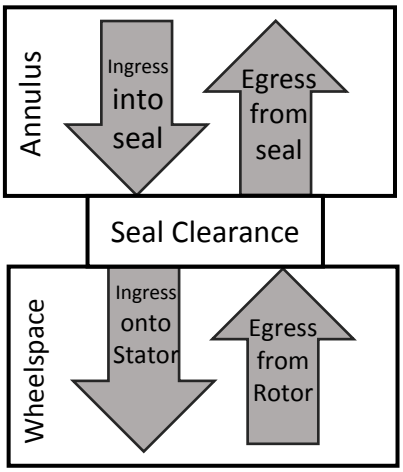

Figure 5.14: Simplified flow streams in the seal clearance

In the previous model described in Section 5.2 it was assumed that any ingress flow entering the seal clearance also all entered the cavity and flowed onto the stator. The model could be changed to differentiate between the amount of ingress entering the seal clearance and the cavity. This new model is shown in Figure 5.15 which is comparable to the original model in Figure 5.2.

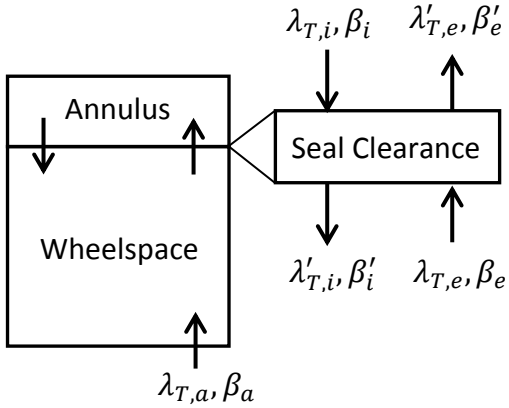

Figure 5.15: Simplified model of the seal clearance between the annulus and wheelspace.

The swirl ratio and flow parameters are slightly different to the originally proposed model. For the flows *into* the seal clearance:

- Ingress entering the seal clearance from the annulus has β_i and $\lambda_{T,i}$
- Egress entering the seal clearance from the wheelspace has β_e and $\lambda_{T,e}$

For the flows *out of* the seal clearance:

- Ingress exiting the seal clearance and entering the wheelspace has β'_i and $\lambda'_{T,i}$
- Egress exiting the seal clearance and entering the annulus has β'_e and $\lambda'_{T,e}$

The dash is used to denote any quantity leaving the system. These new definitions will change the momentum correction. The model still assumes that there is continuity of mass in the seal clearance, leading to

$$\lambda_{T,e} + \lambda_{T,i} = \lambda'_{T,e} + \lambda'_{T,i} \tag{5.17}$$

and within the wheelspace

$$\lambda_{T,e} = \lambda'_{T,i} + \lambda_{T,a} \tag{5.18}$$

As was shown in equation (5.4) for the original model in Section 5.2 a momentum equation can be defined by assuming angular momentum of the two fluid streams must be conserved while neglecting shear stresses from the surfaces of the seal:

$$\lambda_{T,i}\beta_i + \lambda_{T,e}\beta_e = \lambda'_{T,e}\beta'_e + \lambda'_{T,i}\beta'_i \tag{5.19}$$

It is still assumed that any flows leaving the seal clearance must have the same swirl so by replacing both β'_i and β'_e by β'_1 this leads to a simplification of equation (5.19):

$$\lambda_{T,i}\beta_i + \lambda_{T,e}\beta_e = \left(\lambda'_{T,e} + \lambda'_{T,i}\right)\beta'_1 \tag{5.20}$$

Similar to the working of Section 5.2 a new momentum balance equation can be derived

$$\beta'_1 = \frac{\left(\lambda'_{T,i} + \lambda_{T,a}\right)\beta_{\mathrm{e}} + \lambda_{T,i}\beta_i}{\lambda'_{T,i} + \lambda_{T,a} + \lambda_{T,i}} \tag{5.21}$$

to give another correction for the swirl ratio at the exit of the wheelspace in the presence of ingress. This equation differs from the original model (5.8) as here it has been assumed that the mass flow of ingress flowing into the seal clearance may not be equal to the mass flow of ingress entering the cavity. This has not been modelled yet but it could be future work to assume that $\lambda'_{T,i}$ is some percentage of $\lambda_{T,i}$ to see if this gives improved agreement with the radial seal data.

CHAPTER 6 : EMPIRICAL MODEL FOR ROTOR BUFFERING

This chapter moves away from the cavity models and instead describes the derivation and application of a theoretical model for the 'buffering' that occurs on the rotor within the wheelspace. The sealing air attaches itself to the rotor, creating a buffering effect that reduces the amount of ingested fluid that can reach the surface of the rotor. The theoretical model shows that the maximum buffering effect occurs at a critical flow rate of sealing air, the value of which depends on the seal geometry. The model, which requires two empirical constants, is validated using experimental data, obtained from infra-red (IR) temperature measurements of taken on the Bath rig and presented in Cho *et al*. (2015). The work presented in this chapter has formed the basis of the paper Mear *et al.* (2015).

Most of wider research on ingress has focused on the determination of sealing effectiveness using concentration measurements on the stator. As discussed in the literature review, the orifice model developed by Owen (2011) was successful in fitting the concentration measurements on the stator. Recent publications, reviewed in detail in Chapter 2 Section 2.3.4, have overcome difficulties and successfully measured the effectiveness on the rotor. It is known that, unlike stator concentration, the rotor concentration is not constant with radius. Understanding the effect of ingress on the rotor would be useful for engine designers as this is lacking in current literature.

The model is described in Section 6.2 and the application of the model to predict adiabatic effectiveness is discussed in Section 6.3. A comparison between the model and previously published data is given in Section 6.4. In Section 6.5 comparisons are given between the definition presented here and definitions of other authors. The principal conclusions are given in Section 6.6.

6.1 FLOW STRUCTURE WITH INGRESS AND SEALING FLOW

The following section describes the expected flow structure within the rotor-stator wheelspace with both ingress and sealing flow, culminating in the definition of two key parameters: the *buffering effect* and the *buffer ratio.* A model, which includes two empirical constants, is then developed to determine these parameters.

As for the previous flow structure descriptions, rotor-stator flow with ingress and sealing flow is based upon flow structure discussions in Owen and Rogers (1989) and Childs (2010).

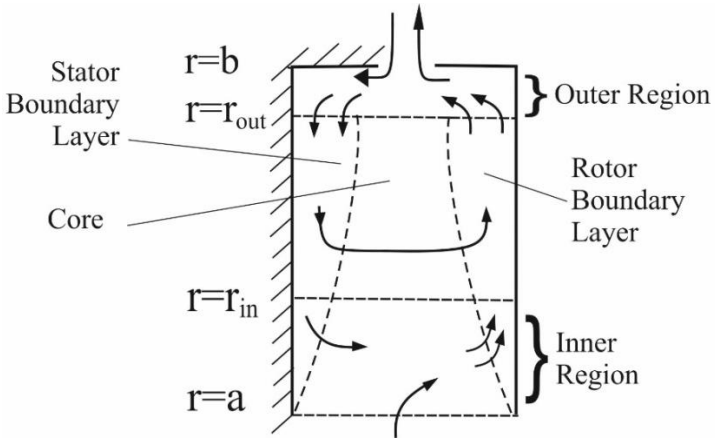

Figure 6.1: Simplified flow structure for rotor-stator system with superposed sealing flow and ingress

Figure 6.1 shows the flow structure in a rotor-stator system for the case where there is a superposed radial flow, with swirl, together with ingress through the rim seal. The gap ratio, G, is large enough to ensure separate boundary layers on the two discs, both of which start at $r = a$ (equivalent to $x = x_a$). Fluid moves radially outward in the boundary layer on the rotor and inward in the boundary layer on the stator. Over much of the wheelspace, fluid moves axially across the rotating inviscid core from the boundary layer on the stator to that on the rotor.

Just as for the Superposed Flow, No Ingress model the superposed flow enters the system through an *inner region* which extends to $r = r_{in}$ (where $x_{in} \coloneqq r_{in}/b$), by which point all the available flow has been entrained by the boundary layer on the rotor. In the *outer region* for $r_{out} < r < b$ (where $x_{out} \coloneqq r_{out}/b \approx 0.87$ as predicted by the SFNI Model) fluid leaves the system through the rim seal, with a flow rate equal to that of the superposed flow plus some unknown ingress flow rate. The additional fluid entrained by the boundary layer on the rotor flows axially across the outer region to be entrained by the boundary layer on the stator. The inner and outer regions are the sources for the flow in the boundary layers on the rotor and stator respectively.

As for the SFNI model, as $\lambda_{T,a}$ increases the core is suppressed. Note that the sealing flow parameter Φ_o will be used when discussing flow through the rim seal. Whereas $\lambda_{T,a}$ will be used in discussions of flow structure as it is appropriate for flow through the boundary layer.

6.2 BUFFERING EFFECT OF SEALING FLOW

Concentration values in the wheelspace can be used in the context of mass transfer to explain the buffering effect, the phenomenon where sealing air attaches itself to the rotor, reducing the amount of ingress that can reach the surface of the rotor. In most of the other ingress papers, experimental measurements show that the concentration is constant over most of the stator surface (see Cho *et al.* (2015)). This is consistent with Figure 6.1 and with the discussion above that, except in the outer region, no fluid is entrained by the stator boundary layer. It also implies that the fluid in the boundary layer on the stator is fully mixed, so that c_s, the concentration at the surface of the stator, must equal c_∞, the concentration in the inviscid core at the edge of the boundary layer. As the fluid leaving the boundary layer on the stator flows axially across the core, it follows that the concentration throughout the core must equal c_s, which is therefore the concentration of the fluid that is entrained into the boundary layer on the rotor. In the concentration experiments of Cho *et al*, the sealing flow was seeded with CO_2 as the tracer gas. Consequently, the concentration of gas measured in the annulus, denoted c_{an}, is always less than or equal to that of the sealing flow, c_o.

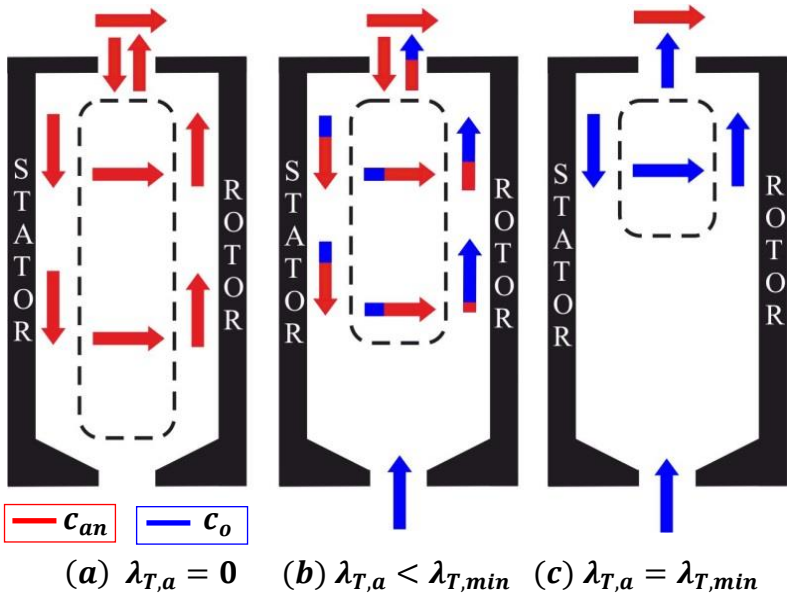

Figure 6.2: Simplified representation of buffering effect within the cavity

Figure 6.2 shows the effect of increasing sealing flow rate on the flow structure in the wheelspace, with added details of the concentration within the boundary layers (where $c_o > c_{an}$). The arrows on the stator and rotor are coloured to represent the concentration inside the boundary layer on the respective surfaces.

For case (a) there is no sealing flow ($\lambda_T = 0$); this means that all the fluid inside the wheelspace must all have the same concentration, so $c_r = c_s = c_{an}$. In the limit as $\lambda_{T,a} \to 0$, $c_r \to c_s$. For this case there will be no buffering.

For case (b), where there is not enough sealing flow to prevent ingress, sealing air with concentration $c = c_o > c_{an}$ enters the wheelspace at $r = a$. The fluid from the boundary layer on stator will flow across the core and mix with the sealing flow in the boundary layer on the rotor, and consequently $c_r > c_s$. It also follows that c_r will decrease as the fluid moves radially outward in the rotor boundary layer. However, in the outer region, where the fluid flows from the rotor to the stator, the concentration on the rotor should be invariant with radius. For this case there will be some buffering.

For case (c) where $\lambda_{T,a} = \lambda_{T,min}$ the system is fully protected from ingress, and $c_r = c_s = c_o$. In the limit as $\lambda_{T,a} \to \lambda_{Tmin}$, $c_r \to c_o$.

6.2.1 DEFINITIONS OF BUFFERING EFFECT AND BUFFER RATIO

The sealing effectiveness on the stator is defined as

$$\varepsilon_s := \frac{c_s - c_{an}}{c_o - c_{an}} \tag{6.1}$$

and the effectiveness on the rotor is

$$\varepsilon_r := \frac{c_r - c_{an}}{c_o - c_{an}} \tag{6.2}$$

where

- c_{an} is the concentration in the mainstream annulus
- c_o is the concentration of the sealing flow
- c_s and c_r are the concentrations in the stator and rotor boundary layers.

For both definitions (ε_s and ε_r), when there is no ingress then the effectiveness will be one, and when there is no sealing flow the effectiveness will be zero. The *buffer effect,* $\Delta\varepsilon$, is defined as the difference between ε_r and ε_s, such that

$$\Delta\varepsilon := \varepsilon_r - \varepsilon_s = \frac{c_r - c_s}{c_o - c_{an}} \tag{6.3}$$

As it is known that ε_s is typically constant with radius, whereas ε_r is not, the buffer effect may vary with radius as well as with sealing flow rate. Figure 6.3 below attempts to explain the behaviour of $\Delta\varepsilon$ radially in terms of the differences in concentration on the rotor and the stator.

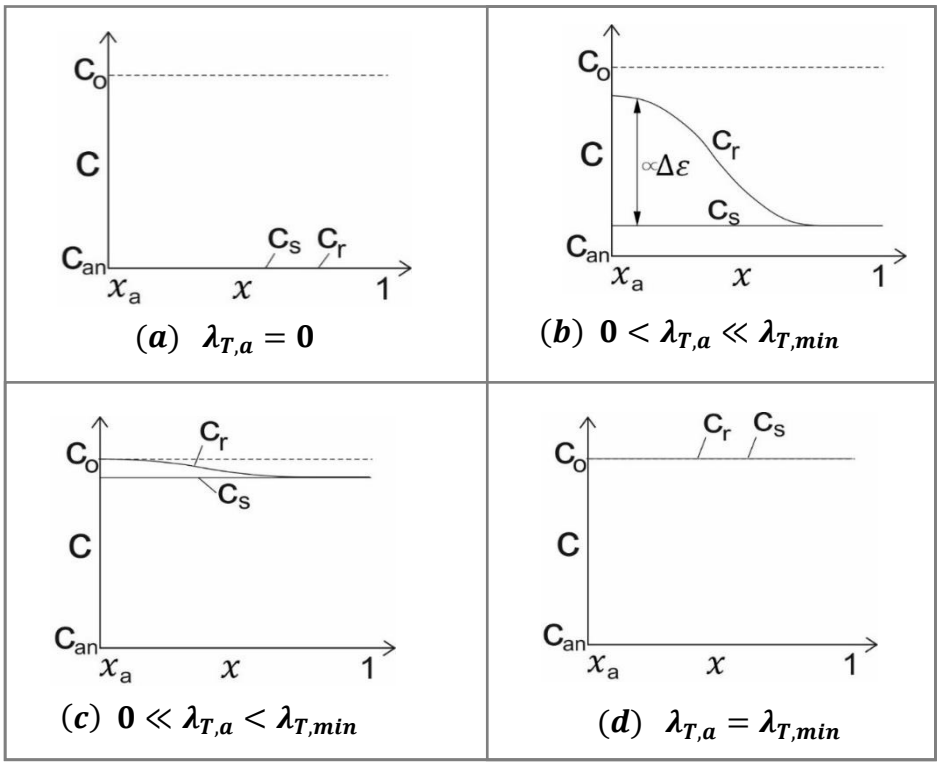

Figure 6.3: Expected radial variation of buffering effect with sealing flow rate

Firstly Figure 6.3(a): when no sealing flow is supplied, there is no difference in the concentration in the wheelspace and the annulus, hence $c_s = c_r = c_{an}$ at every radial location. Secondly Figure 6.3(b): as some sealing flow is supplied, seeded with CO_2, the concentration on the rotor and stator wall increases. The concentration on the rotor rises faster than that of the stator; this is because the sealing air enters straight into the inner region which acts as a source region for the rotor. As $\Delta\varepsilon = (c_r - c_s)/(c_o - c_{an})$ where c_o and c_{an} are not changing, consider simply $c_r - c_s = \Delta\varepsilon(c_o - c_{an}) \propto \Delta\varepsilon$ (so the difference in the rotor and stator concentration is proportional to the buffering effect). It can be seen that the buffering effect $\Delta\varepsilon$ decreases with radius. It is expected that at high radial locations within the outer region $c_r = c_s$, this is consistent with experimental measurements. Next Figure 6.3(c): as the sealing flow increases, the concentration on the stator will continue to rise while remaining constant radially. As $\lambda_{T,a} \to \lambda_{T,min}$ at each radial location $c_r \to c_s$, apart from at high radial locations where that convergence has already occurred. Finally Figure 6.3(d): as the cavity is sealed ($\lambda_{T,a} = \lambda_{T,min}$) at each radial location $c_r = c_s$.

It is useful to consider the *buffer effect,* $\Delta\varepsilon$, but as it does not vary between 0 and 1 it would be difficult to model. Instead consider the *buffer ratio*, BR, a scaled quantity defined as

$$BR := \begin{cases} \dfrac{\varepsilon_r - \varepsilon_s}{1 - \varepsilon_s} = \dfrac{c_r - c_s}{c_o - c_s} & if \quad \varepsilon_s < 1 \\ 1 & if \quad \varepsilon_s = 1 \end{cases} \tag{6.4}$$

As can be seen by the far right equality in equation (6.4), the buffer ratio eliminates c_{an} from the equation, so the true relation between rotor and stator concentration can be seen. When the concentration on the rotor equals that on the stator then there is no buffering and $BR = 0$. When the concentration on the rotor equals that of the sealing flow, then the rotor is fully buffered and $BR = 1$.

It follows that the *buffer effect* can be restated as

$$\Delta\varepsilon = BR(1 - \varepsilon_s) \tag{6.5}$$

Notice that as ε_s can be modelled by the orifice model and if BR can be modelled then this means the two models can be combined to get a model for the buffer effect.

6.2.2 MODEL FOR BUFFER RATIO

By considering the flow structure description in Section 6.1, two limits were deduced:

- As $\lambda_{T,a} \to 0$ then $c_r \to c_s$ (and consequently $BR \to 0$)
- As $\lambda_{T,a} \to \lambda_{T,min}$ then $c_r \to c_o$ (and consequently $BR \to 1$).

A simple model that follows these limits is

$$BR = exp\left(-A\left(\frac{\lambda_{T,min}}{\lambda_{T,a}} - 1\right)^n\right) \tag{6.6}$$

where A and n are empirical constants. As$\lambda_{T,min}/\lambda_{T,a} = \Phi_{min}/\Phi_o$ it is more convenient to write

$$BR = exp[-A(\Theta^{-1} - 1)^n] \tag{6.7}$$

where

$$\Theta := \frac{\Phi_o}{\Phi_{min}} \tag{6.8}$$

In the following Section the model is validated, and the empirical constants are determined.

6.3 USING THE MODEL

6.3.1 CALCULATION OF BUFFER RATIO FROM EXPERIMENTAL DATA

In order to validate the proposed model above, experimental values of the buffer ratio are required. This section discusses how these can be obtained. Equation (6.4) can be rewritten as

$$BR(\Theta) = \frac{\varepsilon_r - \varepsilon_s}{1 - \varepsilon_s} \tag{6.9}$$

where ε_r and ε_s, which are measured experimentally, depend on Θ. Ideally, the values of ε_r and ε_s should be measured at the *same* value of Θ, but this was not the case for the experimental data that is available. Instead it was necessary to take the measured values of ε_r and use the effectiveness equation to obtain values of ε_s at the same flow

rates. The effectiveness equation, originally stated in equation (2.63), is restated here with updated notation,

$$\Theta = \frac{\varepsilon_s}{\left[1 + \Gamma_c^{-\frac{2}{3}}(1-\varepsilon_s)^{\frac{2}{3}}\right]^{\frac{3}{2}}} \tag{6.10}$$

where Γ_c is the ratio of the discharge coefficients determined from the correlation for each seal.

A typical experimental set from Cho *et al.* (2015) contained measurements of ε_r at 17 different flow rates, therefore 17 values of Θ were used to calculate BR. Within the paper the effectiveness on the rotor are *adiabatic effectiveness* measurements – that is based on temperature rather than concentration. The definition of *adiabatic effectiveness* is

$$\varepsilon_{ad} := \frac{T_{ad} - T_{an}}{T_{ad}^* - T_{an}} \tag{6.11}$$

where T_{ad} is the adiabatic wall temperature when ingress occurs, T_{an} is the temperature in the annulus, and $T_{ad}^*$is the adiabatic wall temperature when the wheel-space is fully sealed, so that there is no ingress. Using the analogy between the transfer of mass and energy, it is assumed that $\varepsilon_r = \varepsilon_{ad}$. This assumption is supported by the computations of Tian (2014). Both definitions of effectiveness, (6.2) and (6.11), have the same value at the limits, such that:

$$As\ \Theta \to 0\text{: } T_{ad} \to T_{an} \Rightarrow \varepsilon_{ad} \to 0 \text{ and } c_r \to c_{an} \Rightarrow \varepsilon_r \to 0$$
$$As\ \Theta \to 1\text{: } T_{ad} \to T_{ad}^* \Rightarrow \varepsilon_{ad} \to 1 \text{ and } c_r \to c_o \Rightarrow \varepsilon_r \to 1$$

The procedure to find experimental values of BR is as follows:

For given seal where rotor and stator effectiveness measurements are known:

1. Fit for the stator effectiveness data using the orifice model to find Φ_{min} and Γ_c.
2. Take the N flow rates at which rotor effectiveness is defined, and calculate $\Theta_\mathrm{i} = \Phi_{o,i}/\Phi_{min}$ for $i = 1, \dots, N$.
3. For the range of flow rates Θ_i for $i = 1, \dots, N$ use effectiveness equation (6.10) with constants Φ_{min} and Γ_c from step. 1 to calculate corresponding stator effectiveness measurements ε_s.
4. Given ε_r and ε_s are now known for each flow rate, define $\Delta\varepsilon$ by (6.3) and BR based on (6.4) for Θ_i for $= 1, \dots, N$.

Now BR is known for an experimental data set.

6.3.2 DETERMINATION OF EMPIRICAL CONSTANTS

Zhou *et al.* (2013b) successfully used Maximum Likelihood Estimation (MLE) to determine two empirical constants (Φ_{min}, Γ_c) from correlations of the effectiveness equation with concentration measurements. MLE is used here to determine two empirical constants (A, n) by correlating equation (6.7) for BR with the measured values determined from equation (6.9). The MLE method involves finding values of A and n that were most likely to have made the observed data that is being fitted. This is done by minimising the *log-likelihood function*:

$$l(A, n, \sigma) = N \log(\sigma) + \sum_{i=1}^{N} \frac{\left[BR_{exp}(\Theta_i) - BR_{model}(A, n, \Theta_\mathrm{i})\right]^2}{2\sigma^2} \tag{6.12}$$

where N is the number of experimental data points, $BR_{j,exp}$ the buffer ratio based on the experiments is as calculated from step 4 in the procedure described above, BR_{model} is the function shown in (6.7) and σ is the standard deviation.

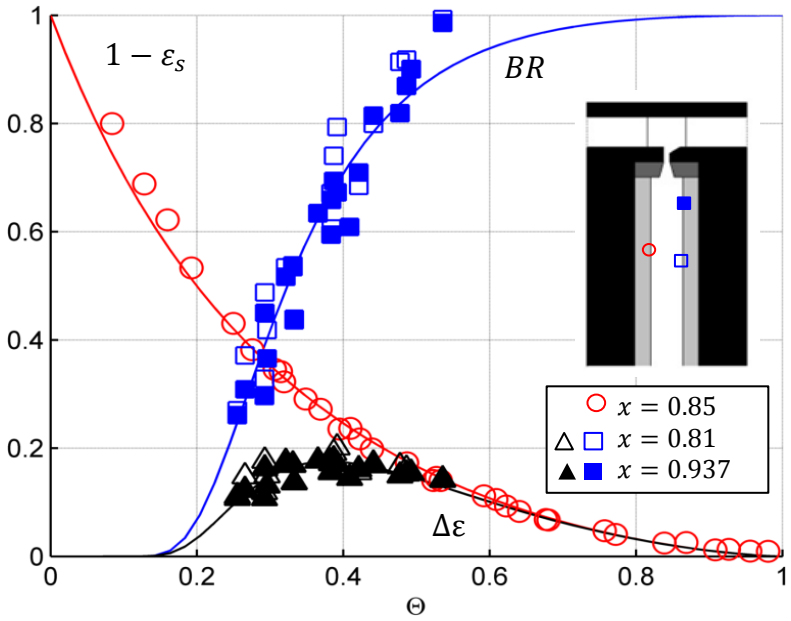

(a) Axial-clearance seal

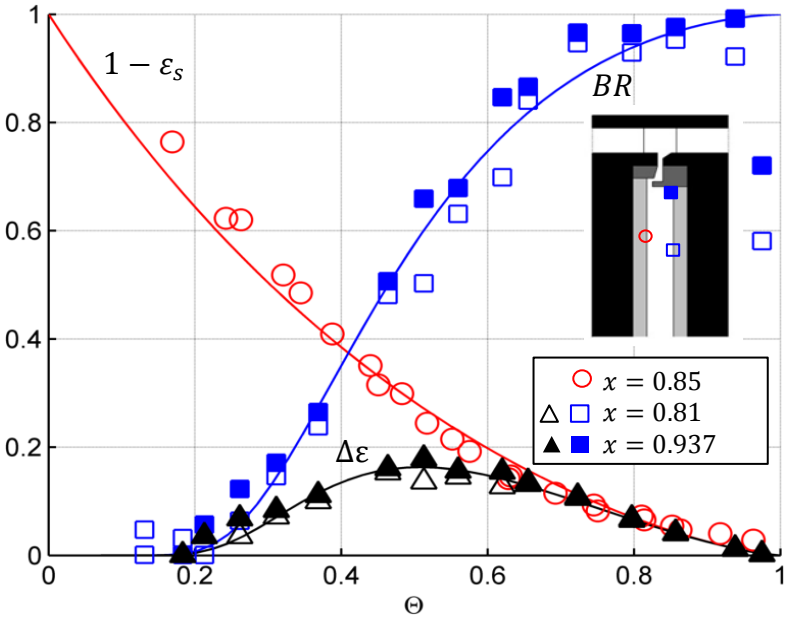

(b) Radial-clearance seal

Figure 6.4: Buffer ratio and buffer effect for single seals. (Symbols denote experimental data and curves are determined from theoretical models).

Figure 6.4 shows the correlations for the two single seals, based upon data from Cho *et al.* (2015). Outlines of the wheelspace and measurement locations on the stator and rotor have been added to these, and subsequent, figures. For the experimental data and curves, red is used for $(1 - \varepsilon_s)$, blue for BR, and black for $\Delta\varepsilon$. The three curves are based on equations (6.10), (6.7) and (6.5) respectively. For both seals, the values of $\varepsilon_r = \varepsilon_{ad}$ were determined at two radial locations ($r/b = 0.81$ and

0.937). The value of ε_s was determined at $r/b = 0.85$, though this was independent of radius.

Although, in general, the correlation of BR would be expected to depend on the radial location of the measurements, these two locations are expected to be in (or close to) the outer region in the wheelspace where fluid flows from the rotor to the stator. As explained in Section 6.1, the concentration, and therefore ε_r, should be invariant with radius in this region. Consequently, the data from both radial locations is used to determine A and n for each seal.

Figure 6.4(a) shows the results from the single axial-clearance seal, the values of A and n were found, using MLE, to be 0.147 and 2.10 respectively. Despite the scatter on the data the fit of BR seems reasonable, although the model does not predict the steep gradient near $\Theta \approx 0.5$. The buffer effect, $\Delta\varepsilon$, defined as the difference between the rotor and stator effectiveness, captures the essence of the buffering phenomenon. The curve for $\Delta\varepsilon$ shows a turning point at $\Theta \approx 0.4$, this maximum will be referred to as Θ_{crit}, where the value of $\Delta\varepsilon \approx 0.2$. For $\Theta < 0.15$, the values of $\Delta\varepsilon$ and BR are virtually zero, indicating that at high radial locations and low flow rates the buffering effect is negligible.

Figure 6.4(b) shows similar results for the radial clearance seal, where the values of A and n were found to be 0.552 and 1.58. Although the fit of BR is good, near $\Theta = 1$ there are two data points that are well below the theoretical curve. This anomaly is due to the inability of the effectiveness equation for ε_s to predict accurately the value of Φ_{min} for this seal. An under-prediction of Φ_{min} for the stator causes the effectiveness on the stator to reach unity Figure 6.5 below shows the stator effectiveness data of Cho *et al.* (2015) for all of the Φ_o cases available, fitting with three different version of the effectiveness equation. It can be seen clearly that Φ_{min} for this radial seal is not accurate, whichever fit is used. Consequently the Φ_{min} value at which $\varepsilon_s = 1$ is reached is under predicted, which in turn causes BR calculated from equation (6.9) to be inaccurate near $\Theta = 1$, due to ε_r being less than ε_s. As the effectiveness fit cannot be improved the anomaly could be removed by simply following the explicit buffer ratio definition equation (6.4), such that as $\varepsilon_s = 1$ for both of the anomalous points, it would be that $BR = 1$.

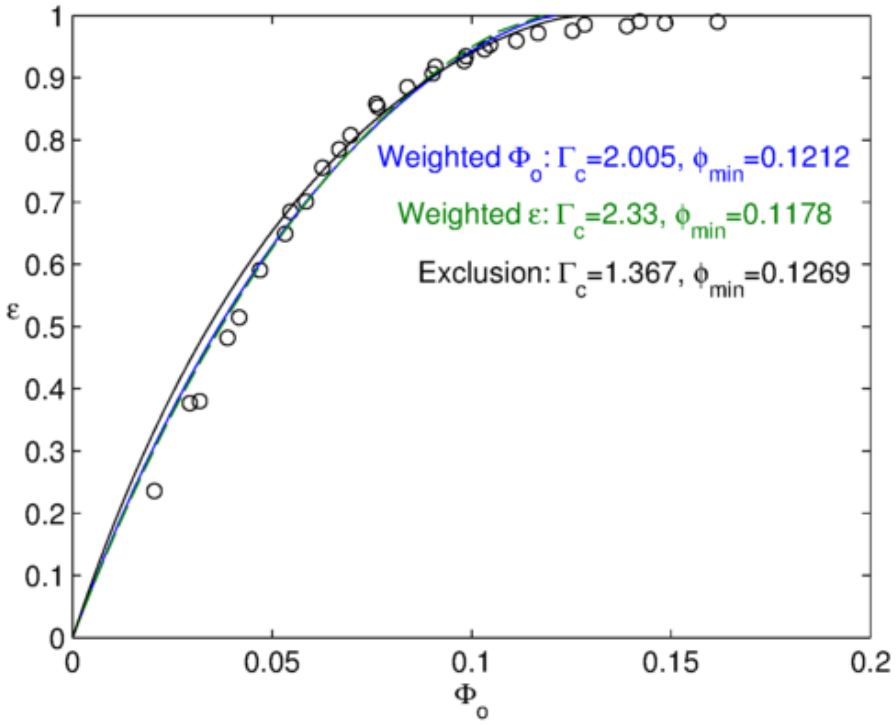

Figure 6.5: Comparison of effectiveness equation fits for ε_s for the radial seal at $x = 0.937$.

Usually the effectiveness equations fit experimental concentration measurements well. This is not the case for the measurements of Cho *et al.* (2015). Figure 6.5 shows the attempts to improve the fit of stator effectiveness data by the effectiveness equation. Three methods were attempted: *'exclusion', 'weighted* Φ_o*'* and '*weighted* ε'. The first method *exclusion* [black line] only fitted the data where $\varepsilon_s > 0.6$. This is to exclude data at lower values of Φ_o where the experimental uncertainties are highest. The *weighted* Φ_o and ε methods [blue and green lines respectively] simply added a weighting term in the MLE analysis such that the higher the effectiveness value or flow rate, the higher the weighting. The two weighted methods gave similar results, and the Φ_o weighting was used in the buffering fits as it provided the largest Φ_{min} with excluding data points and thus sacrificing the fit at lower radial locations.

Figure 6.6 shows the correlations for the double seals, where there are separate correlations for $r/b = 0.81$ and 0.937, which are in the inner and outer wheelspaces respectively. The distributions at both radial locations show a very similar shape (and thus have a similar n value) but for the inner radial location, where the sealing effectiveness is higher, the buffer-ratio distribution reaches one faster (shown as a shift to the left and thus a decrease in the empirical constant A). For both double seals there is a reduction in the maximum buffer effect, $\Delta\varepsilon$, compared to the corresponding single seals. For the single seals the maximum value of $\Delta\varepsilon$ was around 0.2 but for the double seals $\Delta\varepsilon \approx 0.13$.

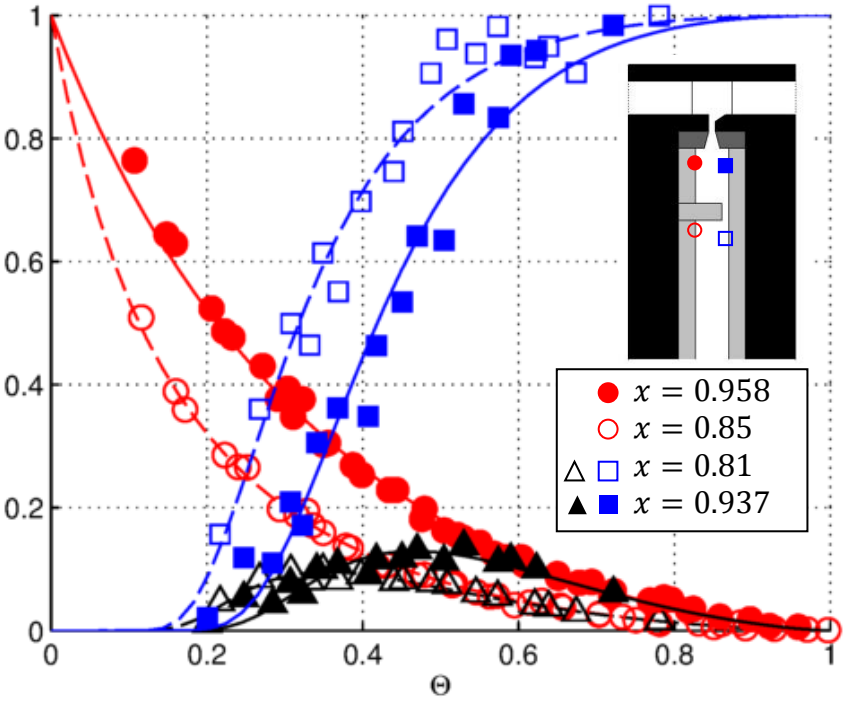

(a) Double axial clearance seal

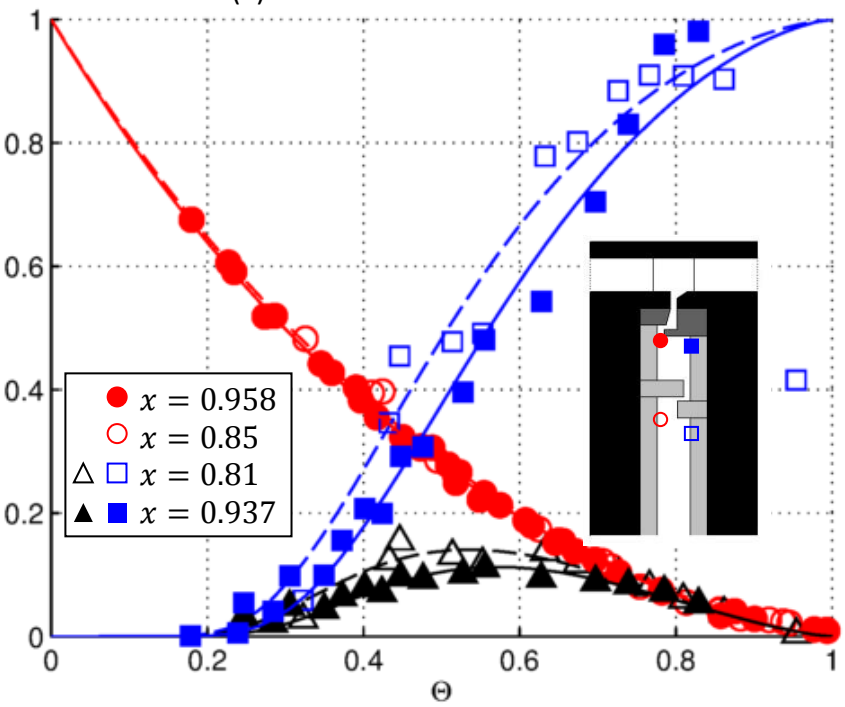

(b) Double radial clearance seal

Figure 6.6: Buffer ratio and buffer effect for double seals. (Symbols denote experimental data and curves are determined from theoretical models. Solid and dashed lines denote outer and inner cavity measurements respectively).

The values of A and n, and other relevant data, for all the test cases are given in Table 6.1. Also listed in the Table are the parameters $\Phi'_{min,s}$ and $\Phi'_{min,r}$; these are defined to be the sealing flow rates when $\varepsilon_s = 0.95$ and $\varepsilon_r = 0.95$ respectively. Typically $\Phi'_{min,s}$ is significantly greater than $\Phi'_{min,r}$ which implies that the rotor can be protected from the effects of ingress even if the wheelspace is not fully sealed.

Seal	Φ_{min}	Γ_c	A	n	$[\Delta\varepsilon]_{max}$	Θ_{crit}	$\Phi'_{min,s}$	$\Phi'_{min,r}$
Axial	0.200	0.644	0.147	2.10	0.175	0.388	0.148	0.086
Radial	0.121	2.01	0.552	1.58	0.163	0.510	0.102	0.073
Double Axial Outer	0.180	0.743	0.354	2.05	0.129	0.469	0.136	0.091
Double Axial Inner	0.166	0.227	0.147	2.03	0.095	0.347	0.099	0.062
Double Radial Outer	0.111	1.90	0.979	1.41	0.113	0.571	0.093	0.073
Double Radial Inner	0.061	2.08	0.729	1.45	0.141	0.531	0.052	0.039

Table 6.1: Summary of empirical constants for fitting data of Cho *et al.* (2015)

To use these results for design purposes, it would be necessary to produce a correlation for *A* and *n*. Although it seems probable that these constants are related to Γ_c, more seals would need to be tested to find such a correlation. However, the good agreement between the theoretical curves and the experimental data provides evidence that the theoretical model of the buffering effect described in Section 6.1 is basically correct. This physical insight should be helpful to both designers and research workers.

6.4 COMPARISON BETWEEN PREDICTED AND MEASURED ADIABATIC EFFECTIVENESS

Once the two empirical constants A and n have been found for the buffer ratio model for a specific seal, a fit for the rotor effectiveness data can be found. The definition for the buffer ratio can be rearranged to give:

$$\varepsilon_r = \varepsilon_s + BR(1 - \varepsilon_s) \tag{6.13}$$

Recall that by (6.5) the final term is exactly the *buffer effect* so this can be written

$$\varepsilon_r = \varepsilon_s + \Delta\varepsilon \tag{6.14}$$

Equation (6.13) is used in the following section to compare the predicted values of ε_r with the measured values of ε_{ad}. The values of BR and ε_s are obtained from equation (6.7) and (6.10) respectively, using the empirical constants given in Table 1.

6.4.1 SINGLE SEALS OF CHO *ET AL.* (2015)

Firstly the buffer ratio fits found for the single seals, as shown in Figure 6.4, are used as described above to find fits for rotor effectiveness. Figure 6.7 shows the comparisons between the predicted results and the measured values for the single seals. It can be seen that, despite some scatter on the data, the agreement between the predicted and measured adiabatic effectiveness is very good. Although the measurements of adiabatic effectiveness were made at two radial locations on the rotor, both sets of data are correlated by the single theoretical curve. The convergence between the effectiveness curves for the rotor and stator for $\Theta < 0.15$ for the axial seal and $\Theta < 0.2$ is a characteristic of the model, as explained in Section 6.1. Interestingly even when the fit for the buffer ratio was at its worst for the axial seal, at

$\Theta \approx 0.55$ in Figure 6.4(a), this does not translate to bad agreement between the predicted and measured adiabatic effectiveness.

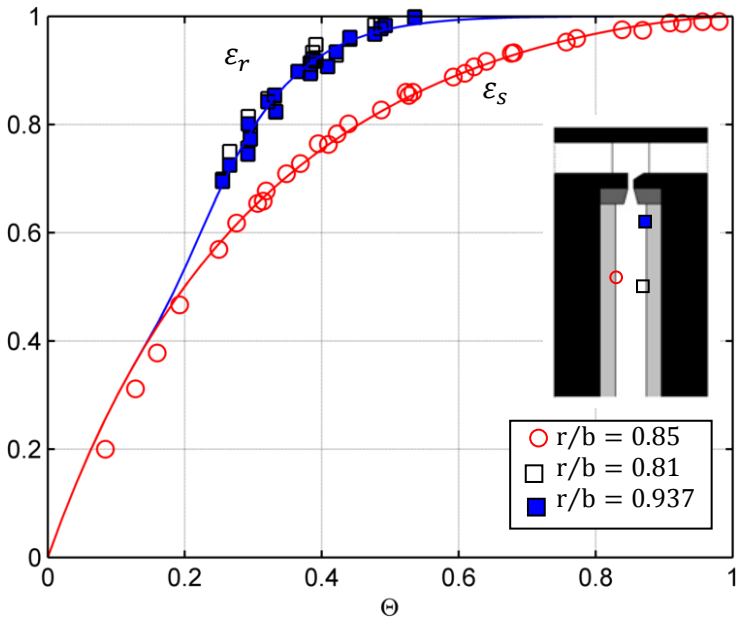

(a) Axial Seal

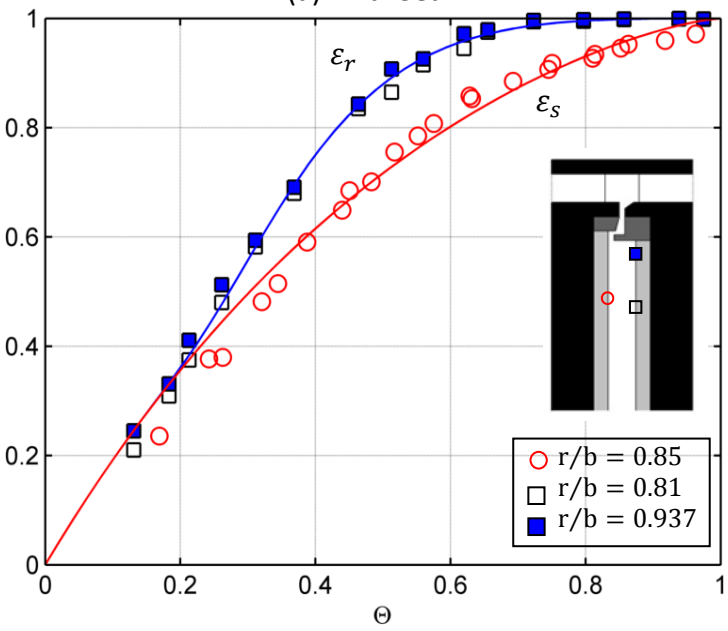

(b) Radial Seal

Figure 6.7: Variation of effectiveness with sealing flow rate for single seals. (Symbols denote experimental data, and curves are determined from theoretical models).

6.4.2 DOUBLE SEALS OF CHO *ET AL.* (2015)

The double seals require stator concentration measurements taken at two radial locations, one inside the outer wheelspace and the other inside the inner wheelspace. Consequently there are two curves for the buffer model. Also, as can be seen from Table 6.1, the measured values of Φ_{min} for the inner seal are less than those for the outer one.

Figure 6.9 and Figure 6.8 for the double seals show similar characteristics to those discussed above for the single seals, and the agreement between the

experimental data and the theoretical curves is very good. Again, the convergence of the theoretical curves for ε_r and ε_s is clearly visible for $\Theta < 0.15$.

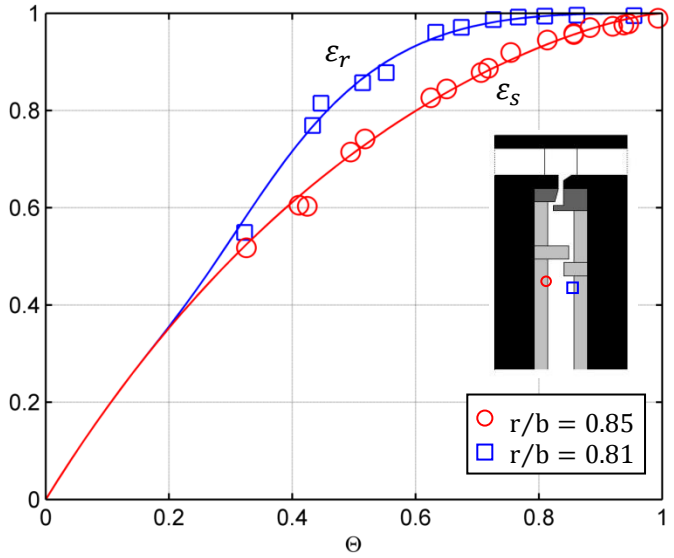

(a) Inner Wheelspace

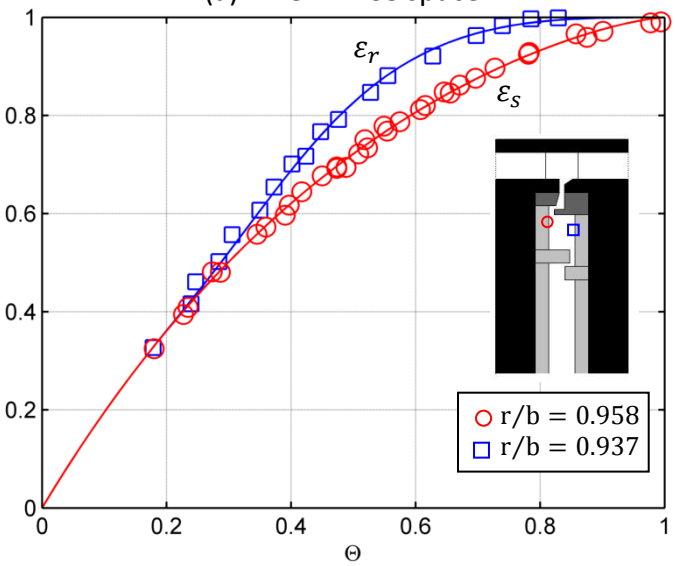

(b) Outer Wheelspace

Figure 6.8: Variation of effectiveness with sealing flow rate for double radial-clearance seal. (Symbols denote experimental data, and curves are determined from theoretical models).

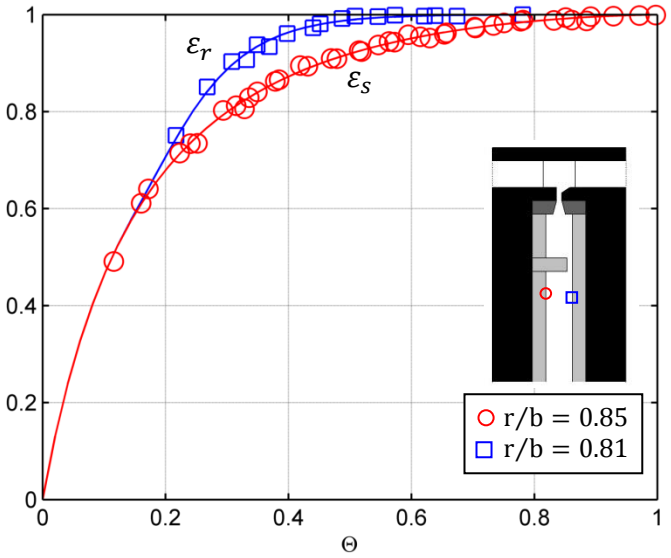

(a) Inner Wheelspace

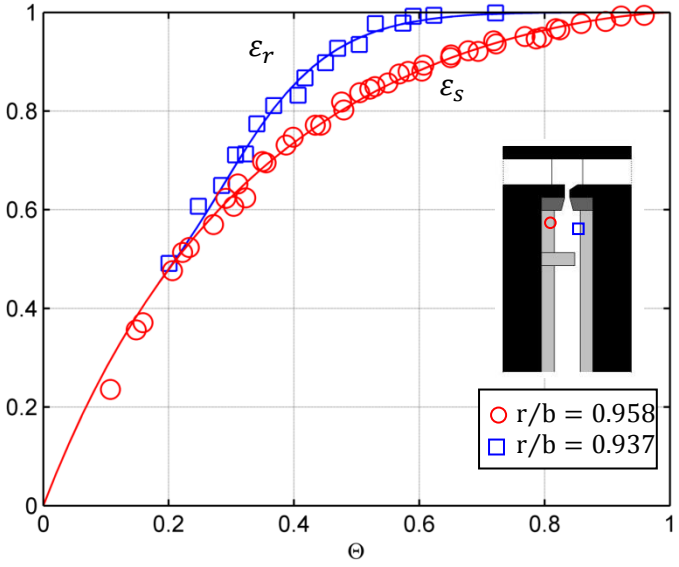

(b) Outer Wheelspace

Figure 6.9: Variation of effectiveness with sealing flow rate for double axial-clearance seal. (Symbols denote experimental data, and curves are determined from theoretical models).

6.4.3 SINGLE SEALS OF POUNTNEY *ET AL.* (2012)

As well as the effectiveness measurements of Cho *et al.* (2015) there are also appropriate results by Pountney *et al.* (2012) that could be fitted using the buffer ratio model. Pountney *et al.* (2012) made measurements of adiabatic effectiveness on the same rig as that used by Cho *et al.* (2015), but with small changes in the axial seal configuration, see Figure 6.10. Cho *et al*. (2015) added layers of Rohacell foam on the rotor and stator to increase the thermal insulation and to improve the measurement of the adiabatic effectiveness. This meant that the gap ratios for the two experiments were different, with $G = 0.105$ for the Pountney *et al*. experiments and $G = 0.05$ for the Cho *et al.* experiments. Both are still within the turbulent flow, separate boundary layer regime.

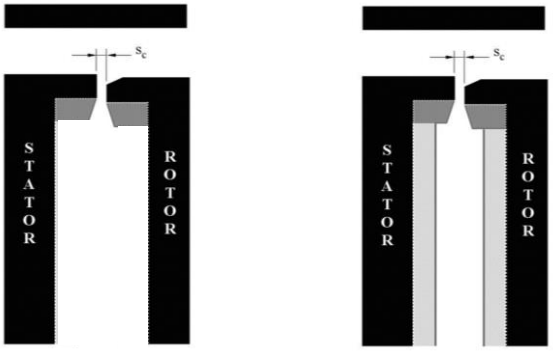

(a) Pountney *et al.* (2012) (b) Cho *et al*.(2015)

Figure 6.10: Two axial-clearance seal configurations within the Bath rig

The measurements of rotor effectiveness, ε_{ad}, and stator effectiveness, ε_c, by Pountney *et al.* (2012) were taken for two rotational speeds: *on-design* ($Re_w/Re_\phi = 0.538$) and *overspeed* ($Re_w/Re_\phi = 0.326$). Values of $\varepsilon_r \coloneqq \varepsilon_{ad}$ and $\varepsilon_s \coloneqq \varepsilon_c$ were determined at $r/b = 0.898$ and 0.958 respectively.

Figure 6.11 shows the calculated buffer ratio values from the experimental data, along with the fitting using the buffer ratio model. The empirical constants for the buffer ratio model for *on-design* were $A = 0.036$ and $n = 1.80$ and *over-speed* were $A = 0.504$ and $n = 1.62$. As the data range is smaller for these experiments it is hard to draw conclusions are to whether the fits are appropriate, but given the model predicted the form well for the data of Cho *et al.* (2015) it is reasonable to assume the fit is representative at flow rates outside of the experimental range too.

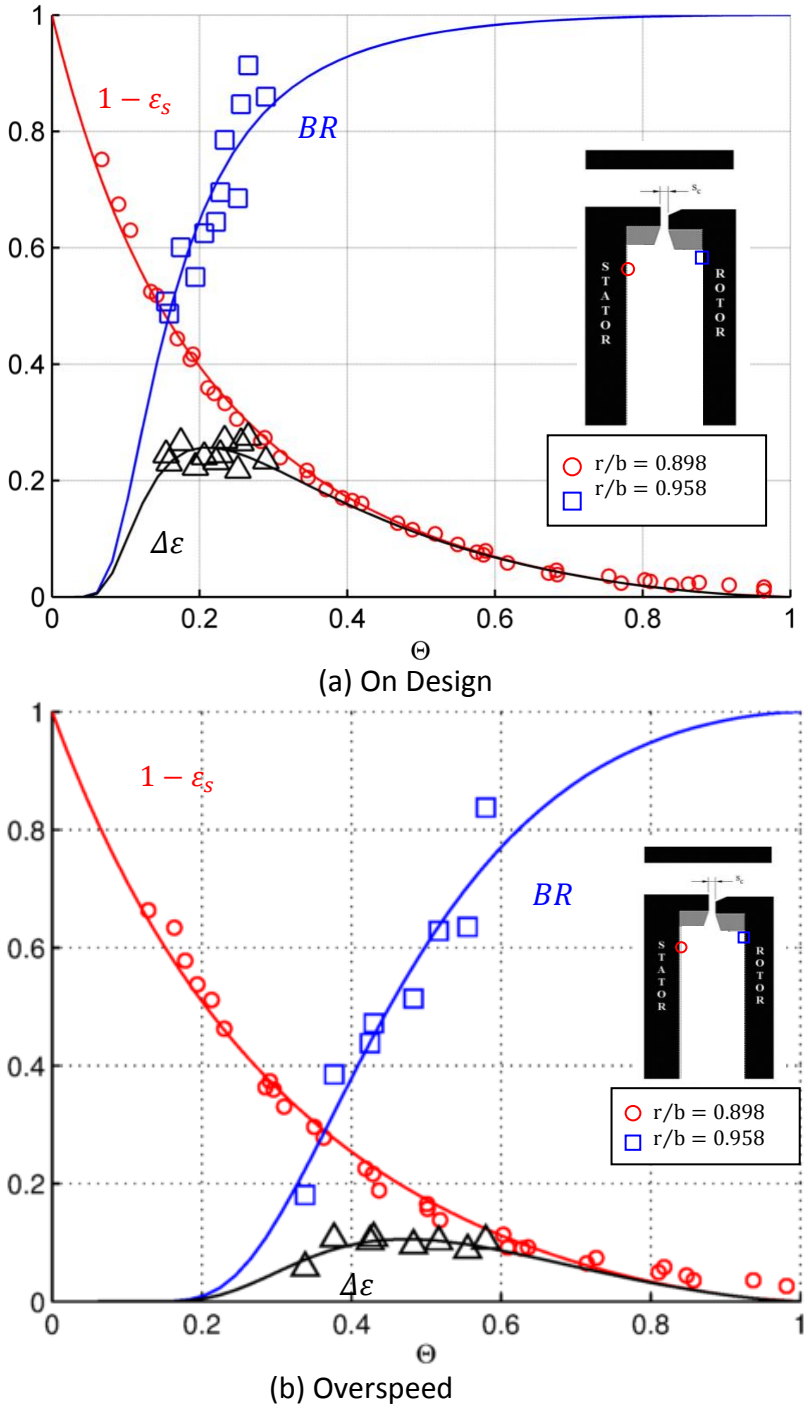

Figure 6.11: Buffer ratio and buffer effect for single axial-clearance seal of Pountney *et al.* (2012). (Symbols denote experimental data, and curves are determined from theoretical models).

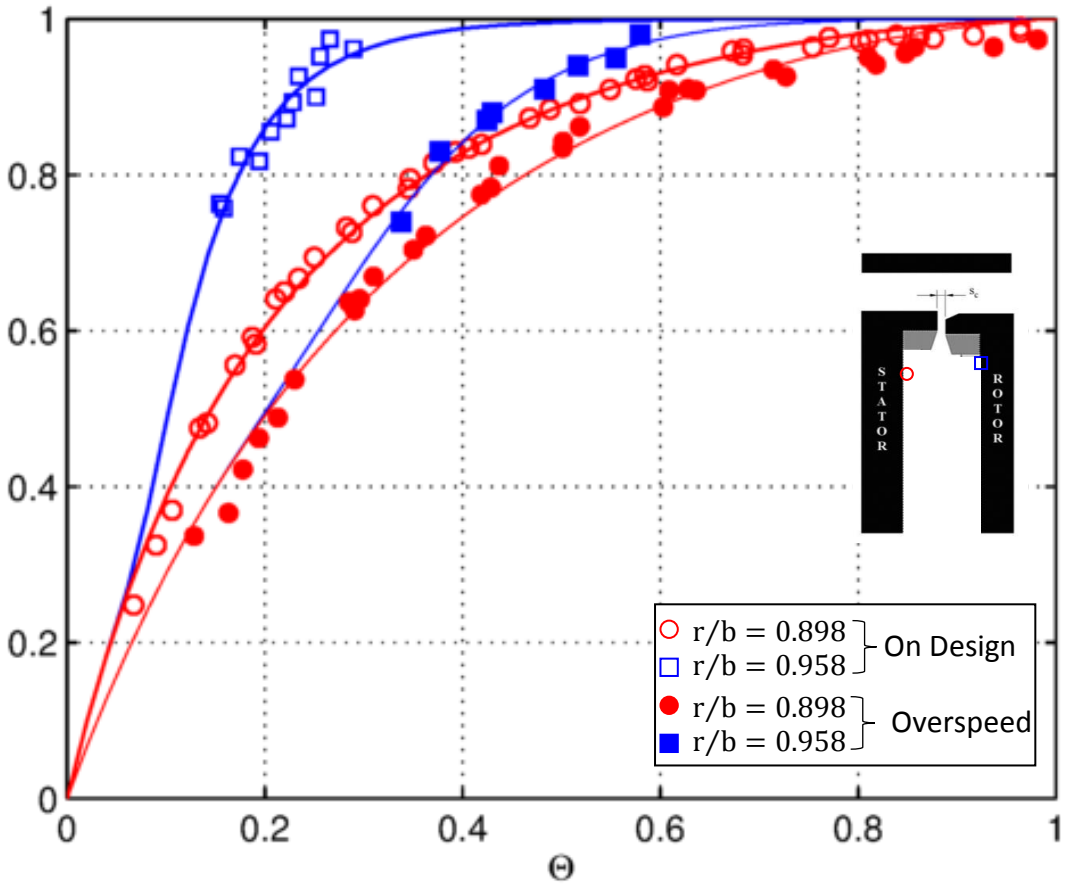

Figure 6.12: Variation of effectiveness with sealing flow rate for single axial-clearance seal *on-design* and *overspeed* cases of Pountney *et al.* (2012). (Symbols denote experimental data, and curves are determined from theoretical models).

Figure 6.12 shows that once again the fitting of the experimental buffer ratio values has led to good agreement between the experimental and predicted values of rotor effectiveness. All of the important quantities from the models are shown in Table 6.2.

Seal	Φ_{min}	Γ_c	A	n	$[\Delta\varepsilon]_{max}$	Θ_{crit}	$\Phi'_{min,s}$	$\Phi'_{min,r}$
Axial (On Design)	0.275	0.348	0.036	1.80	0.257	0.204	0.181	0.077
Axial (Overspeed)	0.118	0.687	0.504	1.62	0.139	0.388	0.088	0.063

Table 6.2: Summary of empirical constants for fitting data of Pountney *et al.* (2012)

6.5 COMPARISON WITH BUFFER RATIO OF TIAN *ET AL.* (2014)

As originally discussed in the literature review Section 2.3.4, previously published works have given different definitions of buffer ratio. This section gives context for the work shown in this chapter and shows the work agrees with conclusions of recently published work.

Tian *et al.* (2014) defined a thermal buffer ratio as $\eta := \varepsilon_s/\varepsilon_r$. By considering the radial distribution of η for three sealing flow rates it was concluded by Tian *et al.* (2014) that the thermal buffer ratio η increases as the sealing flow rate increases, even though only a 1% change was observed (see Figure 6.13).

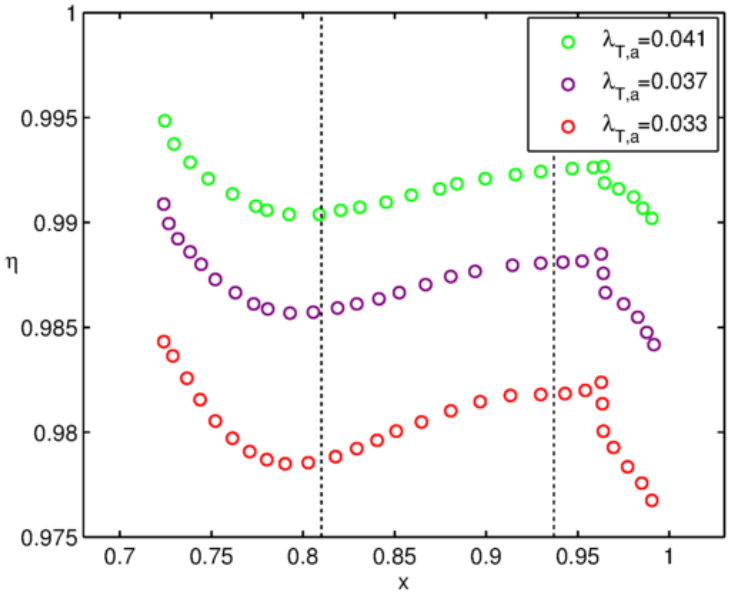

Figure 6.13: Radial variation of thermal buffer ratio for three sealing flow rates [Tian *et al.* (2014)].

By considering the rotor effectiveness measurements from Cho *et al.* (2015) for the axial seal at $x = 0.937$, together with the effectiveness equation fit, the buffer ratio can be calculated for a wider range of flow rates than shown by Tian *et al.* (2014) and the two definitions can be compared.

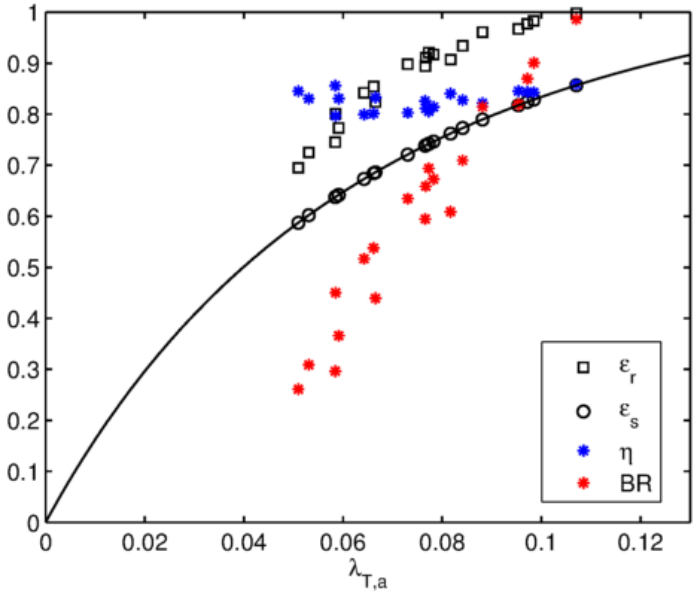

Figure 6.14: Comparison of two buffer ratio definitions using effectiveness measurements of axial seal at $x = 0.937$ from Cho *et al.* (2015)

It was concluded by Tian that the definition of buffer ratio $\eta := \varepsilon_s/\varepsilon_r$ increased with increasing sealing flow rate. It is seen that this is not the case for the Cho data with the Tian definition of buffer ratio. Figure 6.14 shows rotor and stator effectiveness measurements from Cho *et al.* (2015), for the axial seal, which have been used to compute two versions of the buffer ratio. Shown in blue is η, the buffer ratio defined by Tian *et al.* (2014) as $\eta := \varepsilon_s/\varepsilon_r$. The buffer ratio of Tian is fairly constant, meaning it is in line with the findings of Pountney *et al.* (2013) whose definition $\eta := \Phi_o/\Phi_{ad}$ was also constant with increasing sealing flow rate (which was discussed in the literature review). However, shown in red BR is the buffer ratio definition

proposed in this work, defined by (6.4). This definition of buffer ratio *does* increase with increasing sealing flow rate, and is therefore in agreement with the conclusion of Tian *et al.* (2014).

6.6 SUMMARY

In this chapter a simple theoretical model to determine the effect of ingress on turbine discs has been validated using measurements of adiabatic effectiveness obtained from Cho *et al.* (2015). The model is based on the known flow structure in rotor-stator systems along with hypothesised concentration behaviours, which have been informed by experiments. Two new parameters were defined: the *buffer effect*, $\Delta\varepsilon$, which is the difference between the effectiveness of the rotor and stator, and the *buffer ratio*, BR, which is the ratio of the two values of effectiveness. The *buffer effect* quantifies how the sealing air protects the rotor from ingress compared to the stator. The *buffer ratio* simply scales this phenomenon to make it easier to model. Two empirical constants are needed in the model for *BR*, and these constants were determined for both single and double axial and radial seals.

The model showed that the buffering effect for each seal, $\Delta\varepsilon$, is virtually zero at small values of the sealing flow rate. This is important because it means that a significant amount of ingress can occur in the wheelspace before it affects the rotor. For all seals, except the axial seal of Pountney *et al.* (2013) where the gap ratio has changed, it was found that buffering occurred only for flow rates where $\Theta > 0.2$. This gives engine designers an idea of how much sealing flow is needed to start protecting the rotor. The maximum value of the buffering effect was denoted Θ_{crit} and it was found that $0.35 < \Theta_{crit} < 0.53$ for all seals.

For the two single seals tested, there was a negligible effect of the radial location of the measurements on the adiabatic effectiveness of the rotor. It is thought that this is because both measurement locations are in the outer region – where concentration on the rotor is expected to be constant. As such the model fitted both radial locations simultaneously. For the double seals, the values of adiabatic effectiveness were significantly different for the two wheelspaces, meaning the buffering model fitted the two cases separately. In all cases, the adiabatic effectiveness predicted by the model was in good agreement with the experimental measurements.

In order to quantify the protection of the rotor the parameters $\Phi'_{min,s}$ and $\Phi'_{min,r}$ are defined to be the sealing flow rates when $\varepsilon_s = 0.95$ and $\varepsilon_r = 0.95$ respectively; these are listed in Table 6.3. Here $\Phi'_{min,s}$ is significantly greater than $\Phi'_{min,r}$ which implies that the rotor can be protected from the effects of ingress even if the wheelspace is not fully sealed.

Seal	$\Phi'_{min,s}$	$\Phi'_{min,r}$
Axial	0.148	0.086
Radial	0.102	0.073
Double Axial Outer	0.136	0.091
Double Axial Inner	0.099	0.062
Double Radial Outer	0.093	0.073
Double Radial Inner	0.052	0.039

Table 6.3: Comparison of rotor and stator sealing parameters for 95% effectiveness values

It was also shown that even though the definition of buffer ratio is different to those of Pountney *et al.* (2013) and Tian *et al.* (2014), the definition presented here does vary with sealing flow, as concluded by Tian *et al.* (2014).

CHAPTER 7 : CONCLUSIONS

7.1 MOMENTUM-INTEGRAL CAVITY MODELS

It has been shown that the momentum-integral equations can be used to model fluid flow within rotor-stator systems without ingress. The equations can be solved using an iterative scheme that is not computationally intensive and as such could be used within 1D design codes.

Two cavity models based upon numerical solutions to the momentum-integral equations were presented:

- A *Closed Cavity* which has no ingress and no superposed flow
- A cavity with *Superposed Flow, No Ingress*

For both cases the momentum-integral equations were solved in two forms: the first being the *original* momentum-integral equations (as presented by previous authors but never solved in this coupled cavity way) and the secondly *variable* momentum-integral equations. It is the first time the momentum-integral equations have been derived with swirl ratio as a variable of radius, and the equations have been derived not only for the typical $1/7^{th}$ power law, but also in general $1/n^{th}$ power law form, which should provide useful if higher Reynolds number flow is studied. For both cavity models the original equation version, based on the assumption that swirl ratio is constant in the wheelspace, could be solved with a simpler iterative procedure due to there being only four differential equations. This meant the computation time was faster than that of the variable equations.

For the Closed Cavity model the swirl ratio results from the variable momentum-integral equations were higher at each radial location compared with the original results, with a difference of less than 10%. This corresponded to lower pressure coefficients and mass flow rates. These changes led to the moments on the rotor and stator being equal from the results of the variable momentum-integral equations compared to the results from the original momentum-integral equations where there was around a 12% difference. Good qualitative agreement was found between the model and the experimental measurements of swirl ratio and pressure coeffcicents of Sangan *et al.* (2014) for an axial seal. Exact agreement was found for the moment coeffcicients between the model and CFD model of Lalwani (2014).

For the Superposed Flow, No Ingress model a detailed flow structure was hypothesised where the model was separated into two distinct sections: the so called *inner region* (where continuity was not satisfied), and the *core and outer region* (where continuity was satisfied). Both were successfully modelling using the momentum-integral equations. Three models were proposed for the inner region: assuming there was no swirl, constant swirl or a free vortex, along with a no inner region approach. Each of the inner region models was able to capture the key behaviour that increasing x_a, β_a or $\lambda_{T,a}$ increases the value of x_{in} (due to a smaller cavity or it taking longer to entrain the flow). It is thought that the free vortex distribution substituted into the variable equations gave the best model, with the value of x_{in} increasing almost linearly for high values of x_a. Unfortunately these models have not been validated as part of this work and it is hoped that this could be done in the future. The swirl ratios and mass flow rates from the models were then presented for range of flow rates. The mass flow rates confirmed the expected flow structure and the swirl ratios showed the

expected trend that increasing $\lambda_{T,a}$ decreases $\beta(x)$. It was found that the location of the outer region did not vary with sealing flow rate.

The swirl ratios from both the original and variable models were compared to experimental data. The results from the model based upon the original momentum-integral equations showed poor agreement with swirl ratio measurements over a range of flow rates for an axial seal subject to RI ingress. The agreement with measurements for an axial seal subject to EI ingress was qualitatively good, but gave an under prediction. This provides evidence that the original momentum-integral equations are not very good at modelling rotor-stator cavities, and that the extra computational effort of using the variable equations is warranted. The results from the model based upon the variable momentum-integral equations show better agreement with the experimental and computational measurements of swirl ratio and moment coefficients. For an axial seal subject to RI ingress the model initially over predicted the swirl ratio at low sealing flow rates, but as $\lambda_{T,a} \rightarrow \lambda_{T,min}$ agreement variable, with very good agreement at $\lambda_{T,a} = \lambda_{T,min}$. There was also very good agreement between the model based upon the variable equations and the CFD model of Lalwani (2014) that had no ingress present. Given this good agreement it shows this form of modelling has the potential to be just as accurate as CFD only much faster.

The models allowed conclusions to be made about the flow structure within cavities. The Closed Cavity model showed that the maximum mass flow rate reached on the rotor and stator would not change depending on cavity size. The Superposed Flow, No Ingress model showed that even with changing amounts of sealing flow the location of the outer region did not move, this suggests that even as the core is being supressed the region in which the flow is leaving the rotor and entraining onto the stator stays a constant size up.

Given the good agreement for most cases between the cavity models based upon the variable momentum-integral equations and the experimental or computational measurements it can be concluded that the differential swirl ratio term is necessary for accurate modelling, particularly in the presence of sealing flow.

7.2 EFFECT OF INGRESS ON SWIRL RATIO

Leading on from the cavity model with no ingress, where the model under predicted experimental measurements of swirl ratio when ingress was present, it was clear that ingress does affect the swirl ratio. A simple model based upon momentum balance in the seal clearance brought together the cavity model with no ingress and the orifice model to predict the exit swirl ratio in the presence of ingress. The model was able to predict the behaviour of exit swirl for the single and double axial seal well. The model under predicted the exit swirl for the single and double radial seal. There are two possible causes for the under prediction. Either it is caused by the under prediction of Φ_{min} by the effectiveness equations for the single and double radial seals or it is due to an incorrect assumption in the model. It is thought that one possible incorrect assumption could be how ingress affects the wheelspace. It was assumed that all of the ingress flow entering the seal clearance reaches the cavity. An alternative model is suggested where only a fraction of the ingress entering the seal clearance actually reaches the cavity.

7.3 EMPIRICIAL INGRESS MODEL

In a cavity with both ingress and sealing flow, it can be observed from experimental measurements that the rotor is protected from some of the ingress, as effectiveness values are lower on the rotor compared to the stator. This is attributed to the buffering phenomenon. Two new parameters have been defined: the *buffer effect* (which is the difference between the effectiveness of the rotor and stator) and the *buffer ratio* (which is the ratio of the two values of effectiveness). A model for the buffer ratio was presented and then validated against experimental measurements for four different rim seals: axial, radial, double axial and double radial. The model, which depends on two empirical constants A and n, was in good agreement with the experimental data. Given the empirical constants it seems likely that n varies with seal design but not radial location. From quantifying the buffer effect it was found that for each seal $\Delta\varepsilon$ is virtually zero at small values of the sealing flow rate. This is important because it means that a significant amount of ingress can occur in the wheelspace before it affects the rotor. Further to this the model allows the sealing flow rate where the difference between the rotor and stator is at a maximum, denoted Θ_{crit}, to be found. This has interesting design applications for if protecting the rotor was the priority. It was found that $0.35 < \Theta_{crit} < 0.53$ for all seals.

Even though the model for the cavity with both ingress and superposed flow is empirical, whereas the other cavity models have been completely theoretical, it still has use. The buffer ratio model allows rotor effectiveness measurements to be fitted by working together with the already industry established orifice model that is used to fit stator effectiveness measurements. The constants Γ_c and Φ_{min} are currently being integrated into design codes, so with a bit more research there is no reason to stop the buffer ratio model being integrated alongside the orifice model.

7.4 PRACTICAL IMPORTANCE TO THE ENGINE DESIGNER

The purpose of this work has been to offer something new that would be of benefit to industrial engine designers. It has been noted that the typical route of CFD is expensive, time consuming and requires detailed experimental validation. The simple fast mathematical modelling methods presented in this thesis could ultimately to be used in 1D design codes.

The cavity models, based upon the momentum-integral equations, have been used to successfully model the rotor-stator interactions for two key cases. They are able to predict the flow structure, flow rates, swirl ratios and pressure in the wheelspace – all of which is useful information for the designer. These cavity models are a stepping stone to cavity models which would include ingress. As solving the cavity models is not computationally intensive, these could be integrated into design codes.

As well as the cavity models, the empirical model for the buffer ratio could also be of use to engine designers. It has been seen with the orifice model, where empirical constants for the effectiveness equations depend on geometry, that designers can consult a 'bank' of empirical coefficients found for many geometries to inform their designs. A similar approach could be taken for the empirical constants of the buffer ratio model. On top of this, the theoretical model has provided insight into the buffering and can qualitatively inform the designer of secondary air systems.

7.5 FUTURE WORK

Firstly future work based upon the cavity models is considered:

- **Investigation into effects of varying 1/nth power law**
  The equations have been given for a general n power law. This means the results from the cavity models can be explored for different values of n, where higher values may be more appropriate for higher Reynolds number flow.

- **Extension of cavity models to heat transfer**
  For the cavity models, the solutions could be used to predict Nusselt number. This could be done using the Reynolds analogy which allows Nusselt number to be calculated from swirl ratio and shear stress. This would be particularly useful for engine designers, who are always interested in the heat transfer within the wheelspace – especially on the rotor disc where it is difficult to measure temperature changes.

- **Further validation, especially of inner region model**
  Even though three inner region models were presented, none could be validated due to lack of experimental results.

- **Extend model for ingress and superposed flow**
  This work presented cavity models for two cases: a natural progression from the Closed Cavity through to a cavity with Superposed Flow and No Ingress. As the cavity modelling approach based on the variable momentum model works well for these two cases, it would be good to extend these cavities to involve ingress.

- **Integration of model into design codes**
  In 1D design codes, used by engine designers to model the complete engine design, a rotor stator cavity is modelled by single node in a wider network representing the entire engine. Currently this node only attributes a single swirl ratio value to the entire wheelspace, and as such predictions of quantities within the wheelspace are modelled fairly in accurately. The ultimate goal for this work would to see the rotor-stator node updated to encompass a cavity model based on the variable momentum-integral equations that could incorporate ingress and superposed flow, together with Φ_{min} values for the rotor and stator based on the rim seal being implemented.

Secondly future work based upon the empirical model for rotor buffering:

- **Investigation into radial variation of buffer ratio**
  As the effectiveness measurements are only known at two radial locations from Cho *et al.* (2015), the buffer ratio and buffering effect has only been investigated at two radial locations. If experimental measurements were available at a wide radial range it would be of use to investigate if the radial form varied with seal design. This would also allow validation of the descriptions of flow structure in Section 6.1.

- **Correlation for Empirical Constant**
  The empirical constants within the buffer ratio model could be generalised by finding correlations. For example it seems likely that the empirical constant A is a function of Γ_c, but more data is needed to confirm this. A correlation would be extremely useful for engine designers but requires more measurements of adiabatic effectiveness on the rotor for different rim seal geometries.

REFERENCES

Batchelor, G. K., 1951, "Note on a Class of Solutions of the Navier-Stokes Equations Representing Steady Rotationally-Symmetric Flow," Quarterly Journal of Mechanics and Applied Mathematics 4 (1), pp. 29-41.

Bayley, F. J. and Owen, J. M., 1970, “Fluid Dynamics of a Shrouded Disk System with a Radial Outflow of Coolant,” ASME J. Eng. Power, 92(3), pp. 335-341.

Blasius, H., 1908, "The Boundary Layers in Fluids with Little Friction," NACA Technical Memorandum, 1256.

Chew, J. W., 1991, “A Theoretical Study of Ingress for Shrouded Rotating Disk Systems With Radial Outflow,” ASME J. Turbomach. 113(1), pp. 91-97.

Chew, J. W., Green, T. and Turner, A. B., 1994, “Rim Sealing of Rotor-Stator Wheelspaces in the Presence of External Flow,” ASME Paper 94-GT-126.

Coren D., Childs P. R. N., and Long C. A., 2009, “Windage sources in smooth-walled rotating disc systems,” Proc. IMechE Part C: J. Mech. Eng. Sci. 223(1), pp. 873-888.

Childs, P. R. N., 2011, Rotating Flow, Oxford: Butterworth-Heinemann.

Cho, G., Sangan, C. M., Owen, J. M., and Lock, G. D., 2015, “Effect of Ingress on Turbine Discs” ASME Paper GT2015-42324.

Daily, J. W. and Nece, R. E., 1960, “Chamber Dimension Effects on Induced Flow and Frictional Resistance of Enclosed Rotating Disks,” Journal of Basic Engineering, 82(1), pp. 217-230.

Dorfman, L. A., 1963. *Hydrodynamic Resistance and the Heat Loss of Rotating Solids.* Edinburgh, Oliver and Boyd.

Federal Aviation Administration, 2004, *Airplane Flying Handbook*, U.S. Department of Transportation, Federal Aviation Administration, Federal Aviation Administration: 59.

Gentilhomme, O., Hills, N. J., Turner, A. B. and Chew, J. W., 2003, “Measurement and Analysis of Ingestion through a Turbine Rim Seal.” Journal of Turbomachinery 125(3): pp. 505-512.

Grohne, D., 1955, "Über die laminare Stromung in einer Kreiszylindrischen Dose mit rotierendem Deckel." Nachr. Akad. Wiss. Göttingen, Math.-Phys.Kl, pp. 263-282.

Graber, D. J., Daniels, W. A. and Johnson, B. V., 1987, “Disk Pumping Test: Final Report”, Air Force Wright Aeronautical Laboratories.

Hills, N. J., Chew, J. W. and Turner, A. B., 2002, “Computational and Mathematical Modeling of Turbine Rim Seal Ingestion.”, Proceedings of the ASME Turbo Expo 4: pp.1155-1165.

Jakoby, R., Zierer, T., Lindblad, K., Larsson, J., deVito, L., Böhn, D. E., Funcke, J., and Decker, A., 2004, “Numerical Simulation of the Unsteady Flow Field in an Axial Gas Turbine Rim Seal Configuration,” ASME Paper No. GT2004-53829.

Julien, S., Lefrancois, J., Dumas, G., Boutet-Blais, G., Lapointe, S. and Caron, J. F., 2010, “Simulations of Flow Ingestion and Related Structures in a Turbine Disk Cavity,” ASME Paper No. GT2010-22729.

Karman, T. von, 1921, "On Laminar and Turbulent Friction." Zeitschrift Fur anglewandta Mathematik und Mechanik 1(4).

Kreiss, H. O. and S. V. Parter, 1983, "On the Swirling Flow between Rotating Co-Axial Disks - Existence and Non-Uniqueness." Communications on Pure and Applied Mathematics 36(1), pp. 55-84.

Lalwani, Y., 2014 “Computational Modelling of Ingestion through Turbine Rim-Seals,” Thesis (Doctor of Philosophy (PhD)), University of Bath.

Lalwani, Y., Sangan, C. M., Wilson, M., and Lock, G. D., 2015, "Steady Computations of Ingress through Gas Turbine Rim Seals," Proc. IMechE Part A: J. Power and Energy, 229(1), pp. 2-15.

Mear, I., Owen, J. M., and Lock, G. D., 2015, “Theoretical Model to Determine Effect of Ingress on Turbine Discs” ASME Paper GT2015-42326.

Mellor, G. L., Chapple, P. J., and Stokes, V. K., 1968, "On Flow between a Rotating and a Stationary Disk." J. of Fluid Mech, 31(1), pp. 95-112.

Mirzamoghadam, A. V., Heitland, G. and Hosseini, K. M., 2009, “The Effect of Annulus Performance Parameters on Rotor-Stator Cavity Sealing Flow,” Proceedings of the ASME Turbo Expo, pp. 1163-1172.

Morse, A. P., 1991, “Assessment of Laminar-Turbulent Transition in Closed Disk Geometries”. ASME J. Turbomach., 113(1), pp. 131-138.

Myung, I. J., 2001, “Tutorial on Maximum Likelihood Estimation,” Journal of Mathematical Psychology, 47, pp. 90–100.

Nikuradse, J., 1932, "Laws of Turbulent Flow in Smooth Pipes (English translation)." NASA Technical Memorandum.

Owen, J. M., 1988, “An Approximate Solution for the Flow between a Rotating and Stationary Disc,” Paper No. 88-GT-293.

Owen, J. M., 2011a, “Prediction of Ingestion through Turbine Rim Seals. Part I: Rotationally Induced Ingress,” ASME J. Turbomach., 133(3), pp. 031005.

Owen, J. M., 2011b, “Prediction of Ingestion through Turbine Rim Seals. Part II: Externally Induced and Combined Ingress,” ASME J. Turbomach., 133(3), pp. 031006.

Owen, J. M. and Rogers, R. H., 1989, *Flow and Heat Transfer in Rotating-Disc Systems, Volume 1: Rotor-Stator Systems*, Taunton: Research Studies Press Ltd.

Owen, J. M., Zhou, K., Pountney, O. J., Wilson, M., and Lock, G. D., 2012a, “Prediction of Ingress through Turbine Rim Seals. Part 1: Externally-Induced Ingress,” ASME J. Turbomach., 134, pp. 031012.

Owen, J. M., Pountney, O. J., and Lock, G. D., 2012, “Prediction of Ingress through Turbine Rim Seals. Part 2: Combined Ingress,” ASME J. Turbomach., 134, pp. 031013.

Phadke, U. P. and Owen, J. M., 1988a, “Aerodynamic Aspects of the Sealing of Gas-Turbine Rotor-Stator Systems. Part 1: The Behavior of Simple Shrouded Rotating Disk Systems in a Quiescent Environment,” Int. J. Heat Fluid Flow, 9(2), pp. 98-105.

Phadke, U. P. and Owen, J. M., 1988b, “Aerodynamic Aspects of the Sealing of Gas-Turbine Rotor-Stator Systems. Part 2: The Performance of Seals in a Quasiaxisymmetric External Flow,” Int. J. Heat Fluid Flow, 9(2), pp. 106-112.

Phadke, U. P. and Owen, J. M., 1988c, “Aerodynamic Aspects of the Sealing of Gas-Turbine Rotor-Stator Systems. Part 3: The Effect of Nonaxisymmetric External Flow on Seal Performance,” Int. J. Heat Fluid Flow, 9(2), pp. 113-117.

Picha, K. G. and Eckert, E. R., 1958, “Study of the Air Flow between Coaxial Disks Rotating with Arbitrary Velocities in an Open or Enclosed Space,” U.S. Nat. Cong. Appl. Mech.

Pountney, O. J., Sangan, C. M., Lock, G. D. and Owen, J. M., 2013, “Effect of Ingestion on Temperature of Turbine Discs,” ASME J. Turbomach., 135(5), pp. 051010.

Prandtl, L. 1905, “Motion of Fluids with Very Little Viscosity,” 3rd. Int. Math. Kongr. Heidelberg.

Rolls-Royce, 1996, *The Jet Engine*, 5th ed. Derby: Rolls-Royce plc.

Sangan, C. M., 2011, “Measurement of Ingress through Gas Turbine Rim Seals”, Thesis (Doctor of Philosophy (PhD)), University of Bath.

Sangan, C. M., Pountney, O. J., Zhou, K., Wilson, M., Owen, J. M., and Lock, G. D., 2013a, “Experimental Measurements of Ingestion through Turbine Rim Seals. Part 1: Externally-Induced Ingress,” ASME J. Turbomach., 135, pp. 021012.

Sangan, C. M., Pountney, O. J., Zhou, K., Wilson, M., Owen, J. M., and Lock, G. D., 2013b, “Experimental Measurements of Ingestion through Turbine Rim Seals. Part 2: Rotationally-Induced Ingress,” ASME J. Turbomach., 135, pp. 021013.

Sangan, C. M., Pountney, O. J., Scobie, J.A., Wilson, M., Owen, J. M., and Lock, G. D., 2013c, “Experimental Measurements of Ingestion through Turbine Rim Seals. Part 3: Single and Double Seals,” ASME J. Turbomach., 135, pp. 051011.

Sangan, C. M., Lalwani, Y., Owen, J. M., and Lock, G. D., 2014, “Fluid Dynamics of a Gas Turbine Wheel-space with Ingestion,” Proc. IMechE Part A: J. Power and Energy, 228(5), pp. 508-524.

Schlichting, 1968, *Boundary-Layer Theory*, McGraw-Hill Book Company.

Scobie, J., Sangan, C. M., Wilson, M., Lock, G. D., Teuber, R., and Li, Y. S., 2015, “Design of an Improved Turbine Rim-Seal,” ASME Paper GT2015-42327

Stewartson, K., 1953, “On the Flow Between Two Rotating Coaxial Discs,” Proceedings of the Cambridge Philosophical Society, 49(1), pp. 333-341.

Tian, S., Zhang, Y., Su, W., 2014, “Effects of Gas-Ingestion through Turbine Rim Seals on Flow and Heat Transfer in the Wheel-space” ASME Paper GT2014-26635

Wieghardt, K., 1946, “Turbulente Grenzschichten,” Göttinger Monographie, Part 5B.

Zhou, K., Wood, S. N., and Owen, J. M., 2013a, “Statistical and Theoretical Models of Ingestion through Turbine Rim Seals,” ASME J. Turbomach., 135, pp. 021014.

Zhou, K., Wilson, M., Owen, J. M., and Lock, G. D., 2013b, “Computation of Ingestion through Gas Turbine Rim Seals,” Proc. IMechE Part G: J. Aerospace Engineering, 227, pp. 1101-1113.

APPENDIX A : DERIVATION OF VARIABLE MOMENTUM-INTEGRAL EQUATIONS

In the following section the variable momentum-integral equations for the rotor and stator are derived, along with an expression for the differential equation for the swirl ratio. The methodology is the same as for the derivation of the momentum-integral equations presented in the literature review, however now the swirl β is considered a function of radius, so there are extra term when evaluating the derivatives.

The ordinary differential equations, derived from the integrated forms of the Navier Stokes equations for boundary layer flow over discs, as shown in the literature review, are given by:

$$\frac{343}{1656}\frac{d}{dr}\left(r\alpha^2\delta\left(v_{\phi,0}-v_{\phi,\infty}\right)^2\right)-\frac{\delta}{8}\left(v_{\phi,0}^2-v_{\phi,\infty}^2\right)+\frac{\delta}{72}\left(v_{\phi,0}-v_{\phi,\infty}\right)^2=\frac{-r}{\rho}\tau_{r,0} \tag{A1}$$

$$\frac{49}{720}\frac{d}{dr}\left(r^2\alpha\delta\left(v_{\phi,0}-v_{\phi,\infty}\right)^2\right)+\frac{\dot{m}}{2\pi\rho}\frac{d}{dr}\left(rv_{\phi,\infty}\right)=\frac{-r^2}{\rho}\tau_{\phi,0} \tag{A2}$$

$$\dot{m}=\frac{49\pi}{60}r\rho\alpha\left(v_{\phi,0}-v_{\phi,\infty}\right)\delta \tag{A3}$$

where $v_{\phi,0}, v_{\phi,\infty}, \tau_{r,0}, \tau_{\phi,0}, \alpha$ and δ will change depending on whether the rotor or stator is being considered.

A1 EQUATIONS FOR ROTOR

The ordinary differential equations for the rotor are given by (A1), (A2) and (A3) where

- $\tau_{r,0}=0.0225\rho\left(\frac{\mu}{\rho\delta_o}\right)^{\frac{1}{4}}\left(v_{\phi,0}-v_{\phi,\infty}\right)^{\frac{7}{4}}\alpha_o(1+\alpha_o^2)^{3/8}$
- $\tau_{\phi,0}=-0.0225\rho\left(\frac{\mu}{\rho\delta_o}\right)^{\frac{1}{4}}\left(v_{\phi,0}-v_{\phi,\infty}\right)^{\frac{7}{4}}(1+\alpha_o^2)^{3/8}$
- $\delta=\delta_o=\gamma_o\left(x^2Re_\phi\right)^{-\frac{1}{5}}(1-\beta)^{\frac{3}{5}}r$
- $v_{\phi,0}=\Omega r$ and $v_{\phi,\infty}=\Omega r\beta$.

To derive the new variable momentum-integral equations the expressions above are substituted into the equations. First consider equation (A1), with the substitutions defined above, which gives

$$\begin{aligned}&\frac{343}{1656}\frac{d}{dr}\left[r\alpha_o^2\gamma_o\left(x^2Re_\phi\right)^{-\frac{1}{5}}(1-\beta)^{\frac{3}{5}}r(\Omega r(1-\beta))^2\right]\\&-\gamma_o\left(x^2Re_\phi\right)^{-\frac{1}{5}}(1-\beta)^{\frac{3}{5}}r\left[\frac{1}{8}\{(\Omega r)^2-(\Omega r\beta)^2\}-\frac{7}{72}\{\Omega r(1-\beta)\}^2\right]\\&=-r0.0225\left(\frac{\mu}{\rho r}\right)^{\frac{1}{4}}\left(\Omega r(1-\beta)\right)^{\frac{7}{4}}\alpha_o(1+\alpha_o^2)^{\frac{3}{8}}\left[\gamma_o\left(x^2Re_\phi\right)^{-\frac{1}{5}}(1-\beta)^{\frac{3}{5}}\right]^{-\frac{1}{4}}\end{aligned} \tag{A4}$$

Assuming that $\Omega, r, \beta > 0$ to expand to powers the equation becomes

$$\frac{343}{1656}\Omega^2 Re_\phi^{-\frac{1}{5}}\frac{d}{dr}\left(r^4\alpha_o^2\gamma_o\, x^{\frac{-2}{5}}(1-\beta)^{\frac{13}{5}}\right)$$
$$-\gamma_o\left(x^2Re_\phi\right)^{-\frac{1}{5}}(1-\beta)^{\frac{3}{5}}r\frac{(\Omega r)^2(1+8\beta)(1-\beta)}{36} \quad \text{(A5)}$$
$$=-r0.0225\left(\frac{\mu}{\rho\Omega r^2}\right)^{\frac{1}{4}}(\Omega r)^2(1-\beta)^{\frac{8}{5}}\alpha_o(1+\alpha_o^2)^{\frac{3}{8}}\gamma_o^{-\frac{1}{4}}\left(x^2Re_\phi\right)^{\frac{1}{20}}$$

The d/dr term now has to account for β as a function r. Evaluating the derivative in the first term, using the change of variable $x \coloneqq r/b$, dividing each term by $x^{13/5}\alpha_o^2\gamma_o b^3\Omega^2 Re_\phi^{-1/5}(1-\beta)^{13/5}$ and recalling that $\mu/\rho\Omega r^2 = (x^2Re_\phi)^{-1}$ gives

$$\frac{343}{1656}\left(\frac{18}{5}+\frac{2x}{\alpha_o}\frac{d\alpha_o}{dx}+\frac{x}{\gamma_o}\frac{d\gamma_o}{dx}-\frac{13x}{5(1-\beta)}\frac{d\beta}{dx}\right)$$
$$-\frac{(1+8\beta)}{36\alpha_o^2(1-\beta)} \quad \text{(A6)}$$
$$=-\frac{0.0225(1+\alpha_o^2)^{\frac{3}{8}}}{\alpha_o\gamma_o^{5/4}(1-\beta)}$$

Multiplying equation by $Y_o \coloneqq \alpha_o^2\gamma_o$ then rearranged for $d(\alpha_o^2\gamma_o)/dx$ gives,

$$\frac{dY_o}{dx}=\frac{1}{x}\left[\frac{1656}{343}\left\{-0.0225\frac{\alpha_o(1+\alpha_o^2)^{\frac{3}{8}}}{(1-\beta)\gamma_o^{\frac{1}{4}}}+\frac{(1+8\beta)\gamma}{36(1-\beta)}\right\}+\frac{13x}{5(1-\beta)}Y_o\frac{d\beta}{dx}-\frac{18}{5}Y_o\right] \quad \text{(A7)}$$

In order to obtain explicit equations for $d\alpha_o/dx$ and $d\gamma_o/dx$ another expression involving both of these terms needs to be derived. This is done by considering equation (A2) with the same substitutions as for the previous equation,

$$\frac{49}{720b}\frac{d}{dx}\left(\alpha_o\gamma_o b^5 x^{\frac{23}{5}}Re_\phi^{-\frac{1}{5}}(1-\beta)^{\frac{13}{5}}\Omega^2\right)$$
$$+\frac{49}{120}x^3b^4\alpha_o\gamma_o\left(x^2Re_\phi\right)^{-\frac{1}{5}}(1-\beta)^{\frac{8}{5}}\Omega^2\left[2x\beta+x^2\frac{d\beta}{dx}\right] \quad \text{(A8)}$$
$$=\frac{r^2}{\rho}0.0225\rho\left(\frac{\mu}{\rho r}\right)^{\frac{1}{4}}(\Omega x b(1-\beta))^{\frac{7}{4}}(1+\alpha_o^2)^{3/8}\left[\gamma_o\left(x^2Re_\phi\right)^{-\frac{1}{5}}(1-\beta)^{\frac{3}{5}}\right]^{-1/4}$$

Assuming that $\Omega, r, \beta > 0$ to expand to powers and applying the change of variables throughout such that $x \coloneqq r/b$, the equation becomes

$$\frac{49}{720}Re_\phi^{-\frac{1}{5}}b^4\Omega^2\frac{d}{dx}\left(\alpha_o\gamma_o x^{\frac{23}{5}}(1-\beta)^{\frac{13}{5}}\right)$$
$$+\frac{49}{120}x^{13/5}Re_\phi^{-\frac{1}{5}}b^4\Omega^2\alpha_o\gamma_o(1-\beta)^{\frac{8}{5}}\left[2x\beta+x^2\frac{d\beta}{dx}\right] \quad \text{(A9)}$$
$$=Re_\phi^{-\frac{1}{5}}b^4\Omega^2x^{18/5}0.0225\,(1-\beta)^{\frac{8}{5}}(1+\alpha_o^2)^{3/8}\gamma_o^{-\frac{1}{4}}$$

Once again the differential term now has to account for β as a function r. Evaluating the derivative in the first term, dividing each term by $x^{18/5}\alpha_o\gamma_o b^4\Omega^2 Re_\phi^{-1/5}(1-\beta)^{13/5}$ gives,

$$\frac{49}{720}\left(\frac{23+37\beta}{5(1-\beta)}+\frac{x}{\gamma_o}\frac{d\gamma_o}{dx}+\frac{x}{\alpha_o}\frac{d\alpha_o}{dx}+\frac{17x}{5(1-\beta)}\frac{d\beta}{dx}\right)=\frac{0.0225(1+\alpha_o^2)^{\frac{3}{8}}}{\alpha_o\gamma_o^{\frac{5}{4}}(1-\beta)} \quad \text{(A10)}$$

Rearranging the equation for $d\alpha_o\gamma_o/dx$, where $X_o \coloneqq \alpha_o\gamma_o$, gives

$$\frac{dX_o}{dx}=\frac{1}{x}\left[\frac{720}{49}\frac{0.0225(1+\alpha_o^2)^{\frac{3}{8}}}{\gamma_o^{\frac{1}{4}}(1-\beta)}-\frac{17x}{5(1-\beta)}X_o\frac{d\beta}{dx}-\frac{23+37\beta}{5(1-\beta)}\mathrm{X}_o\right] \quad \text{(A11)}$$

Now the equations (A10) and (A6) can be uncoupled to give the final *momentum-integral equations for the rotor:*

$$\frac{d\alpha_o}{dx}=\frac{\alpha_o}{x(1-\beta)}\left[\frac{-6696}{343}F_o+\frac{46(1+8\beta)}{343\alpha_o^2}+6x\frac{d\beta}{dx}+\frac{23+37\beta}{5}-\frac{18}{5}(1-\beta)\right] \quad \text{(A12)}$$

$$\frac{d\gamma_o}{dx}=\frac{\gamma_o}{x(1-\beta)}\left[\frac{11736}{343}F_o-\frac{46(1+8\beta)}{343\alpha_o^2}-\frac{47x}{5}\frac{d\beta}{dx}-2\left\{\frac{23+37\beta}{5}\right\}+\frac{18}{5}(1-\beta)\right] \quad \text{(A13)}$$

where

$$F_o=\frac{0.0225(1+\alpha_o^2)^{\frac{3}{8}}}{\alpha_o\gamma_o^{\frac{5}{4}}} \quad \text{(A14)}$$

The term F_o has no special significance but it makes the equations more compact. Notice that the final two terms in each equation could be simplified, but it is deemed beneficial to keep the symmetry between the two equations. For completion, the equivalent simplified equations are:

$$\frac{d\alpha_o}{dx}=\frac{\alpha_o}{x(1-\beta)}\left[\frac{-6696}{343}F_o+\frac{46(1+8\beta)}{343\alpha_o^2}+6x\frac{d\beta}{dx}+11\beta+1\right] \quad \text{(A15)}$$

$$\frac{d\gamma_o}{dx}=\frac{\gamma_o}{x(1-\beta)}\left[\frac{11736}{343}F_o-\frac{46(1+8\beta)}{343\alpha_o^2}-\frac{47x}{5}\frac{d\beta}{dx}-\frac{4}{5}(23\beta+7)\right] \quad \text{(A16)}$$

The equations in corresponding general n power law form are

$$\frac{d\alpha_o}{dx}=\frac{\alpha_o}{x(1-\beta)}\left[-F_{o,n}\frac{(n+1)(n+2)^2(4n+3)}{3n^3}+\frac{2(\beta+\beta n+1)(3n+2)}{n^3\alpha_o^2}+\frac{2(n+2)}{3}x\frac{d\beta}{dx}+\frac{(4n+5)}{3}\beta+1\right] \quad \text{(A17)}$$

$$\frac{d\gamma_o}{dx}=\frac{\gamma_o}{x(1-\beta)}\left[F_{o,n}\left[\frac{(n+1)(n+2)(8n^2+13n+6)}{3n^3}\right]-\frac{2(\beta+\beta n+1)(3n+2)}{n^3\alpha_o^2}-\frac{d\beta}{dx}x\left[\frac{(4n^2+11n+9)}{3(n+3)}\right]-\frac{2(3\beta+4\beta n^2+11\beta n+9n+21)}{3(n+3)}\right] \quad \text{(A18)}$$

where

$$F_{o,n}=\frac{K(1+\alpha_o^2)^{\frac{n-1}{2(n+1)}}}{\alpha_o\gamma_o^{\frac{n+3}{n+1}}} \quad \text{(A19)}$$

with the subscript n relating to the value of power law used. The rotor and stator equations can be solved independently of each other for different n values if $d\beta/dx = 0$. This allows the effect of varying n to be seen for each equation.

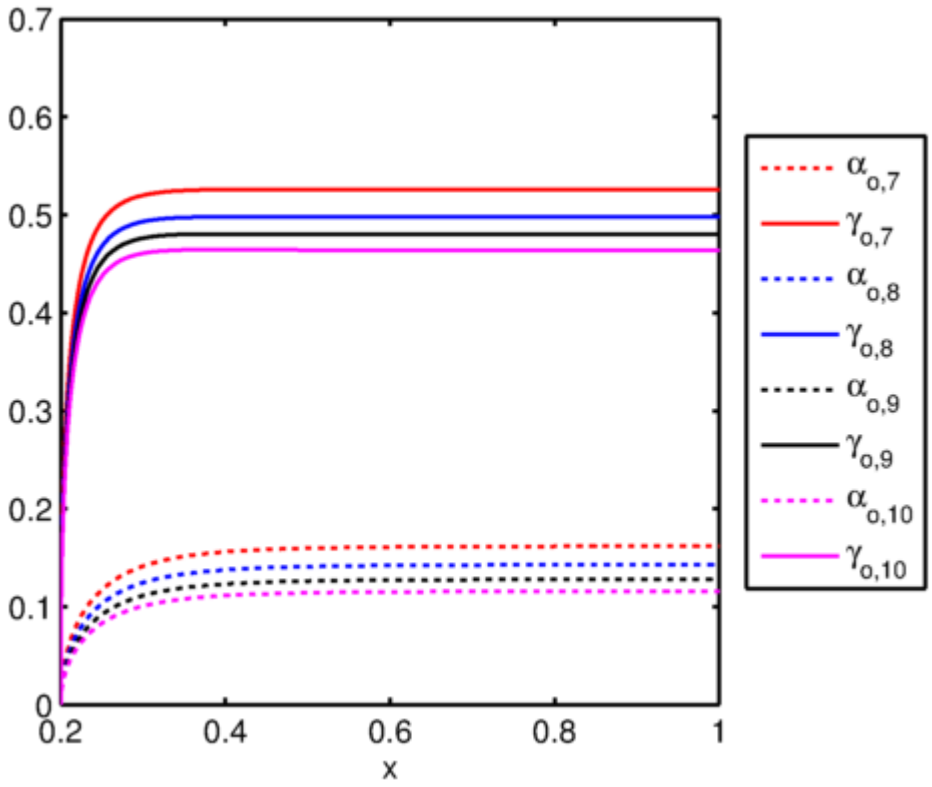

Figure A1.1: Solutions to momentum-integral equations for rotor for general n power law

Figure A1.1 shows the solutions of (A13)(A17) and (A18) solved with $\beta = 0$ for $x_a = 0$. The solid lines denote values of γ_o and the dotted lines values of α_o. Both α_o and γ_o decrease with increasing n.

A2 EQUATIONS FOR STATOR

The ordinary differential equations (A1), (A2) and (A3) can be stated specifically for the stator

$$\frac{343}{1656}\frac{d}{dr}\left(r\alpha_s^2\delta_s\left(v_{\phi,0}-v_{\phi,\infty}\right)^2\right)-\frac{\delta_s}{8}\left(v_{\phi,0}^2-v_{\phi,\infty}^2\right)+\frac{\delta_s}{72}\left(v_{\phi,0}-v_{\phi,\infty}\right)^2 = \frac{-r}{\rho}\tau_{r,0} \tag{A20}$$

$$\frac{49}{720}\frac{d}{dr}\left(r^2\alpha_s\delta_s\left(v_{\phi,0}-v_{\phi,\infty}\right)^2\right)+\frac{\dot{m}_s}{2\pi\rho}\frac{d}{dr}\left(rv_{\phi,\infty}\right)=\frac{-r^2}{\rho}\tau_{\phi,0} \tag{A21}$$

$$\dot{m}_s=\frac{49\pi}{60}r\rho\alpha_s\left(v_{\phi,0}-v_{\phi,\infty}\right)\delta_s \tag{A22}$$

where

- $\tau_{r,0}=0.0225\rho\left(\frac{\mu}{\rho\delta_o}\right)^{\frac{1}{4}}\left(v_{\phi,0}-v_{\phi,\infty}\right)^{\frac{7}{4}}\alpha_s(1+\alpha_s^2)^{3/8}$
- $\tau_{\phi,0}=-0.0225\rho\left(\frac{\mu}{\rho\delta_s}\right)^{\frac{1}{4}}\left(v_{\phi,0}-v_{\phi,\infty}\right)^{\frac{7}{4}}(1+\alpha_s^2)^{3/8}$
- $\delta_s=\gamma_s\left(x^2Re_\phi\right)^{-\frac{1}{5}}\beta^{-\frac{1}{5}}r$

- $v_{\phi,0} = 0$ and $v_{\phi,\infty} = \Omega r\beta$.

To derive the new variable momentum-integral equations the expressions above are substituted into the equations. First consider equation (A20), with the substitutions, which gives

$$\frac{343}{1656}\frac{d}{dr}\left[r\alpha_s^2\gamma_s\left(x^2Re_\phi\right)^{-\frac{1}{5}}\beta^{-\frac{1}{5}}r(0-\Omega r\beta)^2\right]$$
$$-\gamma_s\left(x^2Re_\phi\right)^{-\frac{1}{5}}\beta^{-\frac{1}{5}}r\left[\frac{1}{8}\{-(\Omega r\beta)^2\}-\frac{7}{72}\{(0-\Omega r\beta)\}^2\right] \quad \text{(A23)}$$
$$=-r0.0225\left(\frac{\mu}{\rho r}\right)^{\frac{1}{4}}(0-\Omega r\beta)^{\frac{7}{4}}\alpha_s(1+\alpha_s^2)^{\frac{3}{8}}\left[\gamma_s\left(x^2Re_\phi\right)^{-\frac{1}{5}}\beta^{-\frac{1}{5}}\right]^{-\frac{1}{4}}$$

This can be simplified by grouping like terms, applying the change of variable: $x \coloneqq r/b$ and assuming that $(0-\Omega r\beta)^{\frac{7}{4}} = -(\Omega r\beta)^{\frac{7}{4}}$,

$$\frac{343}{1656}\Omega^2Re_\phi^{-\frac{1}{5}}b^3\frac{d}{dx}\left[x^{\frac{18}{5}}\alpha_s^2\gamma_s\beta^{\frac{9}{5}}\right]$$
$$+\frac{2}{9}\Omega^2Re_\phi^{-\frac{1}{5}}b^3\gamma_s x^{\frac{13}{5}}\beta^{\frac{9}{5}} \quad \text{(A24)}$$
$$=r0.0225\left(\frac{\mu}{\rho\Omega r^2}\right)^{\frac{1}{4}}(\Omega r\beta)^{\frac{7}{4}}(\Omega r)^{\frac{1}{4}}\alpha_s(1+\alpha_s^2)^{\frac{3}{8}}\gamma_s^{-\frac{1}{4}}\beta^{\frac{1}{20}}\left(x^2Re_\phi\right)^{\frac{1}{20}}$$

Now evaluating the differential in the first term and dividing each term by $\Omega^2Re_\phi^{-\frac{1}{5}}b^3x^{13/5}\alpha_s^2\gamma_s\beta^{\frac{9}{5}}$ gives:

$$\frac{343}{1656}\left[\frac{18}{5}+2\frac{x}{\alpha}\frac{d\alpha}{dx}+\frac{x}{\gamma}\frac{d\gamma}{dx}+\frac{9}{5}\frac{x}{\beta}\frac{d\beta}{dx}\right]+\frac{2}{9\alpha_s^2}=\frac{0.0225(1+\alpha_s^2)^{\frac{3}{8}}}{\alpha_s\gamma_s^{\frac{5}{4}}} \quad \text{(A25)}$$

Rearranging the equation for $d\alpha_s^2\gamma_s/dx$, where $Y_s \coloneqq \alpha_s^2\gamma_s$, gives

$$\frac{dY_s}{dx}=\frac{1}{x}\left\{\frac{1656}{343}\left[\frac{0.0225(1+\alpha_s^2)^{\frac{3}{8}}\alpha}{\gamma_s^{\frac{1}{4}}}-\frac{2}{9}\gamma_s\right]-\frac{9xY_s}{5\beta}\frac{d\beta}{dx}-\frac{18}{5}Y_s\right\} \quad \text{(A26)}$$

Now consider second equation (A21) with (A22) and the other substitutions, which gives

$$\frac{49}{720}\frac{d}{dr}\left(r^5\alpha_s\gamma_s\left(x^2Re_\phi\right)^{-\frac{1}{5}}\beta^{-\frac{1}{5}}(\Omega\beta)^2\right)$$
$$-\frac{49\pi\Omega r^3\beta^{\frac{4}{5}}\rho\alpha_s\gamma_s\left(x^2Re_\phi\right)^{-\frac{1}{5}}}{120\pi\rho}\frac{d}{dr}(\Omega r^2\beta) \quad \text{(A27)}$$
$$=\frac{r^2}{\rho}0.0225\rho\left(\frac{\mu}{\rho r}\right)^{\frac{1}{4}}(0-\Omega r\beta)^{\frac{7}{4}}(1+\alpha_s^2)^{\frac{3}{8}}\left[\gamma_s\left(x^2Re_\phi\right)^{-\frac{1}{5}}\beta^{-\frac{1}{5}}\right]^{-\frac{1}{4}}$$

This can be simplified by grouping like terms, applying the change of variable: $x \coloneqq r/b$ and assuming that $(0-\Omega r\beta)^{\frac{7}{4}} = -(\Omega r\beta)^{\frac{7}{4}}$,

$$\frac{49}{720}\Omega^2 b^4 Re_\phi^{-\frac{1}{5}}\frac{d}{dx}\left(x^{23/5}\alpha_s\gamma_s\beta^{\frac{9}{5}}\right)$$
$$-\Omega^2 b^4 Re_\phi^{-\frac{1}{5}}\frac{49}{120}x^{13/5}\beta^{\frac{4}{5}}\alpha_s\gamma_s\left[2x\beta+x^2\frac{d\beta}{dx}\right] \quad \text{(A28)}$$
$$=-Re_\phi^{-\frac{1}{5}}\Omega^2 b^4 x^{\frac{18}{5}}0.0225(1+\alpha_s^2)^{\frac{3}{8}}\gamma_s^{-\frac{1}{4}}\beta^{\frac{1}{20}}\beta^{\frac{7}{4}}$$

Dividing by $\Omega^2 b^4 Re_\phi^{-\frac{1}{5}}x^{\frac{18}{5}}\beta^{\frac{9}{5}}\alpha_s\gamma_s$ and regrouping the terms gives

$$\frac{49}{720}\left[\frac{-37}{5}+\frac{x}{\alpha_s}\frac{d\alpha_s}{dx}+\frac{x}{\gamma_s}\frac{d\gamma_s}{dx}-\frac{21}{5}\frac{x}{\beta}\frac{d\beta}{dx}\right]=-0.0225\frac{(1+\alpha_s^2)^{\frac{3}{8}}}{\alpha_s\gamma_s^{\frac{5}{4}}} \quad \text{(A29)}$$

Rearranging the equation for $d\alpha_s\gamma_s/dx$, where $X_s \coloneqq \alpha_s\gamma_s$, gives

$$\frac{dX_s}{dx}=\frac{1}{x}\left\{\frac{720}{49}\left[\frac{-0.0225(1+\alpha_s^2)^{3/8}}{\gamma_s^{\frac{1}{4}}}\right]+\frac{37X_s}{5}+\frac{21x}{5\beta}X_s\frac{d\beta}{dx}\right\} \quad \text{(A30)}$$

Now uncoupling the two stator equations by using equations (A25) and (A29) gives:

$$\frac{d\alpha_s}{dx}=\frac{\alpha_s}{x}\left[\frac{6696}{343}\left(\frac{0.0225(1+\alpha_s^2)^{\frac{3}{8}}}{\alpha_s\gamma_s^{\frac{5}{4}}}\right)-\frac{1656}{343}\frac{2}{9{\alpha_s}^2}-11-\frac{6x}{\beta}\frac{d\beta}{dx}\right] \quad \text{(A31)}$$

$$\frac{d\gamma_s}{dx}=\frac{\gamma_s}{x}\left[\frac{-11736}{343}\left(\frac{0.0225(1+\alpha_s^2)^{\frac{3}{8}}}{\alpha_s\gamma_s^{\frac{5}{4}}}\right)+\frac{1656}{343}\frac{2}{9{\alpha_s}^2}+\frac{92}{5}+\frac{51x}{5\beta}\frac{d\beta}{dx}\right] \quad \text{(A32)}$$

where the term F_s can be used for simplification, where

$$F_s=\frac{0.0225(1+\alpha_s^2)^{\frac{3}{8}}}{\alpha_s\gamma_s^{\frac{5}{4}}} \quad \text{(A33)}$$

The uncoupled stator equations in corresponding general n power law form are given by

$$\frac{d\alpha_s}{dx}=\frac{\alpha_s}{x}\left[F_{s,n}\frac{(n+1)(n+2)^2(4n+3)}{3n^3}-\frac{(2n+2)(3n+2)}{n^3\alpha_s^2}-\frac{(4n+5)}{3}-\frac{2(n+2)}{3}\frac{x}{\beta}\frac{d\beta}{dx}\right] \quad \text{(A34)}$$

$$\frac{d\gamma_s}{dx}=\frac{\gamma_s}{x}\left[-F_{s,n}\frac{(n+1)(n+2)(8n^2+13n+6)}{3n^3}+\frac{(2n+2)(3n+2)}{n^3\alpha_s^2}+\frac{2(4n^2+11n+3)}{3(n+3)}+\frac{2(n+2)(2n+3)x}{3(n+3)\beta}\frac{d\beta}{dx}\right] \quad \text{(A35)}$$

where

$$F_{s,n}=K\frac{(1+\alpha_s^2)^{\frac{n-1}{2(n+1)}}}{\alpha_s\gamma_s^{\frac{n+3}{n+1}}} \quad \text{(A36)}$$

with the subscript n relating to the value of power law used. As mentioned above the rotor and stator equations can be solved independently of each other for different n values if $d\beta/dx=0$. This allows the effect of varying n to be seen for each equation.

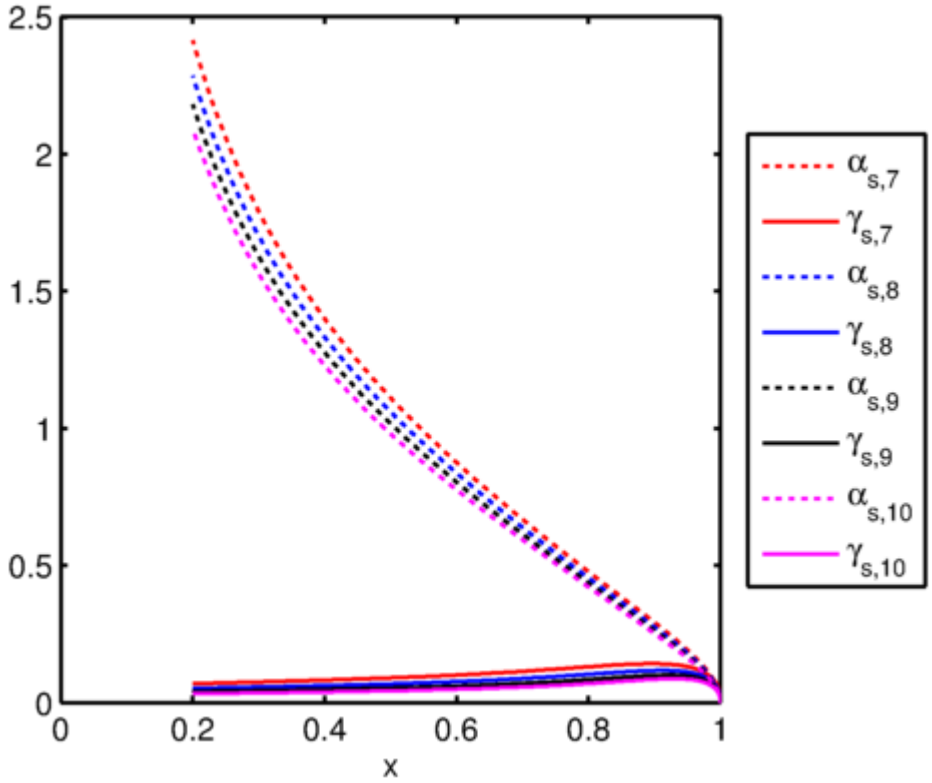

Figure A1.2: Solutions to momentum-integral equations for stator for general n power law

Figure A1.2 shows the solutions of (A13)(A34) and (A35) with $\beta = 0$ and $x_a = 0.2$. The solid lines denote values of γ_s and the dotted lines values of α_s. As for α_o and γ_o with the rotor equations both α_s and γ_s decrease with increasing n.

A3 EQUATION FOR SWIRL RATIO

A3.1 WITHOUT SUPERPOSED FLOW

Starting with the continuity equation for the closed cavity:

$$\alpha_o \gamma_o (1-\beta)^{\frac{8}{5}} = \alpha_s \gamma_s \beta^{\frac{4}{5}} \tag{A37}$$

Differentiate and rearrange, making the differential of swirl the subject, to gain:

$$\frac{d\beta}{dx} = \frac{(1-\beta)^{\frac{8}{5}}\left[\frac{d\gamma_o}{dx}\alpha_o + \gamma_o \frac{d\alpha_o}{dx}\right] - \beta^{\frac{4}{5}}\left[\alpha_s \frac{d\gamma_s}{dx} + \gamma_s \frac{d\alpha_s}{dx}\right]}{\left[\alpha_o \gamma_o \frac{8}{5}(1-\beta)^{\frac{3}{5}} + \alpha_s \gamma_s \frac{4}{5}\beta^{\frac{-1}{5}}\right]} \tag{A38}$$

Substitute in all the differential terms on the right hand side with the equations (A12), (A13), (A31) and (A32). Group the differential beta terms together on the left hand side,

$$\begin{aligned} &\frac{d\beta}{dx}\left[\alpha_o \gamma_o \frac{8}{5}(1-\beta)^{\frac{3}{5}} + \alpha_s \gamma_s 5\beta^{\frac{-1}{5}} + \frac{17}{5}X_o(1-\beta)^{\frac{3}{5}} + \frac{21}{5}X_s\beta^{\frac{-1}{5}}\frac{d\beta}{dx}\right] \\ &= \frac{\alpha_o \gamma_o (1-\beta)^{\frac{8}{5}}}{x}\left[\frac{720}{49}\frac{C_o}{X_o} - \frac{23+37\beta}{5(1-\beta)}\right] - \frac{\alpha_s \gamma_s \beta^{\frac{4}{5}}}{x}\left[-\frac{720}{49}\frac{C_s}{X_s} + \frac{37}{5}\right] \end{aligned} \tag{A39}$$

where

$$C_S = 0.0225\frac{(1+\alpha_s^2)^{\frac{3}{8}}}{\gamma_s^{\frac{1}{4}}} \text{ and } C_o = \frac{0.0225(1+\alpha_o^2)^{\frac{3}{8}}}{\gamma_o^{\frac{1}{4}}(1-\beta)} \tag{A40}$$

such that $F_o \coloneqq C_o/X_o$ and $F_s \coloneqq C_s/X_s$. Once simplified the equation becomes,

$$\frac{d\beta}{dx} = \frac{\frac{\alpha_o\gamma_o(1-\beta)^{\frac{3}{5}}}{x}\frac{720}{49}F_o - \frac{\alpha_s\gamma_s\beta^{\frac{4}{5}}}{x}\left[-\frac{720}{49}F_s + \frac{12}{(1-\beta)}\right]}{5\left[\alpha_o\gamma_o(1-\beta)^{\frac{3}{5}} + \alpha_s\gamma_s\beta^{\frac{-1}{5}}\right]} \tag{A41}$$

By substituting $\alpha_s\gamma_s\beta^{\frac{4}{5}} = \alpha_o\gamma_o(1-\beta)^{\frac{8}{5}}$ into the second term in the numerator there are now common factors for the whole numerator

$$\frac{d\beta}{dx} = \frac{144}{49}\frac{\alpha_o\gamma_o(1-\beta)^{\frac{3}{5}}}{x}\frac{\left\{F_o + F_s(1-\beta) - \frac{49}{60}\right\}}{\left[\alpha_o\gamma_o(1-\beta)^{\frac{3}{5}} + \alpha_s\gamma_s\beta^{\frac{-1}{5}}\right]} \tag{A42}$$

Notice that in order to cancel the numerator with the denominator, the denominator needs to be a product rather than an addition of terms. Using the continuity equation, the following equivalence can be shown to be true:

$$\alpha_o\gamma_o(1-\beta)^{\frac{3}{5}} + \alpha_s\gamma_s\beta^{\frac{-1}{5}} = \frac{\alpha_o\gamma_o(1-\beta)^{\frac{3}{5}}}{\beta} \tag{A43}$$

By substituting (A43) into (A42) the equation becomes

$$\frac{d\beta}{dx} = \frac{144}{49}\frac{\beta}{x}\left\{F_o + F_s(1-\beta) - \frac{49}{60}\right\} \tag{A44}$$

Importantly, this simplified form of the equation, when substituted into equations (A31) and (A32) for the stator removes a possible singularity of $1/\beta$ in the differential equation.

A3.2 WITH SUPERPOSED FLOW

The continuity equation for the case of Superposed Flow, No Ingress is given by,

$$\frac{49\pi}{60}\left[\alpha_o\gamma_o(1-\beta)^{\frac{8}{5}} - \alpha_s\gamma_s\beta^{\frac{4}{5}}\right] = \lambda_{T_a}x^{-\frac{13}{5}} \tag{A45}$$

Differentiating and rearranging the continuity equation:

$$\begin{aligned}&(1-\beta)^{\frac{8}{5}}\left[\frac{d\gamma_o}{dx}\alpha_o + \gamma_o\frac{d\alpha_o}{dx}\right] - \beta^{\frac{4}{5}}\left[\alpha_s\frac{d\gamma_s}{dx} + \gamma_s\frac{d\alpha_s}{dx}\right]\\ &= \frac{d\beta}{dx}\left[\alpha_o\gamma_o\frac{8}{5}(1-\beta)^{\frac{3}{5}} + \alpha_s\gamma_s\frac{4}{5}\beta^{\frac{-1}{5}}\right] - \frac{13}{5}x^{\frac{-18}{5}}\left(\frac{60}{49\pi}\lambda_{T_a}\right)\end{aligned} \tag{A46}$$

Substitute in all the differential terms on the right hand side with the equations (A12), (A13), (A31) and (A32). The differential beta terms can be moved to the right hand side and grouped together,

$$\begin{aligned}&\frac{\alpha_o\gamma_o(1-\beta)^{\frac{8}{5}}}{x}\left[\frac{720}{49}\frac{F_o}{(1-\beta)} - \frac{23+37\beta}{5(1-\beta)}\right] - \frac{\alpha_s\gamma_s\beta^{\frac{4}{5}}}{x}\left[-\frac{720}{49}F_s + \frac{37}{5}\right]\\ &= \frac{d\beta}{dx}5\left[\alpha_o\gamma_o(1-\beta)^{\frac{3}{5}} + \alpha_s\gamma_s\beta^{\frac{-1}{5}}\right] - \frac{13}{5}x^{\frac{-18}{5}}\left(\frac{60}{49\pi}\lambda_{T_a}\right)\end{aligned} \tag{A47}$$

where F_o and F_s are given by (3.3) and (A33) respectively. Rearrange the equation so that $d\beta/dx$ is the subject,

$$\frac{d\beta}{dx}=\frac{1}{5\left[\alpha_o\gamma_o(1-\beta)^{\frac{3}{5}}+\alpha_s\gamma_s\beta^{\frac{-1}{5}}\right]}\left\{\frac{\alpha_o\gamma_o(1-\beta)^{\frac{3}{5}}}{x}\left[\frac{720}{49}F_o-\frac{23+37\beta}{5}\right]-\frac{\alpha_s\gamma_s\beta^{\frac{4}{5}}}{x}\left[-\frac{720}{49}F_s+\frac{37}{5}\right]+\frac{13}{5}x^{\frac{-18}{5}}\frac{60}{49\pi}\lambda_{Ta}\right\} \tag{A48}$$

Use the continuity equation to expand out the term involving λ_{Ta}:

$$\frac{13}{5}x^{\frac{-18}{5}}\frac{60}{49\pi}\lambda_{Ta}=\frac{13}{5x}\left(\frac{60}{49\pi}\lambda_{Ta}x^{-\frac{13}{5}}\right)=\frac{13}{5x}\left[\alpha_o\gamma_o(1-\beta)^{\frac{8}{5}}-\alpha_s\gamma_s\beta^{\frac{4}{5}}\right] \tag{A49}$$

Substituting (A49) into (A48) and regrouping term gives

$$\frac{d\beta}{dx}=\frac{1}{5\left[\alpha_o\gamma_o(1-\beta)^{\frac{3}{5}}+\alpha_s\gamma_s\beta^{\frac{-1}{5}}\right]}\left\{\frac{\alpha_o\gamma_o(1-\beta)^{\frac{8}{5}}}{x}\left[\frac{720}{49}\frac{F_o}{(1-\beta)}-\frac{23+37\beta}{5(1-\beta)}+\frac{13}{5}\right]-\frac{\alpha_s\gamma_s\beta^{\frac{4}{5}}}{x}\left[-\frac{720}{49}F_s+\frac{37}{5}+\frac{13}{5}\right]\right\} \tag{A50}$$

which simplifies to the following by cancelling terms:

$$\frac{d\beta}{dx}=\frac{1}{5x\left[\alpha_o\gamma_o(1-\beta)^{\frac{3}{5}}+\alpha_s\gamma_s\beta^{\frac{-1}{5}}\right]}\left\{\alpha_o\gamma_o(1-\beta)^{\frac{8}{5}}\left[\frac{720}{49}\frac{F_o}{(1-\beta)}-\frac{12}{1-\beta}\right]-\alpha_s\gamma_s\beta^{\frac{4}{5}}\left[-\frac{720}{49}F_s\right]+10\left[\alpha_o\gamma_o(1-\beta)^{\frac{8}{5}}-\alpha_s\gamma_s\beta^{\frac{4}{5}}\right]\right\} \tag{A51}$$

Notice that once again the continuity equation can be used (in the final term), giving,

$$\frac{d\beta}{dx}=\frac{1}{5x\left[\alpha_o\gamma_o(1-\beta)^{\frac{3}{5}}+\alpha_s\gamma_s\beta^{\frac{-1}{5}}\right]}\left\{\alpha_o\gamma_o(1-\beta)^{\frac{8}{5}}\left[\frac{720}{49}\frac{F_o}{(1-\beta)}-\frac{12}{1-\beta}\right]-\alpha_s\gamma_s\beta^{\frac{4}{5}}\left[-\frac{720}{49}F_s\right]+10\left[\frac{60}{49\pi}\lambda_{Ta}x^{-\frac{13}{5}}\right]\right\} \tag{A52}$$

And taking out $720/49$ gives,

$$\frac{d\beta}{dx}=\frac{144}{49x\left[\alpha_o\gamma_o(1-\beta)^{\frac{3}{5}}+\alpha_s\gamma_s\beta^{\frac{-1}{5}}\right]}\left\{\alpha_o\gamma_o(1-\beta)^{\frac{3}{5}}\left[F_o-\frac{49}{60}\right]+\alpha_s\gamma_s\beta^{\frac{4}{5}}F_s+\frac{5}{6\pi}\lambda_{T,a}x^{-\frac{13}{5}}\right\} \tag{A53}$$

It would be beneficial to get this differential equation into a similar form as the differential beta equation when there is no superposed flow (see (A44)). Synonymous with equation (A43) the following expression can be derived from the continuity equation:

$$\alpha_o\gamma_o(1-\beta)^{\frac{3}{5}}+\alpha_s\gamma_s\beta^{\frac{-1}{5}}=\frac{-\frac{60}{49\pi}\lambda_{T,a}x^{-\frac{13}{5}}+\alpha_o\gamma_o(1-\beta)^{\frac{3}{5}}}{\beta} \tag{A54}$$

as

$$\frac{60}{49\pi}\lambda_{T,a}x^{-\frac{13}{5}}=\alpha_o\gamma_o(1-\beta)^{\frac{3}{5}}-\alpha_o\gamma_o(1-\beta)^{\frac{3}{5}}\beta-\alpha_s\gamma_s\beta^{\frac{-1}{5}}\beta$$

$$\Rightarrow \alpha_o\gamma_o(1-\beta)^{\frac{3}{5}}\beta+\alpha_s\gamma_s\beta^{\frac{-1}{5}}\beta=-\frac{60}{49\pi}\lambda_{T,a}x^{-\frac{13}{5}}+\alpha_o\gamma_o(1-\beta)^{\frac{3}{5}}$$

Notice that if $\lambda_{T,a} = 0$ then (A43) is exactly (A54). Substituting (A54) into the denominator of (A53) gives

$$\frac{d\beta}{dx} = \frac{144}{49x}\frac{\beta}{\left[-\frac{60}{49\pi}\lambda_{T,a}x^{-\frac{13}{5}} + \alpha_o\gamma_o(1-\beta)^{\frac{3}{5}}\right]}\left\{\alpha_o\gamma_o(1-\beta)^{\frac{3}{5}}\left[F_o - \frac{49}{60}\right] + \alpha_s\gamma_s\beta^{\frac{4}{5}}F_s + \frac{5}{6\pi}\lambda_{T,a}x^{-\frac{13}{5}}\right\} \quad \text{(A55)}$$

Finally, substitute the continuity equation to replace the final $\alpha_s\gamma_s\beta^{\frac{4}{5}}$ term and simplify to give

$$\frac{d\beta}{dx} = \frac{144}{49}\frac{\beta}{x}\frac{\alpha_o\gamma_o(1-\beta)^{\frac{3}{5}}}{\left[-\frac{60}{49\pi}\lambda_{T,a}x^{-\frac{13}{5}} + \alpha_o\gamma_o(1-\beta)^{\frac{3}{5}}\right]}\left\{F_o - \frac{49}{60} + F_s(1-\beta) + \frac{60}{49\pi}\frac{\lambda_{T_a}x^{-\frac{13}{5}}}{\alpha_o\gamma_o(1-\beta)^{\frac{3}{5}}}\left[\frac{49}{72} - F_s\right]\right\} \quad \text{(A56)}$$

If $\lambda_{T,a} = 0$ is set in equation (A56) then it is equivalent to equation (A44).